

**Development of natural silicate minerals based antibacterial
and fluorometric sensors for heavy metal detection in
wastewater and living cells**

Thesis submitted to
Jadavpur University



by

Souravi Bardhan

In partial fulfillment of the requirements for the degree of
Doctor of Philosophy (Ph. D.) in Science

Department of Physics, Jadavpur University

Jadavpur, Kolkata- 700032

India

2022

যাদবপুর বিশ্ববিদ্যালয়
কলকাতা-৭০০০৩২, ভারত



JADAVPUR UNIVERSITY
KOLKATA-700032, INDIA

FACULTY OF SCIENCE : DEPARTMENT OF PHYSICS

Prof. Sukhen Das
MBA, M.Sc, Ph.D

Department of Physics
Jadavpur University
Kolkata 700032, India
E-mail sukhendas29@gmail.com
Tele Fax +91 3324138917

CERTIFICATE

This is to certify that the thesis entitled "Development of natural silicate minerals based antibacterial and fluorometric sensors for heavy metal detection in wastewater and living cells" submitted by Smt. Souravi Bardhan (Registration No: SOPHY1120618; Index No: 206/18/Phys./26); registered on 26th September, 2018) for the award of Ph.D (Science) degree of Jadavpur University, is absolutely based upon her own work under the supervision of Prof. Sukhen Das and that neither this thesis nor any part of it has been submitted for either any degree/ diploma or any other academic award anywhere before.

Sukhen Das
16/03/2022

Prof. Sukhen Das

(Supervisor)

Department of Physics,
Jadavpur University,
Kolkata – 700032, India



Prof. Sukhen Das
Department of Physics,
Jadavpur University
Kolkata-700032

যাদবপুর বিশ্ববিদ্যালয়
কলকাতা-৭০০০৩২, ভারত



JADAVPUR UNIVERSITY
KOLKATA-700 032, INDIA

FACULTY OF SCIENCE : DEPARTMENT OF PHYSICS

Prof. Sukhen Das
MBA, M.Sc, Ph.D

Department of Physics
Jadavpur University
Kolkata 700032, India
E-mail sukhendas29@gmail.com
Tele Fax +91 3324138917

Certificate of similarity check for plagiarism verification

This is to certify that the plagiarism checking for this thesis authored by Smt. Souravi Bardhan has been performed using professional plagiarism prevention software iThenticate. According to the report generated after plagiarism checking there is 09 % similarity in this thesis, which is in category "Level O" (minor similarities) as per "Promotion of Academic Integrity and Prevention of Plagiarism in Higher Educational Institutions Regulations, 2018" of University Grant Commission (UGC) of India. All sentences written/rewritten by providing proper references (treated as quoted work). references (bibliography), table of content, preface, acknowledgements, generic terms used in the subject area of the present thesis, a common knowledge or coincidental terms up to 10 (ten) consecutive words (as prescribed in the above said UGC Regulation up to 14 (fourteen) terms for such common knowledge or coincidental terms can be excluded) and own works of the candidate published in peer reviewed journals (those papers are attached in the thesis) are excluded from similarity checking. It is certified that the present thesis submitted by Souravi Bardhan is plagiarism free and she has followed standard norms of academic integrity and scientific ethics.

Sukhen Das
76/03/2022

Prof. Sukhen Das

(Supervisor)

Department of Physics,
Jadavpur University,
Kolkata – 700032, India



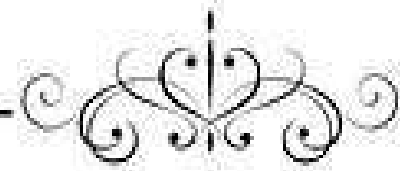
Prof. Sukhen Das
Department of Physics,
Jadavpur University
Kolkata-700032

Declaration

I, hereby, declare the matter described in the thesis entitled, “**Development of natural silicate minerals based antibacterial and fluorometric sensors for heavy metal detection in wastewater and living cells**” is the result of the investigation carried out by me at the Department of Physics, Jadavpur University, Kolkata, India, under the supervision of **Prof. Sukhen Das**. Neither this thesis nor any part thereof has been submitted elsewhere for the award of any degree or diploma.

Souravi Bardhan 16/3/22
Souravi Bardhan

Research Scholar
Department of Physics
Jadavpur University
Kolkata-700032, India



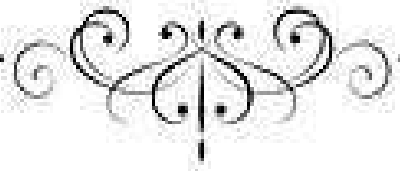
Dedicated to:

My Beloved Family

&

My Supervisor

For their endless Love, Support and Motivation



Abstract

Development of natural silicate minerals based antibacterial and fluorometric sensors for heavy metal detection in wastewater and living cells

Souravi Bardhan

Index No.: 206/18/Phys./26

Registration No.: SOPHY1120618

Various anthropogenic activities like unplanned urbanization and rapid industrialization due to increasing population are ultimately leading to uncontrolled contamination and irreparable damage to the ecosystem. Among the various water pollutants, heavy metal pollution is considered to be one of the crucial issues to be paid immediate attention due to their high toxicity and tendency of bioaccumulation. Detecting the presence of such heavy metals in real-life water is a major challenge in the current time. Compared to other traditional techniques, fluorometric sensing of heavy metals has gained immense popularity due to their several advantages, like high selectivity and sensitivity, ease in onsite handling, no requirement for pre-treatment, and rapid visibility. These eco-friendly, biocompatible, cost-effective, and easily synthesizable sensor materials do not cause secondary pollution and are thus highly desirable for industrial purposes. This work aims toward the synthesis of such fluorescent sensors for heavy metal detection which also exhibits antibacterial properties. Silicate minerals, rather feldspar is the most abundant mineral on earth's crust, yet insufficient interest has been paid on its application as a fluorometric probe. Being a natural compound, it can be quite significant for industrial applications, but very little literature dealt with its optical, electrical, or biological properties. Thus, in this thesis, two naturally formed silicates were used, namely microcline (alkali feldspar, $KAlSi_3O_8$) containing potassium within its structure, and kyanite (Al_2SiO_5), which is devoid of any alkali element like potassium in its structure. Initially, both the collected minerals were ground to their nano-domain by using a ball mill grinder. Three size fractions were obtained, coarse, intermediate, and nano-sized fractions. Detailed characterizations were performed and size-dependent enhancement of electrical and antibacterial properties was analyzed. Further nitrogenous carbon dot was incorporated into the nano-sized minerals in order to enhance their fluorescence properties. While carbon dot-loaded microcline (MCD)

Souravi Bardhan
16/3/22

Sukhen Das
16/03/2022



Prof. Sukhen Das
Department of Physics,
Jadavpur University
Kolkata-700032

successfully exhibited dual sensing of two toxic heavy metals (Fe^{3+} and Cr^{6+}), kyanite could only sense Cr^{6+} (KYCD). Their application as biosensors was also determined and theoretical validation of the sensing mechanism was conducted by employing molecular docking simulations. Further, to achieve a free-standing fluorescent sensor device, MCD, which effectively detects two heavy metals was added into the polymer matrix of poly (vinylidene fluoride-co-hexafluoropropylene) or PVDF-HFP for repetitive use. This membrane exhibited high flexibility, durability, and immense stability under various conditions. Moreover, it can efficiently sense both Fe^{3+} and Cr^{6+} even in real-life water and wastewater. The rapid fluorometric quenching is also visible to the naked eyes under UV illumination. Thus, such natural-mineral-based sensors open up avenues for a wide range of sensor development which can be industrially feasible and significantly perform under harsh environmental conditions without degradation with time.

Souravi Bera
16/3/22

Sukhen Das
16/03/2022



Prof. Sukhen Das
Department of Physics,
Jadavpur University
Kolkata-700032

Outline of the thesis

The aim of the present thesis is to design a natural silicate-based biocompatible, and effective fluorescent sensor for heavy metal ions (Cr^{6+} and Fe^{3+}) having efficient antibacterial efficacy. This includes the following seven chapters to elaborate the works.

Chapter-1: This chapter explores the general background as well as motivation and genesis of the work along with some literature review regarding the present national and international scenario. A brief overview of the silicates minerals (microcline and kyanite) and the various characterization tools adopted are also provided.

Chapter-2: The present chapter illustrates the details of the synthesis procedure of the nano-microcline (M2) and nano-kyanite (KY2), and their comprehensive and meticulous characterization. This chapter also deals with a comparative study on the structural and microstructural properties and size-dependent enhancement of optical and electrical properties.

Chapter-3: In this chapter, the determination of biocompatibility of microcline and kyanite samples along with their size-dependent antibacterial activities are being discussed.

Chapter-4: This chapter deals with the development of carbon dot-loaded nano-microcline and kyanite-based fluorometric sensors and their applications in real-life samples.

Chapter-5: This chapter reports the development of flexible and reusable fluorescent membrane for industrial applications.

Chapter-6: Concludes the whole work presented in the thesis and also depicts a little perception about the future scope and possibility of the current work.

Henceforth, this thesis is directed towards handling environmental issues with materials obtained from the environment itself, or it can be stated as *'from the nature, for the nature'*.

Acknowledgment

"I can no other answer make but thanks,

And thanks; and ever thanks..."

William Shakespeare

As I sit down to pen my Ph.D. thesis, I reminisce about what has been an amazing journey. A journey made memorable by a group of outstanding and wonderful people to whom I owe a great debt of gratitude. Looking over the past few years, I have a great desire to express my deepest gratitude to those I have encountered along my Ph.D. journey, without whom this journey would have been incomplete. It is a pleasure to take the opportunity to acknowledge them all for their unwavering support, motivation, and contribution not only to my work but also to influence me and my growth as a human being.

A journey that began in the winters of 2015 when a sudden call came from my well-wisher and my college teacher-cum-colleague, Dr. Moumit Roy Goswami, Head, Department of Environmental Science, Netaji Nagar College for Women, Kolkata. He introduced me to my supervisor Prof. Sukhen Das and his group for the first time. This journey would have been never possible without his continuous support and immense faith in me. Constant support and continuous guidance from Ruma Di (Dr. Ruma Basu, Dept. of Physics, Jogamaya Devi College, Kolkata) and Prof. Papiya Nandy (Ex-Faculty, Dept. of Physics, Jadavpur University) with their scientific inputs and constructive criticisms have been immensely helpful towards the fruition of my work.

During my initial days in this prestigious institution, my seniors like Nur Da, Swagata Di, Subrata Da, Somtirtha Di, Bala Da, Biplab Da, Srimoyee Di, Monalisa Di, Santanu Da, Tanumay Da, Arpan Da, Rituparna Di, Farha Di, and Paulami Di have been a constant support and motivation. Their friendly attitude towards me helped me to develop my confidence radically. I never expected to meet such a group of dynamic, skilled, and enthusiastic juniors Dhananjay, Aliva, Subhojit, Ishita, Prosenjit, Tanmoy, Debbethi, Debmalya, Namrata, Indrajit, Piyali, Manisha, Shuvronil, Leenia, Sanghita, Barsha, Kaustav, Shaaista, and Shivam. Their immense support, friendly nature, kind efforts, and respect towards me are something I will remember throughout my life. Even my lab mates and friends Anupam, Subha, Dheeraj, Satarupa, Minarul Da Somen Da, and Ananda Da helped me and saved me

from any difficulties. I will specially mention four names, Saheli, Solanky, Jhilik, and Shilpa, who has been beside me through thick and thin, without whom such journey would have never been so smooth. They are more like my friends-cum-sisters than lab mates. This journey would have been incomplete without the immense help received from Dipak Da (Dr. Dipak Kr. Chanda, CGCRI), who have always agreed to help me with all possible means.

This Ph.D. journey not only helped me to hone my skills, meet eminent personalities and friends, this journey also introduced me to my husband Shubham Roy. His continuous motivation, skillful hands and thinking capacity, immense faith in me, and unconditional love became one of the pillars of my journey.

A lifetime opportunity of taking part in the Anveshan-2019 organized by the Association of Indian Universities boosted my confidence a lot. The immense help and support from Dr. Rajat Ray, Dean of Students, Jadavpur University during the zonal and national competitions helped us to achieve second position in the finale.

I am thankful to the Department of Science and Technology, Govt. of India for providing me the SERB fellowship (EEQ/2018/000747) to continue my research work. The instrument and chemical suppliers Monoranjana babu (Mono Enterprise), Sayak (Equations group), and Kallol da (K. K. Enterprise) never let me down. Being a "foodie", sips of tea and snacks from the stalls of Joydeb da, Mama, Hara da, and Milan da, accompanied by brisk chats with my campus friends was a boost to my energy towards my work.

Last but not the least, I take this opportunity to express my gratitude to my 'Thamma', 'Baba' and 'Ma' and for accepting my decision to pursue Ph.D. They have always motivated me to chase my dreams and provided all possible help whenever required.

Thank you all...

Souravi Bardhan
(Souravi Bardhan) 16/3/22

Contents

ABBREVIATIONS

LIST OF PUBLICATIONS

LIST OF CONFERENCES/ SEMINARS ATTENDED

LIST OF AWARDS

LIST OF FIGURES

LIST OF TABLES

Chapter 1: Introduction: Literature review & methodology

1.1 Introduction to heavy metal pollution	1
1.1.1 Sources and behaviour of toxic heavy metals	3
1.1.2 Heavy metals mobility in the aquatic environment.....	7
1.1.3 Global scenario of heavy metal pollution.....	8
1.1.4 Indian status of heavy metal pollution.....	9
1.2 Techniques for heavy metal detection.....	10
1.2.1 Conventional techniques for heavy metal detection	10
1.2.2 Non-conventional techniques for heavy metal detection	11
1.2.2.1 Fluorescent sensors.....	12
1.2.2.2 Colorimetric sensors.....	12
1.3 Application of nanoparticles for fluorometric sensing of heavy metals.....	13
1.4 Background of the present work.....	16
1.5 Material selection.....	18
1.6 Preparation of natural silicate minerals (microcline and kyanite) for sensing and biological applications.....	19
1.7 Instrumentation and sample preparation for different characterization	

Techniques.....	20
1.7.1 Structural and morphological characterizations.....	20
1.7.1.1 X-Ray Diffraction (XRD)	20
1.7.1.2 Field Emission Scanning Electron Microscopy (FESEM)	21
1.7.1.3 Transmission Electron Microscope (TEM)	21
1.7.2 Purity and bonding network analysis.....	22
1.7.2.1 Fourier Transform Infrared Spectroscopy (FTIR)	22
1.7.2.2 Energy-Dispersive X-ray Spectroscopy (EDS) and elemental Mapping.....	22
1.7.3 Surface property analysis.....	23
1.7.3.1 Brunauer-Emmett-Teller (BET) and Barrer-Joyner-Halenda (BJH) methods.....	23
1.7.4 Thermal stability analysis.....	23
1.7.4.1 Thermo-Gravimetric Analysis (TGA)/Differential Thermal Analysis (DTA)	23
1.7.5 Optical property analysis.....	24
1.7.5.1 Ultraviolet-Visible (UV-Vis or UV/Vis) spectroscopy.....	24
1.7.5.2 Fluorescence spectroscopy.....	25
1.7.5.3 Time-Correlated Single Photon Counting (TCSPC) technique.....	26
1.7.6 Electrical characterization.....	26
1.7.6.1 Impedance Spectroscopy (LCR meter)	26
1.8 Theoretical techniques.....	28
1.8.1 Rietveld Refinement.....	28
1.8.2 Density Functional Theory (DFT)	28

Chapter 2: Synthesis and characterization of microcline and kyanite in varying sizes to assess their application domain

2.1 Overview.....	36
2.2 Materials and methods.....	37
2.3 Characterization techniques of coarse-sized (M1 and KY1) and finer-sized (M2 and KY2) samples.....	37
2.3.1 Physical characterization of different size fractions of (M1 and M2), and kyanite (KY1 and KY2)	37
2.3.2 Elemental analysis of nano-sized microcline (M2) and kyanite (KY2)	41
2.3.3 Optical characterization of microcline and kyanite.....	42
2.3.4 Electrical characterization of different size fractions of microcline and kyanite.....	43
2.4 Summary.....	48

Chapter 3: Investigation of biocompatibility & antibacterial efficacy of bulk microcline (M1), kyanite (KY1) & their nano-fractions (M2 and KY2)

3.1 Overview.....	52
3.2 Methodology.....	53
3.2.1 Materials.....	53
3.2.2 Biocompatibility assay.....	54
3.2.3 Antibacterial assay.....	54
3.2.3.1 Determination of bacterial viability.....	54
3.2.3.2 Determination of reactive oxidative species (ROS) and bacterial morphological changes.....	56
3.3 Results and Discussion.....	56
3.3.1 Determination of biocompatibility.....	56
3.3.2 Bacterial viability assay.....	57
3.3.3 Mechanisms of Bacterial Growth Inhibition.....	59
3.3.3.1 Oxidative stress generation.....	59
3.3.3.2 Physical interaction of bacteria with samples and bacteria.....	60
3.4 Summary.....	61

Chapter 4: Development of carbon dot loaded nano-microcline (MCD) & nano-kyanite-based (KYCD) fluorometric sensors for Cr⁶⁺ & Fe³⁺ detection in industrial wastewater & living cells

4.1 Overview.....	66
4.2 Methodology.....	67
4.2.1 Materials.....	67
4.2.2 Synthesis of fluorescent nano-sensors.....	68
4.3 Results and discussion.....	69
4.3.1 Structural and morphological analyses.....	69
4.3.2 Determination of optical quality.....	74
4.3.3 MCD and KYCD as a fluorometric probe.....	76
4.3.4 Investigation of the mechanism responsible for the quenching process.....	80
4.3.5 Determination of sensing efficacy of MCD and KYCD for real-life Applications.....	82
4.3.6 Biosensing application.....	83
4.4 Summary.....	84

Chapter 5: Fabrication of a flexible and reusable membrane using carbon dot decorated natural microcline (MCPV): A futuristic probe for multiple heavy metal induced carcinogen

5.1 Overview.....	88
5.2 Experimental details.....	89
5.2.1 Materials.....	89
5.2.2 Fabrication of fluorescent sensor membrane.....	89
5.3 Results and discussion.....	90
5.3.1 Physical characteristics of the microcline-carbon dot loaded PVDF-HFP membrane (MCPV)	90
5.3.2 Determination of thermal stability of MCPV membrane.....	91
5.3.3 Optical characteristics of the MCPV membrane.....	92
5.3.4 Estimation of fluorescence stability the sensor membrane.....	94
5.3.5 Fluorometric detection of the heavy metals in aqueous media using MCPV membrane.....	95
5.3.6 Mechanism of detection.....	98
5.3.7 Performance of the sensor membrane in various conditions.....	99
5.3.7.1 Sensing efficacy of the MCPV membrane in different pH	

conditions.....	99
5.3.7.2 Sensing efficacy of the MCPV membrane in different water sources.....	100
5.3.7.3 Sensing efficacy when used in a repetitive manner.....	102
5.3.8 Heavy metal induced early-stage carcinogen detection applications.....	102
5.4 Summary.....	103

<i>Chapter 6: Conclusion and perspective.....</i>	108
--	------------

Thesis publications

Certificates of conferences & seminars

Certificates of awards

Abbreviations

Abbreviation	Expansion
μM	Micromoles
Ac	Alternating current
BET	Brunauer, Emmett, Teller
BJH	Barrett, Joyner, Halenda
Cdot	Carbon dot
DFT	Density functional theory
DMF	Dimethyl formamide
DMSO	Dimethyl sulphoxide
DTA	Differential thermal analysis
<i>E. coli</i>	<i>Escherichia coli</i>
FESEM	Field emission scanning electron microscopy
FRET	Forster resonance energy transfer
FTIR	Fourier transform infrared spectroscopy
FWHM	Full width at half maximum
HFP	Hexafluoropropylene
IFE	Inner filter effect
JCPDS	Joint Committee on Powder Diffraction Standards
keV	Kilo electron volt
kV	Kilovolt
MPa	Megapascal
MTT	3(4,5 dimethylthiazol2-yl)2,5-diphenyl tetrazolium bromide
nM	Nanomoles
PET	Photoinduced electron transfer
PL	Photoluminescence
ppm	Parts per million

PVDF	Poly(vinylidene fluoride)
ROS	Reactive oxygen species
<i>S. aureus</i>	<i>Staphylococcus aureus</i>
SV plot	Stern-Volmer's plot
$\tan \delta$	Tangent loss
TDDFT	Time dependent density functional theory
TEM	Transmission electron microscopy
TGA	Thermogravimetric analysis
UV-Vis	Ultraviolet visible spectroscopy
XPS	X-ray Photoelectron Spectroscopy
XRD	X-ray diffraction

List of Thesis Publications

Journal Publications

- [1] **Souravi Bardhan**, Kunal Pal, Shubham Roy, Solanky Das, Abhijit Chakraborty, Parimal Karmakar, Ruma Basu, Sukhen Das *Journal of Nanoscience and Nanotechnology*, 19 (2019) 7112–7122.
- [2] **Souravi Bardhan**, Shubham Roy, Dipak Kr. Chanda, Solanky Das, Kunal Pal, Abhijit Chakraborty, Ruma Basu, Sukhen Das, *Crystal Growth & Design* (2019) 19, 4588-4601.
- [3] **Souravi Bardhan**, Shubham Roy, Dipak Kr. Chanda, Saheli Ghosh, Dhananjoy Mondal, Solanky Das, Sukhen Das, *Dalton Transactions* (2020) 49, 10554.
- [4] **Souravi Bardhan**, Shubham Roy, Dipak Kr. Chanda, Dhananjoy Mondal, Solanky Das, Sukhen Das, *Microchimica Acta* (2021) 188, 134.
- [5] **Souravi Bardhan**, Shubham Roy, Sanghita das, Ishita Saha, Dhananjoy Mondal, Jhilik Roy, Dipak Kr. Chanda, Das, Solanky Das, Parimal Karmakar, Sukhen Das *Spectrochimica Acta Part A: Molecular and Biomolecular Spectroscopy* (2022) 273 121061.

Book Chapters

- [6] **Souravi Bardhan**, Shubham Roy, Mousumi Mitra, Sukhen Das, Metal oxide/ graphene nanocomposites and their biomedical applications, in Metal Oxides for Biomedical and Biosensor Applications. *Elsevier* (2022) pp. 569-584.
- [7] **Souravi Bardhan**, Shubham Roy, Sukhen Das, Carbon dots: Fundamental Concepts and Biomedical Applications, in Nanotechnology for Biomedical Applications. *SpringerNature* (2022) pp. 83-108.

List of Additional Publications

Journal Publications

- [8] Shubham Roy, **Souravi Bardhan**, Kunal Pal, Saheli Ghosh, Paulami Mandal, Santanu Das, Sukhen Das, *Journal of Alloys and Compounds* 763 (2018) 749-758.
- [9] Shubham Roy, Anupam Maity, Paulami Mandal, Dipak Kr. Chanda, Kunal Pal, **Souravi Bardhan**, Sukhen Das, *CrystEngComm*, 20 (2018) 6338-6350.
- [10] Shubham Roy, Kunal Pal, **Souravi Bardhan**, Shilpa Maity, Dipak Kr. Chanda, Saheli Ghosh, Parimal Karmakar, Sukhen Das, *Inorganic Chemistry* (2019) 58, 8369–8378.
- [11] Shubham Roy, **Souravi Bardhan**, Dipak Kr Chanda, Anupam Maity, Saheli Ghosh, Dhananjay Mondal, Subhankar Singh, Sukhen Das, *Materials Research Express* (2020) 7, 025020.
- [12] Shubham Roy, **Souravi Bardhan**, Dipak Kr Chanda, Saheli Ghosh, Dhananjay Mondal, Jhilik Roy, Sukhen Das, *Dalton Transactions* (2020) 49, 6607.
- [13] Shubham Roy, **Souravi Bardhan**, Jhilik Roy, Sukhen Das, *Materials Today: Proceedings* (2021) 46, 6223–6229.
- [14] Shubham Roy, **Souravi Bardhan**, Dipak Kr. Chanda, Jhilik Roy, Dhananjay Mondal, and Sukhen Das, *ACS Applied Materials & Interfaces* (2020) 12, 43833–43843.
- [15] Shubham Roy, **Souravi Bardhan**, Dhananjay Mondal, Ishita Saha, Jhilik Roy, Solanky Das, Dipak Kr. Chanda, Parimal Karmakar and Sukhen Das, *Sensors and Actuators B: Chemical* (2021) p.130662.
- [16] Kunal Pal, Dipranjan Laha, Pravat Kumar Parida, Shubham Roy, **Souravi Bardhan**, Ananya Dutta, Kuladip Jana, Parimal Karmakar, *Journal of Nanoscience and Nanotechnology*, 19 (2019) 3720–3733.
- [17] Kunal Pal, Shubham Roy, Pravat Kumar Parida, Ananya Dutta, **Souravi Bardhan**, Sukhen Das, Kuladip Jana, Parimal Karmakar, *Materials Science & Engineering C*, 95 (2019) 204–216.

[18] Debbethi Bera, Kunal Pal, **Souravi Bardhan**, Shubham Roy, Rubia Parvin, Parimal Karmakar, Papiya Nandy, Sukhen Das, *Advances in Natural Sciences: Nanoscience and Nanotechnology* (2019) 10(4), 045017.

[19] Saheli Ghosh, Shubham Roy, **Souravi Bardhan**, Nibedita Khatua, Barsha Bhowal, Dipak K. Chanda, Solanky Das, Dhananjoy Mondal, Ruma Basu, Sukhen Das, *Journal of Electronic Materials* (2021) 50, 3836- 3845.

[20] Solanky Das, Dhananjoy Mondal, **Souravi Bardhan**, Shubham Roy, Dipak Kr. Chanda, Anupam Maity, Subhojit Dutta, Kamalakanta Mukherjee, Kaustuv Das, *Journal of Materials Science: Materials in Electronics* (2022) 1-15.

[21] Dhananjoy Mondal, Shubham Roy, **Souravi Bardhan**, Jhulik Roy, Ishita Kanungo, Ruma Basu and Sukhen Das, *Dalton Transactions* (2022) 51, 451-462.

Book Chapters

[22] Shubham Roy, **Souravi Bardhan**, Nur Amin Hoque, Sukhen Das, A Brief Review on Carbon-Based Nano-Systems for Detection of Pollutants in Industrial Wastewater and Living Cells and Their Subsequent Removal Strategies, in *Novel Applications of Carbon Based Nanomaterials*, CRC Press, Taylor and Francis, 2021.

List of Conferences/Seminars Attended

Conferences/ Seminars/Workshops Presented:

[1] Poster presentation on “**Microbiological Study of some Frequently Occurring Minerals: A Pilot Study**” at Jogamaya Devi College on November 21 and 22, 2016.

[2] Poster Presented on “**A Study on Microbial Properties of some Commonly Occurring Minerals**” at the National Symposium on Nanotechnology: From Materials to Medicines and their Social Impact, March 25, 2017 at Birla Industrial and Technological Museum, Kolkata.

[3] Presented Poster on “**A brief study on bacteria-mineral interaction in different structural extents using natural galena**” in International Conference in Chemical Sciences (ETCS) from 26th to 28th February, 2018 at Dibrugarh University.

[4] Oral presentation on “**Natural calcite nanoparticle mediated sensing of hexavalent chromium**” at International Conference on Chemical and Environmental Sciences held on 19th-21st September, 2019 at IEM, Kolkata.

[5] Poster presented on “**Multifunctional fluorescence based Nanosensor for detection and removal of Cr(VI)**” at National Seminar on New Directions in Physical Sciences 2020 held on 25th February, 2020 at Jadavpur University.

[6] Oral presentation on “**Natural nanoparticle based wastewater remediation**” in One Day Workshop on Material Synthesis and Characterization Techniques held on 29th February, 2020 at Jadavpur University.

Conferences/ Seminars/Workshops Participated:

[1] Participated in “**Two day Workshop on Materials Characterization Techniques**” held on 4-5th October, 2016 at Jadavpur University, Kolkata.

[2] Participated in UGC sponsored International Workshop on “**Advanced Hybrid Separation Techniques in Industrial Wastewater Management**” held on 8-9th December, 2017 at Jadavpur University, Kolkata.

[3] Participated in the Poster presentation as co-presenter of “**Boehmite based MFNS for fluorescent sensing and removal: A waste to wealth conversion**” at National Seminar on Physics at Surfaces and Interfaces of Soft Materials held on 26-27th September, 2019 at Jadavpur University.

[4] Participated in the Poster presentation as co-presenter of “**Waste capacitor: A fresh approach to detect and remove Cr(VI) form water and making it an energy harvesting material.**” in the Third International Conference on Material Science (ICMS2020) held on 4-6th March, 2020 at Central University of Tripura.

List of Awards / Grants

[1] Selected from Jadavpur University for **ANVESHAN 2019-Student Research Convention (Eastern Zone)** organized by **Association of Indian Universities (A.I.U.)** held at Central University of Jharkhand, Ranchi during 18th -19th February, 2019 and secured **first position under category of Basic sciences**.

[2] Represented Eastern zone at **National Level of ANVESHAN 2019** held at Ganpat University, Gujarat during 12th-14th March, 2019, and secured **second position under category of Basic sciences**.

[3] Received **Young Researcher Award** by Institute of Scholars, Bangalore on January, 2021 for the journal paper entitled “Nitrogenous carbon dot decorated natural microcline: an ameliorative dual fluorometric probe for Fe^{3+} and Cr^{6+} detection”.

[4] Awarded Department of Science and Technology-Science and Engineering Research Board (**DST-SERB**) **fellowship** from 21st May, 2020.

List of Figures

Chapter 1

Figure 1.1: Present scenario of ongoing water pollution from industrial effluents

Figure 1.2: Heavy metal-mediated cellular damage

Figure 1.3: Mobility of heavy metals like Cr⁶⁺ in aquatic environments

Figure 1.4: Percentage of Cr emission from the industrial sector into water

Figure 1.5: Carbon dot-loaded nanocomposite for optical sensing of heavy metals

Figure 1.6: Various types of fluorometric sensors

Figure 1.7: Different fluorometric sensing pathways depicting (a) FRET-based sensing technique; (b) DFT based determination of PET-based sensing with carbon dots; (c) Inner Filter Effect using carbon dots showing fluorescence quenching.

Figure 1.8: Photographs of Bantala leather complex area, Kolkata taken during wastewater collection from the contaminated canal

Figure 1.9: Raw silicate minerals (a) microcline and (b) kyanite used in the work

Figure 1.10: Illustration of step-down synthesis performed

Figure 1.11: (a) Bruker D8 Advance XRD machine and (b) FESEM (field emission scanning electron microscope) instrument with EDS attachment situated at the Dept. of Physics, JU

Figure 1.12: FTIR 8400S, Shimadzu situated at the Dept. of Physics, JU

Figure 1.13: The DTA-TGA instrument of Dept. of Physics, JU

Figure 1.14: UV-Vis spectrophotometer instrument of the Dept. of Physics, JU; (b) sample chamber

Figure 1.15: Fluorescence spectrophotometer instrument of the Dept. of Physics, JU; (b) sample chamber

Figure 1.16: The Agilent impedance analyzer set up of the Dept. of Physics, JU

Chapter 2

Figure 2.1: Indexed XRD pattern of the sample (a) yellow for AF1, (b) green for AF2, (c) blue for KY1, and (d) grey for KY2, and the simulated Rietveld refinement plot (continuous red line) obtained by fitting the experimental PXRD pattern using the MAUD program. The respective residue is plotted at the bottom (black line).

Figure 2.2: Unit cells of the sample (a) KY1, (b) KY2, (c) M1, and (d) M2, along with their bond angles and bond lengths

Figure 2.3: Normalized FTIR spectra of the samples (a) Microcline (M1 and M2) and (b) Kyanite (KY1 and KY2)

Figure 2.4: FESEM micrographs of (a) M1, (b) KY1, (c) M2, and (d) KY2, with their corresponding TEM images

Figure 2.5: EDS spectra of (a) microcline and (b) kyanite

Figure 2.6: UV–vis spectra of (a) microcline and (b) kyanite, with their corresponding Tauc plot (bandgap) (inset); PL spectra of (c) microcline and (d) kyanite

Figure 2.7: Variation of Dielectric constant with frequency for the samples (a-d); Variation of Dielectric constant with temperature for the samples (e-h); tangent loss ($\tan\delta$) of the samples (i-l) for M1, M2, KY1 and KY2 respectively

Figure 2.8: Variation of ac electrical conductivity with frequency for the samples (a-d) and corresponding Jonscher's plot for the samples (e-h) for KY2, KY1, M2, and M1 respectively

Figure 2.9: Arrhenius plots for the samples (a) M1, (b) KY1, (c) M2, and (d) KY2.

Chapter 3

Figure 3.1: Cell viability (MTT assay) of the mineral samples

Figure 3.2: Plate count images showing visual display of the surviving colonies on agar plates

Figure 3.3: Mortality % calculated from plate counting (MIC) of (a) microcline and (b) kyanite

Figure 3.4: FACS data of (a) control, (b) M1 and (c) M2

Figure 3.5: (a) MTT assay depicting decreasing bacterial cell viability, and (b) intracellular ROS generation

Figure 3.6: FESEM micrographs of *E. coli* (a-c) and *S. aureus* (d-f) depicting increased membrane disruption in successive finer size fractions in comparison to control

Chapter 4

Figure 4.1: Illustration of synthesis route of nitrogenous carbon dot and loading into mineral matrix

Figure 4.2: (a) Experimental (red), refined (black), and difference plot (blue) of XRD pattern of KYCD; (b) microstructural parameters of KYCD obtained from Rietveld refinement and (c-d) subsequent representation of changes observed in bond lengths and bond angles in KY2 (e-f) and KYCD (g-h) due to carbon dot loading

Figure 4.3: (a) Experimental (red), refined (black) and difference plot (blue) of XRD pattern of MCD; (b) microstructural parameters of MCD obtained from Rietveld refinement and (c) subsequent representation of bond lengths and bond angles

Figure 4.4: FT-IR spectra of (a) microcline and MCD, and (b) kyanite and KYCD; FESEM micrograph of (c) MCD and (d) KYCD, with their corresponding TEM (c-d inset)

Figure 4.5: EDS spectra and elemental mapping of KYCD

Figure 4.6: EDS spectra and elemental mapping of MCD

Figure 4.7: (a) N₂ adsorption/desorption isotherm of (a) MCD and (b) KYCD; pore size distribution data for (c) MCD and (d) KYCD

Figure 4.8: UV-Vis spectra of (a) microcline and MCD and (b) kyanite and KYCD; PL spectra depicting the comparison of fluorescence properties of (c) microcline and MCD and (d) kyanite and KYCD

Figure 4.9: Fluorescence stability in the (a) nano-sensors (picture illustrates that of KYCD nanocomposite) and (b) pure carbon dot

Figure 4.10: Selectivity assay for (a-b) MCD and (c) KYCD

Figure 4.11: Dual sensing of MCD upon addition of (a) Fe³⁺ and (b) Cr⁶⁺

Figure 4.12: CIE-1931 colour space analysis of (a) MCD and (c) KYCD and (b, d) naked eye visualization of bright blue fluorescence on exposure to UV light and simultaneous real-life quenching

Figure 4.13: Fluorescence titration data for MCD using (a) Fe^{3+} and (c) Cr^{6+} respectively as the quencher; Stern-Volmer fitting of the corresponding fluorescence quenching data by (b) Fe^{3+} and (d) Cr^{6+} respectively, and (e) fluorescence quenching with the corresponding (f) Stern-Volmer plot for KYCD, inset of (f) illustrates the upward increment due to dynamic quenching at higher concentrations of Cr^{6+}

Figure 4.14: Fluorescence decay profiles of MCD upon the addition of (a) Cr^{6+} and (b) Fe^{3+} ; molecular orbitals and electronic transitions involved in fluorescence quenching upon (c) Cr^{6+} and (d) Fe^{3+} addition

Figure 4.15: Molecular orbitals and electronic transitions involved quenching process in KYCD upon Cr^{6+} addition, with the corresponding decay in fluorescence lifetime (inset)

Figure 4.16: Sensing performances of the MCD and KYCD (a-b) different pH; (c-d) in different water sources; (e-f) Fluorescence quenching observed using industrial wastewater

Figure 4.17: (a-c) Biosensing capacity and cellular permeability studies of the human cervical cancer cell line, which shows bright blue fluorescence on interacting with sensor, but diminishes (d-f) on addition of quencher ion

Chapter 5

Figure 5.1: (a) X-ray diffractogram of MCPV and pure PVDF-HFP film; (b) FTIR spectra of MCPV and pure PVDF-HFP film; (c) FESEM micrograph of the smooth surface of pure PVDF-HFP (d) FESEM micrograph of MCPV with TEM micrographs of carbon dot loaded microcline (inset)

Figure 5.2: TGA and DTA (inset) of (a) PVDF-HFP and (b) MCPV; (c) Tensile strength of PVDF-HFP and MCPV film showing flexibility and mechanical stability of the film (inset)

Figure 5.3: (a) Absorbance spectra of MCPV film; (b) Fluorescence spectra of MCPV at different excitation wavelengths ranging from 370 nm-420 nm; (c) Fluorescence intensity variation of the film for different carbon dots concentration (0 %, 2.5 %, 5 % and 7.5 %) in MCPV; (d) Excitation and emission spectra of the sensor film

Figure 5.4: (a) Time-dependent fluorescence obtained on 240 h study; (d) Fluorescence stability of MCPV at various temperature

Figure 5.5: (a) Selectivity study of the sensor towards various cations and anions; (b) naked eye visualization of bright blue fluorescence on exposure to UV light and simultaneous real-life quenching on exposure to Cr⁶⁺ and Fe³⁺ (c) CIE-1931 colour space analysis of the sensor upon heavy metal exposure

Figure 5.6: Fluorescence titration data for MCPV sensor using (a) Cr⁶⁺ and (b) Fe³⁺ respectively as the quencher; Stern-Volmer fitting of the corresponding fluorescence quenching data by (c) Cr⁶⁺ and (d) Fe³⁺ respectively, with the corresponding whole range of Stern-Volmer plot (inset of c and d) showing an upward increment due to dynamic quenching of the fluorophores at higher concentrations

Figure 5.7: Fitted fluorescence decay profiles of the sensor upon the addition of the heavy metals

Figure 5.8: Molecular orbitals and electronic transitions involved in fluorescence quenching of the sensor upon (a) Cr⁶⁺ and (b) Fe³⁺ addition respectively

Figure 5.9: Sensing performances of the sensor upon Cr⁶⁺ and Fe³⁺ exposure at (a) different pH and (b) different water sources; (c) Fluorescence quenching observed using industrial wastewater and ICP-OES data of the collected tannery wastewater sample (inset); (d) Repetitive sensing using the same MCPV membrane illustrating its reusability

Figure 5.10: (a) Molecular docking simulation depicting interaction between fluorophore and glutathione; (b) Sensing of Cr⁶⁺ and Fe³⁺ in Glutathione solution and simultaneous naked eye observation under UV illumination

List of Tables

Chapter 1

Table 1.1: Types of heavy metals and their effect on human health with their permissible limits in drinking water

Table 1.2: Comparative study between optical sensing mechanisms

Chapter 2

Table 2.1: Structural and microstructural parameters of the samples obtained from Rietveld analysis of XRD pattern

Table 2.2: Calculated activation energies of the samples from Arrhenius plots at different frequencies

Chapter 3

Table 3.1: MIC values of mineral samples for *E. coli* and *S. aureus*

Chapter 4

Table 4.1: Estimated BET Surface Area, Pore Diameter, and Pore Volume Data of MCD and KYCD.

Chapter 5

Table 5.1: Detection and sensing performance in various water samples

Table 5.2: Molecular docking results showing various poses between MCPV and glutathione



Chapter 1

*Introduction: Literature review &
methodology*



Chapter 1

1.1 Introduction to heavy metal pollution

Water is an exceptionally essential element for the existence of life on the earth. Even though water is a wellspring of life, a considerable number of people around the world suffer from the crisis of the availability of clean and potable water. A recent report by World Health Organization (WHO) indicates that in the year 1990, around 2.6 billion people worldwide have accessed the enhanced drinking water source, which by 2015 increased to 663 million [1]. It was assessed by the World Water Council that by 2030 [2], around 3.9 billion individuals will live in water scarcity zone. The demand for a continual supply of clean water is increasing with time and it is becoming practically unfeasible to keep pace with the exponentially growing population. Moreover, rapid industrialization, population explosion, human activities, unskilled utilization of water resources, and unplanned urbanization have resulted in serious contamination of water. The freshwater contamination can be ascribed to the enormous daily discharge of untreated or toxic industrial effluents, dumping of industrial and domestic wastewater, and runoff from various agrarian fields [3]. In 70-80% of cases, the contaminants discharged are found to reach beyond the threshold levels, changing the physicochemical properties of the water, rendering it unfit for consumption or any other use. Various substances, such as toxic metals, pesticides, dyes, surfactants, pharmaceuticals, sewage, and other pollutants are also detrimental to aquatic organisms, which can further lead to bioaccumulation and biomagnification [4-6], thus ultimately destroying the environment. Among the various toxic pollutants, heavy metal pollution is becoming a serious concern globally, especially in developing nations.

Heavy metal is a group of metal and metalloids having a relative density between 4.5 g cm^{-3} and 22.5 g cm^{-3} [7] and most of them exhibit ecotoxicity and can be hazardous even at very low concentrations [8]. Various anthropogenic activities like mining activities, industrial productions, underground storage leakages, marine dumping, agricultural runoff, and natural processes like leaching from rocks, erosion, acid rain, and forest fires cause the accumulation of heavy metals in the environment [9]. In view of the intense human activity, the release of heavy metals from natural sources is usually of little importance [10]. Some of the examples of heavy metals include arsenic, chromium, cadmium, mercury, lead, iron, nickel, zinc, cobalt, copper, etc. Heavy metals such as copper, zinc, nickel, boron, iron, and

molybdenum are sometimes considered as micronutrients and serve the basic needs for the growth of the plants, proper functioning of the human body, and for biochemical processes [11] but can be harmful to the environment when their concentrations go beyond the permissible limits. Certain heavy metals such as arsenic, mercury, lead, chromium, and cadmium are not much essential for the growth of plants and animals [12]. Heavy metals when entering the body through ingestion, inhalation, or through topical exposure, tend to bioaccumulate in living beings, causing biological and physiological complications and inducing various ailments, DNA damage, oxidative stress, cell membrane destruction, lipid peroxidation, cell cycle modulation, apoptosis or carcinogenesis [13]. Exposure to certain heavy metals, even in minute amounts might cause serious ailments, for example, neurological and congenital disease, osteoporosis, damage to immunity system, cardiovascular issues gastrointestinal disorders, renal toxicity, tumors, dermal irritation, hematic, melancholy, tubular and glomerular dysfunctions [14]. Most of them are carcinogenic and mutagenic, which on continuous exposure can even cause death. Industrial exposure mostly harms adults while children are most commonly exposed to heavy metals through ingestion [15]. Moreover, heavy metals are non-biodegradable and cannot be broken down, which makes their removal tough, hence they are harder to handle. Most of the countries have taken legal steps and framed norms for the heavy metals allowable limit in the drinking water or food to avoid its consumption. A major portion of the heavy metal contaminations in aquatic systems are from industrial wastewater which includes pharmaceuticals, mining, electroplating, tanneries, paper and pulp, rubber and plastics, organic chemicals, pesticides, and so forth [16].

1.1.1 Sources and behaviour of toxic heavy metals

The heavy-metal contamination issues began since the time when humans started processing ores, which accelerated during the 19th and 20th centuries due to rapid modernization. Some of the heavy metals like mercury, chromium, cadmium, arsenic, lead, and iron is omnipresent in the environment due to the rapid contest of industrialization and urbanization, but their tendency to inflict harm and toxicity even in minute quantity has become a matter of concern worldwide. The transport of heavy metals from various contamination sites and their inherent nature of accumulation in biological entities which can pass on to the next trophic level via the food chain has directed various researches towards their early detection and understanding reactions of metals in the natural environment [17].



Figure 1.1: Present scenario of ongoing water pollution from industrial effluents

The toxicity of heavy metal is determined by its various properties like nature, solubility, biological role, the organism exposed, and the period of exposure [18]. Since humans are generally lying in the last of the food chain, chances of accumulation increase. The types of heavy metals, their impact on health and the environment, and their permissible limits are summarized in Table 1.1.

Table 1.1: Types of heavy metals and their effect on human health with their permissible limits in drinking water [19-20].

Heavy metal	Permissible limits (mg L ⁻¹)			Sources	Effects
	WHO, 2008	ISI	US EPA, 2008		
Mercury (Hg)	0.006	0.001	0.002	Pesticides, batteries, paper industries	Tremors, gingivitis, minor psychological changes, acrodynia characterized by pink hands and feet, spontaneous abortion, protoplasm poisoning, respiratory failure and death, damage the brain, damage to central nervous system and kidney; gastrointestinal disorder
Arsenic (As)	0.01	0.01	0.01	Pesticides, fungicides, metal smelters	Bronchitis, dermatitis, poisoning, damage to cardiovascular, dermatologic, nervous, renal, gastrointestinal and respiratory systems; cancer of bladder, kidney, skin, liver

Introduction: Literature review & methodology

Cadmium (Cd)	0.003	0.01	0.005	Welding, electroplating, pesticides, fertilizer, batteries, nuclear fission plant	Renal dysfunction, lung disease, lung cancer, bone defects like osteomalacia and osteoporosis, increased blood pressure, liver and kidney damage, bronchitis, gastrointestinal disorder, bone marrow, cancer
Chromium (Cr)	0.05	0.05	0.1	Mining, electroplating, textile, tannery industries	Damage to the nervous system, fatigue, irritability, damage to kidney, liver, blood cells through oxidation reactions; cancer, breathing problem including asthma, cough, shortness of breath
Lead (Pb)	0.05	0.01	0.015	Paint, pesticides, batteries, automobile emission, mining, burning of coal	Mental retardation in children, development delay, fatal infant encephalopathy, congenital paralysis, sensor neural deafness, and, acute or chronic damage to the nervous system, epilepticus, liver, kidney, gastrointestinal damage, damage to the liver, brain, reproductive system, kidney, nervous system; hair loss, lung fibrosis, skin allergies, anaemia
Copper (Cu)	1.0	2.0	1.3	Mining, pesticides, chemical industry, metal piping electroplating	Anaemia, liver and kidney damage, stomach and intestinal irritation abdominal pain, nausea, vomiting, diarrhea, acne, hair loss, arthritis, autism, cancer, depression, diabetes, heart attack, inflammation
Zinc (Zn)	5.0	5.0	5.0	Refineries, brass manufacture, metal plating, immersion of painted idols	Diarrhea, liver failure, bloody urine, kidney failure, stomach cramps, abdominal cramps, nausea, and vomiting, cause damage to the nervous membrane
Iron (Fe)	0.1	0.3	0.3		Cellular toxicity, anemia, renal failure, heart and liver injury and can even result in serious ailments like Alzheimer's disease

WHO: World Health Organization, USEPA: United States Environmental Protection Agency, ISI: Indian Standard Institution

This thesis deals with the simultaneous detection of two such heavy metal ions, hexavalent chromium (Cr^{6+}) and trivalent iron (Fe^{3+}). Chromium is known to be extremely toxic at low levels and is considered a serious environmental pollutant. Named for the various bright

colours of its compounds, chromium plays a significant role in industries for its various characteristics such as oxidizing capabilities, resistance to corrosion, strength, and hardness [21]. This carcinogenic agent enters the environment mainly through industrial wastewater discharge from the tannery, refractories (chrome and chrome-magnesite), metallurgical (steel, ferro- and nonferrous alloys), and chemical (dyes, paints, pigments, electroplating) industries and is found in much higher concentration in the effluents in the vicinity of industries [22]. Although chromium has various valence states, other than the trivalent Cr^{3+} and the hexavalent Cr^{6+} species, the rest are unstable and short-lived. The harmfulness lies in its oxidation state; Cr^{6+} is considered to be the most toxic, mobile, highly oxidizing, and soluble form of chromium and generally occurs in association with oxygen as chromate (CrO_4^{2-}) or dichromate ($\text{Cr}_2\text{O}_7^{2-}$) oxyanions. Contrary to Cr^{6+} , Cr^{3+} is lesser toxic and soluble, hence having low portability and prevalently bound to the organic matter in nature. While Cr^{6+} is extremely soluble in all pH and considered as a powerful epithelial irritant and carcinogen, poisonous to humans, plants, animals, and microorganisms, Cr^{3+} is considered as a micronutrient in humans required for lipid and sugar metabolism and to promote growth and yield in plants [23]. Since its discovery in 1798 by the French chemist Vauquelin in the Siberian red lead ore (crocoite) [24], various studies on its mobilization, uptake by biota, and toxicity have been performed.

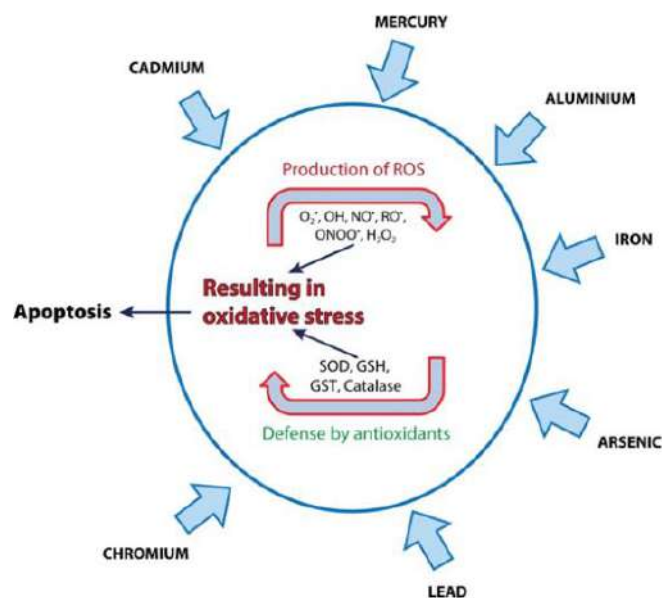


Figure 1.2: Heavy metal-mediated cellular damage [25]

Iron (Fe) enters the aquatic system mainly from anthropogenic sources like landfill leachate, industrial effluent, acid-mine drainage, and sewage [26]. As iron has a tendency to get converted into complex hydroxy compounds that may eventually precipitate, which may

eventually result in co-precipitation of other metals in the aquatic system [27], thus increasing the concentration of many metals in the environment.

1.1.2 Heavy metals mobility in the aquatic environment

Heavy metal enters the aquatic system as a result of various physical, chemical, and biological processes. The movement of heavy metals in the aquatic environment depends on temperature, pH, molecular stability, partition coefficient, polarity, air mass circulation, the direction of surface waters [13]. The mobility of any heavy metal in the environment is expressed by the ratio of dissolved and solid fractions [28]. Heavy metals can be mobilized naturally by weathering processes such as erosion or dissolution, or through anthropogenic activities. The literature suggests mainly three factors that influence the distribution of heavy metals between solution and particulate [29]; (a) concentration and composition, especially the surface properties, (b) chemical form of dissolved metal, and (c) type of interactive processes such as sorption-desorption or precipitation-controlled mechanisms. Once the metals enter the aquatic environment, they are partitioned among the various aquatic compartments like water, suspended solids, sediments, and biota, hence they are found in dissolved, particulates, or complex forms in the aquatic environment [30]. In most cases, metal solubility depends on water pH, and an increase in heavy metal toxicity is caused by the localization of a higher amount of metal. Hence, most of the streams or rivers adjacent to industries and mining areas are polluted, which when flowing into the sea may ultimately precipitate as their solubility reduces due to a decrease in pH [13].

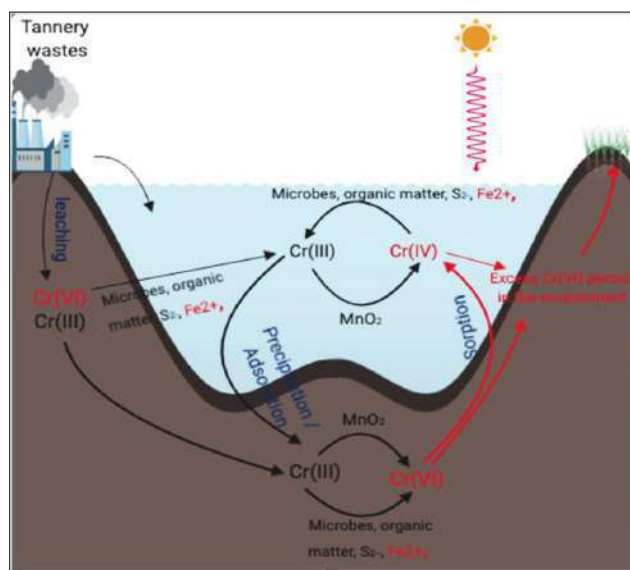


Figure 1.3: Mobility of heavy metals like Cr⁶⁺ in aquatic environments [31]

1.1.3 Global scenario of heavy metal pollution

Water pollution and ordeals associated with contaminated water is being a matter of concern since ancient days since various evidence of wastewater management systems are found from the earliest civilizations like Egyptian, Greek, Indus, and Roman [32]. The Industrial Revolution and the massive evolution of technology during the mid-19th century resulted in an exponential rise in water pollution from industrial wastes. Heavy metals are one of the main components of the industrial effluents which in major cases are directly dumped into the aquatic environment which is ultimately causing various disasters repeatedly throughout the world. The Minamata disease which took place in Japan in 1956 is a notable incident from severe mercury poisoning. This disease was a neurological syndrome from organic mercury intoxication that resulted from bioaccumulation of methylmercury in the aquatic organisms of Minamata Bay as wastewater was dumped into the bay from the nearby chemical plant [33]. A similar methylmercury epidemic occurred in the Agano River basin in Japan during 1965 due to the consumption of contaminated fish [34]. Similarly, heavy metal contamination of water from mining and acid mine drainage has also resulted in various disasters in the past decades. The Pb, Cd, and Zn contamination in Oklahoma, Kansas, and Missouri districts [35] during the late 1960s had severely affected the local environment. Even the Tisza River, which has one of the largest drainage basins and is shared by five countries (Hungary, Ukraine, Romania, Slovakia, and Serbia) has severe heavy metals (Pb, Cd, Cu, and Zn) pollution. As the river flows through Hungary and the border of Romania, metal contaminations take place due to the presence of major industrial complexes and several mining activities which is directly polluting the river, which spreads downstream [36]. Similarly, a significant enrichment with heavy metals like Pb, Cd, Cu, and Zn is occurring in Szamos, another river of Hungary from the gold mine, which caused a serious impact during 2000 [37]. These are only some of the examples of various toxic disasters related to heavy metals occurring throughout the world where contamination, even in trace quantity has resulted in dire consequences.

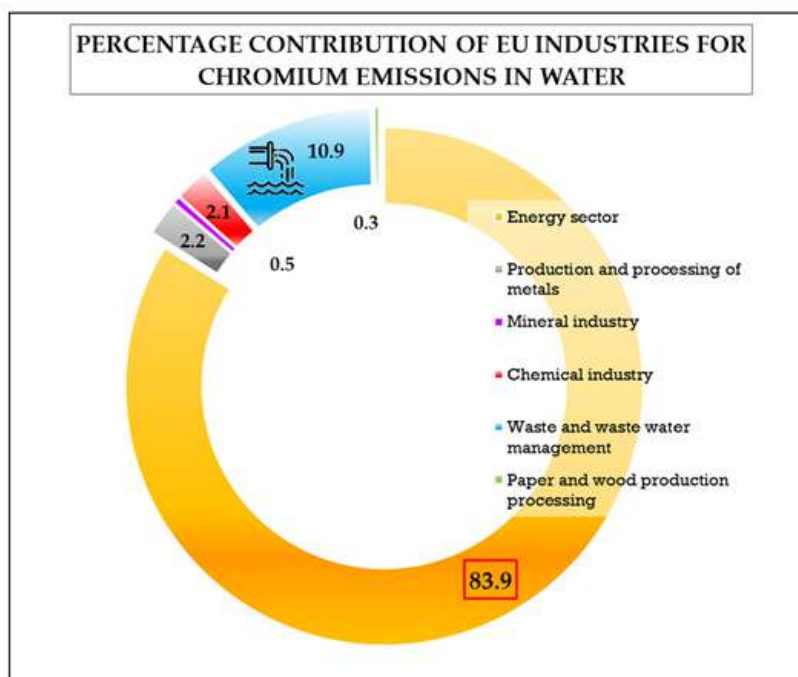


Figure 1.4: Percentage of Cr emission from the industrial sector into water [Source: European Environmental Agency, 2017] [38]

1.1.4 Indian status of heavy metal pollution

The rapid growth of industries, widespread urbanization, and other anthropogenic activities are burdening the historical lakes and rivers of India with loads of pollution. In India, heavy metal pollution is not a modern problem that began due to industrialization, rather this issue started with the processing of ores [39]. In developing countries, sustainable, effective, and efficient management of water bodies can be an acceptable strategy for economic growth, yet in the recent past, ineffective utilization of resources and improper planning or management has resulted in an increase of heavy metals contamination from various sources [40]. According to UN Survey reports [41] it is estimated that by the year 2025, the two-thirds population of the world will be facing water stress and a shortage in availability of potable water. Moreover, India being one of the most populated countries will face severe crisis due to increased water pollution and drying up of water bodies. River Ganga, one of the most important and largest rivers of India is suffering from immense pollution from several industries. Extensive studies are continually conducted to assess the pollution load and water quality of the river. A detailed study of heavy metal concentrations in Ganga by Ansari et al. [42] in the Kanpur-Unnao industrial region suggests nearly 90 % content of Cd, Cr, and Sn, along with the high concentration of Cu, Zn, Co, Ni, and Pb. Even the Ganga Plain in Lucknow, Mirzapur, Delhi, Agra is found to be dangerously polluted with heavy

metals [43]. Another river, Yamuna, which is the lifeline of Delhi is regarded as the most polluted river of the country where most of the pollutants come from domestic sources [44]. Similarly, South Indian water bodies are also facing the same issues. Kabini River of Karnataka is found to be heavily polluted by Cu and Cr which is attributed to the paper mill effluents [45]. The heavy metal pollution is also causing several issues in the largest delta of the world, the Sundarbans. Since the rivers and ecosystem of this ecologically significant place have gathered the interest of people globally, scientists around the world are putting their effort to find ways to protect the ecosystem from pollution [46-48]. In fact, numerous NGOs and government bodies like the Council of Scientific and Industrial Research (CSIR), University Grants Commission (UGC), Department of Science and Technology (DST), Department of Biotechnology (DBT) are providing funds and infrastructure for research regarding developing new ideas and techniques to combat such issues. River projects like Ganga Action Plan (GAP) or Yamuna Action Plan (YAP) are also initiated for proper treatment and monitoring of the water bodies.

1.2 Techniques for heavy metal detection

There is a great demand for water quality monitoring and assessment on regular basis due to the ever-increasing pollution load in the water. In order to prevent heavy metal pollution, detection of the metals in water is greatly required. Hence various effective and selective techniques are developed for the detection and analysis of heavy metals in surface water, groundwater, and wastewater on a continuous or regular basis. The various conventional and non-conventional techniques used for heavy metal detection are discussed herein.

1.2.1 Conventional techniques for heavy metal detection

One of the most widely practiced detection techniques is Atomic absorption spectrometry (AAS). This method can determine over 70 different elements directly in liquid or solid samples [49]. The absorption of optical radiation (light) by free atoms is used for the quantitative determination of chemical elements. Although it is relatively inexpensive and convenient for regular use, it suffers certain drawbacks like the requirement of a larger quantity of samples, a tedious protocol for sample processing, the sample needs to be transparent and colourless and multiple elements cannot be determined at a time. Graphite furnace atomic absorption spectroscopy (GFAAS) is also a similar method for the detection of metals in liquid and in solid samples even in trace amounts. Although this technique is

highly suitable for routine analysis of environmental samples, it is expensive and requires trained personnel.

Another traditional technique regularly practiced for heavy metal detection is inductively-coupled plasma optical emission spectroscopy (ICP-OES) and inductively-coupled plasma mass spectroscopy (ICP-MS). In contrast to the absorption spectroscopy technique, ICP is based on emission spectrometry involving high-temperature argon plasma to excite the samples for optical emission and also enables multi-elemental detection with excellent sensitivity [50]. Although this sophisticated technique can detect heavy metals in ppb level in the water, it has various limitations like continuum background emission, spectral overlaps, matrix effects, and trained personnel for handling. In ICP-MS, the mass spectrometer is further used to separate and quantify those ions.

Other than AAS and ICP, certain other techniques like X-ray absorption fine structure spectroscopy (XAFS), extended X-ray absorption fine structure (EXAFS) and energy-dispersive X-ray fluorescence (EDXRF) are also practiced for determining the elemental composition of the samples. In XAFS or EXAFS, information regarding the bond length, coordination number, chemical environment, and structural ordering of the heavy metal can be determined by probing the local structural environment and the electronic state of specific elements [51]. The EDXRF is a non-destructive and multi-elemental analytical technique EDXRF is used for the simultaneous determination of different elements, but sensitivity for trace-level analysis is limited.

1.2.2 Non-conventional techniques for heavy metal detection

The electrochemical sensing technique is one of the most economical and simple techniques for the direct analysis of water. This technique requires a working/sensing electrode as the major component that detects the target ions present in water. Among the electrochemical methods used, the voltammetry method is widely applied for field monitoring of environmental samples because of the high sensitivity and ability for *in situ* detection of heavy metals [52-53]. Various modifications of electrodes are made and in the recent past various nanomaterial-based metals, metal oxides, and composites are used for electrochemical detection.

Optical sensor is another technique that is gaining huge recognition throughout the world because of the high selectivity and sensitivity, real-time data reproducibility without the need of any expensive tool, capability for on-site detection without sample purification or

enrichment, and does not require professional personnel. Optical sensors depend on optical changes attributed to reversible or irreversible chemical interactions between the reagent and the metal ion, complex binding, or direct spectroscopic analysis for identification and measurements of heavy metals in aqueous solutions. Mainly two types of optical sensors are widely explored in the recent past; fluorescent and colorimetric sensors.

1.2.2.1 Fluorescent sensors

Fluorescence detection of heavy metal ions is based on changes in the physicochemical properties of fluorophores upon binding to the ion or due to charge transfer or energy transfer processes [54]. The presence of the target ion is exhibited by changes in its fluorescence properties, intensity, lifetime, and anisotropy. This technique is often useful in the biological domain for detecting the presence of any heavy metal in living organisms through bioimaging or biosensing methods.

1.2.8.2 Colorimetric sensors

Colorimetric sensing is one of the fastest and most straightforward sensing techniques which is based on the change of solution colour on the presence of the target heavy metal ion. Nowadays, to achieve better sensitivity and selectivity, samples are accordingly functionalized with recognizing molecules that can interact or bind with the specific metal ion and trigger significant colour change due to optical absorption or localized surface plasmon resonance [55].

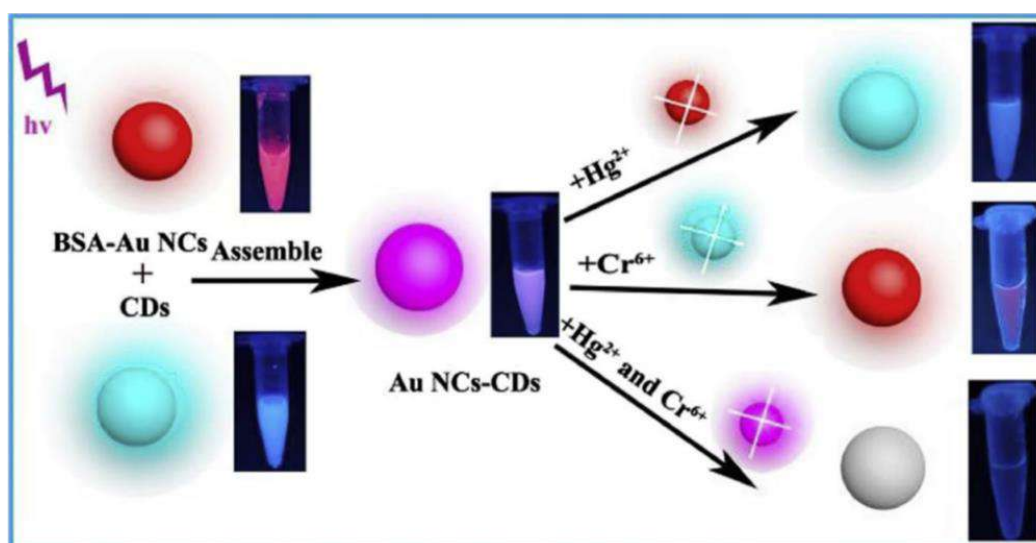


Figure 1.5: Carbon dot-loaded nanocomposite for optical sensing of heavy metals [56]

Thus, the conventional techniques like AAS, ICP OES, ICP MS, X-ray fluorescence spectroscopy, capillary electrophoresis, ion chromatography ultraviolet-visible spectroscopy, microprobes, etc. requires expensive instruments, tedious sample preparation, laborious, pre-concentration procedures, regular maintenance of instruments, highly trained technicians and cannot be used as a portable device for *in situ* detection. Furthermore, sample collection, proper storage, and transportation are needed, which can contaminate the water samples or can change physicochemical parameters if not properly handled. On contrary, the optical sensors can overcome all such limitations and can be useful for collecting rapid and real-time data on-field. Hence optical sensing, more precisely fluorometric sensing was adopted for heavy metal detection in water and also at the cellular level.

1.3 Application of nanoparticles for fluorometric sensing of heavy metals

Modern technological advancement, especially in the nanotechnology domain has provided new opportunities for improving the performance of sensors along with the development of eco-friendly, cost-effective, easily synthesizable sensors. Nowadays, nanoscience and nanotechnology offer a new horizon for designing smart functional materials for multidimensional applications by manipulating their optical, electrical, magnetic, structural, microstructural, and hyperfine properties in the nanometer regime. As per, the IUPAC definition, any particle of any shape having dimensions between approximately 1 and 100 nm range is considered to be a nanoparticle [56-57]. In the domain of heavy metal sensing technology, nanomaterials-based sensors have shown great promise. In comparison to conventional sensors due to their large surface area, high surface reactivity, strong adsorption capacity, high catalytic efficiency, large surface to volume ratio, great stability, economically viable, and biocompatible nature [58-59]. Moreover, the sensitivity and performance of the nano-sensor can be improved or modified according to the requirement by surface functionalization, target-induced aggregation, or by modification of size or surface properties [60]. The presence of the target contaminant generally induces changes in the physicochemical properties like fluorescence lifetime, intensity, anisotropy of the nanoparticle, which results in charge transfer or energy transfer processes. Detection of changes in the fluorescence signals in the form of fluorescence quenching (turn-off) or enhancement of fluorescence (turn-on) due to the presence of the target ion or molecule (analyte) is carried out using spectroscopy or by illumination. There is more evidence of ‘turn-off’ sensing than ‘turn-on’, mainly in the field of heavy metal detection as the d-block

ions like Fe^{3+} usually initiate excited state de-excitation pathways through photoinduced electron transfer (PET) and/or electronic energy transfer (EET), involving the metal centre [61]. In ratiometric sensing, there is generally a shift in the fluorescence maxima upon recognition of the target analyte. Although turn-on, turn-off, and ratiometric sensing are generally reversible processes, fluorescent chemodosimeters involve irreversible transduction of a fluorescent signal and are designed according to the specific reaction induced by the analyte of interest [62].

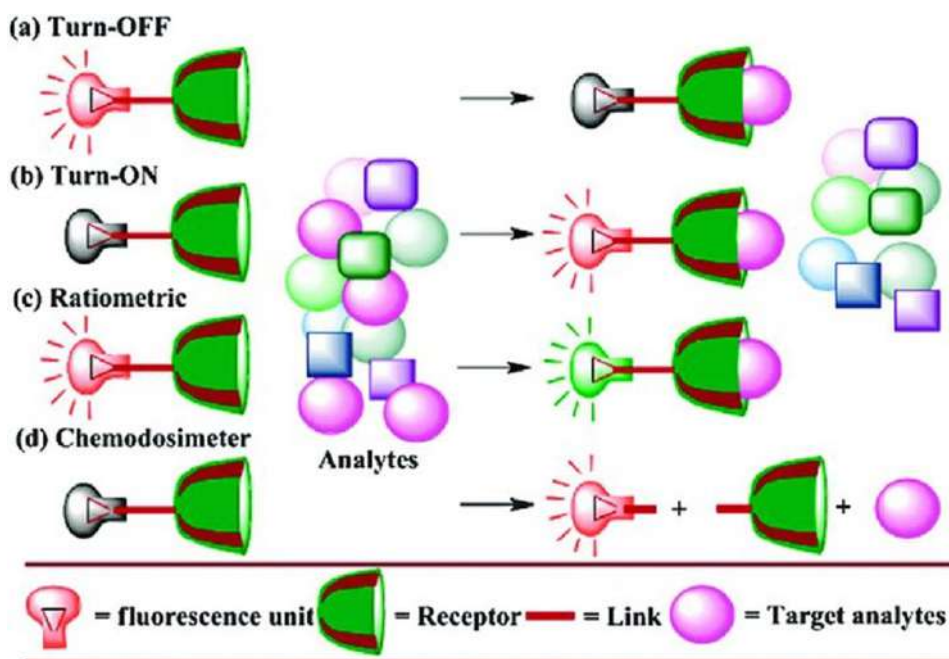


Figure 1.6: Various types of fluorometric sensors [62]

The emissive nanoparticle-based fluorescent sensors can even provide faster quantitative and qualitative detection with higher sensitivity than colorimetric sensors. Hence, they are more preferable over the conventional organic fluorescent dyes for heavy metal ions detection in real water samples and biological systems due to their better biocompatibility, eco-friendly, robust, and lesser toxicity, ease in handling, and excellent performance. Most of the present fluorescent sensors used do not even require elaborate molecular designing of sophisticated synthesis procedures. The fluorometric sensing techniques or mechanisms include static quenching, dynamic quenching, Förster resonance energy transfer (FRET), photoinduced electron transfer (PET), Dexter energy transfer (DET), surface energy transfer (SET), an inner filter effect (IFE) [64]. Few mechanisms are elucidated in the following table.

Table 1.2: Comparative study between optical sensing mechanisms

	Static Quenching	Dynamic Quenching	Photoinduced electron transfer (PET)	Förster resonance energy transfer (FRET)	Inner filter effect (IFE)
Occurrence/ mechanism	When non-fluorescent ground-state Complex form due to the interaction of fluorophore and quencher but can cause a change in the absorption spectrum of fluorophore	Occurs as an effect when the excited state comes back to the ground state on collision between the quencher and fluorophore due to energy or charge transfer	The donor-acceptor pair in an excited state collides with each other and electrons get transported to the acceptor moiety causing a rapid alteration of the fluorescence intensity.	As photonic energy of the first fluorophore (donor) is acquired by the second fluorophore (acceptor), and then emitted by the second fluorophore.	When the absorption spectrum of quencher in The detection system overlaps the excitation or emission Spectra of fluorophore
Distance	Temperature Dependent	Viscosity dependent	<10 nm	1–10 nm	>20 nm
Fluorescence lifetime	Average fluorescence lifetime remains unchanged	Changes	Changes	Decreases	Remains unchanged
Spectral overlapping	Not required	Not required	Not required	Mandatory	Required
Orientation	Not critical	Not critical	Redox potentials should be High enough to allow For transfer of electron	Not important	Not critical

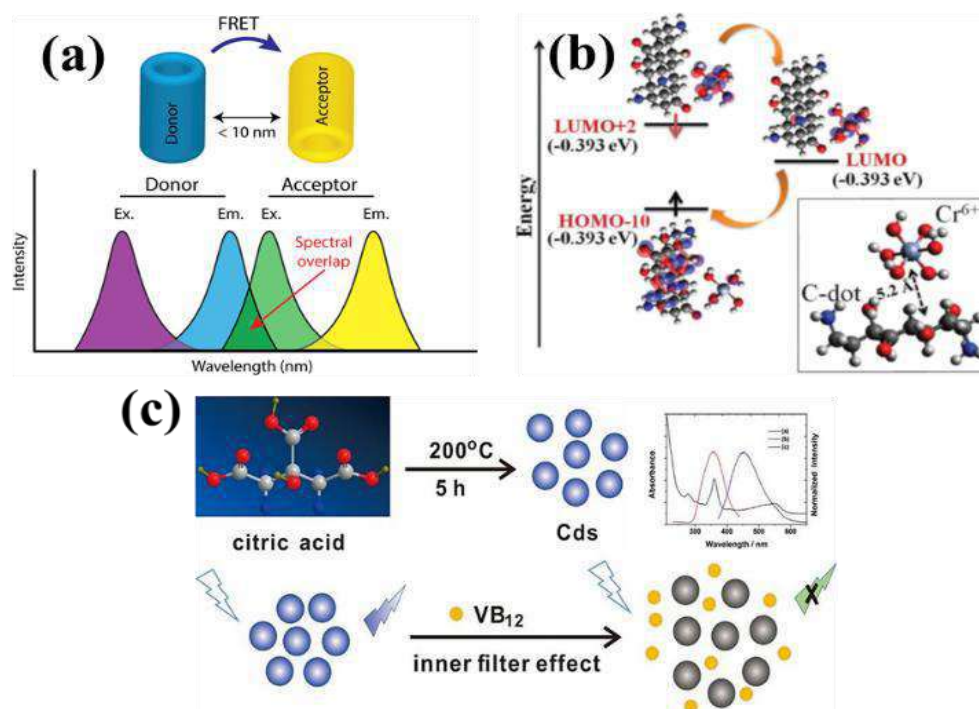


Figure 1.7: Different fluorometric sensing pathways depicting (a) FRET-based sensing technique [65]; (b) DFT based determination of PET-based sensing with CD's [66]; (c) Inner Filter Effect using carbon dots showing fluorescence quenching [67]

1.4 Background of the present work

The advent of technology and accelerated industrial processes have significantly increased toxic waste pollution to a level where immediate action is necessary. The conventional laboratory-based techniques are unable to meet the demand due to the expensive instrumentation and requirement of highly trained technical staff. The minimization of environmental risk and sustainability issues resulting from domestic and industrial usage of different synthetic products has become a major current concern. The last century has witnessed the synthesis and development of various essential products and by-products to improve our quality of life [68]. Various studies regarding the development of fluorescent sensors for heavy metal detection are ongoing worldwide due to the pressing need for sensitive and accurate detection to combat the dire consequences of heavy metal pollution [69-71]. The fluorescent ion sensors are gaining prominence due to their immense potential, yet there are certain limitations of the synthetic fluorescent sensors as they can produce secondary toxicity due to their persistence and composition, and can have cumbersome synthesis procedures or resource-consuming processes. Moreover, certain nanoparticles owing to their small size have greater potential to find their way easily to enter the human

body and cross the various biological barriers and may reach the most sensitive organs along with its tendency to hamper the ecosystem structure and function [72]. Hence the development of sustainable future technologies from abundant, green, and renewable materials has become one of the major concerns in modern research. Thus, greater emphasis is now given to the development of efficient, economical, eco-friendly, easily synthesizable nanoparticles from widely accessible materials so that they can minimize the raw material and labor cost when fabricated on an industrial level or on large scale.

The genesis of this work takes us back to early 2018, when various reports circulated on the dire consequences of industrial wastewater contamination and subsequent health effects in the surroundings of Bantala [73-75], situated in East Kolkata suburban area, West Bengal, India. The water collected from the local streams of Bantala revealed alarming results of the presence of an alarming quantity of heavy metals like hexavalent chromium. The local populations are heavily dependent on the streams that are ultimately connected to various industrial outlets. Although governments are taking enough precautionary measures, yet such ongoing heavy metal pollution has become a concerning issue. Such incidents are common worldwide and it is tough and time-taking to identify contaminated water through conventional detection methods. Hence the research work aimed towards synthesizing biocompatible sensors for rapid detection of heavy metals in water. Moreover, it is also essential to determine the presence of such heavy metals at cellular levels too. Hence biosensing assays were also designed using the sensors.



Figure 1.8: Photographs of Bantala leather complex area, Kolkata taken during wastewater collection from the contaminated canal

1.5 Material selection

The natural environment has a huge influence on our daily lifestyle as the rocks and minerals form an integral part of our life since most of the significant products and by-products we require are extracted from nature. Minerals exert their influence by constituting the bulk of this rocky planet and having a wide range of composition and structure that is expressed in a marked diversity of physical and chemical properties. The physical properties of minerals have great technological significance because they have important industrial uses that depend on their physical properties. In the present work, minerals collected from nature were used to accomplish the purpose of fabricating sensors for heavy metal detection. Moreover, silicates are the most abundant component of the earth's crust and are reported to have great physical and thermal stability with a comparatively good chemical inertness [76]. Although widely available, an insufficient amount of interest has been paid regarding the application of silicate minerals in the domain of antibacterial fluorometric sensors. Moreover, these silicate minerals reportedly biocompatible than other natural minerals [77] like sulphide and ferrites.

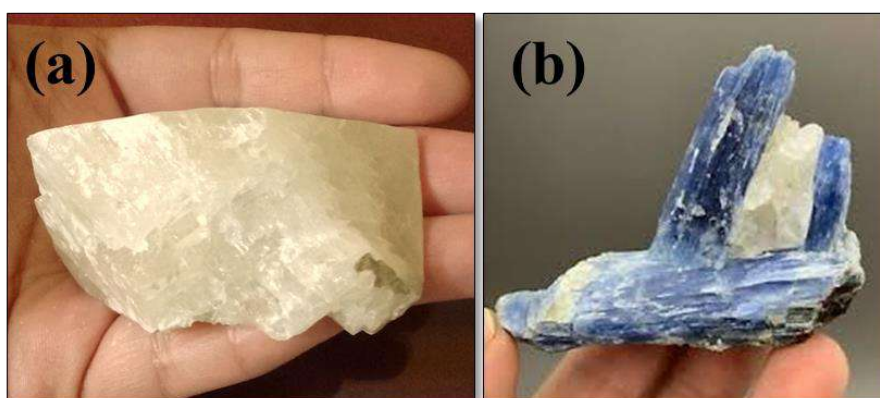


Figure 1.9: Raw silicate minerals (a) microcline and (b) kyanite used in the work

Hence, two naturally formed silicates, namely, potassium aluminum silicate or microcline (KAlSi_3O_8), and aluminum silicate or kyanite (Al_2SiO_5) have been selected for these works.

The microcline (M) is the triclinic polymorph, a low-temperature form of potassium aluminosilicate, or as commonly named as potash feldspar. The other two polymorphs are orthoclase and sanidine, depending upon the degree of order-disorder of Al^{3+} and Si^{4+} ions in the tetrahedral units forming their crystal network [78]. Compared to other polymorphs, microcline is relatively stable, mainly at lower temperatures. AlO_4 and SiO_4 have linked

structures and contain mainly K^+ , with Na, Ca, and Ba sometimes as impurities in trace quantity [79].

Kyanite (KY) is a colourless to blue-coloured, triclinic crystalline regionally-metamorphosed rock, which forms under high or medium pressure and low temperature [80]. Kyanite has polymorphs like andalusite and sillimanite. This rock is mostly used in ceramic and refractory industries, and for the production of lightweight aluminum-silicon alloys that are used for the fabrication of metallic fiber, parts of supersonic aircraft, and spaceships [81]. Kyanite contains octahedral AlO_6 stacked together with two corners shelved SiO_4 tetrahedra which are shared by an oxygen molecule [82].

1.6 Preparation of natural silicate minerals (microcline and kyanite) for sensing and biological applications

Minerals in nature are found in bulk-sized crude form, which is generally not bioavailable and cannot be used directly. Moreover, these minerals have enhanced properties in their nano-sized form.

Initially, the silicate minerals (microcline and kyanite) were purchased from Hindustan Minerals, Kolkata, India. Both the purchased minerals (1kg block each) were rinsed thoroughly with Millipore water (resistivity~18.2 $M\Omega$ -cm) to remove debris and then ground in an agate mortar to reduce the size. The minerals were then sieved through a 100 mesh (149 μ m) sieve and washed several times with Millipore water and ethanol. These sieved mineral samples were marked as M1 (microcline) and KY1 (kyanite).

In industrial sectors, the raw minerals collected for various applications are generally pulverized by using various types of milling machines. Since this work involves modification of naturally occurred minerals for the development of antibacterial fluorometric sensors, the step-down synthesis was performed using a high-energy ball mill.

Herein, a Fritsch Planetary Mono Mill Pulverisette 6 mechanical ball mill was employed for size reduction of the minerals. A portion of the coarse fraction of microcline and kyanite was crushed in the milling machine operated at 300 rpm for 12 h using the ball to sample mass ratio of 20:1 for further studies. The tungsten carbide vials and balls were used for this purpose. The ball-milled samples were finally marked as M2 (microcline) and KY2 (kyanite).

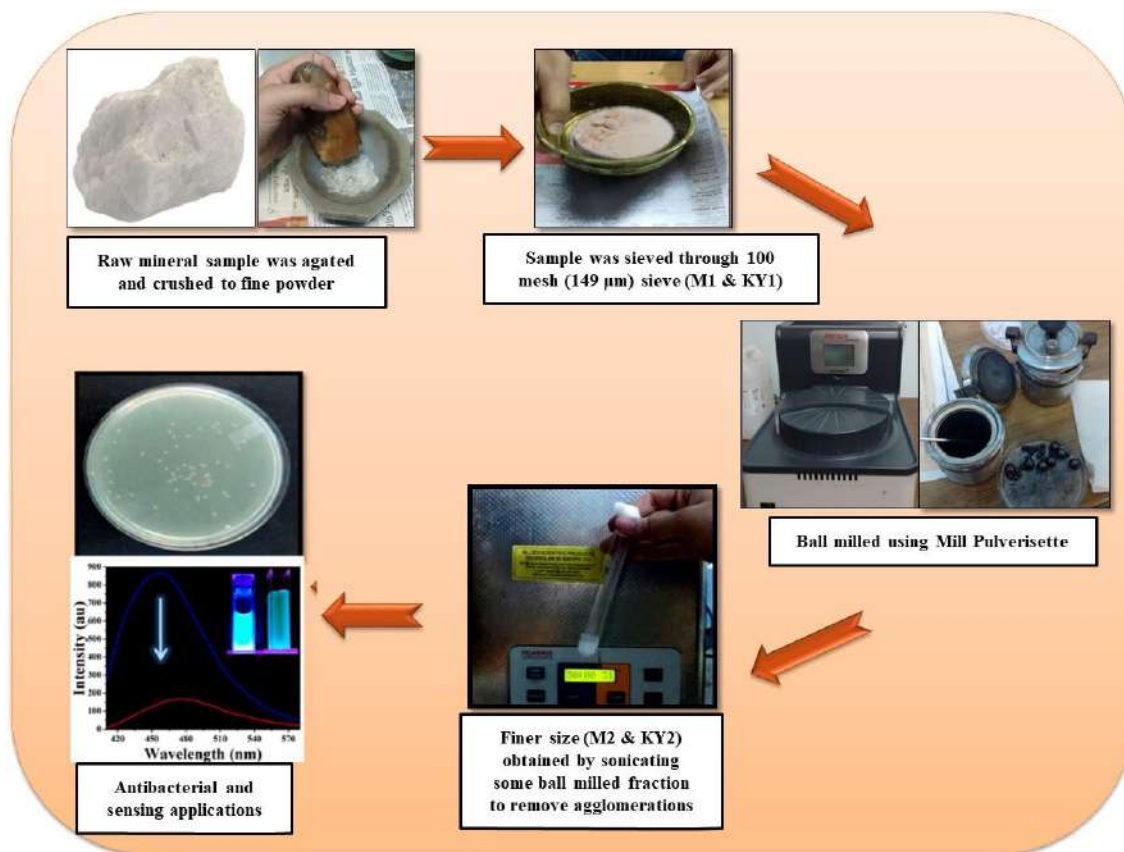


Figure 1.10: Illustration of step-down synthesis performed

1.7 Instrumentation and sample preparation for different characterization techniques

1.7.1 Structural and morphological characterizations

1.7.1.1 X-Ray Diffraction (XRD)

X-ray powder diffraction or XRD is an efficient, non-destructive analytical technique that is widely used for the identification of unknown crystalline materials (such as minerals or other inorganic compounds), quantification and detection of crystalline phases and impurities or defect states (quantity/location) associated with the crystals and for probing the structural alignment to determine crystal structures and unit cell dimensions [83].

In these works, the determination of crystal structure is needed to assess the sample purity and crystal defects. Both the Scherrer equation and Rietveld refinement [84-85] have been introduced to obtain the crystallite size and structural features of the samples. A Bruker X-ray diffractometer (D8, Bruker AXS, USA) equipped with Germanium monochromator and

Cu-K α target (wavelength (λ) = 1.5418 Å) is employed operating at 35kV, 35mA with a scan speed of 0.3 s/step in the range of 2θ from 20° to 60°.

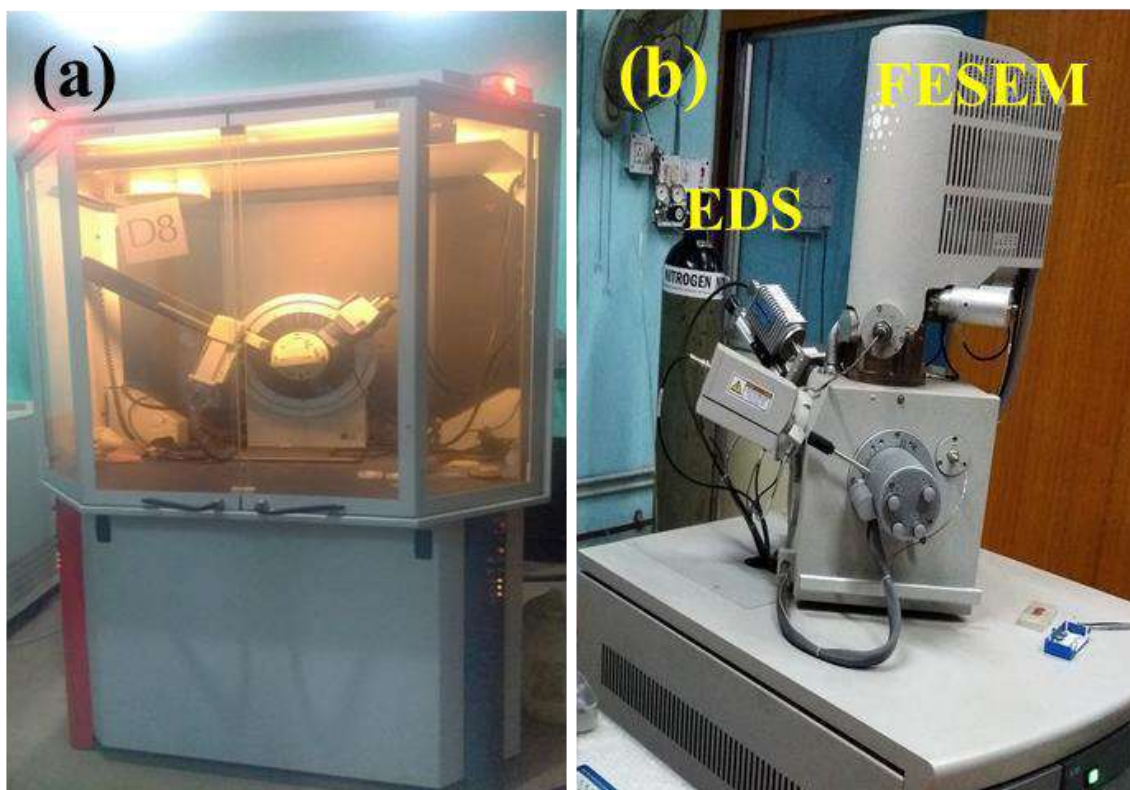


Figure 1.11: (a) Bruker D8 Advance XRD machine and (b) FESEM (field emission scanning electron microscope) instrument with EDS attachment situated at the Dept. of Physics, JU

1.7.1.2 Field Emission Scanning Electron Microscopy (FESEM)

The morphological features (shape and size) of the synthesized samples have been estimated using the FESEM technique [86-87]. Herein, the FESEM micrographs are acquired from FEI INSPECT F50, Netherlands FESEM equipment. Samples were placed on conducting carbon tape, followed by gold coating, and then placed in the FESEM instrument which operated at room temperature under vacuum conditions (chamber pressure of 3×10^{-4} Pa) at 5-20 kV bias voltages. The dimensions were measured using ImageJ software.

1.7.1.3 Transmission Electron Microscope (TEM)

In order to obtain the particle sizes and their orientation, TEM characterization has been performed [88]. Since precise information regarding size and morphology is a significant aspect in these works, the TEM study was performed using JEOL JEM-2000, which

operated at 200 kV. Well dispersed powder samples in HPLC-grade acetone (1mg in 5mL, followed by 1 h sonication) were drop cast onto a 300-carbon coated copper grid and dried.

1.7.2 Purity and bonding network analysis

1.7.2.1 Fourier Transform Infrared Spectroscopy (FTIR)

To ascertain the purity of the natural minerals at a molecular component level along with the determination of the functional groups, bond structures, and to identify the polymorph used, FTIR study was performed [89-91] using FTIR-8400S, Shimadzu in the wavenumber ranging from 400 cm^{-1} to 4000 cm^{-1} . In the case of potash feldspar, a detailed study of absorption peaks revealed that the microcline was used for the research work. Similarly, it was found that the kyanite form was used in the work. The powder samples were mixed with potassium bromide (KBr) at a ratio of 1:50 (1 mg sample homogenized with 50 mg KBr) and the mixture was pressed at 5 tons for 5 min in a hydraulic hand press and dried in a hot air oven at $80\text{ }^{\circ}\text{C}$ for 4 h to remove excess moisture prior to analysis.



Figure 1.12: FTIR 8400S, Shimadzu situated at the Dept. of Physics, JU

1.7.2.2 Energy-Dispersive X-ray Spectroscopy (EDS) and elemental mapping

It is very important to know elemental composition prior to any kind of application. Hence EDS technique and elemental mapping have been executed using Bruker Quantax EDS analyzer which is associated with the FESEM instrument, to gather information regarding the constituent elements and elemental distribution in the mineral samples [92]. The sample

preparation is the same as that of the FESEM technique and the filament operating was set at 20 kV voltage.

1.7.3 Surface property analysis

BET method is performed to estimate the surface area and volume of the sample while the BJH technique is a useful tool to determine the pore size distribution of the sample [93-94], which is related to the adsorption of gas molecules physically on a solid surface at a fixed temperature. The sensing mechanism involved in the study is dependent on the mesoporous nature of samples, hence mesoporosity and the surface area analysis was performed using BET-BJH and the nitrogen adsorption-desorption isotherms were analyzed. A Twin Surface Area Analyzer from Quanta-chrome Instruments (USA) was used and the nitrogen gas adsorption-desorption isotherms were investigated using a minute amount of powder sample at 77 K for 1 h.

1.7.4 Thermal stability analysis

TGA-DTA is a gravimetric method that records the temperature-dependent change in the mass of a material with time and is thus useful for measuring thermo-physical properties, temperature-dependent and chemical changes [95], and for the prediction of thermal stability and safe operating range of material. Minerals generally change the phase beyond a certain temperature which can be studied, such as kyanite used in the study can transform into mullite by heat treatment of 1500 °C due to microstructural changes [96-97]. Furthermore, the stability of a sensor is also an important factor for widespread use, hence thermal properties were measured using this technique. The TGA-DTA analysis was done using DTG-60H, Shimadzu under nitrogen atmosphere at 5-10 °C min⁻¹ heating rate, and the samples were placed in the platinum crucibles for the study.



Figure 1.13: The DTA-TGA instrument of Dept. of Physics, JU

1.7.5 Optical property analysis

1.7.5.1 Ultraviolet-Visible (UV-Vis or UV/Vis) spectroscopy

This spectroscopic technique is useful for justifying the optical activity of the minerals by using an absorption spectrum [98-99]. In these works, size reduction due to ball milling can be justified from the peak broadening and slight blue shift of optical absorption spectra. Moreover, change in bandgap due to size reduction can also be studied. UV-Vis spectroscopy has been performed using PerkinElmer Lambda-365 UV-Vis spectrometer at room temperature. The powdered samples were well-suspended in Millipore water at a concentration of 1 mg mL^{-1} prior to experimentation and a quartz cuvette was used for spectroscopy.



Figure 1.14: UV-Vis spectrophotometer instrument of the Dept. of Physics, JU; (b) sample chamber

1.7.5.2 Fluorescence spectroscopy

This is a significant contactless and non-destructive technique for fluorometric detection of pollutants in water. Since the present thesis aims towards the development of fluorometric sensors, it is essential to have promising fluorescence quality and great stability [100-101]. Fluorescence spectroscopy is a common technique for determining the emission spectrum by measuring the energy distribution of emitted photons of the atoms or molecules that are excited by absorption of electromagnetic radiation and then dissipates the excess energy as photons while relaxing back to ground state [102-103]. Fluorescence spectra of the samples were obtained by a Cary Eclipse Fluorescence Spectrometer, Agilent Technologies maintaining both excitation and emission slit sizes at 5 nm. Sample preparation of powder sample was the same as that for UV-Vis spectroscopy.

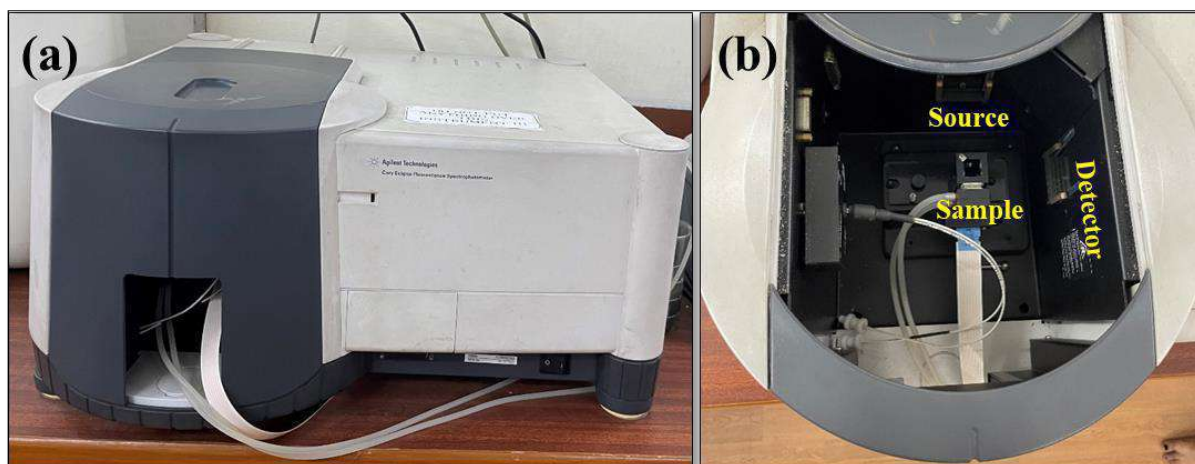


Figure 1.15: Fluorescence spectrophotometer instrument of the Dept. of Physics, JU; (b) sample chamber

1.7.5.3 Time-Correlated Single Photon Counting (TCSPC) technique

This technique is useful in determining the sensing mechanism followed and can trace the pathway for the fluorometric changes. TCSPC is a common technique that measures the time spent by a fluorophore in its excited state prior to returning back to the ground state in picoseconds to microseconds range [104]. In this study, measurement of fluorescence decay of the sensor due to exposure to the heavy metal ions has been performed using a time-resolved spectrofluorometer from IBH, UK.

1.7.6 Electrical characterization

In order to fabricate futuristic hand-held sensing devices using mineral samples, it is crucial to investigate their electrical properties. Hence, size-dependent variation in electrical properties of microcline and kyanite was measured using a LCR meter. The LCR meter is a versatile electronic test equipment that is used to measure various electronic parameters of any material by determining the impedance to investigate the inductance (L), capacitance (C), and resistance (R) [105]. In this thesis entire electrical measurements have been performed using a digital LCR meter (Agilent 4294A Precision Impedance Analyzer) in a frequency ranging from 40 Hz to 100 MHz at 0.5 V bias voltages. The powdered samples were pressed at 5 tons for 5 min in a hydraulic hand press to obtain a 10 mm thin pellet. The pellets were kept in a hot air oven at 80°C for 1 h prior to the experiment to prevent the interference effect of moisture.

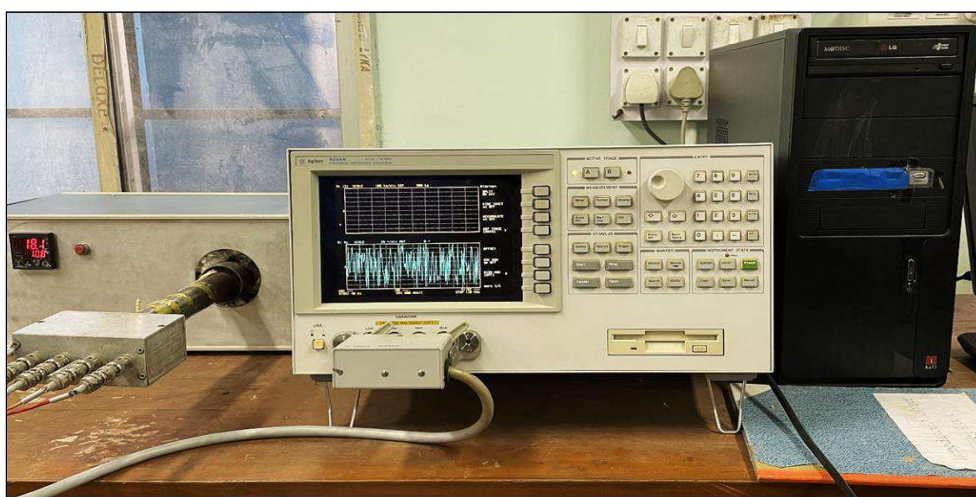


Figure 1.16: The Agilent impedance analyzer set up of the Dept. of Physics, JU

Dielectric constant (ϵ), or relative permittivity was measured for the mineral samples. It is an electrical property that exhibits the ability of a dielectric material (electrically insulating material that is capable of electric charge storage due to dipolar polarization) to be polarized when an electric field is applied. The dielectric response can be expressed as [106]:

$$\epsilon = \epsilon' + j \epsilon'' \quad (1.1)$$

Where, ϵ' denotes the real part that represents the amount of charge/energy stored due to polarization effect, while ϵ'' denotes the imaginary part of the relative dielectric constant which is associated with the energy which is dissipated during polarization. The real part of the dielectric constant is calculated using the following formula [107]:

$$\epsilon' = (C.d)/(\epsilon_0 A) \quad (1.2)$$

Where, C is the capacitance of the material, d is the area and A is the thickness of the pellet used, ϵ_0 is the permittivity in free space ($8.85 \cdot 10^{-12} \text{ F m}^{-1}$). Insertion of dielectric material between the plates (such as a parallel-plate capacitor) increases the capacitance (ability to store opposite charges on each plate) in comparison to the capacitance of the plates when separated by a vacuum. Various factors influence the dielectric response of a nanomaterial, such as chemical composition, synthesis route, temperature, moisture content, frequency of the external applied electric field, etc. Moreover, the dielectric properties can be modulated according to requirements by modifying the surface morphology or defect states.

Dielectric loss tangent ($\tan\delta$) measured in these works is the physical quantity associated with the amount of electromagnetic energy dissipated within the material. It is calculated using the ratio of imaginary part (ϵ'') of complex dielectric constant to that of the real part (ϵ'), and can be expressed as [108]:

$$\tan\delta = \epsilon''/\epsilon' \quad (1.3)$$

This includes dielectric damping loss and conductivity loss of the material. This loss is in the form of electromagnetic energy (e.g., heat) dissipation or some form of leakage current, which is an intrinsic property of a material. Materials with high dielectric constant value with low losses are beneficial for industrial and device applications.

Another significant electrical parameter to be measured is electrical conductivity. The A.C electrical conductivity (σ_{ac}) is an intrinsic property of a material that quantifies how strongly a given material allows the flow of electric current and is calculated using the formula [109],

$$\sigma_{ac} = 2\pi f \tan\delta \epsilon_r \epsilon_0 \quad (1.4)$$

Here, σ_{ac} , f , $\tan\delta$, ϵ_r , and ϵ_0 represents AC conductivity, frequency (in Hz), tangent loss factor, the dielectric constant of the material and vacuum permittivity respectively. Within the dielectric materials motion of free charge, carriers create conduction current and this ac conductivity has both temperature and frequency response which are also strongly correlated.

1.8 Theoretical techniques

1.8.1 Rietveld Refinement

The ball milling process reduces the particle size drastically by reducing unit cells dimensions. This process also introduces various defect states along with augmented microstrain values [110]. Since the sensor materials were developed from the ball-milled fractions, detailed microstructural parameters were analysed from these theoretical studies. Moreover, to validate the variations of various properties in the bulk and finer fractions of microcline and kyanite, this theoretical characterization is significant. In this thesis, two Rietveld-based software packages viz., MAUD (Material Analysis Using Diffraction) (v2.9) VESTA (Visualisation for Electronic Structural Analysis) (v3.5.2) program has been used to refine XRD diffractograms. Such refinements were performed to analyze structural (lattice parameter and atomic coordinates) and microstructural parameters (crystallite size, microstrain, density, etc.), as well as the phase purity and bonding network of the samples [112]. Visual representation and calculation of bond lengths and bond angles for estimating the crystal defects and vacancy spaces created during mechanical milling were determined using this software.

1.8.2 Density Functional Theory (DFT)

To identify the mechanism behind the fluorescence quenching and for a detailed understanding of the electronic transitions, density functional theory (DFT) and time-dependent density functional theory (TDDFT) was employed. Density-functional theory or

DFT calculations were performed using Becke, 3-parameter, Lee-Yang-Parr (B3LYP) functional coupled with the continuum aqueous solvent mode (CPCM) for geometrical optimizations of the fluorophore and for understanding ion sensing mechanism. The functional in Orca v4.2 software helped to elucidate the structures of the complex compounds [111], especially the nitrogenous carbon dot structure. Avogadro v1.2 program was used for molecular modeling and geometrical optimizations. The elements involved in the interactions were described using a 6-31G** basis set prior to the theoretical calculations 6-31G** basis set along with RIJCOSX auxiliary basis function was used to describe the elements (C, H, O, N) along with quenching ions (Cr⁶⁺ and Fe³⁺ ions). The TDDFT method was implemented to analyse the electronic transitions for the fluorophore in presence of the quenching ions.

References

1. Vardhan, K.H., Kumar, P.S. and Panda, R.C., 2019. *J. Mol. Liq.* 290, 111197.
2. Xu, J., Cao, Z., Zhang, Y., Yuan, Z., Lou, Z., Xu, X. and Wang, X., 2018. *Chemosphere* 195, 351-364.
3. Bhatnagar, A. and Sillanpää, M., 2010. *Chem. Eng. J.* 157, 277-296.
4. Quesada, H.B., Baptista, A.T.A., Cusioli, L.F., Seibert, D., de Oliveira Bezerra, C. and Bergamasco, R., 2019. *Chemosphere* 222, 766-780.
5. Liu, Y., Wang, P., Gojenko, B., Yu, J., Wei, L., Luo, D. and Xiao, T., 2021. *Environ. Pollut.* 118209.
6. Bhatnagar, R. and Jain, D., 2016. *Sustain. Water Resour. Manag* 2(2), 161-173.
7. Duffus, J.H., 2002. *Pure Appl. Chem.* 74(5), 793-807.
8. Duruibe, J.O., Ogwuegbu, M.O.C. and Egwurugwu, J.N., 2007. *Int. J. Phys. Sci.* 2(5), 112-118.
9. Babel, S. and Kurniawan, T.A., 2003. *J. Hazard. Mater.* 97, 219-243.
10. Dixit, R., Malaviya, D., Pandiyan, K., Singh, U.B., Sahu, A., Shukla, R., Singh, B.P., Rai, J.P., Sharma, P.K., Lade, H. and Paul, D., 2015. *Sustainability* 7(2), 2189-2212.
11. Alloway, B.J., 2013. Springer, Dordrecht. 195-209
12. Rahman, Z. and Singh, V.P., 2019. *Environ. Monit. Assess.* 191(7), 1-21.
13. Briffa, J., Sinagra, E. and Blundell, R., 2020. *Heliyon*, 6(9), 04691.
14. Yang, Q., Li, Z., Lu, X., Duan, Q., Huang, L. and Bi, J., 2018. *Sci. Total Environ.* 642, 690-700.
15. Masindi, V. and Muedi, K.L., 2018., R. (ed.), IntechOpen: London, 10, 115-132.
16. Ghorbani, M., Izadi, Z., Jafari, S., Casals, E., Rezaei, F., Aliabadi, A., Moore, A., Ansari, A., Puentes, V., Jaymand, M. and Derakhshankhah, H., 2021. *Nanomedicine*, 16(13), 1133-1151.
17. Malik, N., Biswas, A.K., Qureshi, T.A., Borana, K. and Virha, R., 2010. *Environ. Monit. Assess.* 160(1), 267-276.
18. Egorova, K.S. and Ananikov, V.P., 2017. *Organometallics* 36(21), 4071-4090.
19. Kumar, M. and Puri, A., 2012. *Indian J. Occup. Environ. Med.* 16(1), 40-44.

20. Paul, D., 2017. *Ann. Agrar. Sci.* 15(2), 278-286.
21. Ukhurebor, K.E., Aigbe, U.O., Onyancha, R.B., Nwankwo, W., Osibote, O.A., Paumo, H.K., Ama, O.M., Adetunji, C.O. and Siloko, I.U., 2021. *J. Environ. Manage.* 280, 111809.
22. Suh, M., Wikoff, D., Lipworth, L., Goodman, M., Fitch, S., Mittal, L., Ring, C. and Proctor, D., 2019. *Crit. Rev. Toxicol.* 49(2), 140-159.
23. Shanker, A.K., Cervantes, C., Loza-Tavera, H. and Avudainayagam, S., 2005. *Environ. Int.* 31(5), 739-753.
24. Losi, M.E., Amrhein, C. and Frankenberger, W.T., 1994. *Rev. Environ. Contam. Toxicol.* 91-121.
25. Masindi, V. and Muedi, K.L., 2018. *Heavy metals*, 10, 115-132.
26. Tiwary, R.K., 2001. *Water Air Soil Pollut.* 132(1), 185-199.
27. Jonathan, M.P. and Ram Mohan, V., 2003. *Mar. Pollut. Bull.* 46(2), 263-268.
28. Cipullo, S., Snapir, B., Tardif, S., Campo, P., Prpich, G. and Coulon, F., 2018. *Sci. Total Environ.* 645, 662-673.
29. Miranda, L.S., Wijesiri, B., Ayoko, G.A., Egodawatta, P. and Goonetilleke, A., 2021. *Water Res.* 202, 117386.
30. Namieśnik, J. and Rabajczyk, A., 2010. *Chem. Speciat. Bioavailab.* 22(1), 1-24.
31. Angelakis, A.N. and Spyridakis, D.S., 2010. *Water Science and Technology: Water Supply*, 10(4), 618-628.
32. Duruibe, J.O., Ogwuegbu, M.O.C. and Egwurugwu, J.N., 2007. *Phys. Sci. Int. J.* 2(5), 112-118.
33. Yorifuji, T., Takaoka, S. and Grandjean, P., 2018. *Neurotoxicol Teratol.* 69, 49-53.
34. Díez, S., 2008. *Rev. Environ. Contam. Toxicol.* 111-132.
35. Beyer, W.N., Dalgarn, J., Dudding, S., French, J.B., Mateo, R., Miesner, J., Sileo, L. and Spann, J., 2004. *Arch. Environ. Contam. Toxicol.* 48(1), 108-117.
36. Nguyen, H.L., Braun, M., Szaloki, I., Baeyens, W., Van Grieken, R. and Leermakers, M., 2009. *Water Air Soil Pollut.* 200(1), 119-132.
37. Kraft, C., Von Tuempling Jr, W. and Zachmann, D.W., 2006. *Acta Hydrochim. Hydrobiol.* 34(3), 257-264.
38. Tumolo, M., Ancona, V., De Paola, D., Losacco, D., Campanale, C., Massarelli, C. and Uricchio, V.F., 2020. *Int. J. Environ. Res. Public Health* 17(15), 5438
39. Renberg, I., Persson, M.W. and Emteryd, O., 1994. *Nature* 368, 323-326.
40. Kumar, V., Sharma, A., Kumar, R., Bhardwaj, R., Kumar Thukral, A. and Rodrigo-Comino, J., 2020. *Hum Ecol Risk Assess* 26(1), 1-16.
41. United Nations Intergovernmental Panel on Climate Change- Fifth Assessment Report; Climate Change 2014: Impacts, Adaptation and Vulnerability, Yokohoma, Japan.
42. Ansari, A.A., Singh, I.B. and Tobschall, H.J., 1999. *Environ. Geol.* 38(1), 25-33.
43. Singh, M., Müller, G. and Singh, I.B., 2002. *Water Air Soil Pollut.* 141(1), 35-54.
44. Malik, D., Singh, S., Thakur, J., Singh, R.K., Kaur, A. and Nijhawan, S., 2014. *Int. J. Curr. Microbiol. App. Sci.* 3(10), 856-863.
45. Hejabi, A.T., Basavarajappa, H.T., Karbassi, A.R. and Monavari, S.M., 2011. *Environ. Monit. Assess.* 182(1), 1-13.

- 46 Bhattacharya, B.D., Nayak, D.C., Sarkar, S.K., Biswas, S.N., Rakshit, D. and Ahmed, M.K., 2015. *J. Clean. Prod.* 96, 233-243.
47. Sarkar, S.K., Bhattacharya, B., Debnath, S., Bandopadhaya, G. and Giri, S., 2002. *Aquat Ecosyst Health Manag* 5(4), 467-472.
48. Tüzen, M., 2003. *Food Chem.* 80(1), 119-123.
49. Rubio, R., Sahuquillo, A., Rauret, G. and Quevauviller, P., 1992. *Int. J. Environ. Anal. Chem.* 47(2), 99-128.
50. Ghosh, S., Prasanna, V.L., Sowjanya, B., Srivani, P., Alagaraja, M. and Banji, D., 2013. *Asian J. Pharm. Anal.* 3(1), 24-33.
51. Manceau, A., Lanson, B. and Drits, V.A., 2002. *Geochim. Cosmochim. Acta* 66(15), 2639-2663.
52. McComb, J.Q., Rogers, C., Han, F.X. and Tchounwou, P.B., 2014. *Water, Air, & Soil Pollut.* 225(12), 1-10.
53. Aragay, G. and Merkoçi, A., 2012. *Electrochim. Acta* 84, 49-61.
54. Muthusamy, S., Rajalakshmi, K., Zhu, D., Zhu, W., Wang, S., Lee, K.B., Xu, H. and Zhao, L., 2021. *Sens. Actuators B: Chem.* 346, 130534.
55. Quang, D.T. and Kim, J.S., 2010. *Chem. Rev.* 110(10), 6280-6301.
56. Yu, L., Zhang, L., Ren, G., Li, S., Zhu, B., Chai, F., Qu, F., Wang, C. and Su, Z., 2018. *Sens. Actuators B: Chem.* 262, 678-686.
57. Trotta, F. and Mele, A., 2019. *Nanosponges: Synthesis and Applications: First Edition*, Wiley, London.
58. Mohanraj, V.J. and Chen, Y., 2006. *Trop. J. Pharm. Res.* 5(1), 561-573.
59. De, M., Ghosh, P.S. and Rotello, V.M., 2008. *Adv. Mater.* 20(22), 4225-4241.
60. Lewinski, N., Colvin, V. and Drezek, R., 2008. *Small*, 4(1), 26-49.
61. Thomford, N.E., Senthebane, D.A., Rowe, A., Munro, D., Seele, P., Maroyi, A. and Dzobo, K., 2018. *Int. J. Mol. Sci.* 19(6), 1578.
62. Sekar, A., Yadav, R. and Basavaraj, N., 2021. *New J. Chem.* 45(5), 2326-2360.
63. Yin, H., Truskewycz, A. and Cole, I.S., 2020. *Microchim. Acta* 187(6), 1-25.
64. Ahmadian-Fard-Fini, S., Ghanbari, D., Amiri, O. and Salavati-Niasari, M., 2020. *Carbohydr. Polym.* 229, 115428.
65. Broussard, J. A. and Green, K. J., 2017. *J. Invest. Dermatol.* 137(11), 185-191.
66. Bardhan, S., Roy, S., Chanda, D.K., Ghosh, S., Mondal, D., Das, S. and Das, S., 2020. *Dalton Trans* 49(30), 10554-10566.
67. Ding, L., Yang, H., Ge, S. and Yu, J., 2018. *Spectrochim. Acta, Part A* 193, 305-309. 68. Thomford, N.E., Senthebane, D.A., Rowe, A., Munro, D., Seele, P., Maroyi, A. and Dzobo, K., 2018. *Int. J. Mol. Sci.* 19(6), 1578.
68. Lewinski, N., Colvin, V. and Drezek, R., 2008. *Small*, 4(1), 26-49.
69. Sekar, A., Yadav, R. and Basavaraj, N., 2021. *New J. Chem.* 45(5), 2326-2360.
70. Yin, H., Truskewycz, A. and Cole, I.S., 2020. *Microchim. Acta* 187(6), 1-25.
71. Ahmadian-Fard-Fini, S., Ghanbari, D., Amiri, O. and Salavati-Niasari, M., 2020. *Carbohydr. Polym.* 229, 115428.
72. Maurer-Jones, M.A., Gunsolus, I.L., Murphy, C.J. and Haynes, C.L., 2013. *Anal. Chem.* 85(6), 3036-3049.

73. Banerjee, A., Tripathi, S., Mukherjee, K. and Mukherjee, S., 2018. *Int. J. Chem. Stud.* 6(6), 185-189.
74. Panda, J. and Sarkar, P., 2012. *Environ. Sci. Pollut. Res.* 19(5), 1809-1817.
75. Chattopadhyay, B., Chatterjee, A. and Mukhopadhyay, S.K., 2002. *Aquat Ecosyst Health Manag* 5(2), 191-203.
76. Swaddle, T.W., Salerno, J. and Tregloan, P.A., 1994. *Chem. Soc. Rev.* 23(5), 319-325.
77. Kang, C.M., Seong, S., Song, J.S. and Shin, Y., 2021. *Materials*, 14(2), 305.
78. Jackson, M. and Mantsch, H.H., 1995. *Crit. Rev. Biochem. Mol. Biol.* 30(2), 95-120.
79. Bailey, S.W., 1969. *Mineralogical Society of America (United States)* 54, 1540-1545.
80. Bohlen, S.R., Montana, A. and Kerrick, D.M., 1991. *Am Min* 76, 677-680.
81. Hietanen, A., 1956. *Am. Mineral.* 41, 1-27.
82. Burnham, C.W., 1963. *Z. Kristallogr. Cryst. Mater.* 118, 337-360.
83. Monshi, A., Foroughi, M.R. and Monshi, M.R., 2012. *World J Nano Sci Eng*, 2012, 2, 154, 160.
84. Chauhan, A. and Chauhan, P., 2014. *J Anal Bioanal Tech*, 5(5), 1-5.
85. Patterson, A.L., 1939. *Phys. Rev.* 56(10), 978.
86. Hamdan, H., Muhid, M.N.M., Endud, S., Listiorini, E. and Ramli, Z., 1997. *J. Non-Cryst. Solids* 211(1-2), 126-131.
87. Sharma, S., Rasool, H.I., Palanisamy, V., Mathisen, C., Schmidt, M., Wong, D.T. and Gimzewski, J.K., 2010. *ACS Nano* 4(4), 1921-1926.
88. Giannuzzi, L.A. and Stevie, F.A., 1999. *Micron* 30(3), 197-204.
89. Movasaghi, Z., Rehman, S. and ur Rehman, D.I., 2008. Fourier transform infrared (FTIR) spectroscopy of biological tissues. *Appl. Spectrosc. Rev.* 43(2), 134-179.
90. Jackson, M. and Mantsch, H.H., 1995. *Crit. Rev. Biochem. Mol. Biol.* 30(2), 95-120.
91. Jackson, M. and Mantsch, H.H., 1995. *Crit. Rev. Biochem. Mol. Biol.* 30(2), 95-120
92. Shindo, D. and Oikawa, T., 2002. In *Analytical electron microscopy for materials science* Springer, Tokyo, 81-102
93. Naderi, M., 2015. *Surface area: brunauer–emmett–teller (BET)*. Academic Press.
94. Bardestani, R., Patience, G.S. and Kaliaguine, S., 2019. *Can J Chem Eng* 97(11), 2781-2791.
95. Hwang, N. and Barron, A.R., 2011. *The Connexions project* 1-11.
96. Marotta, A., Buri, A. and Branda, F., 1981. *J. Mater. Sci.* 16(2), 341-344.
97. Charsley, E.L. and Warrington, S.B., 1992. *Thermal analysis-techniques and applications*.
98. Akash, M.S.H. and Rehman, K., 2020. In *Essentials of Pharmaceutical Analysis*. Springer, Singapore.
99. Coulter, J.B. and Birnie III, D.P., 2018. *Phys. Status Solidi B* 255(3), 1700393.
100. Ma, Z., Ming, H., Huang, H., Liu, Y. and Kang, Z., 2012. *New J. Chem.* 36(4), 861-864.
101. Janke, E.M., Williams, N.E., She, C., Zherebetsky, D., Hudson, M.H., Wang, L., Gosztola, D.J., Schaller, R.D., Lee, B., Sun, C. and Engel, G.S., 2018. *J. Am. Chem. Soc.* 140(46), 15791-15803.
102. Gilliland, G.D., 1997. *Mater. Sci. Eng. R Rep.* 18(3-6), 99-399.
103. Empedocles, S.A., Norris, D.J. and Bawendi, M.G., 1996. *Phys. Rev. Lett.* 77(18), 3873.
104. Phillips, D., Drake, R.C., O'Connor, D.V. and Christensen, R.L., 1985. *Instrumentation Science & Technology* 14, 267-292.

105. Rehman, M., Abu Izneid, B.A., Abdullah, M.Z. and Arshad, M.R., 2011. *Int. J. Food Sci.* 46(6), 1303-1309.
106. Robertson, J., 2004. *EPJ Appl. Phys.* 28(3), 265-291.
107. Booth, F., 1951. *J. Chem. Phys.* 19(4), 391-394
108. Breeze, J.D., Perkins, J.M., McComb, D.W. and Alford, N.M., 2009. *J. Am. Ceram. Soc.* 92(3), 671-674.
109. Pollak, M. and Pike, G.E., 1972. *Phys. Rev. Lett.* 28(22), 1449.
110. Sakata, M.T. and Cooper, M.J., 1979. *J. Appl. Crystallogr.* 12(6), 554-563.
111. Obot, I.B., Macdonald, D.D. and Gasem, Z.M., 2015. *Corros. Sci.* 99, 1-30.



Chapter 2

*Synthesis and characterization of
microcline and kyanite in varying sizes to
assess their application domain*



Chapter 2

2.1 Overview

Nanoscience and nanotechnology have gathered huge attention in the modern world [1-2]. As compared to the coarse-sized particles, the enhanced surface-to-volume ratios in nano-regime radically change the physicochemical properties like electrical, optical, magnetic, catalytic behaviour, etc [3-4]. Such enhancement in various properties and stability is now widely utilized in novel applications like fabrication of cost-effective devices, supercapacitors, antimicrobial agents, sensors, etc [5]. Hence, the determination of variation of various properties with sample size is crucial prior to sensor development.

Although the silicate minerals are most abundant in nature [6], an insufficient amount of interest has been paid on their applications in sensor development or as an antibacterial agent. It is a challenge to bring naturally occurring minerals to usable form, mainly due to their bulk size and presence of impurities [7]. Moreover, it is very tough to disperse silicate minerals in an aquatic medium [8]. Biological applications, especially biosensing and antibacterial assays require the bioavailability of the samples. This can be achieved by mechanical disintegration of coarse materials to colloidal or finer sizes ($<0.2 \mu\text{m}$) [9]. Size reduction not only enhances various physicochemical and biological properties, the process of size reduction also introduces various defect states [10] that influence the sensing efficacy and fluorescence properties as required for the sensor development. Thus, this chapter emphasizes on “size-tuned” variation of various properties.

As discussed in the previous chapter, two commonly found silicate minerals (microcline and kyanite) were selected for the work. Top-down synthesis was performed using a mechanical ball mill to bring down the size to a finer range for applications in the sensing and biological domain. The coarse-sized fractions of microcline and kyanite were marked as M1 and KY1 respectively. The ball-milled finer sized fractions were marked as M2 and KY2 respectively.

2.2 Materials and methods

In the following work, the coarser fractions of silicate minerals (microcline and kyanite) are physically disintegrated into a finer fraction in nano-regime size using a common top-down approach using ball milling techniques. As discussed in the previous chapter (Chapter 1), the purchased minerals were initially rinsed thoroughly to remove debris and impurities prior to size fractionation. The coarse fraction was obtained by grinding in an agate mortar, followed by sieving through 100 mesh. The sieved samples were marked as M1 (microcline) and KY1 (kyanite). Then a portion of the coarse samples (M1 and KY1) was subjected to mechanical ball milling for 12 h at 300 rpm. In order to reduce any kind of agglomerations, the ball-milled samples were dispersed in acetone, sonicated in a bath-sonicator for an hour, and then dried to obtain the finer fractions. The finer-sized fractions of microcline and kyanite obtained were marked as M2 and KY2 respectively.

2.3 Results and discussion

2.3.1 Physical characterization of different size fractions of microcline (M1 and M2), and kyanite (KY1 and KY2)

Phase purity, crystalline properties, and microstructural analysis were investigated from X-ray diffraction measurements. Since naturally formed minerals may contain various impurities, detection of the presence of any such impurity at the crystal level is of utmost importance prior to other experimentations. The diffraction patterns of both the minerals are in good agreement with JCPDS card no. 84-0708 and 11-0046 respectively [11-12]. The absence of any unwanted peak indicates the high purity of the samples [13]. Moreover, peak broadening in the case of M2 and KY2 suggests a reduction in crystallite sizes [14]. Reitveld refinement was performed following the standard methodology for microstructural characterization using MAUD v2.8 (Material Analysis Using Diffraction) software [15], and the XRD pattern of the samples was superimposed with corresponding miller indices.

Well-matched peak positions of experimental and the computed patterns of both the samples (Figure 2.1) at different size fractions confirm the high purity at crystal level [16]. Table 2.1 illustrates the results obtained from the microstructural parameters obtained after the final cycle of refinement. Microcline and kyanite exhibit triclinic structures belonging to the C-1

and P-1 space groups respectively [17-18]. The structural properties and bonding networks obtained from Vesta v3.4.3 are depicted in Figure 2.2.

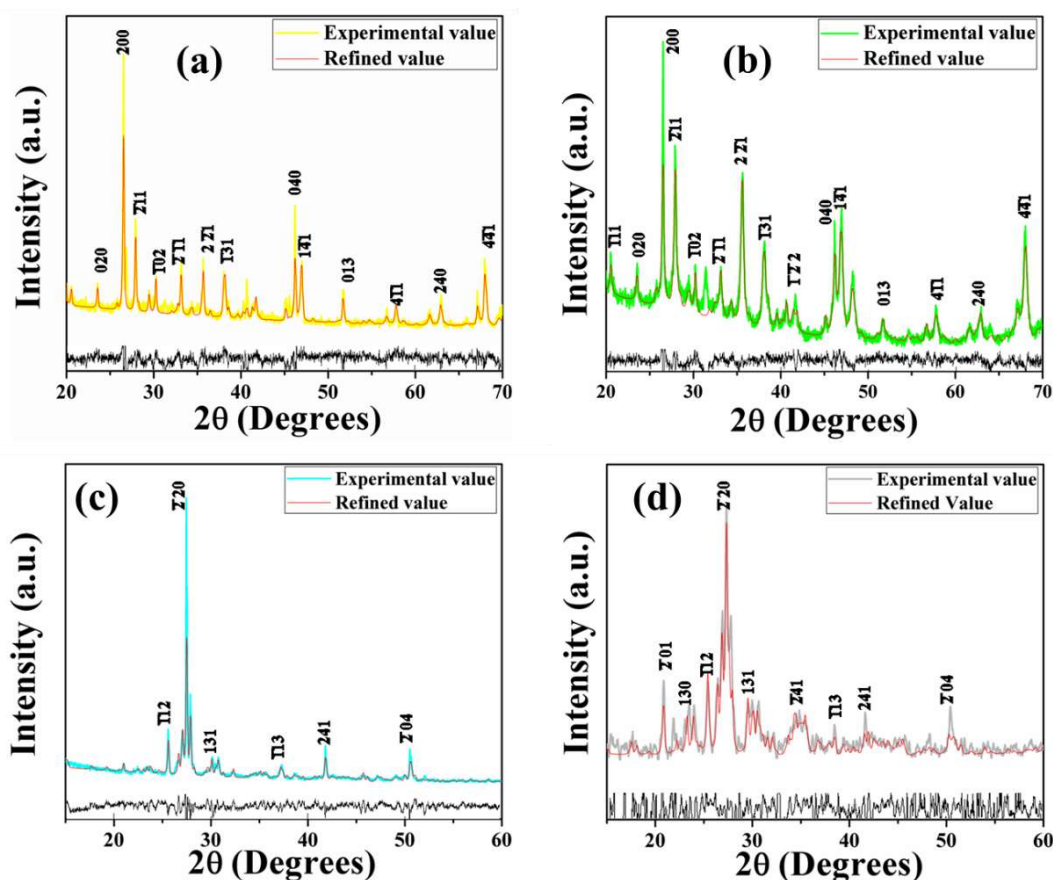


Figure 2.1: Indexed XRD pattern of the sample (a) yellow for AF1, (b) green for AF2, (c) blue for KY1, and (d) grey for KY2, and the simulated Rietveld refinement plot (continuous red line) obtained by fitting the experimental PXRD pattern using the MAUD program. The respective residue is plotted at the bottom (black line)

In M1, the silicon and aluminium polyhedron is shared by oxygen and potassium polyhedron on either side, maintaining a symmetry, which is missing in the case of M2. Refinement also detected the presence of certain impurities like Na, Ca, and Ba, but at a very low occupancy, hence no prominent effect is visible in XRD studies. A commendable change in bond lengths and bond angles due to the mechanical action of ball-milling is observed in M1 and M2 (Figure 2.2c-d). The defect states thus formed can be beneficial for the enhancement of various physicochemical properties [19]. Similarly, in the case of kyanite, octahedral AlO_6 stacked with SiO_4 tetrahedra is observed (Figure 2.2a-b), and oxygen is shared between them forming a zigzag pattern in KY1. In the case of KY2, the mechanical ball milling altered the bond lengths and bond angles. Absence of certain oxygen molecules in the kyanite

crystals generated oxygen vacancy states and the prominent symmetry as seen in KY1 has changed in KY2 due to such oxygen vacancies.

Table 2.1: Structural and microstructural parameters of the samples obtained from Rietveld analysis

	KY1	KY2	AF1	AF2
a (Å)	7.11	7.13	8.58	8.63
b (Å)	7.83	7.85	12.95	12.91
c (Å)	5.58	5.58	7.21	7.26
alpha (°)	89.88	90.02	89.92	90.71
beta (°)	101.23	101.19	116.01	116.16
gamma (°)	106.10	106.07	89.12	88.02
V (Å³)	292.30	293.76	719.96	725.86
Size (Å)	2238.63	427.108 ± 6.62	2050.82 ± 235.62	669.31 ± 25.52
	±214.85			
strain	1.78E-4	7.31E-5 ± 0.001	0.001 ± 1.36E-4	1.81E-4 ± 2.08E-5
	±5.39E-5			
χ²	1.79	1.84	1.66	1.77
R_p	0.16	0.07	0.12	0.43
R_{wp}	0.22	0.09	0.16	0.57

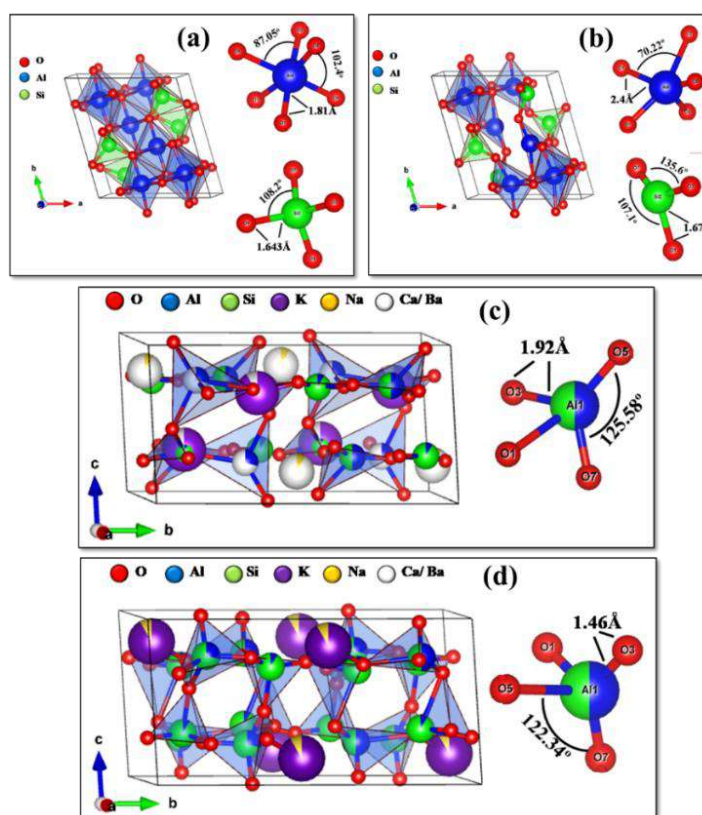


Figure 2.2: Unit cells of the sample (a) KY1, (b) KY2, (c) M1, and (d) M2, along with their bond angles and bond lengths.

Purity at the molecular component level for both size fractions of natural microcline and kyanite was investigated using FTIR spectrometry (Figure 2.3). In the case of kyanite, absorption bands were observed at 542, 567, 602, 637, 672, 730, 892, and 934 cm^{-1} . The bands located between 500 to 700 cm^{-1} attributed to the vibration of Al-O octahedron and deformation vibration of Si-O tetrahedron. At 892 and 934 cm^{-1} , the Si-O tetrahedron exhibits the dominant vibrations [18, 20-21]. In the case of M1 and M2, the absorption bands were detected at 536 cm^{-1} (coupling between the O-Si-O bending vibration and K-O stretching), 579 cm^{-1} and 648 cm^{-1} (O-Si(Al)-O bending vibrations), 728 cm^{-1} and 772 cm^{-1} (Si-Al(Si) and the Si-Si stretching), broader peak at 998 cm^{-1} and 1054 cm^{-1} (Si(Al)-O stretching), 1090 cm^{-1} (Si-O stretching) [17]. Among the three polymorphs of natural K-feldspars from igneous rocks (microcline, orthoclase, and sanidine), the FT-IR spectrum matches best with that of microcline [22], thus confirming that the K-feldspar used in the study was microcline.

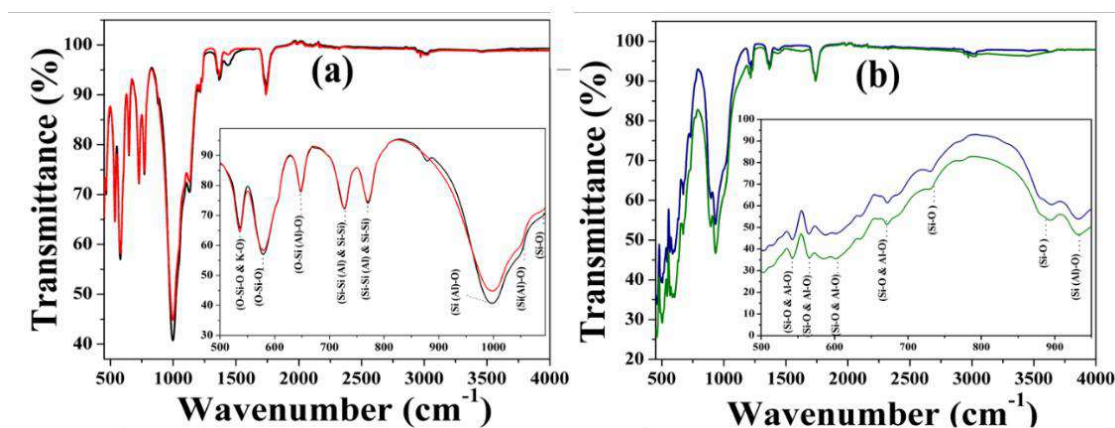


Figure 2.3: Normalized FTIR spectra of the samples (a) Microcline (M1 and M2) and (b) Kyanite (KY1 and KY2)

The morphological features and changes in the sample shape due to the physical impact of ball milling were investigated using electron microscopy (Figure 2.4). The FESEM micrographs of microcline shows that the distinctly large and spherical particles of M1 acquire a finer size in the M2 fraction. Similarly, the roughly rod-shaped particles of kyanite in coarse form (KY1) form a more rounded shape having blunt edges, with evenly distributed smaller particle size range. Thus it is evident from FESEM micrographs that the action of ball milling has successfully changed the morphology and reduced overall particle sizes, thus enhancing surface to volume ratio. For a more precise understanding of the particle reduction, TEM study was performed (Figure 2.4 inset). Size distribution was estimated by randomly considering 20 particles in each case.

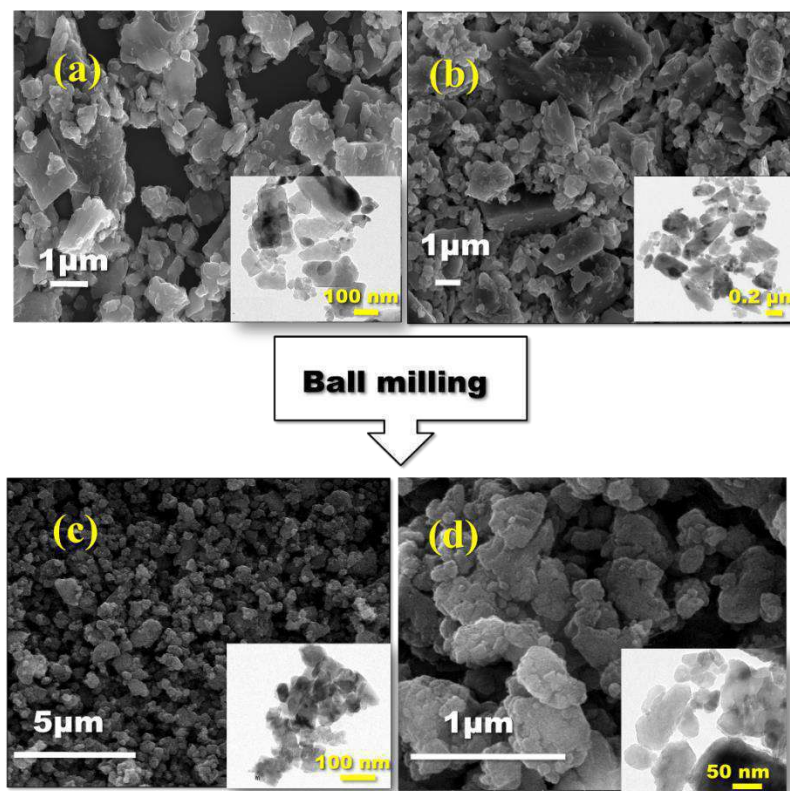


Figure 2.4: FESEM micrographs of (a) M1, (b) KY1, (c) M2, and (d) KY2, with their corresponding TEM images

The average size from TEM micrographs for M1 and KY1 is 104 and 103 nm, which distinctly reduces in M2 and KY2 to 62 and 44 nm respectively. Thus both FESEM and TEM studies confirmed the particle size reduction and changes in morphology due to the mechanical action of ball milling.

2.3.2 Elemental analysis of nano-sized microcline (M2) and kyanite (KY2)

Since the determination of purity is a pivotal factor in this study as it deals with natural minerals, elemental analysis was performed by Energy Dispersive X-ray (EDS) analysis. Since the sensors were developed using the minerals in their nano-regime (M2 and KY2), their elemental purity was investigated. The study confirmed the presence of silicon, oxygen, aluminium, potassium in microcline (Figure 2.5a), while that of kyanite shows the presence of silicon, oxygen, and aluminium (Figure 2.5b). EDS spectra of kyanite confirm high purity while that of microcline shows the presence of a minute quantity of impurities like sodium and calcium, which is concordant with the Rietveld data.

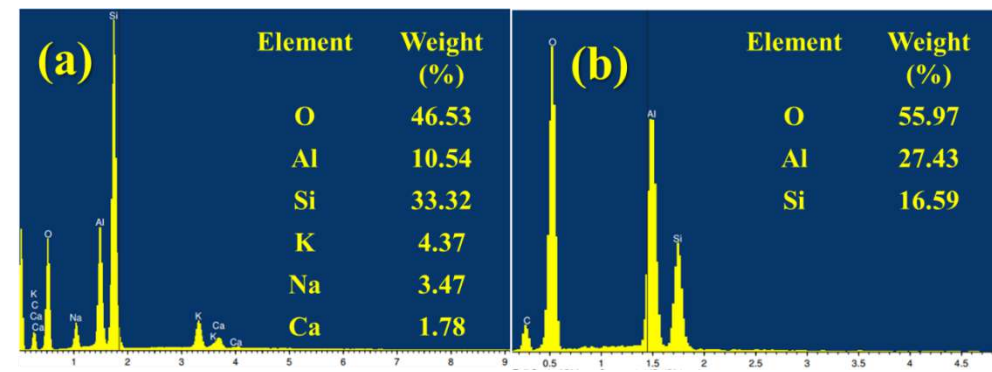


Figure 2.5: EDS spectra of (a) microcline and (b) kyanite

2.3.3 Optical characterization of microcline and kyanite

Sample size and presence of defect states plays a crucial role in influencing the optical quality and modulating the optical bandgap. Initially, absorption spectra of the samples were measured by UV-Vis spectroscopy. The absorption maxima of M1 and KY1 were observed at 219.8 nm and 220 nm respectively, which in the case of M2 and KY2 exhibited peak broadening and shifted to 219.4 nm and 219.5 nm respectively (Figure 2.6). A slight blue shift was also observed for M1 and M2 samples. Hence changes in the optical band gap were determined by calculating the bandgap energies using the following formula [23]

$$\alpha E = A(E - E_g)^n \quad (2.1)$$

Here, E and E_g represent photon energy ($h\nu$) and optical band gap energy (in electron volt or eV) respectively, A is the absorbance and α represents absorption coefficient ($\alpha = 2.303 A/t$, where t is the thickness of the cuvette). In the Tauc plot, $(\alpha h\nu)^2$ is plotted against photon energy $h\nu$, energy is calculated by extrapolating the linear region and by intersecting the linear portion to the energy axis (Figure 2.6 inset). Bandgap for M1 and M2 was found to be 2.99 eV and 3.38 eV respectively, while kyanite exhibited insulating properties due to a wider bandgap of 5.34 eV and 5.06 eV for KY1 and KY2 respectively.

The emission spectra for all four samples measured at the excitation wavelength 370 nm are represented in Figure 2.6(c-d). In the case of microcline, a strong emission band at 430 nm was observed, with certain smaller bands located at 460, 290, 510, and 530 nm. Similarly, in kyanite, bands were observed at 430, 495, and 525 nm. Slight enhancement of the emission intensity with prominent bands indicates different defect states in the crystals that occurred during mechanical grinding [24].

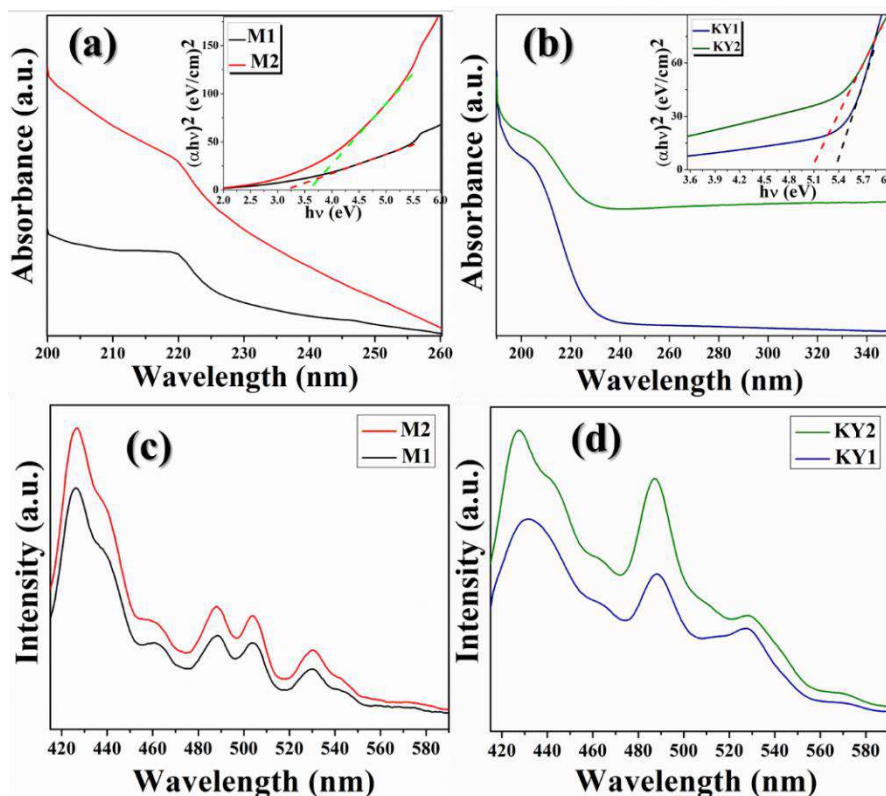


Figure 2.6: UV-vis spectra of (a) microcline and (b) kyanite, with their corresponding Tauc plot (bandgap) (inset); PL spectra of (c) microcline and (d) kyanite

Moreover, a larger surface area provides a greater number of defects [25], hence M2 and KY2 exhibits better emission intensity. Thus it is evident from the optical studies that ball milling and subsequent size reduction influenced the absorption and emission properties of the mineral samples. Moreover, better fluorescence properties in M2 and KY2 suggests the usage of the finer fractions for further studies.

2.3.4 Electrical characterization of different size fractions of microcline and kyanite

As discussed in the previous chapter, a detailed understanding of the electrical properties of both minerals at different size ranges is required prior to the development of sensing devices. Moreover, the determination of the effect of temperature on various electrical properties is also necessary for real-life or industrial applications. Enhancement of electrical properties with a decrease in size can be very useful for futuristic sensing device development. In this work, microstructure and size-dependent alteration of dielectric properties was measured for microcline and kyanite in its bulk (M1 and KY1 respectively) and fine (M2 and KY2 respectively) form. Moreover, the influence of temperature was also analyzed at different temperatures ranging from 30°C to 200°C.

As illustrated in Figure 2.7, at lower frequencies, the dielectric constant shows higher values which gradually reduces with an increase in frequencies. Such phenomenon was attributed to the Maxwell-Wagner [26] interfacial polarization effect that occurs due to various structural inhomogeneities like vacancies, imperfect crystal alignment, or other crystal defects formed during sample preparation. The observation is in good accordance with Koop's theory [27], according to which the free charge carriers (formed due to structural defects) get trapped within the non-conducting grain boundaries and result in oscillating dipoles that produce polarization effect at lower frequency regime. Hence high permittivity values are obtained which gradually declines at higher frequency domain as the rapidly changing external field cannot be trailed by the dipoles, thus resulting in reduced permittivity.

Dielectric behaviour varies greatly with the size, temperature, and chemical composition of the samples. Dielectric constant value is found to be significantly higher in M2 and KY2 as compared to M1 and KY1 respectively. In the experiment, at 1 MHz the dielectric constant value of KY1 and KY2 was found to be 10.03 and 12.79 respectively, whereas, for M1 and M2, the value was 8.8 and 17.2 respectively. Silicate minerals are reported to have a low dielectric constant value (approximately 3-8), hence have limited applications in designing semiconductor devices, microelectronics, and integrated circuit. The reported dielectric value at 1 MHz by U.S. Geological Survey Report (1979) [28] for microcline is 5.48, and for kyanite is 7.831. Initially, at room temperature (~30 °C), a high dielectric value was observed which decreases with increasing temperature due to insufficient nano-dipole energy for overcoming inter-dipolar frictional force at initial temperatures. The lattice and crystal defect states present in nano-regime (M2 and KY2) as evident from XRD and FESEM data play a significant role in dielectric permittivity enhancement. The oxygen vacancies formed in both the finer fractions can efficiently trap the free charges which in turn creates nano-dipoles, thus resulting in the space charge polarization and a higher degree of dielectric values (7.8×10^4 in M2 and 8.2×10^3 in KY2 at 40 Hz). The lesser number of crystal defects and more aligned and symmetric crystallographic structure in the bulk fraction causes low dielectric values (48.25 for M1 and 450.88 for KY1 at 40 Hz). Even the chemical composition influences the dielectric value as the dielectric permittivity value was found to be higher in kyanite than in microcline in the bulk size range at room temperature. The potassium atom present in the microcline restricts the trapping mechanism because of its larger shape and size, but it is absent in kyanite. Hence, the probability of

trapping free charges in the vacant region increases the chances of nano-dipoles formation in bulk-sized kyanite samples, resulting in a higher value of dielectric constant. The tangent loss variation illustrated in Figure 2.7 is in good accordance with the dielectric constant values. A gradual shift of the peak position towards lower frequencies at higher temperatures suggests a reduction of polar active elements [29] such as surface adsorbed moisture in the samples.

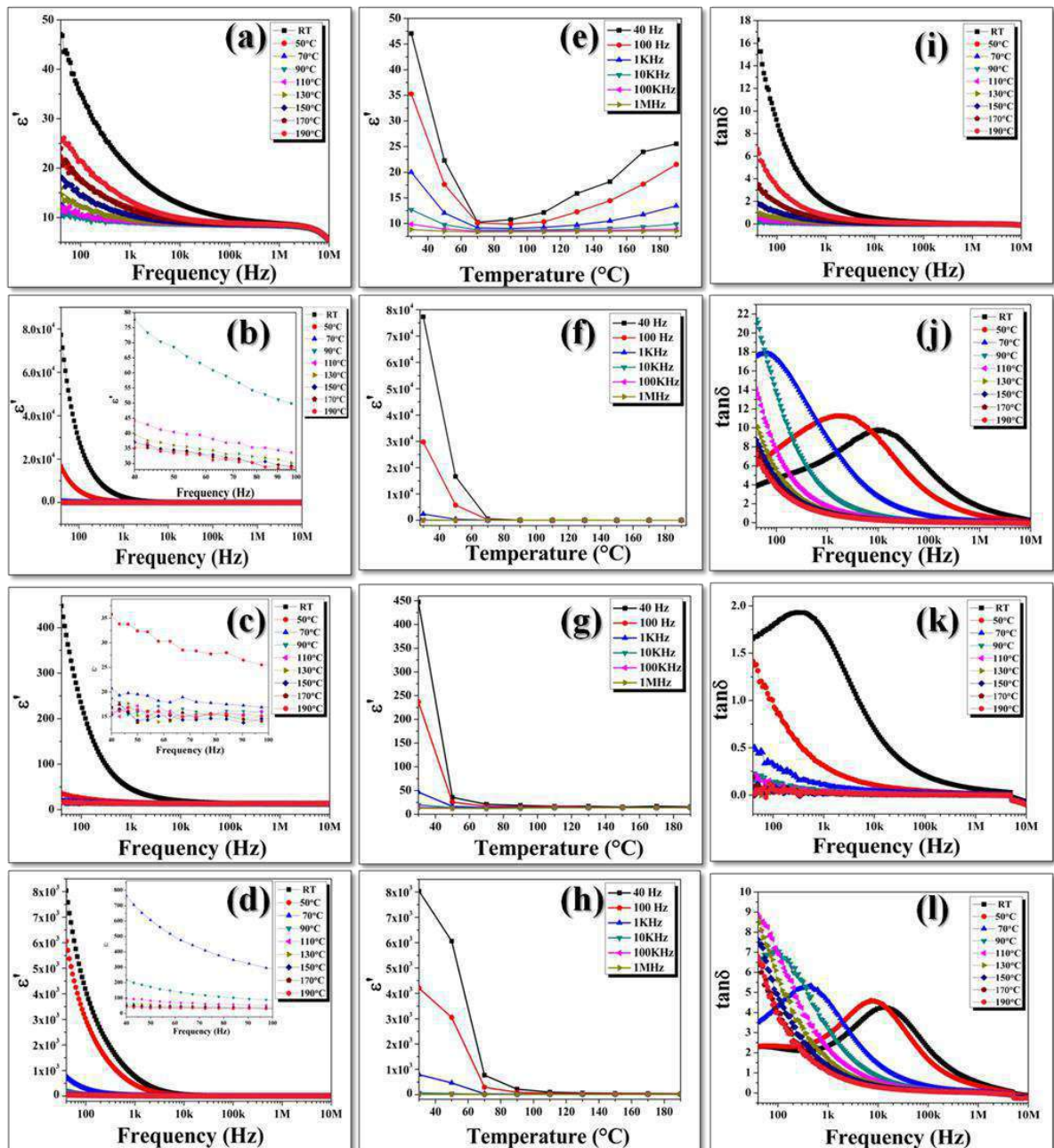


Figure 2.7: Variation of Dielectric constant with frequency for the samples (a-d); Variation of Dielectric constant with temperature for the samples (e-h); tangent loss ($\tan\delta$) of the samples (i-l) for M1, M2, KY1 and KY2 respectively

In order to analyze the charge transport mechanism, size and temperature-dependent variation of ac conductivity were carried out. The ac conductivities of the samples were found to be highest at room temperature, which decreases with a subsequent increase in temperature. Moreover, the values of ac conductivity increased with an increase in frequency (Figure 2.8). Such a phenomenon occurred due to the higher mobility and hopping of electrons at higher frequencies [30]. There is a decrease in conductivity with the decrease in size. The frequency response of ac conductivity has been investigated using Jonscher's power law relation [31]:

$$\sigma_{ac} = B\omega^n \quad (2.2)$$

Here, 'B' and 'n' are constants. The value of 'n' has been estimated by plotting $\ln\sigma$ Vs $\ln\omega$ (Figure 2.8) and found to be around 0.2819 and 0.3119 for M1 and KY1, which reduces to 0.0775 and 0.2062 for M2 and KY2 respectively. The non-zero value of all the samples confirms that they do not follow perfectly Debye type conduction mechanism (where $n = 0$), and the diffusion-limited hopping dominates in ac conductivity. The dc conductivities have also been studied for all the samples in the same manner (Figure 2.9). To overcome the potential barrier to escape from the grain boundaries for initiating the charge hopping mechanism, the free charge carriers require a sufficient amount of external energy. Hence, the activation energy required was estimated from the Arrhenius equation stated below [32],

$$\sigma = \sigma_0 \exp(-E_a/K_B T) \quad (2.3)$$

Here, σ_0 , E_a , K_B , and T represent the pre-exponential factor, activation energy, Boltzmann constant, and absolute temperature. The activation energies obtained from the Arrhenius plot (Figure 2.9) at frequencies 10 Hz, 100 kHz, and 1 MHz, and also for dc is given in Table 2.2.

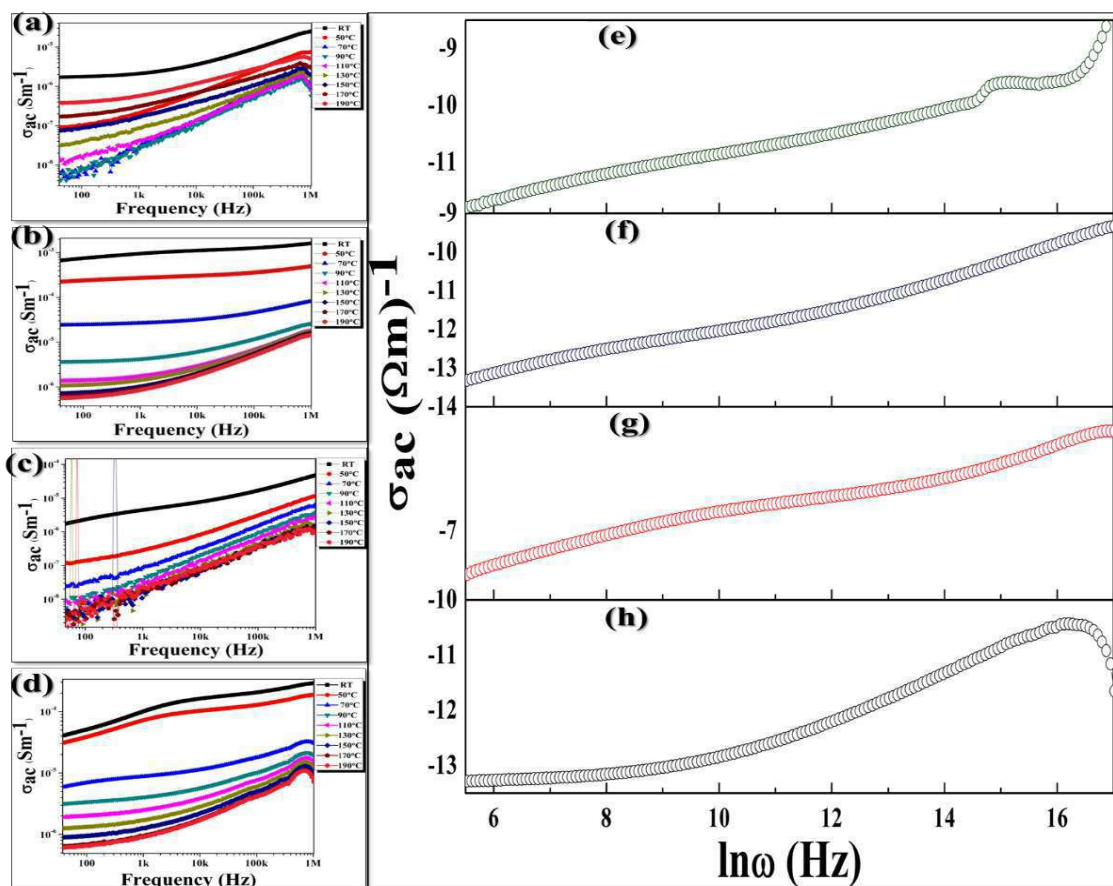


Figure 2.8: Variation of ac electrical conductivity with frequency for the samples (a–d) and corresponding Jonscher's plot for the samples (e–h) for KY2, KY1, M2, and M1 respectively

Table 2.2: Calculated Activation Energies of the Samples from Arrhenius Plots at Different Frequencies

Sample		Frequency			
		DC	kHz	kHz	1 MHz
Activation Energy (eV)	M1	0.29	0.72	0.63	0.55
	M2	0.34	0.74	0.72	0.59
	KY1	0.24	0.42	0.31	0.28
	KY2	0.29	0.38	0.33	0.24

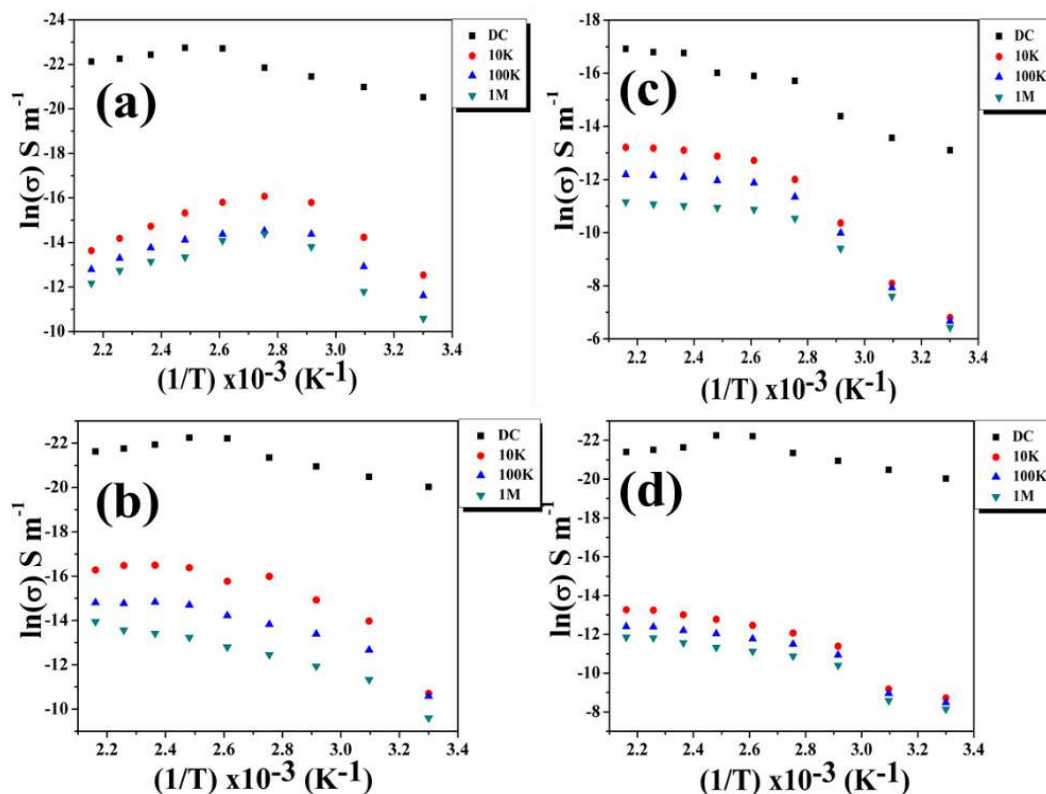


Figure 2.9: Arrhenius plots for the samples (a) M1, (b) KY1, (c) M2, and (d) KY2.

2.4 Summary

The size fractionation of microcline and kyanite from coarser (M1 and KY1 respectively) to a finer fraction (M2 and KY2 respectively) has been successfully carried out through a top-down approach using the mechanical ball milling technique. Reduction in particle size influences their structure-property correlation as there is a drastic change in various properties in the finer size fractions compared to their bulk counterpart. The microstructural and electron microscopy confirms the size-reduction and morphological changes. The crystallographic studies suggest that defect states have been introduced by mechanical milling. The high purity of the natural samples was confirmed from various techniques like XRD, FT-IR, EDS, and elemental mapping. The size reduction has a prominent enhancement in the optical and electrical properties. Moreover, the nano-size fraction can be well-dispersed in an aqueous medium and forms stable suspension, which is an essential factor in biological studies. As the optical properties, along with electrical properties and solubility greatly improves in finer sized fractions, the sensor development was executed using M2 (nano-sized microcline) and KY2 (nano-sized kyanite)

References

1. Kagan, C.R., 2016. ACS Nano 10(3), 2985-2986.
2. Patra, D., Ejnavarzala, H. and Basu, P.K., 2009. Curr. Sci. 651-657.
3. Mahouche-Chergui, S., Guerrouache, M., Carbonnier, B. and Chehimi, M.M., 2013. Colloids Surf. A: Physicochem. Eng. Asp. 439, 43-68.
4. Rana, S.B., Singh, R.P.P. and Arya, S., 2017. J. Mater. Sci.: Mater. Electron. 28(3), 2660-2672.
5. Shipway, A.N., Katz, E. and Willner, I., 2000. ChemPhysChem 1(1), pp.18-52.
6. Baur, W.H., 1972. Nature 240(5382), 461-462
7. Bardhan, S., Roy, S., Chanda, D.K., Das, S., Pal, K., Chakraborty, A., Basu, R. and Das, S., 2019. Cryst. Growth Des. 19(8), 4588-4601.
8. Subramani, T., Rajmohan, N. and Elango, L., 2010. Environ. Monit. Assess. 162(1), 123-137.
9. Klaine, S.J., Alvarez, P.J., Batley, G.E., Fernandes, T.F., Handy, R.D., Lyon, D.Y., Mahendra, S., McLaughlin, M.J. and Lead, J.R., 2008. Environ. Toxicol. Chem. 27(9), 1825-1851.
10. Gogate, P.R. and Kabadi, A.M., 2009. Biochem. Eng. J. 44(1), 60-72.
11. Kalita, J.M. and Chithambo, M.L., 2020. J. Lumin. 224, 117320.
12. Pimentel, C., Gnecco, E. and Pina, C.M., 2015. Surf. Sci. 635, 123-127.
13. Kamal, S.K., Sahoo, P.K., Vimala, J., Shanker, B., Ghosal, P. and Durai, L., 2016. J. Alloys Compd. 678, 403-409.
14. Pike, J., Chan, S.W., Zhang, F., Wang, X. and Hanson, J., 2006. Appl. Catal. A: Gen. 303(2), 273-277.
15. Aryal, S., Rulis, P. and Ching, W.Y., 2008. American Mineralogist 93(1), 114-123.
16. Madsen, K.H., Ates, S., Liu, J., Javadi, A., Albrecht, S.M., Yeo, I., Stobbe, S. and Lodahl, P., 2014. Phys. Rev. B 90(15), 155303.
17. Burt, J.B., Ross, N.L., Gibbs, G.V., Rossman, G.R. and Rosso, K.M., 2007. Phys. Chem. Miner. 34(5), 295-306.
18. Theodosoglou, E., Koroneos, A., Soldatos, T., Zorba, T. and Paraskevopoulos, K. M., 2010. Bull. Geol. Soc. Greece, 43 (5), 2753.
19. Yoshimatsu, K., Reimhult, K., Krozer, A., Mosbach, K., Sode, K. and Ye, L., 2007. Anal. Chim. Acta 584(1), 112-121.
20. Klopogge, J.T. and Wood, B.J., 2015. Spectrochim. Acta, Part A 137, 711-716.
21. Jin, J., Gao, H., Ren, Z. and Chen, Z., 2016. Minerals 6(3), 90.
22. Bambauer, H.U. and Krause, C., 1989. Eur J Mineral 47-58.
23. Das, S., Das, S. and Sutradhar, S., 2017. J. Alloys Compd. 726, pp.11-21.
24. Wang, J.A., Bokhimi, X., Morales, A., Novaro, O., Lopez, T. and Gomez, R., 1999. J. Phys. Chem. B 103(2), 299-303.
25. Das, S., Das, S. and Sutradhar, S., 2017. Ceram. Int. 43(9), 6932-6941.
26. Das, S., Mondal, D., Bardhan, S., Roy, S., Chanda, D.K., Maity, A., Dutta, S., Mukherjee, K. and Das, K., 2022. J. Mater. Sci.: Mater. Electron. 1-15.
27. Koops, C. G., 1951. Phys. Rev. 83(1), 121-124.
28. Olhoeft, G. R., 1979. United States Department of the Interior Geological Survey, Open File Report. 79-993.

29. Duarte, D. and Dodabalapur, A., 2012. *J. Appl. Phys.* 111(4), 044509.
30. Kabashima, S. and Kawakubo, T., 1968. *J. Phys. Soc. Jpn.* 24(3), 493-497.
31. Jonscher, A. K., 1981. *J. Mater. Sci.*, 16, 2037-2060.
32. Sudha, L.K., Sukumar, R. and Uma Rao, K., 2014. *Int. J. Mater., Mech. Manuf.* 2(1), 96-100.



Chapter 3

*Investigation of biocompatibility
& antibacterial efficacy of bulk
microcline (M₁), kyanite (KY₁)
& their nano-fractions (M₂ and KY₂)*



Chapter 3

3.1 Overview

Minerals are well known for their impact on human health for ages, and there exists an integral relationship between the environment and health [1]. Although certain minerals like stibnite, cinnabar, and galena are reported to have high toxicity [2], silicate minerals are reported to have biocompatibility [3]. Biocompatibility of a material is a crucial factor that distinguishes a material from others in terms of its ability to exist in contact with living cells without causing an unacceptable degree of harm or toxicity to the cells or tissues [4-5]. Most of the fluorometric sensors developed from various metals, metal oxides, organic materials and metal-organic frameworks (MOF) may induce protein denaturation, membrane damage, oxidative stress, and other secondary toxicities when in contact with living beings [6-7]. Moreover, prolonged usage can also render various alterations in the biochemical properties of a biological system. Low or absence of cytotoxic nature is a very important factor for a sensor so that it further does not result in any kind of harm to the biological systems when used on a commercial scale [8]. Since this thesis aims towards the development of a sensor that can be used in industrial and real-life applications, biocompatibility or cytotoxicity studies have also been performed.

In modern society, to cut down the industrial production cost, and to develop various products having antibacterial nature, researchers around the world are focussing on the determination of antibacterial properties of various minerals [9-10]. Various products like antibacterial ceramics and tiles, coatings, paints, medical and dermatological materials, etc are already developed from certain minerals like Talc, Halloysite, Sericite, which exhibits antibacterial properties [11-12]. Since this thesis encompasses the development of sensors, antibacterial nature can be an additional benefit in order to simultaneously treat the water alongside sensing. Moreover, the various antibacterial agents have a negative impact on prolonged use. The widely used antibacterial agents like silver nanoparticles can disrupt endocrine functioning, prolonged use of ZnO can cause cellular and DNA damage, CuO nanoparticles have toxic effects on the liver and kidney [13-14]. Not much focus has been paid to developing antibacterial products from rock-forming minerals. Hence in this chapter,

size-tuned variation in antibacterial properties of the microcline and kyanite has been discussed.

Other than biocompatibility, antibacterial efficacy is also an important parameter useful for wastewater treatment. Certain bacteria like *Escherichia coli* (*E. coli*), *Vibrio cholera*, *Pseudomonas sp.*, etc are commonly found in the aquatic environment [15-16], especially in the wastewater. Hence, for the determination of antibacterial efficacy of microcline (M1 and M2) and kyanite (KY1 and KY2), gram-positive bacteria and gram-negative bacteria were used. The *E. coli* used in the experiments is a commonly found rod-shaped, Gram-negative bacteria that are also present in the lower intestine of warm-blooded animals other than wastewater [17]. Although not all strains are harmful, certain strains like serotype O157:H7 [18] can cause serious food poisoning in living beings. On the other hand, *S. aureus* used for the antibacterial assays are spherical, Gram-positive bacteria which is commonly found on the skin or in the nose, and causes infection in respiratory organs, soft tissue, bones, joints, endovascular system, and staph infection in humans [19].

MTT assay was performed to determine the cytotoxicity of microcline and kyanite in bulk (M1 and KY1) and finer (M2 and KY2) size fractions. Since the respective median lethal (LD50) doses for the samples were found to be average at 800 $\mu\text{g mL}^{-1}$, this concentration was considered for MTT and various antibacterial assays. LD50 was determined from the minimum inhibitory concentration (MIC) assay [20]. MIC is defined as the lowest concentration of an antibacterial agent that visibly inhibits microbial growth [21-22].

3.2 Methodology

3.2.1 Materials

The phosphate buffer saline (PBS), agar-agar, Luria-Bertani (LB) were purchased from HiMedia Pvt. Ltd., India; Thiazolyl blue formazan (MTT) and 2', 7'-dichlorofluorescein diacetate (DCFHDA) were obtained from Sigma-Aldrich. Dulbecco's modified eagle's medium (DMEM) and fetal bovine serum (FBS) used for biocompatibility assay were purchased from Thermo Fisher Scientific (Waltham, MA, USA). (DMSO), ethanol and glutaraldehyde were purchased from Merck, India. The bacterial strains *Escherichia coli* DH5 α (*E. coli*) (MTCC-1652) and *Staphylococcus aureus* (*S. aureus*) (MTCC 25923) were collected from the Institute of Microbial Technology, Chandigarh, India. All the reagents

used were of analytical grade and were used without further purification. Millipore water (resistivity $\approx 18 \Omega \cdot \text{cm}$) was used throughout the experiment.

3.2.2 Biocompatibility assay

To investigate any toxicity associated with the mineral samples, a cytotoxicity assay (MTT) was performed using WI38 human lung fibroblast cells which were purchased from National Centre for Cell Science (NCCS Pune, India). The cells were cultured in DMEM medium supplemented with 10 % FBS and maintained at 37 °C under a 5 % CO₂ humidified atmosphere. Cells were washed with sterile PBS (pH 7.4, 1x solution) and a fresh medium was added on the following day to maintain the culture. For MTT assay, 10⁴ cells per well of 96-well plate were seeded and allowed to adhere. The plate was incubated for 24 h with DMEM medium (containing 10 % FBS). Homogeneous solutions of mineral samples were prepared by dispersing the powdered sample in filtered PBS solution (0.5 mg mL⁻¹) and a concentration of 800 $\mu\text{g mL}^{-1}$ was used to treat the cells. An untreated well was kept as control. After 24 h of incubation at 37 °C, the culture medium was replaced with 450 $\mu\text{g mL}^{-1}$ MTT solution, and further incubated for 3 h. Then the MTT solution was discarded and was used to dissolve the cells. The intracellular formazan crystals thus formed were dissolved in MTT solubilization buffer, and the intensity of formation of formazol crystal was measured at 570 nm absorbance using a micro-plate reader (Biotek, USA).

3.2.3 Antibacterial assay

3.2.3.1 Determination of bacterial viability

Bacterial viability at varied concentrations and different sizes of microcline and kyanite was evaluated using the minimum inhibitory concentrations (MIC) technique and colony counting method. All the glassware and media used and the samples were sterilized in an autoclave for 15 min operating at 121 °C prior to the experiments. Bacterial strains (*E. coli* and *S. aureus*) were grown overnight diluted with fresh medium to achieve an approximate density of 1.5×10^8 CFU mL⁻¹ (adjusted to the 0.5 McFarland standards) [23]. Test tubes containing 4mL of LB broth were inoculated with this culture and various concentrations of minerals (0.2 mg mL⁻¹ to 1 mg mL⁻¹ well suspended in Millipore water by 1 h sonication) were added and were maintained at 37 °C for 24 h in shaking conditions in an incubator. A control (untreated) was maintained which doesn't contain any mineral. Then the inhibitory values were determined by colony counting method after spreading 100 μl from each tube

on agar plates (2 % agar). Triplicates were done in each case to obtain the standard error. The treated agar plates were then kept for incubation at 37 °C and the colonies formed were documented after 24 h. The antibacterial effect was calculated using the following equation [24]:

$$M (\%) = \frac{(B-C)}{B} \times 100 \quad (3.1)$$

Where, M, B, and C represent the mortality rate (%), the mean number of bacteria in the control samples (CFU mL⁻¹), and on the treated samples (CFU mL⁻¹) respectively.

Analysis of the effect of size on bacteria was also performed in a standard flow cytometer (Becton-Dickinson-FACS Aria) according to the method followed by Joshi *et al.* (2010) [19]. *E. coli* was grown to mid-log phase in LB broth and then the bacterial suspension was inoculated in 4 mL of fresh broth with approximately 10⁴ CFU mL⁻¹ and treated with 800 µg of microcline samples for 4 h, while untreated culture was set as control. After 4 h the bacterial suspension was centrifuged and washed thrice in Phosphate Buffer Saline (PBS) (pH: 7.4). Propidium iodide (PI), a non-cell-permeable dye that binds to DNA in dead or membrane compromised cells was used at a concentration of 10 µg mL⁻¹ was used in fixing the suspension for 15 min before analyzing. Flow cytometric reading was obtained at 448 nm excitation.

MTT [3(4, 5-dimethylthiazol-2-yl)-2, 5-diphenyl tetrazolium bromide] assay was performed to determine the bacterial viability when treated with the samples. The fresh culture was prepared and 800 µg mL⁻¹ samples were added to approximately 10⁴ CFU mL⁻¹ culture, which was then maintained at temperature 37 °C for 4 h. then the cultures were centrifuged for 5 min at 3000 rpm, and then washed twice and suspended in PBS buffer. The MTT stock of 5 mg ml⁻¹ was added and incubated for an hour for intracellular formazan formation. 500 µl DMSO was added to each and the intensity of formazan produced (violet colour) was measured in Biotek 96 well plate reader at 570 nm intensity. The bacterial viability was calculated from the following equation and expressed in percentage [25]:

$$\text{Cell survivality (\%)} = \frac{(A_t - A_b)}{(A_c - A_b)} \times 100 \quad (3.2)$$

Here, A_t, A_b and A_c represent the absorbance value of the sample, blank and control respectively.

3.2.3.2 Determination of reactive oxidative species (ROS) and bacterial morphological changes

To check the oxidative stress generated due to interactions with the minerals and the ability to induce intracellular oxidation and superoxide formation, reactive oxidative species or ROS generation was measured according to Su *et al.* (2009) [26]. A fluorescent probe (DCFHDA) was used as an indicator of ROS generation [27]. The fresh broth was inoculated with approximately 10^4 CFU mL⁻¹ for overnight culture and treated with 800 µg mL⁻¹ mineral samples and incubated at 37 °C for 1 h. The untreated sample was taken as a control. The cultures were then washed thrice with PBS buffer. 10 µM DCFHDA was then added to the bacterial cells and kept in dark for 30 min at 37 °C so that the dye diffuses through cellular membrane and get enzymatically hydrolyzed by intracellular esterases, and on oxidation produces 2',7'-dichlorofluorescein (DCF) in the presence of oxidative species [28]. The level of intracellular ROS generation which is proportional to the fluorescent DCF production was measured by exciting at 504 nm and emission was taken at 529 nm in a fluorescence microplate reader (BIOTEK).

The morphological characteristics and extent of damage caused due to interaction of bacterial cells with the mineral samples were observed by FESEM. 1 mL of the overnight treated cells (800 µg mL⁻¹) along with the control (untreated) was centrifuged at 4000 rpm for 4 min and the pellets obtained were washed thrice with sterile-filtered PBS (containing 2 % glutaraldehyde) and subsequently dehydrated using a serial dilution of ethanol. 5 µL of each suspension was ten drop-casted on a clean glass coverslip, dried under laminar airflow, sputter-coated with gold for FESEM (FEI, INSPECT F50, Netherlands) analysis.

3.3 Results and discussion

3.3.1 Determination of biocompatibility

Biocompatibility is a crucial factor to be considered for potential applications in real-life areas and in the fabrication of any anti-bacterial material [29]. The cytotoxicity data obtained for the mineral samples were verified using the WI38 human lung fibroblast cell line (Figure 3.1). Even after 24 h exposure to the samples at a concentration of 800 µg mL⁻¹, metabolic activity was observed and no significant reduction of viability of the cells occurred. A slight reduction is observed in case of M2 and KY2 compared to their bulk

counterpart, owing to their nano-dimension, although it is an insignificant change as more than 92 % of cells survived. This implies that M2 and KY2 can be potential candidates for fabrication of fluorometric sensors for real-life applications.

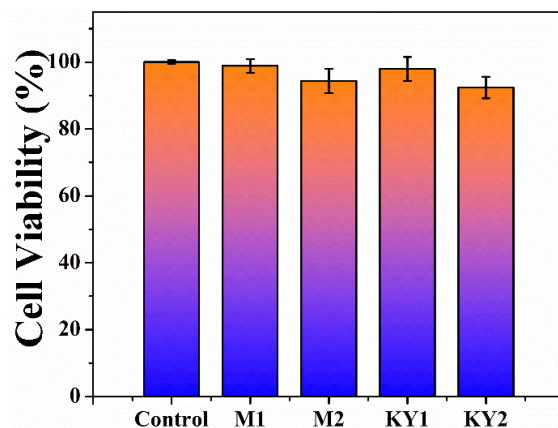


Figure 3.1: Cell viability (MTT assay) of the mineral samples

3.3.2 Bacterial viability assay

The antibacterial activity of both the minerals at varying concentrations and different sizes against *E. coli* and *S. aureus* was investigated in LB broth by plate count or colony counting method (Figure 3.2), and the MIC values have been presented in Table 3.1.

Table 3.1: MIC values of mineral samples for *E. coli* and *S. aureus*

	MIC (mg mL ⁻¹)			
	M1	M2	KY1	KY2
<i>E. coli</i>	1.6	0.6	2.0	0.8
<i>S. aureus</i>	1.2	0.8	1.4	0.8

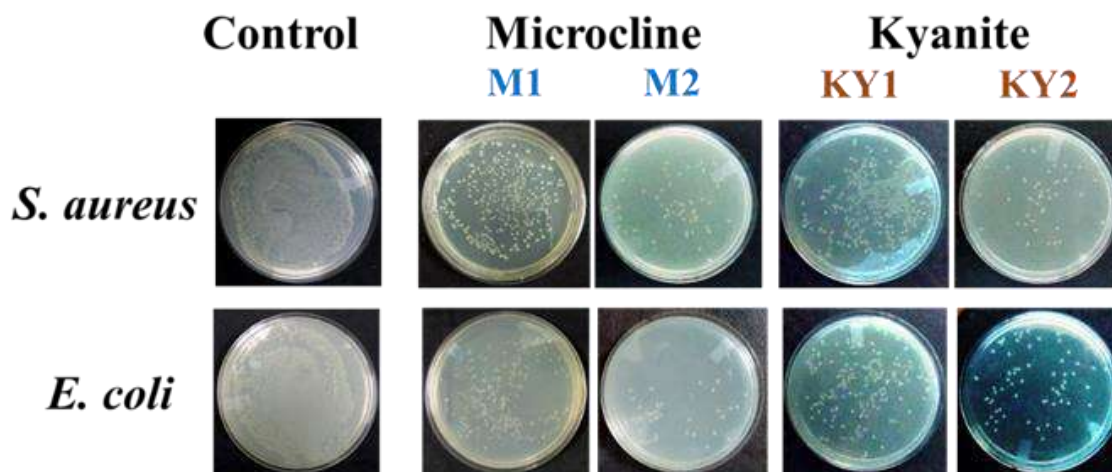


Figure 3.2: Plate count images showing visual display of the surviving colonies on agar plates

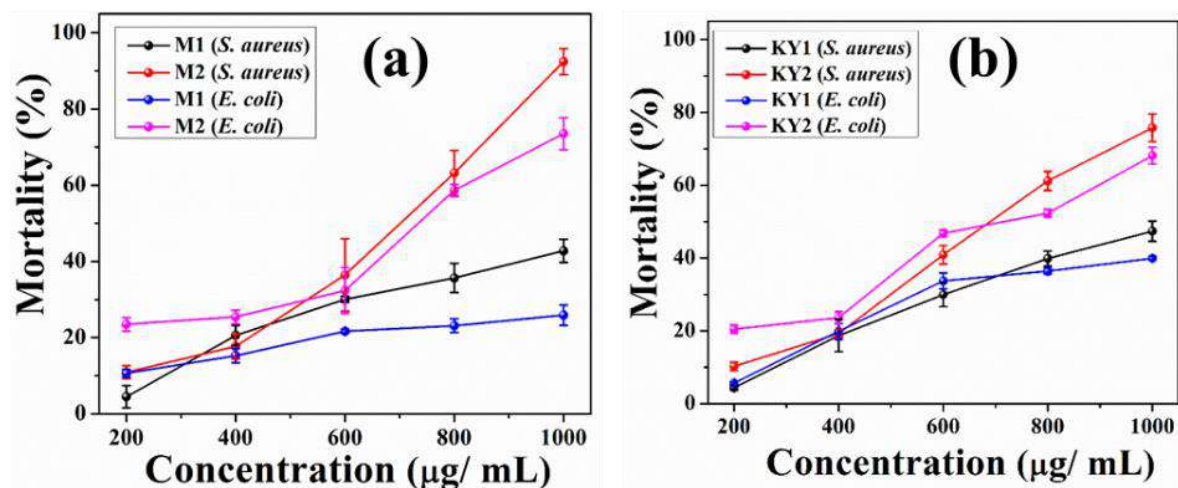


Figure 3.3: Mortality % calculated from plate counting (MIC) of (a) microcline and (b) kyanite

The mortality rate was found to be higher in the *S. aureus* compared to *E. coli* as illustrated in Figure 3.3. The result shows that the antibacterial effect of microcline was found to be higher than kyanite, especially the M2 fraction. The bulk-sized samples (M1 and KY1) showed a feeble antibacterial effect as only a slight deviation in MIC was noticed compared to the control. On the contrary, a pronounced antibacterial effect was observed in both the finer fraction (M2 and KY2). Figure 3.2 depicts the comparative analysis of residual colony count (CFU mL⁻¹) for both the minerals at different size fractions at 10⁻⁷ serial dilution for the concentration 800 µg mL⁻¹. A considerable reduction in colonies and inhibition of cell growth with an increase in concentration was observed in all the cases. Hence it is evident from the MIC values that size plays a major role in inducing significant bacteriostatic effects. This was further validated by the flow cytometry technique. The internalization of propidium iodide (PI) in the *E. coli* cells was measured to distinguish between treated and untreated cells. Since the PI dye binds to the DNA of dead cells or in those having compromised membrane [30], hence greater the uptake, the more is the number of dead or damaged cells. As microcline exhibited better antibacterial properties than kyanite, FACS was performed using the two size fractions of microcline (M1 and M2). The PI uptake for control was found to be 0.02 %, whereas, for M1 and M2, it was found to be 6.64 % and 29.28 % respectively (Figure 3.4), signifying that interaction with finer fraction might result in loss of plasma membrane integrity, thus exhibiting better antibacterial nature.

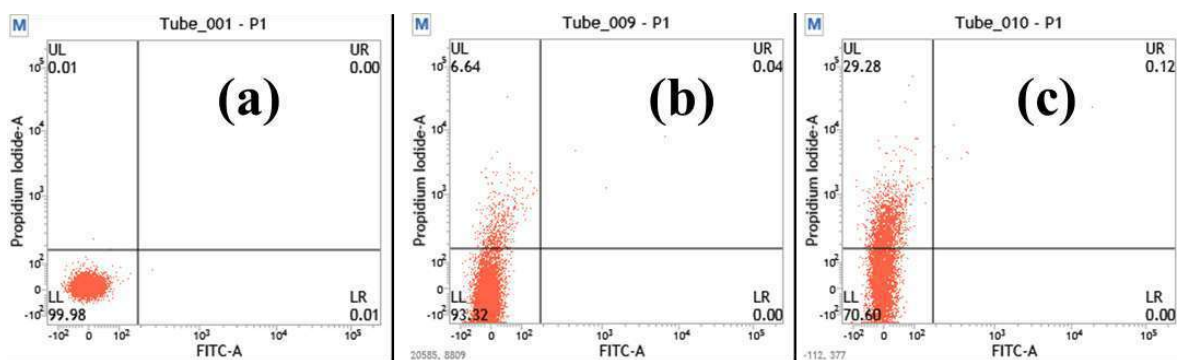


Figure 3.4: FACS data of (a) control, (b) M1 and (c) M2

The cell viability assay or MTT assay shows a substantial decrease in absorbance with the decrease in size (Figure 3.5a). This signifies that for both the bacterial strains, the bulk-sized samples (M1 and KY1) show more formazan formation indicating high viability [31], which reduces in finer fractions. The OD value of blank was estimated to be 0.042. From the MTT, it was clear that M2 exhibits slightly higher antibacterial behaviour compared to KY2.

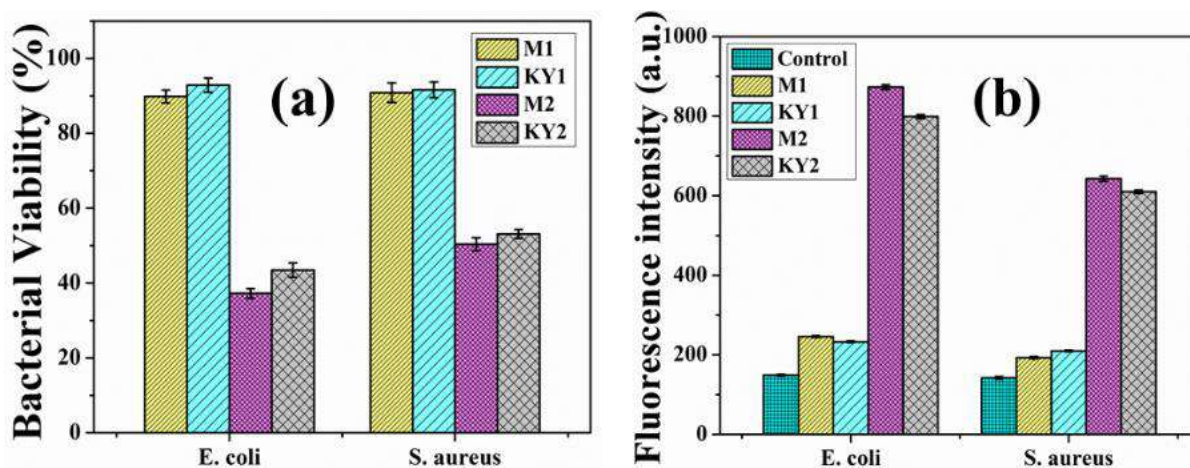


Figure 3.5: (a) MTT assay depicting decreasing bacterial cell viability, and (b) intracellular ROS generation

3.3.3 Mechanisms of Bacterial Growth Inhibition

3.3.3.1 Oxidative stress generation

Figure 3.5b illustrates that in both the Gram-positive and Gram-negative bacteria, the coarse fraction induces very less ROS production, which has a sharp increase in finer fractions. This indicates that a higher degree of oxidative stress and superoxide production in the nano-samples (M2 and KY2) is due to the finer size as they can easily penetrate through the membranes and reach the nuclear content of bacteria.

3.3.3.2 Physical interaction of bacteria with samples and bacteria

The evidence of membrane disruption, penetration of mineral samples, perforations and rupture of cytoplasmic material, the release of intracellular content can be understood from the FESEM micrographs (Figure 3.6). The rod-shaped morphology of *E. coli* and distinct spherical morphology of *S. aureus* remains healthy and intact in the case of control and bulk fractions (M1 and KY1). A closer look at the bacterial micrographs for M2 and KY2 reveals enhanced permeability and disruption of cell membrane with the subsequent morphological changes of both the bacteria.

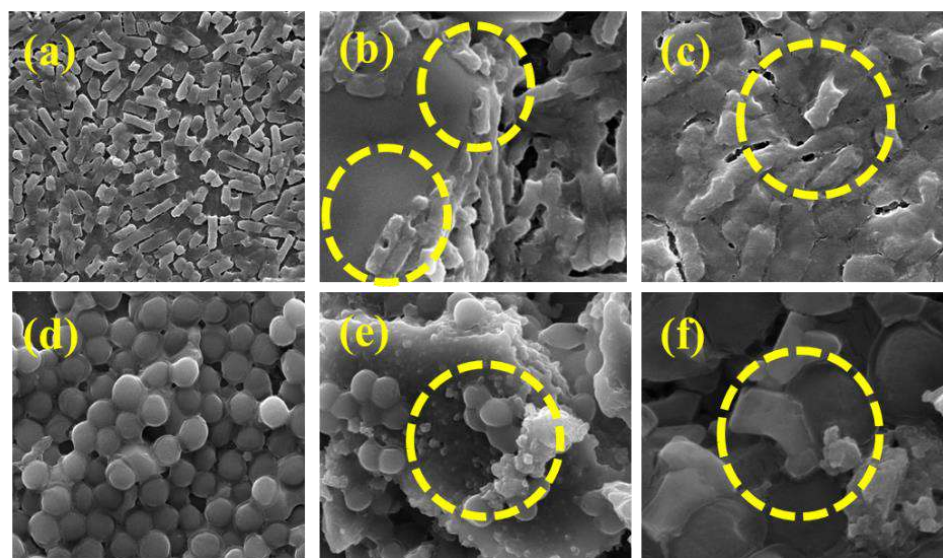


Figure 3.6: FESEM micrographs of *E. coli* (a-c) and *S. aureus* (d-f) depicting increased membrane disruption in successive finer size fractions in comparison to control

All aerobic cells have an inherent property of production of reactive oxygen or reactive nitrogen species on interaction with certain compounds or agents [32]. Generally, there exists a balance between the antioxidant capacity and intracellular oxidant production for the proper functioning of the cells. Sometimes, the concentration of active oxygen/ nitrogen species exceeds a level above the cell's defense capacity and repair capabilities, resulting in progressive deterioration of the subcellular components (DNA, proteins, and cell membranes), decline functional capacity, and can ultimately lead to cell death [33-34]. Hence estimation of intracellular ROS generation as a result of interaction with the samples is an important parameter to determine the pathway for the cellular damage. In this work, both the intensity of ROS production increased with the decrease in mineral size. Such phenomenon can be attributed to due to enhancement in free radicals (O^{2-} , H_2O_2 , $*OH$) production that interrupts trans-membrane electron transfer, attacks polyunsaturated fatty

acids in the membranes, thus initiating lipid peroxidation, disrupting membrane-bound proteins, and altering the membrane properties [35] on interacting with the finer fraction. ROS also targets the nucleic acids (DNA, RNA), proteins, and lipids, damages intracellular enzymes such as NADH [36]. Thus, interference with the normal functioning of enzymes and proteins, damage to DNA, RNA and disruption in membrane fluidity due to greater ROS generation in the case of finer fractions might be the plausible augmentation for higher bactericidal effect and cell mortality. Moreover, finer size has greater penetration capacity, as evident from the FESEM studies.

Thus the mechanism of antibacterial action, especially in the case of finer fractions can be explained in four distinct steps: a. Attachment of mineral samples on bacteria; b. Interaction and subsequent penetration into the cells, resulting in external membrane injury as evident from FESEM micrographs; c. Internalization and interaction of mineral samples with vital biomolecules like DNA, RNA, proteins, lipids, enzymes, and inhibiting biochemical pathways required for proper cell functioning and survival; and d. Oxidative stress generation or ROS production. Thus it is evident from the above studies that in case of finer fractions, the detrimental intracellular ROS generation and membrane damage synergistically aggravated the antibacterial activity.

3.4 Summary

Since this thesis also focuses on sensor development for heavy metal detection in the aqueous medium, biocompatibility and antibacterial properties are important aspects to be considered. Detailed understanding of the effect of the size-variation of minerals in living cells and the pathway of microbe-mineral interaction has been studied. From the MTT assay, it is clear that the mineral samples, even in finer size range (M2 and KY2) do not induce any kind of toxicity in living cells. The survivability of more than 92 % of cells, when exposed to the median MIC ($800 \mu\text{g mL}^{-1}$), confirms the biocompatible nature. This confirmed the potentiality of M2 and KY2 as non-toxic materials for sensor development. The antibacterial activities were investigated against a gram-positive bacteria (*Staphylococcus aureus*) and a gram-negative bacteria (*Escherichia coli*). The finer fractions, especially M2 show considerable antibacterial efficacy, which was analytically determined using FACS and MTT assay. The mechanism of antibacterial action is due to the attachment of the sample on bacteria, localized accumulation, and interaction with the sample, followed by generation of ROS with consequent membrane disruption followed by

cell death. Thus these antibacterial studies proved that the minerals, especially in finer regimes (M2 and KY2) can be useful as an antibacterial agent for the treatment of bacterial-contaminated water samples.

References

1. Van Oostdam, J., Gilman, A., Dewailly, E., Usher, P., Wheatley, B., Kuhnlein, H., Neve, S., Walker, J., Tracy, B., Feeley, M. and Jerome, V., 1999. *Sci. Total Environ.* 230, 1-82.
2. Rebello, S., Anoopkumar, A.N., Aneesh, E.M., Sindhu, R., Binod, P., Kim, S.H. and Pandey, A., 2021. *J. Hazard. Mater.* 402,123474.
3. Hench, L.L. and Wilson, J., 1986. *Silicon Biochemistry* 73, 231.
4. Murray, P.E., García Godoy, C. and García Godoy, F., 2007. *Med Oral Patol Oral Cir Bucal.* 12(3), 258-266.
5. Ai, J., Biazar, E., Jafarpour, M., Montazeri, M., Majdi, A., Aminifard, S., Zafari, M., Akbari, H.R. and Rad, H.G., 2011. *Int. J. Nanomedicine* 6, 1117
6. Duanghathaipornsuk, S., Farrell, E.J., Alba-Rubio, A.C., Zelenay, P. and Kim, D.S., 2021. *Biosensors*, 11(2), 30.
7. Gong, Z., Chan, H.T., Chen, Q. and Chen, H., 2021. *Nanomaterials* 11(7), 1792.
8. Zhou, X., Lee, S., Xu, Z. and Yoon, J., 2015. *Chem. Rev.*115(15), 7944-8000.
9. Gomes, C.D.S.F. and Silva, J.B.P., 2007. *Appl. Clay Sci.* 36, 4-21.
10. Khan, N.A., Ahmed, S., Farooqi, I.H., Ali, I., Vambol, V., Changani, F., Yousefi, M., Vambol, S., Khan, S.U. and Khan, A.H., 2020. *TrAC - Trends Anal. Chem* 129, 115921.
11. Mapelli, F., Marasco, R., Balloi, A., Rolli, E., Cappitelli, F., Daffonchio, D. and Borin, S., 2012. *J. Biotechnol.* 157(4), 473-481.
12. Heimann, R.B., 2010. John Wiley & Sons.
13. Chen, L., Yokel, R.A., Hennig, B. and Toborek, M., 2008. *J Neuroimmune Pharmacol* 3(4), 286-295.
14. Aruoja, V., Dubourguier, H.C., Kasemets, K. and Kahru, A., 2009. *Sci. Total Environ.* 407(4), 1461-1468.
15. Meng, H., Chen, Z., Xing, G., Yuan, H., Chen, C., Zhao, F., Zhang, C. and Zhao, Y., 2007. *Toxicol. Lett.* 175, 102-110.
16. Nugent, M.A., Brantley, S.L., Pantano, C.G. and Maurice, P.A., 1998. *Nature* 395, 588-591.
17. Jang, J., Hur, H.G., Sadowsky, M.J., Byappanahalli, M.N., Yan, T. and Ishii, S., 2017. *J. Appl. Microbiol.* 123(3), 570-581.
18. Ratnam, S.S.R.G.S., March, S.B., Ahmed, R., Bezanson, G.S. and Kasatiya, S., 1988. *J. Clin. Microbiol.* 26(10), 2006-2012.
19. Joshi, S., Bisht, G.S., Rawat, D.S., Kumar, A., Kumar, R., Maiti, S. and Pasha, S., 2010. *Biochim. Biophys. Acta* 1798(10), 1864-1875.
20. Bardaweel, S.K., Tawaha, K.A. and Hudaib, M.M., 2014. *BMC Complement Altern. Med.* 14(1), 1-8.
21. Krishnan, R., Arumugam, V. and Vasaviah, S.K., 2015. *J Nanomed Nanotechnol.* 6(3), 285.

22. Parvekar, P., Palaskar, J., Metgud, S., Maria, R. and Dutta, S., 2020. *Biomater. investig. dent* 7(1), 105-109.
23. Zapata, A. and Ramirez-Arcos, S., 2015. *Curr. Microbiol.* 70(6), 907-909.
24. Bagchi, B., Banerjee, S., Kool, A., Thakur, P., Bhandary, S., Hoque, N.A. and Das, S., 2016. *Phys. Chem. Chem. Phys.* 18(25), 16775-16785.
25. Sarkar, D., Pramanik, A., Jana, S., Karmakar, P. and Mondal, T.K., 2015. *Sens. Actuators B: Chem.* 209, 138-146.
26. Su, H.L., Chou, C.C., Hung, D.J., Lin, S.H., Pao, I.C., Lin, J.H., Huang, F.L., Dong, R.X. and Lin, J.J., 2009. *Biomaterials* 30(30), 5979-5987.
27. Cabiscol Català, E., Tamarit Sumalla, J. and Ros Salvador, J., 2000. *Int. Microb.* 2000, 33-38.
28. Burow, S. and Valet, G., 1987. *Eur J Cell Biol*, 43(1), 128-133.
29. Tan, H.L., Teow, S.Y. and Pushpamalar, J., 2019. *Bioengineering* 6(1), 17
30. Krämer, C.E., Wiechert, W. and Kohlheyer, D., 2016. *Sci. Rep.* 6(1), 1-13.
31. Stockert, J.C., Blázquez-Castro, A., Cañete, M., Horobin, R.W. and Villanueva, Á., 2012. *Acta histochemica* 114(8), 785-796.
32. Sies, H. and Jones, D.P., 2020. *Nat. Rev. Mol. Cell Biol.* 21(7), 363-383.
33. Graves, D.B., 2012. *J. Phys. D: Appl. Phys* 45(26), 263001.
34. Okoye, F.B.C., Nworu, C.S., Akah, P.A., Esimone, C.O., Debbab, A. and Proksch, P., 2013. *Immunopharmacol. Immunotoxicol.* 35(6), 662-668.
35. Yan, L., Du, C., Riaz, M. and Jiang, C., 2019. *Environ. Pollut.* 255, 113254.
36. Tan, S.X., Teo, M., Lam, Y.T., Dawes, I.W. and Perrone, G.G., 2009. *Mol. Biol. Cell* 20(5), 1493-1508.



Chapter 4

Development of carbon dot loaded nano-microcline (MCD) & nano-kyanite-based (KYCD) fluorometric sensors for Cr⁶⁺ & Fe³⁺ detection in industrial wastewater & living cells



Chapter 4

4.1 Overview

Scientists throughout the world are working on the development of sensor probes for early detection of heavy metals even at minute quantity before they generate pollution, most of them suffer various drawbacks like requirement of expensive raw materials or instrumentations, tedious synthesis procedure, instability, time-consuming protocols, the tendency of causing contamination [1-2]. Hence to overcome such limitations, the development of fluorometric and colorimetric sensors is gaining huge popularity [3-4]. Yet most of them are for one-time use purpose, require expensive and harsh chemicals, lacks sensing capability in real-life water samples, can cause secondary pollution and the fluorescence nature tends to degrade with time. Multiple ion detection with a single sensor is much needed. Scientists and engineers are currently working on the production of eco-friendly, cost-effective, portable, rapid, and sensitive sensors that can be useful for on-field applications without the requirement of any expensive instrumentations [5-6].

This chapter focusses on the development of a natural mineral-based fluorescent sensor that can be both industrially and commercially feasible owing to their stability, biocompatibility, specificity towards particular contaminant, cost-effectiveness due to wide availability of raw materials, and simple facile synthesis technique which does not involve tedious steps or involves toxic chemicals during preparation [7]. The incorporation of nitrogenous carbon dots into the matrix of microcline and kyanite (M2 and KY2) to enhance fluorescence properties for sensor applications. The carbon dots, which are also known as “carbon nanodots” or “carbon quantum dots”, the 0-dimensional, newest member carbon family has attracted tremendous attention since its discovery in 2004, due to their magnificent fluorescence emission, excellent photoluminescence, tuneable fluorescence emission, the inherent ability for electron transfer, biocompatible nature, facile synthesis procedure, and versatile optical applications. Since carbon dots can agglomerate in the liquid state and with time fluorescence intensity can diminish [8], microcline and kyanite nanostructures provide solid substrate and better stability to sustain the fluorometric properties for a longer period. While carbon dot loaded kyanite (KYCD) only detects Cr^{6+} , carbon dot loaded microcline (MCD) exhibits simultaneous sensing of Cr^{6+} and Fe^{3+} . The mechanism is elucidated by

theoretical studies like DFT. Furthermore, the ability to detect heavy metals at the cellular level as evident from the bioimaging study opens a new avenue for nano-sensors in biomedical applications.

4.2 Methodology

4.2.1 Materials

HPLC grade Ethylenediamine (EDA), HPLC grade N, N-dimethylformamide (DMF), and anhydrous citric acid were purchased from Merck, India. Salts used for sensing assays, namely potassium dichromate ($K_2Cr_2O_7$) and ferric chloride ($FeCl_3$) were $\geq 98.0\%$ pure and were obtained from Merck, India. All chemicals used for selectivity analysis ($NaCl$, KCl , $CaCl_2 \cdot 2H_2O$, $FeSO_4 \cdot 7H_2O$, $Cr(CH_3COO)_3$, $CdCl_2$, $HgCl_2$, $PbCl_2$, $NaOH$, $NaNO_3$, Na_2CO_3 , Na_2S , Na_2SO_4) were purchased from Merck, India while As_2O_3 was purchased from Sigma-Aldrich. Chemicals used for biosensing applications like Dulbecco's modified eagle's medium (DMEM) and fetal bovine serum (FBS) were purchased from Thermo Fisher Scientific (Waltham, MA, USA). Phosphate buffer saline (PBS) and MTT (3-(4,5-Dimethylthiazol-2-Yl)-2,5-Diphenyltetrazolium Bromide) were purchased from SRL, India. All the reagents and solvents used throughout the experiments were of analytical grade and used without further purification. Millipore water (resistivity $\sim 18.2 M\Omega$ -cm) was used for all experimental and rinsing purposes.

4.2.2 Synthesis of fluorescent nano-sensors

Initially, nitrogenous carbon dot was synthesized via a facile hydrothermal technique as reported by Schneider et al., 2017 [9]. Citric acid solution (5.5 mM) was prepared by dissolving anhydrous citric acid (carbon source) in 70 mL of Millipore water under stirring conditions at room temperature. EDA (nitrogen source) was added dropwise for basification till pH became 12.0 and kept under stirring conditions for 2 h. The solution was then poured into a clean Teflon-lined stainless-steel autoclave and heated in a dust-free hot air oven for 12 h at 190 °C. The solution was then centrifuged and the dark-brown coloured supernatant (carbon dot or CD) was collected and stored for further use.

500 mg of nano-sized samples (M2 and KY2) was added separately to carbon dot solution and kept under stirring conditions overnight. Solutions were then centrifuged, dried and the

powdered samples were labeled as MCD (carbon dot loaded microcline) and KYCD (carbon dot loaded kyanite). The detailed synthesis route is illustrated in Figure 4.1.

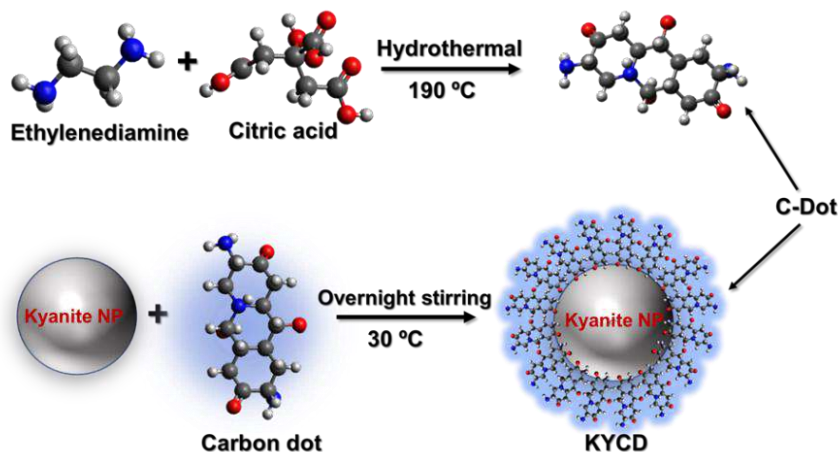


Figure 4.1: Illustration of synthesis route of nitrogenous carbon dot and loading into mineral matrix

4.3 Results and discussion

4.3.1 Structural and morphological analyses

Since this work reports loading carbon dots into the natural mineral, validation of the carbon dot incorporation is essential. Hence XRD was performed to determine the purity of nanosensor samples, along with quantification of various crystallographic parameters. The microstructural details of finer fractions (M2 and KY2) are discussed previously in Chapter 2. The XRD patterns obtained for KYCD (Figure 4.2a) and MCD (Figure 4.3a) corroborate well with JCPDS card no. 11-0046 and 84-0708 respectively [10-12]. The absence of any extra diffraction lines suggests the high purity of the samples. In both cases, the slight shift towards higher diffraction angles was observed due to the loading carbon dot. Such phenomenon is ascribed to the enhancement of microstrain due to the incorporation of carbon dot into the triclinic structure of both the minerals [13], which is evident from the Reitveld analysis. The results obtained after the final cycle of refinement are illustrated in Figure 4.2b and Figure 4.3b. The refined structures along with their bonding networks and crystallographic orientation are visualized from the computed .cif files using Vesta (v3.4.3), and have been illustrated in Figure 4.2 for KYCD, and in Figure 4.3 for MCD.

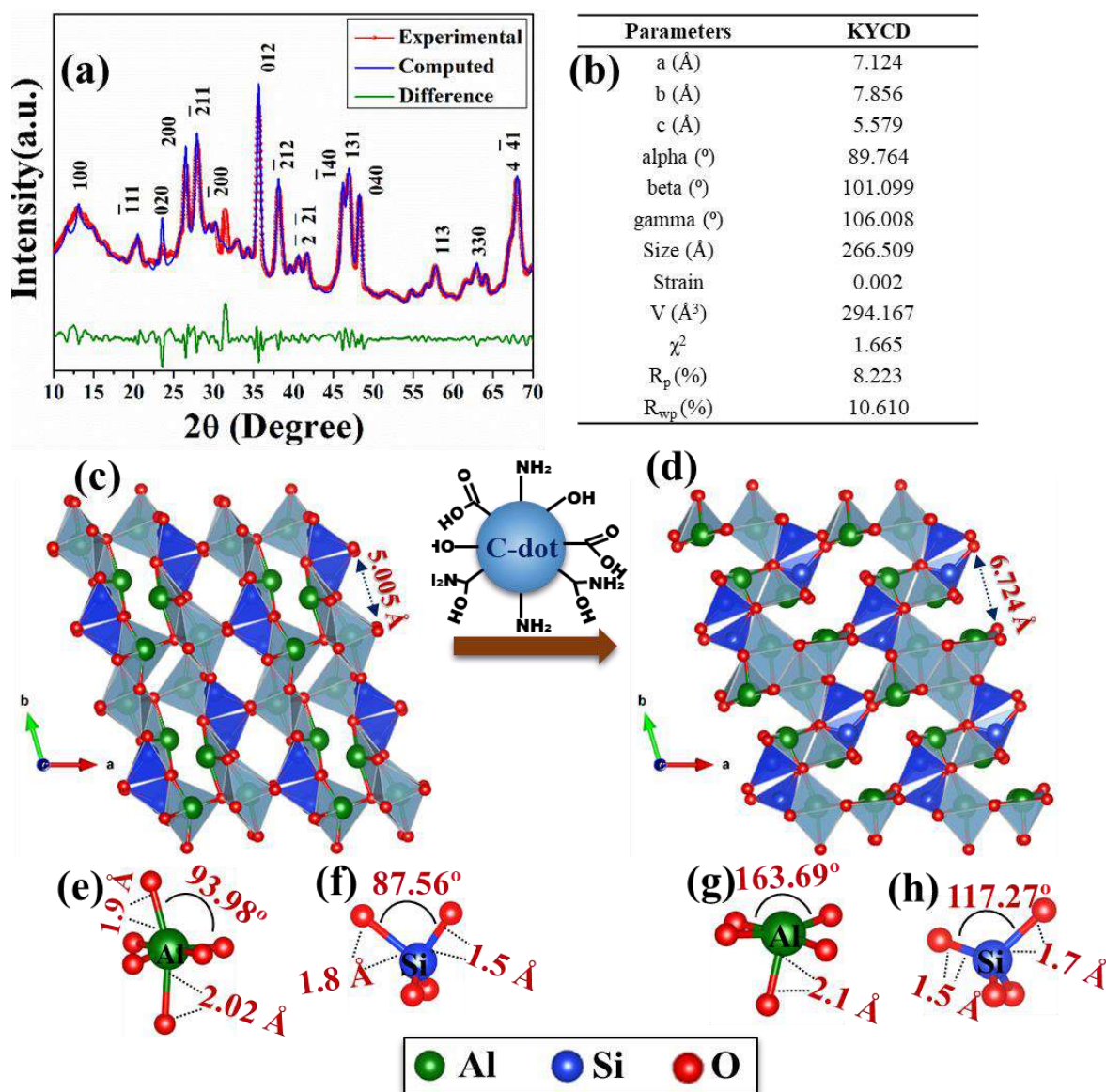


Figure 4.2: (a) Experimental (red), refined (black), and difference plot (blue) of XRD pattern of KYCD; (b) microstructural parameters of KYCD obtained from Rietveld refinement and (c-d) subsequent representation of changes observed in bond lengths and bond angles in KY2 (e-f) and KYCD (g-h) due to carbon dot loading

Due to the addition of carbon-dot into the structure, an alteration from the symmetrical zig-zag pattern of octahedral AlO₆ stacked and SiO₄ tetrahedra, shared by oxygen molecules was observed in KYCD. The refined structure of KYCD shows the absence of oxygen in certain AlO₆ sites (Figure 4.2). Such oxygen vacancies perturb the stacked arrangement of alumina-silica polyhedral structure, thus resulting in enhanced microstrain and interstitial defects. Such defect states influence the emission spectra, as discussed in Chapter 2, and

play a significant role in the enhancement of fluorescence quality in the sensors. Such a phenomenon is also applicable in the case of MCD nano-sensor.

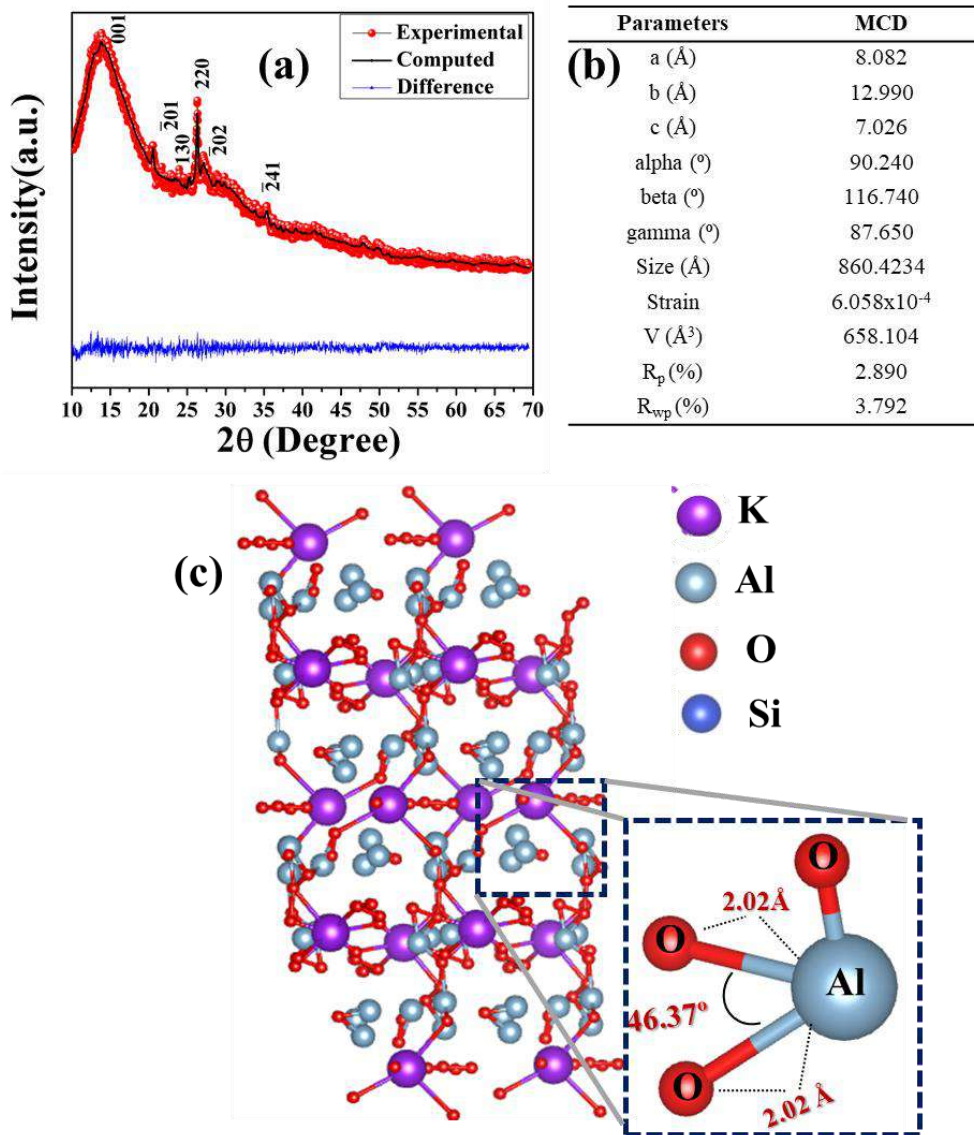


Figure 4.3: (a) Experimental (red), refined (black) and difference plot (blue) of XRD pattern of MCD; (b) microstructural parameters of MCD obtained from Rietveld refinement and (c) subsequent representation of bond lengths and bond angles

The bond structures were further examined by FTIR spectroscopy. In M2 and MCD, spectral bands are located at 578 (O-Si-O bending vibration and the K-O stretching), 728 (Si-Al (Si) stretching), 775 (Si-Si stretching), 1034 (Si(Al)-O stretching), and 2363 cm^{-1} (Al-OH vibration) [14]. In the case of MCD, significant enhancement of the entire set of IR bands was observed and augmentation in IR intensities at 2846 and 2922 cm^{-1} occurred due to incorporation of nitrogenous c-dot in microcline. Absorption bands at were found at 1562

cm^{-1} and 1656 cm^{-1} are due to attributing bending vibration of N-H, C=N, and C=O respectively due to c-dot loading (Figure 4.4a) [9]. Similarly, in KY2 and KYCD, absorption bands are located at 468 and 537 cm^{-1} for Si-O tetrahedron (O-Si-O) vibration, 668 and 970 cm^{-1} attributed to asymmetric Si-O and Al-O stretching vibrations [15], and broader peaks located in the 2974 - 3587 cm^{-1} range signify the vibrations of O-H (Figure 4.4b) [16]. Due to the addition of c-dot, the absorption band at 1559 cm^{-1} (N-H and C=N bending) and 1662 cm^{-1} (C=O and CO-NH bond) was observed [17].

The FESEM was employed to analyze the morphological features of the nano-sensors. For a visual understanding of the c-dot loading, TEM was performed. As illustrated in Figure 4.4c and Figure 4.4d, tiny spherical/ globular structures of c-dots of average diameter nearly 3 - 5 nm are evenly distributed on the surface of both MCD and KYCD.

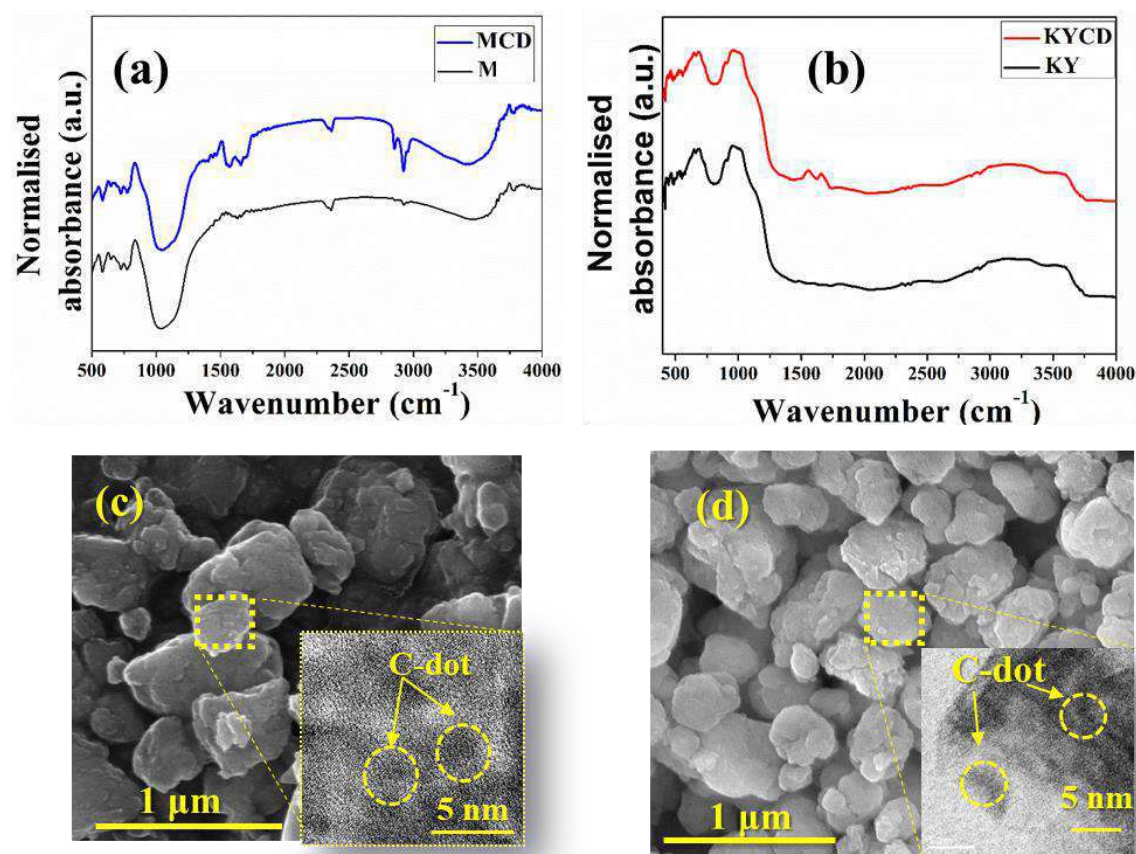


Figure 4.4: FT-IR spectra of (a) microcline and MCD, and (b) kyanite and KYCD; FESEM micrograph of (c) MCD and (d) KYCD, with their corresponding TEM (c-d inset)

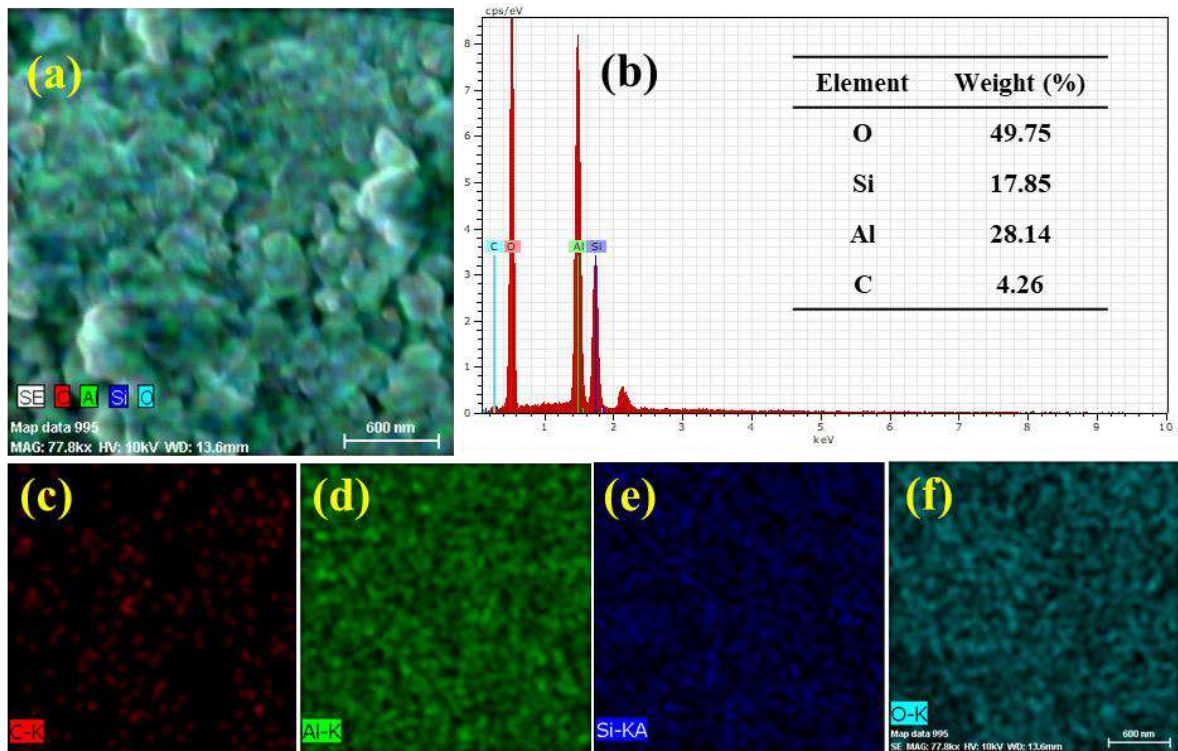


Figure 4.5: EDS spectra and elemental mapping of KYCD

The elemental composition of both the sensors was determined through EDS and elemental mapping. The weight percentage of various elements present in both the sensors (MCD and KYCD) were determined from the EDS study. The studies confirm the presence of oxygen, aluminum, silicon, and carbon in KYCD (Figure 4.5) and oxygen, aluminum, silicon, potassium, and carbon in MCD (Figure 4.6), with traces of sodium as an impurity. This also confirms the presence of carbon in both the mineral nanocomposites, suggesting the inclusion of carbon-dot in both the nano-microcline and nano-kyanite.

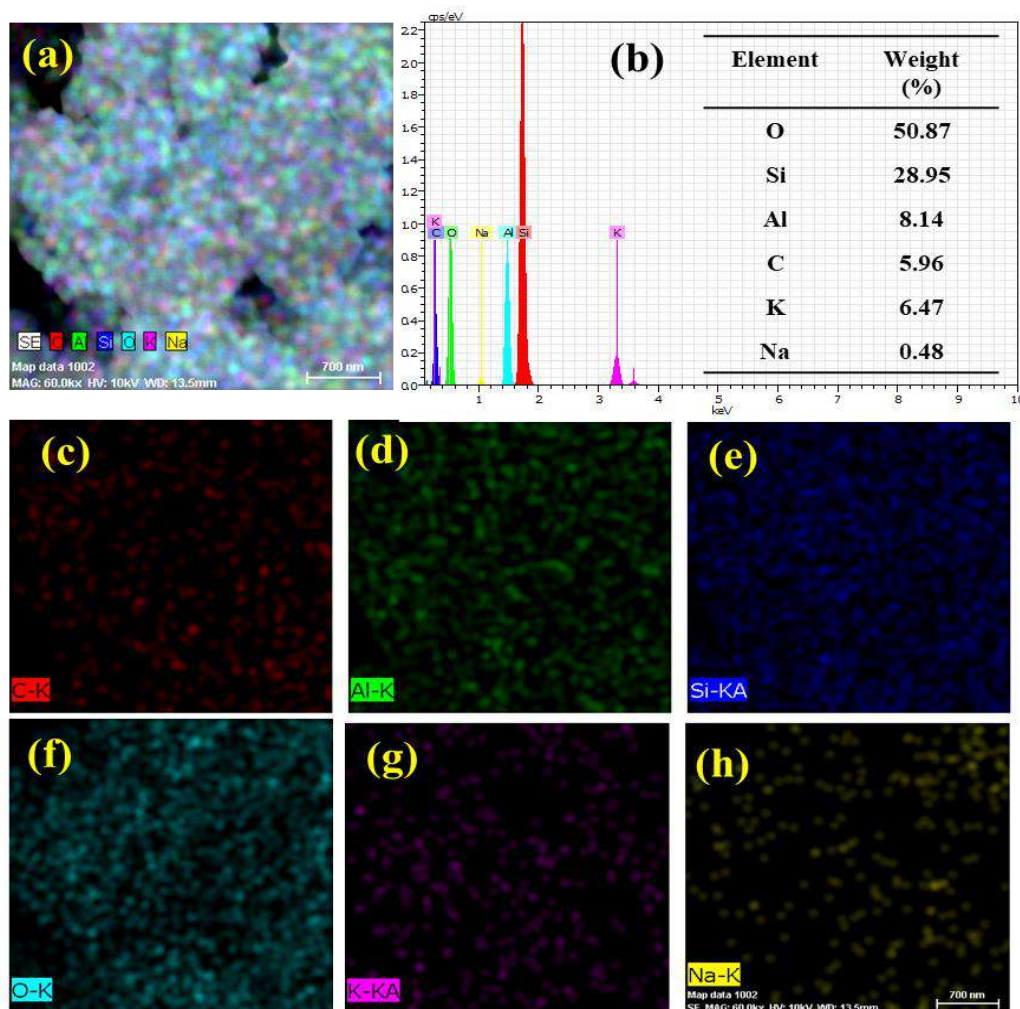


Figure 4.6: EDS spectra and elemental mapping of MCD

The surface properties (average surface area and surface porosity) of the nano-sensors were estimated by using the standard BET and BJH method and corresponding pore size distributions have been illustrated in Figure 4.7. Details of the surface properties are provided in Table 4.1. The hysteresis loop suggests type IV isotherm in both cases, which is mainly dominant in mesoporous materials. Such isotherm is mainly associated with capillary condensation and is known to be useful for the synthesis of industrial adsorbents.

Table 4.1: Estimated BET Surface Area, Pore Diameter, and Pore Volume Data of MCD and KYCD.

Sample name	Surface area (m ² g ⁻¹)	Pore size (nm)	Pore volume (mL g ⁻¹)
MCD	137.266	3.28	0.349
KYCD	134.271	18.77	0.527

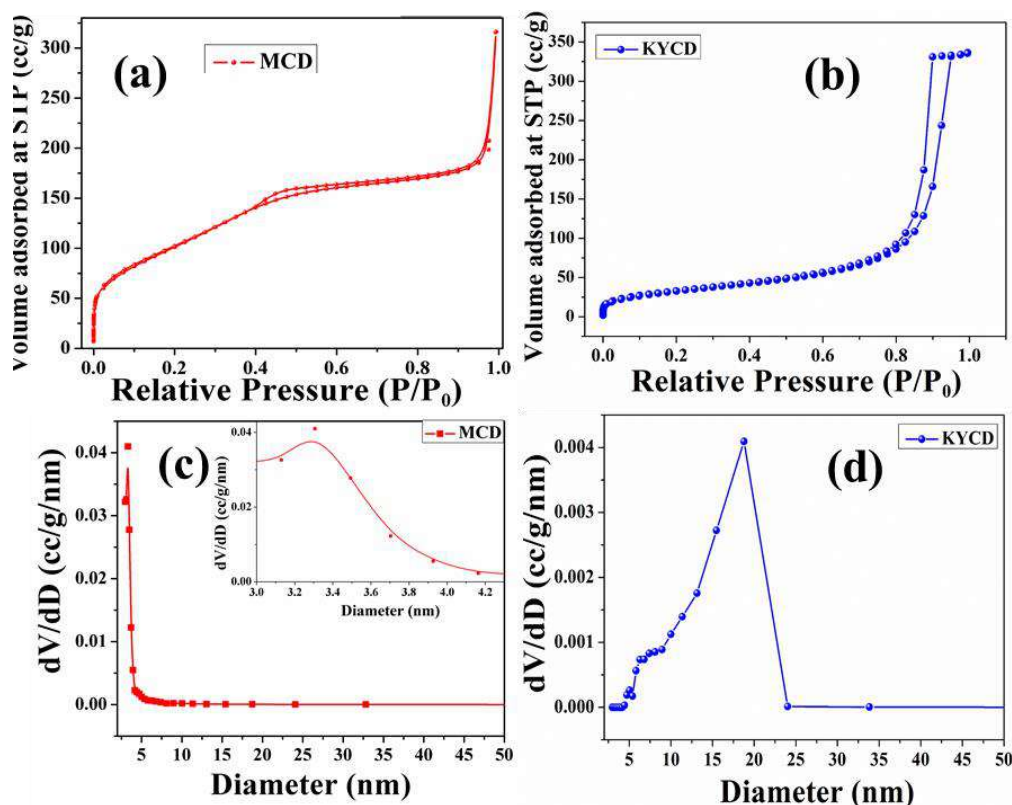


Figure 4.7: (a) N₂ adsorption/desorption isotherm of (a) MCD and (b) KYCD; pore size distribution data for (c) MCD and (d) KYCD

4.3.2 Determination of optical quality

Since the work involves the synthesis of the fluorescent sensor, the determination of optical quality is of utmost importance. The UV-Vis spectroscopy shows absorption maxima at 250 nm (π - π^* transition of C=C bonds) and 350 nm (n- π^* transition of C=O or C=N moiety) [18] in case of MCD, and at 240 and 345 nm for KYCD (Figure 4.8), which are otherwise absent in pristine microcline and kyanite. These two peaks confirm the successful incorporation of nitrogenous carbon dot in M2 and KY2 respectively.

The main purpose for carbon-dot loading was to enhance the fluorescence quality for sensing applications, which was successfully achieved as evident from the emission and fluorescence characteristics (Figure 4.8) since a significant enhancement of fluorescence intensity was observed in both cases. The ethylenediamine precursor introduced nitrogenous functional groups like N-H and C=N (as observed in FT-IR analysis) on the carbon dot surface, inserting new energy levels, modulating the band gaps, and induced charge dislocation that promotes electron transfer ability of carbon [19-20], and resulting in enhanced fluorescence signal. The optimum emission intensity for both MCD and KYCD

is found at an excitation wavelength (λ_{ex}) of 370 nm and the luminescent maxima is located at 460 nm (blue region), hence all the sensing studies were conducted at 370 nm.

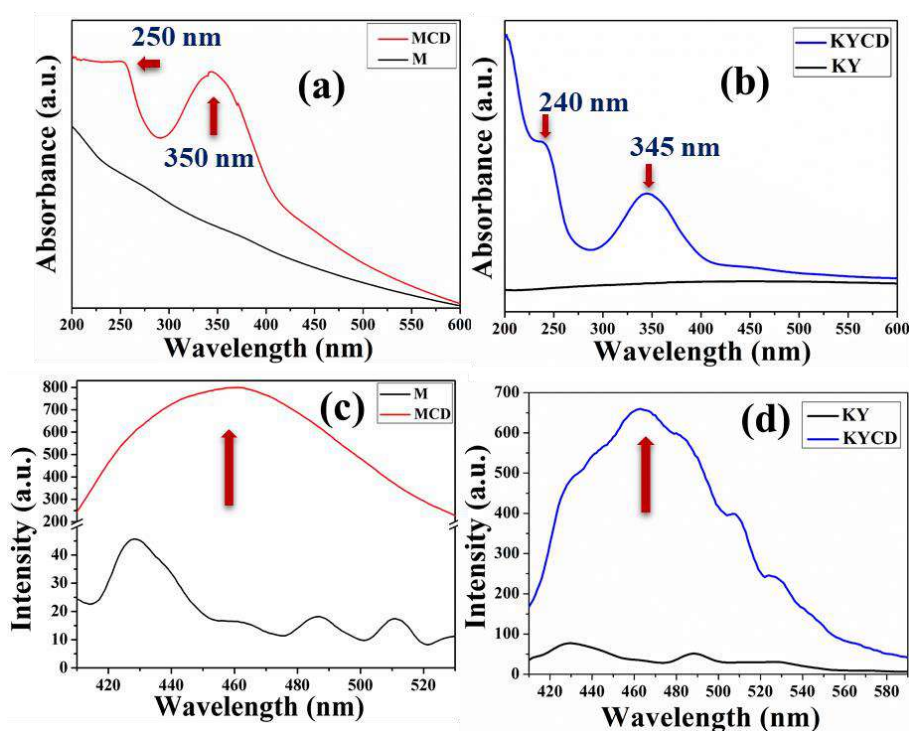


Figure 4.8: UV-vis spectra of (a) microcline and MCD and (b) kyanite and KYCD; PL spectra depicting the comparison of fluorescence properties of (c) microcline and MCD and (d) kyanite and KYCD

As discussed earlier in this chapter, the nano-sized microcline and kyanite basically provide a solid substrate for the carbon dots for better applicability and stability. In order to investigate the fluorescence stability and to determine alterations of fluorescence properties of pure carbon dots and carbon dot loaded microcline/ kyanite, the carbon dot solution and the nano-sensors were exposed to environmental conditions (humidity, light, temperature change), and fluorescence was measured at an interval of 10 min for 3 h. There is no significant change in the fluorescence quality as seen in the case of nano-sensors, whereas there is a gradual decrease in the fluorescence capacity of carbon dot (Figure 4.9).

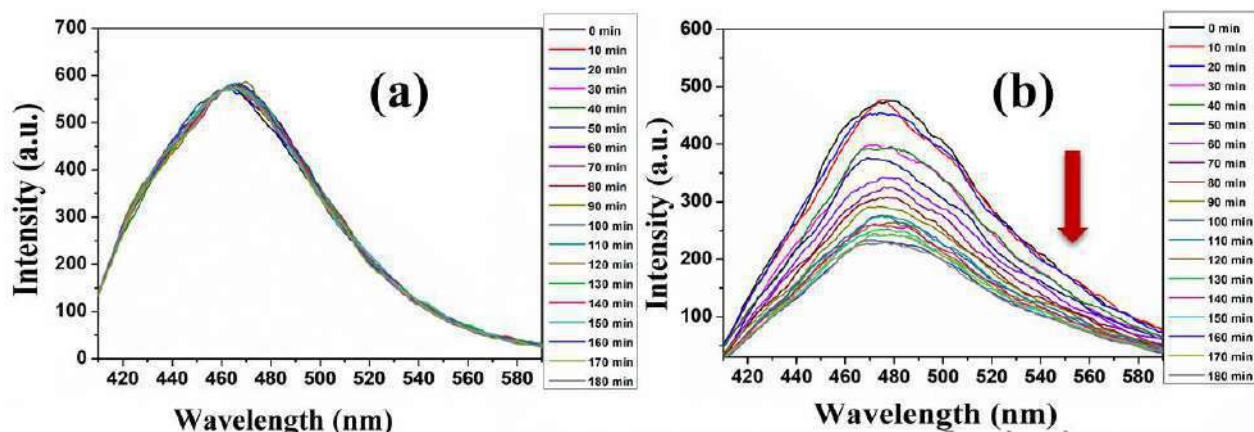


Figure 4.9: Fluorescence stability in the (a) nano-sensors (picture illustrates that of KYCD nanocomposite) and (b) pure carbon dot

4.3.3 MCD and KYCD as a fluorometric probe

One of the crucial parameters in sensing technology is the tendency of the sensing probe to detect a specific target molecule. Initially, the selectivity of MCD and KYCD is evaluated against a range of ions by exposing them to specific concentrations of 500 μM . In the case of MCD, a radical reduction in fluorescence was observed on adding Cr^{6+} and Fe^{3+} , while KYCD detects only the presence of Cr^{6+} (Figure 4.10). This result depicts that MCD has the capability for dual sensing of two heavy metal ions (Cr^{6+} and Fe^{3+}) simultaneously, as on adding of Fe^{3+} , the fluorescence maxima at 460 nm radically drop, while a red-shift to 505 nm alongside quenching takes place on exposure to Cr^{6+} (Figure 4.11).

For more validation, CIE-1931 chromaticity plot [21] was done against the visualized emissions in the colour space. For MCD, the colour coordinate was found at $x = 0.2066$, $y = 0.3822$; which slightly shift in Fe^{3+} ($x = 0.1925$, $y = 0.3977$), but in Cr^{6+} , it shift towards green region ($x = 0.2780$, $y = 0.5717$) (Figure 4.12). Such dual selectivity of MCD and quenching effect in KYCD is also visible through naked eyes under UV illumination (Figure 4.12).

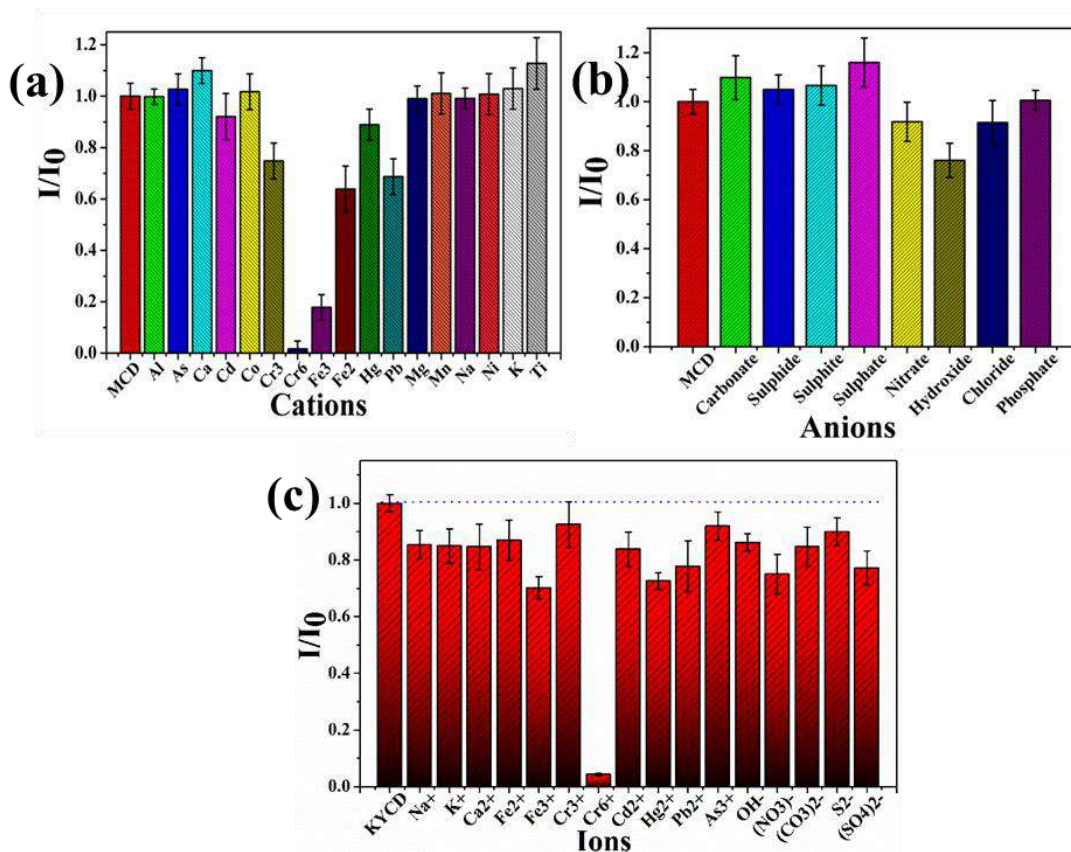


Figure 4.10: Selectivity assay for (a-b) MCD and (c) KYCD

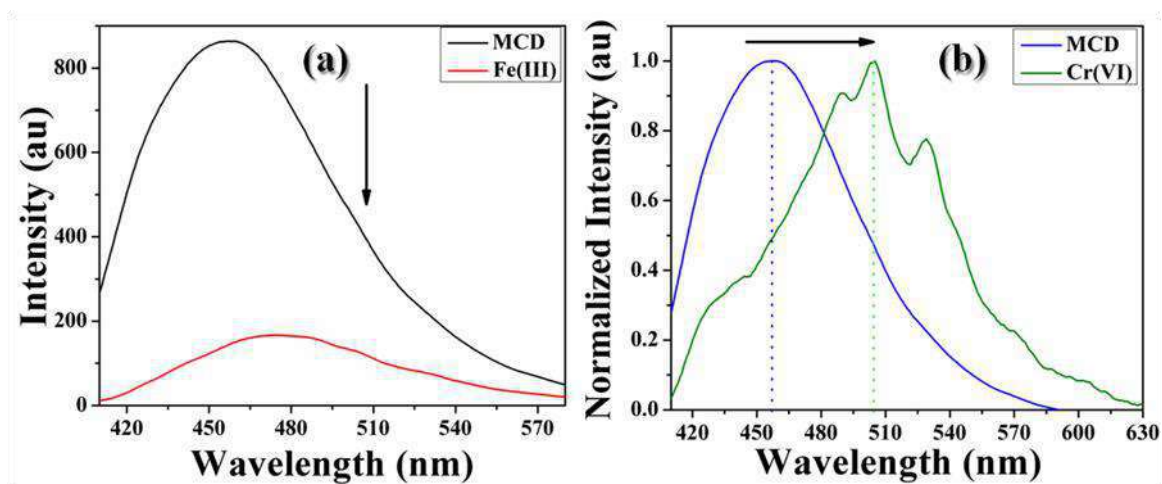


Figure 4.11: Dual sensing of MCD upon addition of (a) Fe³⁺ and (b) Cr⁶⁺

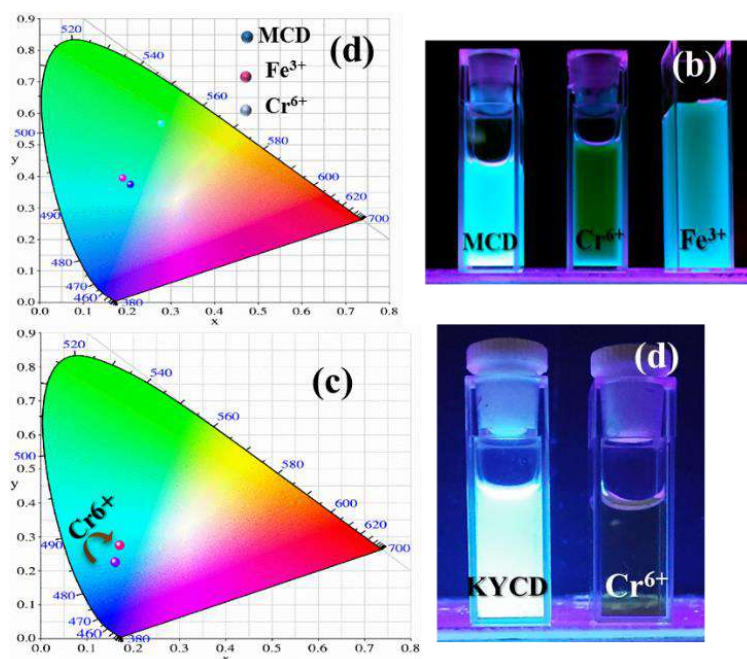


Figure 4.12: CIE-1931 colour space analysis of (a) MCD and (c) KYCD and (b, d) naked eye visualization of bright blue fluorescence on exposure to UV light and simultaneous real-life quenching

The sensitivity (quenching constant and limit of detection) of the sensors were determined against a varying concentration of the quenching ions. The sensitivity of MCD was determined against Fe^{3+} and Cr^{6+} at concentrations ranging from 0 to $68 \mu\text{M}$. Similarly, the sensitivity of KYCD towards Cr^{6+} was evaluated at a concentration ranging from 0 to $34 \mu\text{M}$. The quenching efficiency of MCD and KYCD was calculated using the linear Stern-Volmer equation [22] as stated below:

$$\frac{I_0}{I} = 1 + K_{SV}[M] \quad (4.1)$$

Where, I_0 , I , K_{SV} , and $[M]$ represent the fluorescence intensities prior to and after the addition of both quenching ions respectively, the concentration of the ions and the Stern-Volmer quenching constant (Figure 4.13). Herein I_0 and I represent emission intensity of the sensor prior to and post-incorporation of quenching ions. In MCD, fluorescence intensity for Cr^{6+} was considered at 505 nm due to a shift towards higher emission (green region). The fitting coefficient obtained for Cr^{6+} is 0.99464, while that for Fe^{3+} is 0.99856. In the case of KYCD, linear fitting of the S-V plot was done at a lower concentration ($0\text{--}10.2 \mu\text{M}$) with a fitting coefficient of $R^2 = 0.95435$, while there is an upward increment at higher concentrations with a fitting coefficient of $R^2 = 0.98271$. This suggests that at a lower concentration, only dynamic quenching [23] takes place, while at higher concentration,

simultaneous effect of static and dynamic quenching occurs as the fluorescence intensity decay rapidly. Such a phenomenon occurs as the quencher ions block the emission pathway of the fluorophores at higher concentrations and the inner filter effect takes place.

The limits of detection (LOD) for both the sensors were calculated by using the following expression [24],

$$LOD = \frac{3\sigma}{K_{SV}} \quad (4.2)$$

Herein, σ represents the standard deviation obtained on taking around ten measurements of the sensors in absence of quenching ions. From the linear fitting, the LOD of MCD for Cr^{6+} and Fe^{3+} is estimated to be around 4 μM and 19 μM respectively, while for KYCD, LOD for Cr^{6+} is estimated to be 0.11 μM .

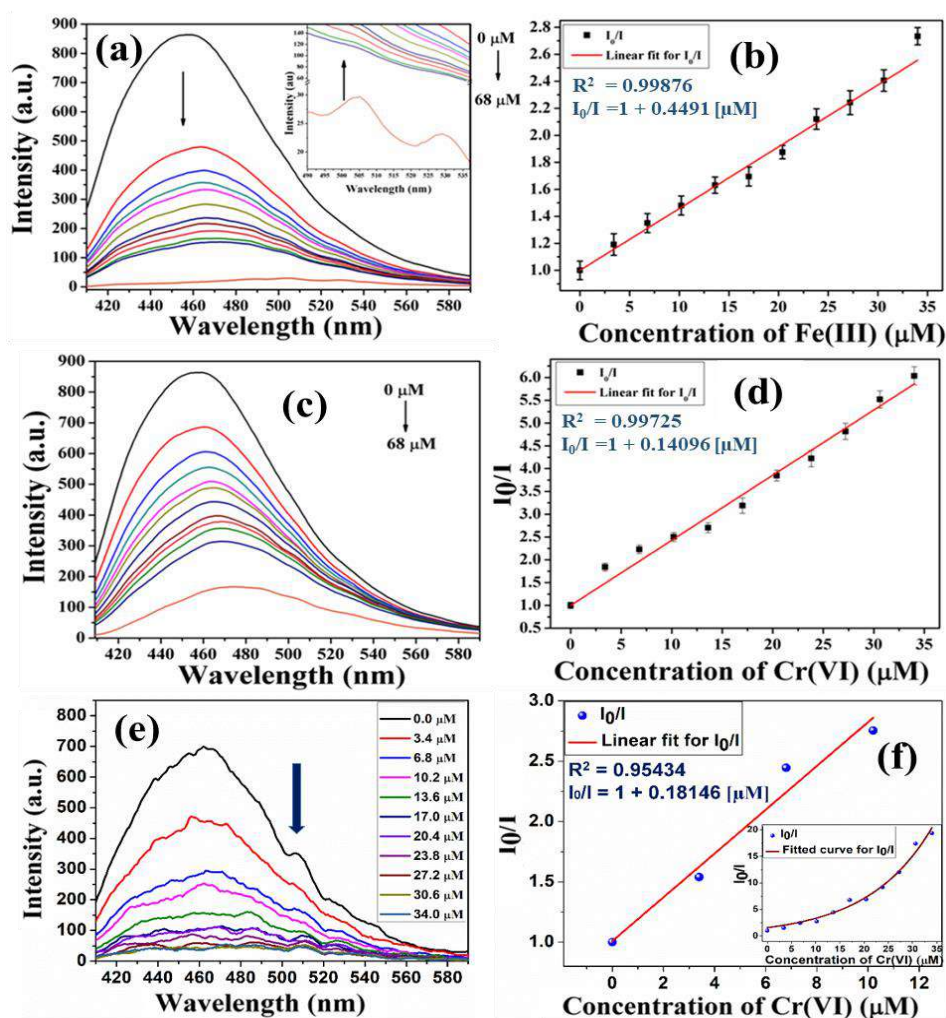


Figure 4.13: Fluorescence titration data for MCD using (a) Fe^{3+} and (c) Cr^{6+} respectively as the quencher; Stern-Volmer fitting of the corresponding fluorescence quenching data by (b) Fe^{3+} and (d) Cr^{6+} respectively, and (e) fluorescence quenching with the corresponding (f) Stern-Volmer plot for KYCD, inset of (f) illustrates the upward increment due to dynamic quenching at higher concentrations of Cr^{6+}

4.3.4 Investigation of the mechanism responsible for the quenching process

The possible pathway for quenching mechanism followed by both the sensors has been analyzed from time-resolved fluorescence spectroscopy (TCSPC) and Time-Dependent Density Functional Theory (TD-DFT). The fluorescence lifetime of pure MCD was found around 13.6 ns, and gradually reduce to 7.75 and 7.14 ns when exposed to Fe^{3+} and Cr^{6+} respectively (Figure 4.14). Similarly, the lifetime of the pure KYCD was found to be 5.71 ns, which reduces to 2.65 and 0.75 ns on the addition of 3.4 and 10.2 μM Cr^{6+} respectively (Figure 4.15). Reduced lifetime values with the addition of Fe^{3+} and Cr^{6+} to MCD and when Cr^{6+} to KYCD suggest that the fluorescence quenching phenomena occur in the excited state.

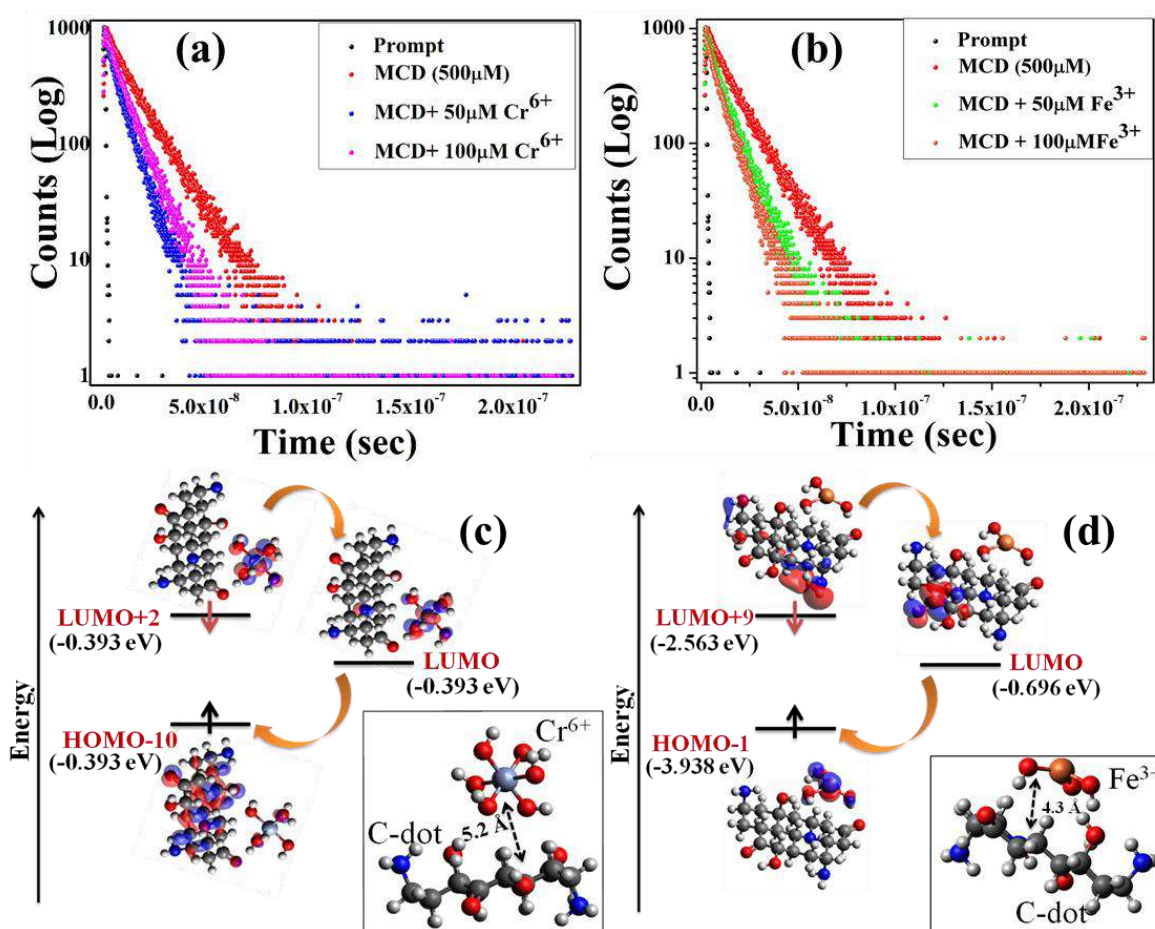


Figure 4.14: Fluorescence decay profiles of MCD upon the addition of (a) Cr^{6+} and (b) Fe^{3+} ; molecular orbitals and electronic transitions involved in fluorescence quenching upon (c) Cr^{6+} and (d) Fe^{3+} addition

For further understanding of the mechanism, theoretical DFT studies were performed, the interaction was studied by placing the fluorophore part (carbon dot) at a distance of 5 \AA from quencher ion (Fe^{3+} and Cr^{6+} for MCD and Cr^{6+} for KYCD). As per Kasha's rule [25],

the fluorescence emission from the lowest singlet excited state and on excitation to a higher electronic state will result in fast relaxation. Thus the theoretical study suggests that upon excitation, photoinduced charges move directly to the LUMO state from the HOMO state and then return to the LUMO state after a non-radiative internal conversion. In the case of Cr^{6+} by MCD, as the band gap value of the radiative path is around 2.49 eV during emission, a green emission is visible (Figure 4.14). Thus, from the above studies, it was confirmed that the photoinduced electron transfer (PET) process [26] plays a pivotal role in the sensing process for both sensors.

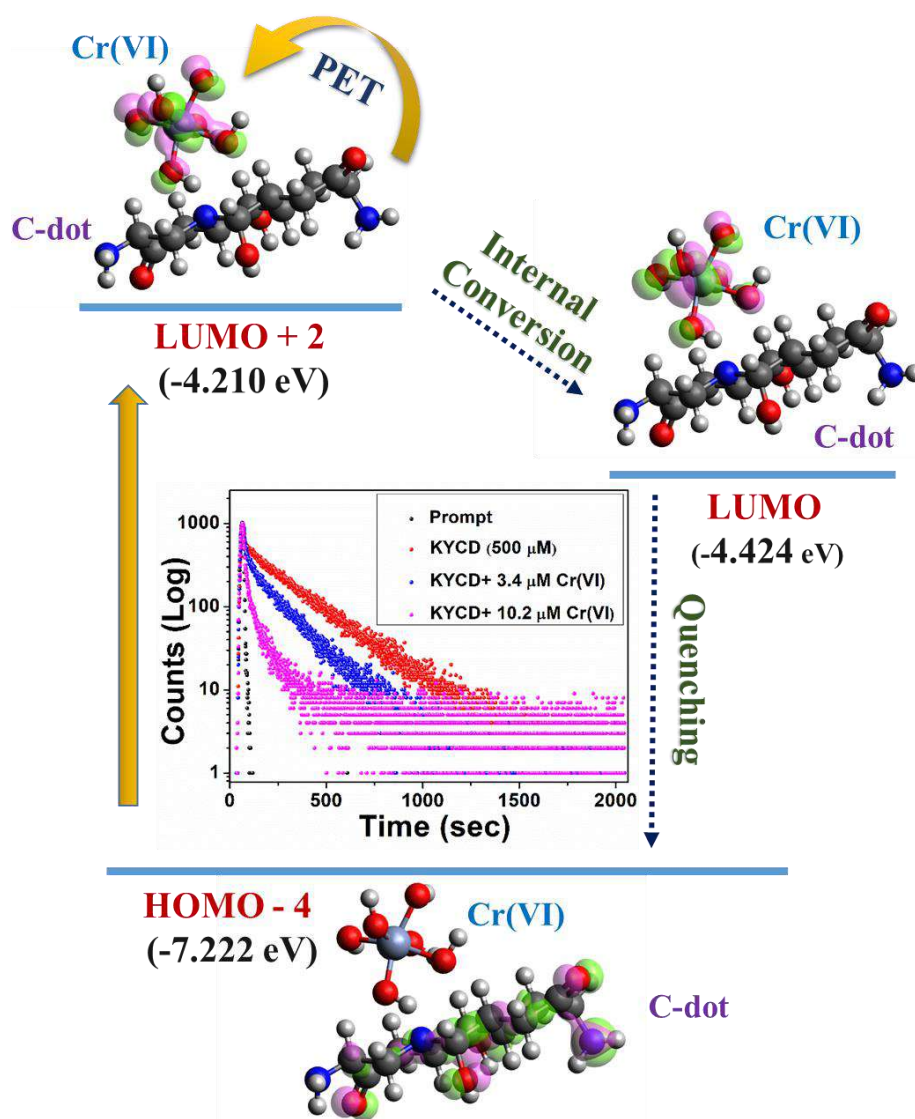


Figure 4.15: Molecular orbitals and electronic transitions involved quenching process in KYCD upon Cr^{6+} addition, with the corresponding decay in fluorescence lifetime (inset)

4.3.5 Determination of sensing efficacy of MCD and KYCD for real-life applications

Additionally, to verify the applicability of the sensor in real life, the sensing efficacy was examined against various pH and in various real-life water samples. In reality, industrial wastewater can have extreme pH ranges and as the work focuses on the fabrication of nano-sensors for heavy metal sensing in real-life water and wastewater, the ability to perform in diverse pH conditions is very important. Three different pH was used (acidic pH of 4.0, basic pH of 9.2, and neutral pH of 7.0), which was maintained by adjusting HCl and NaOH solutions. No significant alteration in fluorescence emission was found, which shows that the sensor can efficiently perform at any pH (Figure 4.16). MCD can effectively detect Fe^{3+} and Cr^{6+} , while KYCD can detect Cr^{6+} in the diverse pH, thus confirming that the sensing efficacy remains unaffected at varied acidic or basic conditions.

As most of the synthesized nano-sensors suffer from the drawback of real-life applicability due to the presence of various interfering ions, the fluorescence properties were investigated using various water samples from different sources. All the water samples were filtered through a membrane filter (pore size 0.45 μm) prior to the experiments. Samples were then spiked with 500 μM quenching ions (Fe^{3+} and Cr^{6+} for MCD and Cr^{6+} for KYCD). As illustrated in Figure 4.16, both MCD and KYCD perform efficiently in all water samples. The sensing efficacy of both the sensing probe was also examined using real-life tannery wastewater collected from a local canal connected to the tannery industry outlet.

ICP-OES was performed for elemental analysis of the wastewater, which shows the presence of alarmingly high chromium concentration (~ 20 ppm) along with iron (~ 5 ppm) and traces of other heavy metals. Significant quenching of the sensors occurs when exposed to wastewater. This confirms that both MCD and KYCD can efficiently perform in a real-life scenario, irrespective of the presence of various interfering ions.

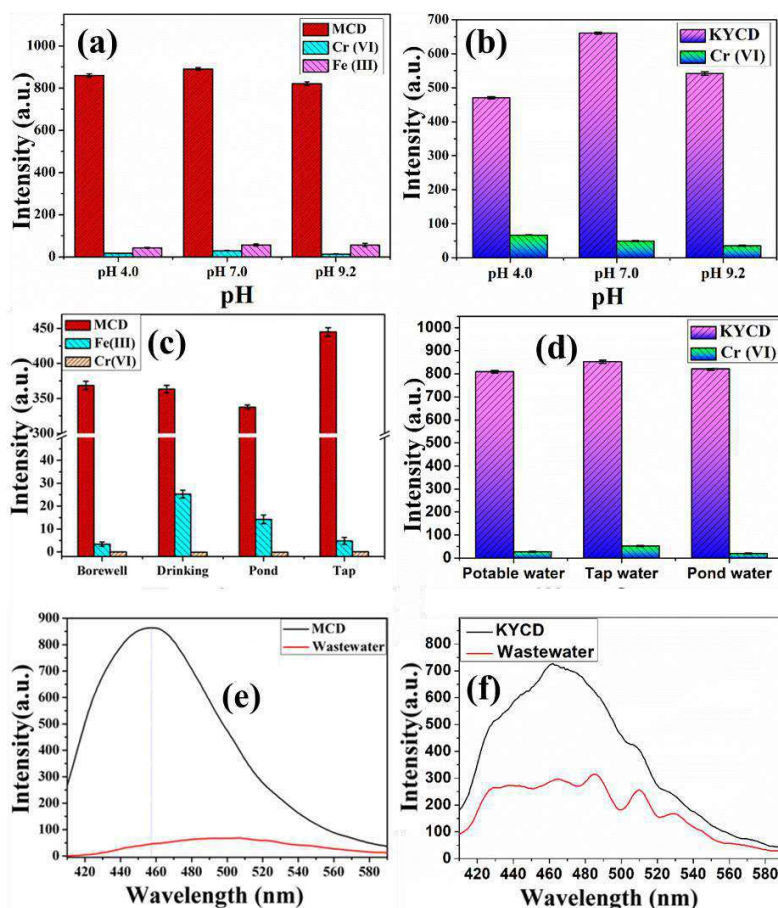


Figure 4.16: Sensing performances of the MCD and KYCD (a-b) different pH; (c-d) in different water sources; (e-f) Fluorescence quenching observed using industrial wastewater

4.3.6 Biosensing application

Biosensing plays a significant role in, the early-stage detection of various diseases, presence of target elements in the cells/tissues, and biomonitoring [26]. Rapid fluorometric sensing of heavy metal ions in the living cells can also be helpful to track the pathway for biomagnification of heavy metals. Reports suggest that pristine carbon dots can easily enter different intracellular compartments and are potential fluorescent imaging agents for cancer cells, microbial cells, and various other cell lines [27]. Hence in this work, other than sensing in real-life water and industrial wastewater, sensing efficacy was also examined in living cells by performing cell imaging using HeLa cells (human cervical cancer cell line).

Upon treatment with the nano-sensor, bright blue fluorescence was observed on UV excitation as observed under a fluorescence microscope. The fluorophore part (carbon dot) is responsible for such bright blue fluorescence, which is unaffected by the culture medium and other cellular components. This confirms that the nano-sensors can effectively penetrate

the cellular membrane of the cancer cells and can be helpful for cancer cell detection through the bioimaging process. The blue fluorescence diminishes as a quenching ion (Cr^{6+} was used for the study) is added to the cells (Figure 4.17). This substantiates the fact that these nano-sensors can effectively detect the presence of heavy metals at the cellular level and they can be potential nanoprobe for different biological labeling and imaging applications.

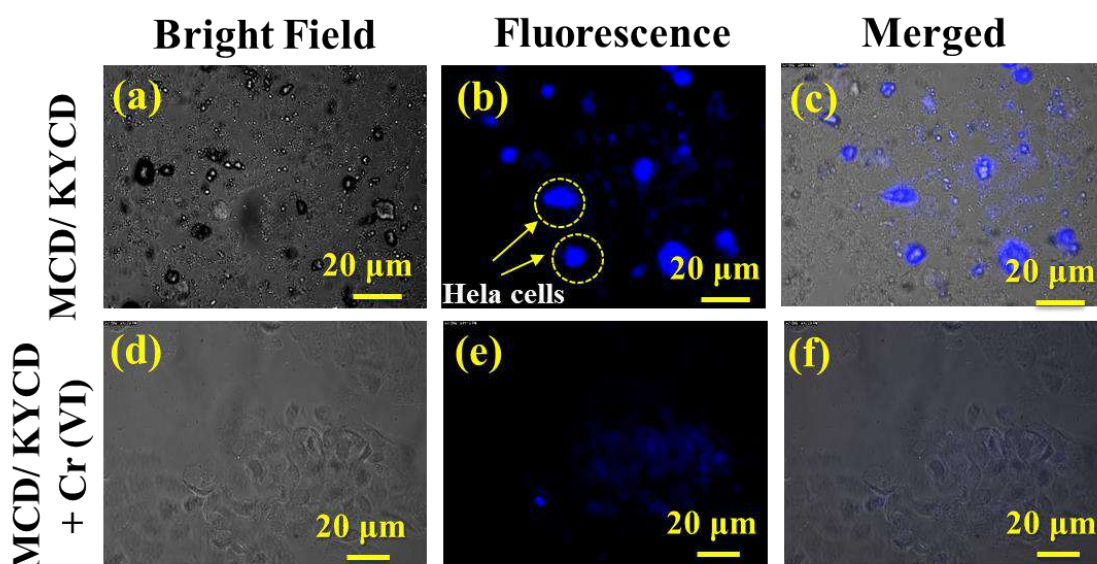


Figure 4.17: (a-c) Biosensing capacity and cellular permeability studies of the human cervical cancer cell line, which shows bright blue fluorescence on interacting with sensor, but diminishes (d-f) on addition of quencher ion

4.4 Summary

This work reports a facile strategy to synthesize effective, sensitive, cost-effective, and simple natural silicate-based sensors, namely MCD for detection of Fe^{3+} and Cr^{6+} , and KYCD for detection of Cr^{6+} in aqueous medium and living cells. The modification of nano-microcline (M2) and nano-kyanite (KY2) using nitrogenous carbon dot not only enhances the fluorescence quality of the mineral samples but also provides photo-stability required for prolonged use. In the case of MCD, the dual-sensing can occur simultaneously as a “turn-off” sensing occurs in presence of Fe^{3+} , whereas a red-shift to a higher wavelength occurs when exposed to Cr^{6+} . The KYCD nano-sensor can only detect the presence of Cr^{6+} by fluorescence quenching. Such sensing does not alter under varied pH conditions or in real-life water samples. Stern Volmer, TCSPC, and theoretical DFT prove that the photo-induced or PET mechanism is responsible for such a quenching effect in both the nano-sensors. Moreover, the ability to detect contaminants at the cellular level proves their potential for

biomedical application. Since MCD exhibits dual-sensing properties, this nano-sensor was further used for the synthesis of the stable and fluorescent membrane, as discussed in the next chapter.

References

1. Hakak, S., Khan, W.Z., Gilkar, G.A., Haider, N., Imran, M. and Alkathairi, M.S., 2020. *IEEE Internet Things J.* 3(2), 38-43.
2. Lu, K.H., Lin, J.H., Lin, C.Y., Chen, C.F. and Yeh, Y.C., 2019. *Microchim. Acta* 186(4), 1-7.
3. Duan, Q., Wang, X., Zhang, B., Li, Y., Zhang, W., Zhang, Y. and Sang, S., 2019. *Microchim. Acta* 186(11), 1-7.
4. Barone, P.W., Parker, R.S. and Strano, M.S., 2005. *Anal. chem.* 77(23), 7556-7562.
5. Umapathi, R., Sonwal, S., Lee, M.J., Rani, G.M., Lee, E.S., Jeon, T.J., Kang, S.M., Oh, M.H. and Huh, Y.S., 2021. *Coord. Chem. Rev.* 446, 214061.
6. Umapathi, R., Park, B., Sonwal, S., Rani, G.M., Cho, Y. and Huh, Y.S., 2022. *Trends Food Sci Technol* 119, 69-89.
7. Hola, K., Zhang, Y., Wang, Y., Giannelis, E.P., Zboril, R. and Rogach, A.L., 2014. *Nano Today*, 9(5), 590-603.
8. Wang, C., Xu, Z., Cheng, H., Lin, H., Humphrey, M.G. and Zhang, C., 2015. *Carbon*, 82, 87-95.
9. Schneider, J., Reckmeier, C.J., Xiong, Y., von Seckendorff, M., Susha, A.S., Kasák, P. and Rogach, A.L., 2017. *J. Phys. Chem. C* 121(3), 2014-2022.
10. Roy, S., Bardhan, S., Chanda, D.K., Roy, J., Mondal, D. and Das, S., 2020. *ACS Appl. Mater. Interfaces* 12(39), 43833-43843.
11. Pimentel, C., Gnecco, E. and Pina, C.M., 2015. *Surf. Sci.* 635, 123-127.
12. Kalita, J.M. and Chithambo, M.L., 2020. *J. Lumin.* 224, 117320.
13. Shiman, O.V., Balogh, L. and Daymond, M.R., 2019. *Surf. Interfaces* 17, 100388.
14. Wu, Y.N. and Wang, Y.F., 2018. *Journal of Earth Science*, 29(1), 21-29.
15. Wu, Y.N. and Wang, Y.F., 2018. *J. Earth Sci.* 29(1), 21-29.
16. Bell, D.R., Rossman, G.R., Maldener, J., Endisch, D. and Rauch, F., 2004. *Am. Min.* 89(7), 998-1003.
17. Chen, J., Liu, J., Li, J., Xu, L. and Qiao, Y., 2017. *J Colloid Interf Sci.* 485, 167-174.
18. Carbonaro, C.M., Chiriu, D., Stagi, L., Casula, M.F., Thakkar, S.V., Malfatti, L., Suzuki, K., Ricci, P.C. and Corpino, R., 2018. *J. Phys. Chem. C* 122(44), 25638-25650.
19. Dong, W., Zhou, S., Dong, Y., Wang, J., Ge, X. and Sui, L., 2015. *Luminescence* 30(6), 867-871.
20. Cho, M.J. and Park, S.Y., 2019. *Sens. Actuators, B* 282, 719-729.
21. Roy, S., Bardhan, S., Mondal, D., Saha, I., Roy, J., Das, S., Chanda, D.K., Karmakar, P. and Das, 2021. S., *Sens. Actuators B: Chem.*
22. Roy, S., Pal, K., Bardhan, S., Maity, S., Chanda, D.K., Ghosh, S., Karmakar, P. and Das, S., 2019. *Inorg. Chem.* 58(13), 8369-8378.

23. Song, Y., Zhu, S., Xiang, S., Zhao, X., Zhang, J., Zhang, H., Fu, Y. and Yang, B., 2014. *Nanoscale*, 6(9), 4676-4682.
24. Bardhan, S., Roy, S., Chanda, D.K., Mondal, D., Das, S. and Das, S., 2021. *Microchimica Acta*, 188(4), 1-12
25. Kasha, M., 1950. *Discussions of the Faraday society*, 9, 14-19
26. Roy, S., Bardhan, S., Chanda, D.K., Ghosh, S., Mondal, D., Roy, J. and Das, S., 2020. *Dalton Trans*, 49(20), 6607-6615.
27. Yan, F., Jiang, Y., Sun, X., Bai, Z., Zhang, Y. and Zhou, X., 2018. *Microchimica Acta*, 185(9), 1-34.



Chapter 5

Fabrication of a flexible and reusable membrane using carbon dot decorated natural microcline (MCPV): A futuristic probe for multiple heavy metal induced carcinogen



Chapter 5

5.1 Overview

The previous chapter (Chapter 4) discussed the strategy of nitrogenous carbon dots preparation and development of natural microcline and kyanite-based carbon dot-loaded fluorescent nano-sensors. The kyanite-carbon dot nanocomposite (KYCD) can successfully detect the presence of hexavalent chromium (Cr^{6+}), while microcline-carbon dot nanocomposite (MCD) exhibits dual sensing of hexavalent chromium and trivalent iron (Fe^{3+}) in aqueous medium and living cells. Moreover, in previous chapters, it was discussed that nano-sized microcline (M2) shows better antibacterial (Chapter 3) and electrical (Chapter 2) properties compared to nano-sized kyanite (KY2). Although both the nano-sensors MCD and KYCD can efficiently detect the presence of heavy metals, they suffer certain drawbacks. Generally, most of such powdered/ liquid nanocomposites are designed for one-time use and have limitations like fluorescence degradation with time, instability, or inconvenience in real-time/ on-field applications [1-2]. It is very difficult to directly use such sensors on a commercial or industrial scale. Hence, this work aims towards the synthesis of a free-standing, efficient, very fast response time (in seconds), flexible, stable, durable, biocompatible, and reusable sensing probe that can instantly and selectively detect heavy metal in an aqueous medium with high precision. The fluorescent membrane can effectively detect the presence of Cr^{6+} and Fe^{3+} and the sensing is also visible under naked eyes on UV illumination.

In this work, MCD was incorporated in the polymer matrix of polyvinylidene fluoride-co-hexafluoropropylene) (PVDF-HFP) that not only enhances the stability, reusability, and mechanical strength but also increases the fluorescence intensity of the membrane (MCPV). Natural microcline basically stabilizes the carbon dots (fluorophores) and PVDF-HFP polymer provides the solid and flexible backbone for sensing applications. The PVDF-HFP copolymer of pristine PVDF contains a chemically inactive, amorphous HFP phase, thus exhibiting excellent hydrophobic nature and mechanical strength [3-4]. This HFP phase also enhances the piezo and ferroelectric properties compared to PVDF. Moreover, the nontoxic nature, dimension tailor ability, flexibility and recyclability, stability, and chemical resistance make it a suitable candidate for sensor membrane synthesis. Owing to the

hydrophobic nature, the membrane will not get dissolved in an aqueous medium and can retain its properties for long-term usage.

Detailed characterization was performed using XRD, FT-IR, FESEM, and UV-Vis spectroscopy. This fluorescent membrane exhibited immense fluorescence and mechanical stability, high selectivity, and great sensing efficacy which remains unaltered irrespective of multiple uses. Moreover, usage of natural microcline and carbon dot and a very simple synthesis route reduces the production cost, making it a potential candidate for sensor probe development at the industrial level. Additionally, various theoretical approaches like density functional theory and molecular docking have been carried out to validate the sensing mechanism in biological applications.

5.2 Experimental details

5.2.1 Materials

PVDF-HFP pellets, N, N-dimethylformamide (DMF) (HPLC grade) and L-Glutathione (C₁₀H₁₇N₃O₆S) were purchased from Sigma-Aldrich Co. All the reagents required for selectivity analysis were of analytical grade ($\geq 98.0\%$ pure) and purchased from Merck, India. The reagents were directly used for synthesis and analytical purposes without any further purification. Millipore water (resistivity~18.2 M Ω -cm) was used throughout the experiments. Stimulated body fluid (SBF) was prepared by dissolving 7.996 g NaCl, 0.350 g NaHCO₃, 0.224 g KCl, 0.228 g K₂HPO₄.3H₂O, 0.305 g MgCl₂.6H₂O, 0.278 g CaCl₂, 0.071 g Na₂SO₄, 6.057 g (CH₂OH)₃CNH₂ and 1.0 M HCl in 1 L Millipore water, maintaining ~7.5 pH.

5.2.2 Fabrication of fluorescent sensor membrane

Nitrogenous carbon dot was synthesized via a two-step hydrothermal technique using the citric acid solution and EDA and MCD was prepared from carbon dot loading in the nano-microcline, as discussed earlier in Chapter 4. Then, 150 mg of PVDF-HFP was dissolved in 10 mL DMF and MCD nanocomposite (5 % w/w) was subsequently added under stirring conditions (800 rpm). The mixture was stirred overnight and then ultrasonicated for 15 min to obtain homogeneity. Hereafter, the homogenous solution was poured on a clean, dirt-free petri dish and dried in the oven at 70 °C. The dried membrane was peeled off and the sensor membrane was named MCPV. Another membrane of pristine PVDF-HFP was prepared

following the same protocol without incorporating MCD nanocomposite and was used as a control.

5.3 Results and discussion

5.3.1 Physical characteristics of the microcline-carbon dot loaded PVDF-HFP membrane (MCPV)

The phase purity and the semi-crystalline nature of the sensor membrane were analyzed using the X-ray diffraction (XRD) technique. Well exhibited diffraction patterns of pure PVDF-HFP and MCPV membrane are illustrated in Figure 5.1a. The characteristic crystalline, non-polar α -phase of PVDF-HFP were observed at 17.6° (020), 26.8° (021), and 38.9° (002), while the diffraction maximum at 20.7° (110) corresponds to the polar β -phase of the membrane [11]. Due to incorporation of MCD nanocomposite in the polymer matrix, enhancement of β -phase (20.7°) occurs with a slight reduction in the diffraction line corresponding to the α -phase (17.6° and 38.9°) due to polarization of the CH_2 - moiety of the positively charged surface of MCD [12].

The bonding networks of the sensor membrane and the pristine PVF-HFP were analyzed by using FT-IR spectroscopy (Figure 5.1b). Characteristic IR-absorption bands of PVDF-HFP associated with the non-polar α -phase were observed at 488 cm^{-1} due to $-\text{CF}_2$ wagging, at 531 cm^{-1} and 762 cm^{-1} due to $-\text{CF}_2$ bending and 877 cm^{-1} due to $-\text{CF}_2$ stretching, while $-\text{CH}_2$ rocking and $-\text{CH}_2$ twisting results in absorption bands at 795 cm^{-1} and 976 cm^{-1} respectively. The absorption band observed at 615 cm^{-1} is due to skeletal bending [13]. The vibrational maxima related to β -phase were observed at 510 cm^{-1} due to $-\text{CF}_2$ stretching and at 840 cm^{-1} due to $-\text{CH}_2$ rocking, $-\text{CF}_2$ asymmetric stretching, and skeletal C-C stretching. C-O-C stretching results in the vibrational band at 1070 cm^{-1} while the band at 1160 cm^{-1} attributes to the deformation vibrations and asymmetric stretching of C-H bond and stretching vibration of C-F [14]. Similar to XRD results, enhancement of β -phase (polar nature of PVDF-HFP) was observed due to MCD incorporation as an increment of the absorption peak at 840 cm^{-1} was observed. The absence of any extra peak in the sensor membrane ascertains its purity.

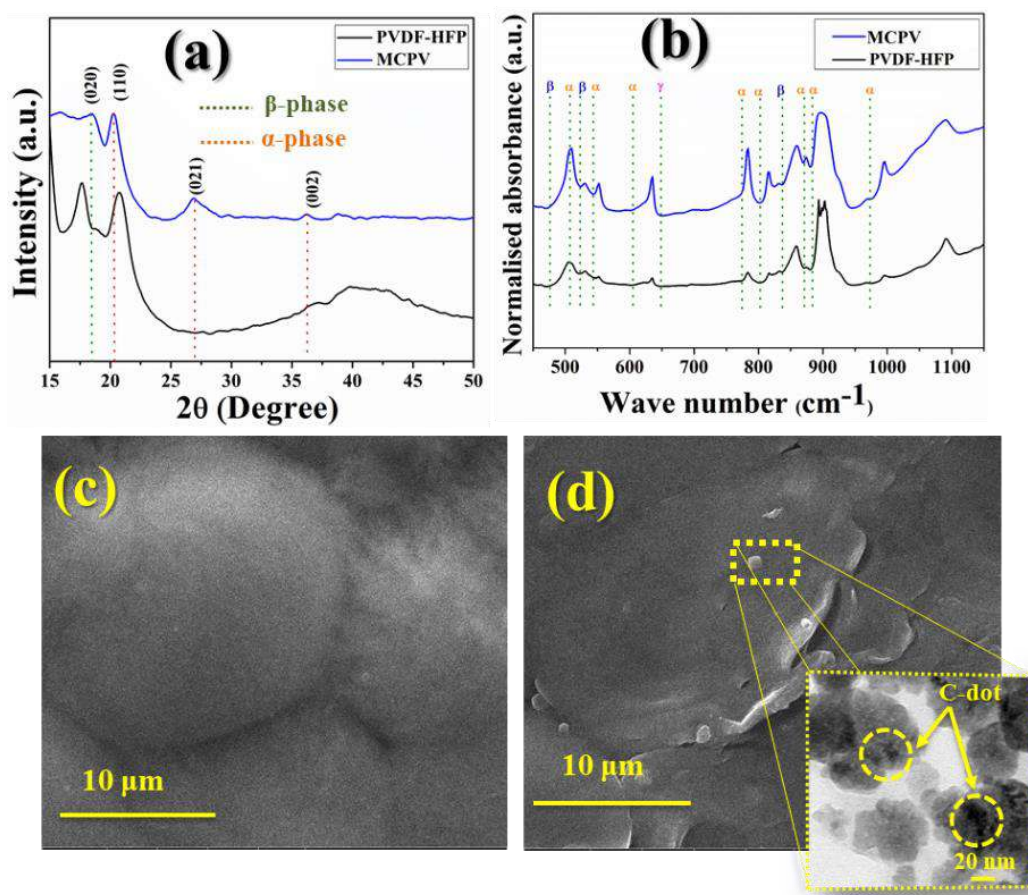


Figure 5.1: (a) X-ray diffractogram of MCPV and pure PVDF-HFP film; (b) FTIR spectra of MCPV and pure PVDF-HFP film; (c) FESEM micrograph of the smooth surface of pure PVDF-HFP (d) FESEM micrograph of MCPV with TEM micrographs of carbon dot loaded microcline (inset)

Morphological features have been studied using FESEM and are illustrated the Figure 5.1(c-d). A relatively smooth and uniform surface was observed in pure PVDF-HFP, which becomes slightly rough and wrinkled in the case of the sensor membrane due to the addition of MCD in the polymer matrix. Further investigation using TEM revealed that the particle size of MCD (dopant) is around 20-40 nm, which contains tiny carbon dots of around 5 nm size embedded on its surface (Figure 5.1d inset).

5.3.2 Determination of thermal stability of MCPV membrane

Temperature stability under a higher temperature range is a vital parameter necessary for application in a real-life scenario, hence the thermal stability was investigated using thermogravimetric analysis (TGA) and differential thermal analysis (DTA). Nominal mass loss of only around 0.5 % was observed till 200 °C, as illustrated in Figure 5.2. Moreover, the

sensor membrane shows great stability till 157 °C (endothermic peak), which otherwise was till 154 °C in the case of the undoped membrane (Figure 5.2a).

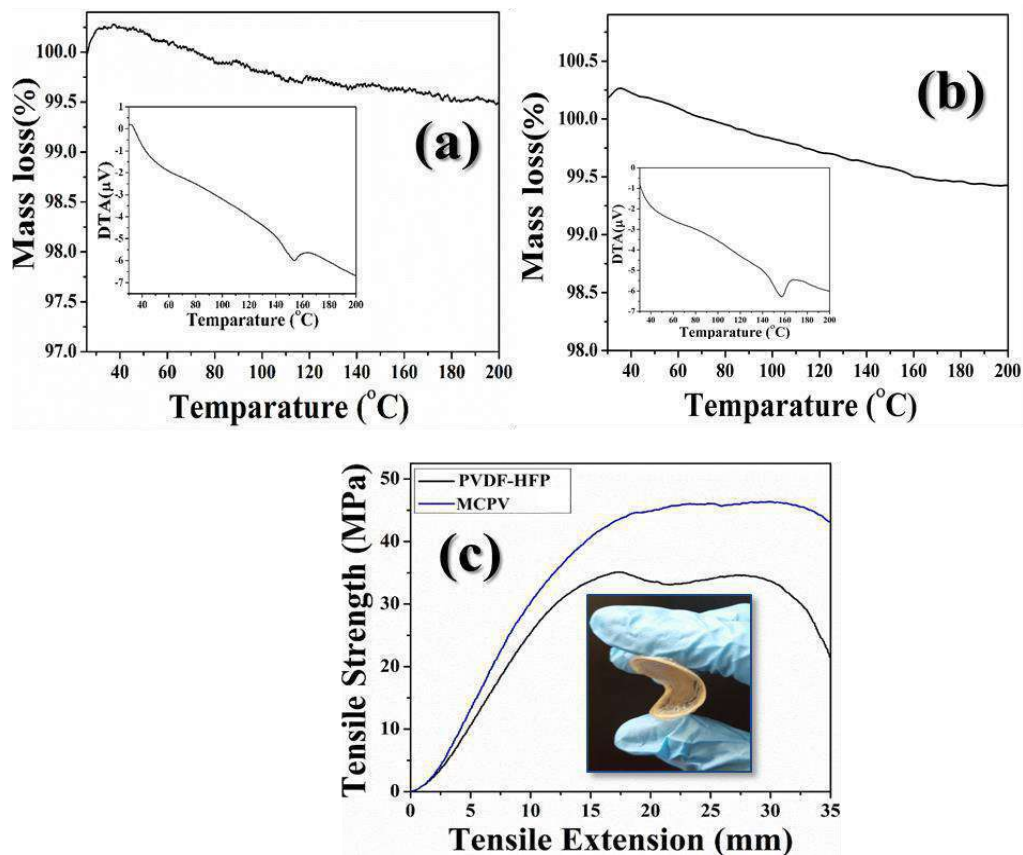


Figure 5.2: TGA and DTA (inset) of (a) PVDF-HFP and (b) MCPV; (c) Tensile strength of PVDF-HFP and MCPV film showing flexibility and mechanical stability of the film (inset)

Other than temperature stability, the mechanical strength of the sensor is also a crucial parameter that is essential for real-life application for regular and repetitive use. Figure 5.2c illustrates the tensile extension data for the membranes of approximately 0.06 mm thickness. Figure 5.2c shows enhancement of tensile strength (46.1 MPa) compared to pure PVDF HFP membrane (34.6 MPa). Thus the MCD nanocomposite acts as a filler into the pores of the polymer matrix and other than enhancing the β -phase of the polymer (as observed from XRD and FT-IR data), it also improves the durability, stability, and mechanical performance of the sensor due to the re-assembly of the bonding networks resulting in stronger interaction between polymer chain and the doped MCD.

5.3.3 Optical characteristics of the MCPV membrane

Carbon dot shows absorption bands centered at 250 and 350 nm, as reported in the literature [15]. The π -stacking of the conjugated π -electrons of carbon dots moiety of the sensor

membrane results in a broad-range absorption from 250 to 450 nm with the maxima centered at 350 nm (Figure 5.3a). Such absorbance bands are otherwise absent of the pure PVDF-HFP. Further, the optimum excitation wavelength was determined by exciting sensor membrane at varying excitation wavelengths from 370 to 420 nm (Figure 5.3b). The fluorometric membrane exhibits excellent blue fluorescence when excited at 414 nm with the fluorescence maxima centered at 489 nm (Figure 5.3d). In order to determine the influence of fluorophore concentration on fluorescence characteristics, various concentration of MCD were loaded (0.0 %, 2.5 %, 5.0 % and 7.5 %). The 5 % (w/w) shows the highest fluorescence compared to other concentrations (Figure 5.3c). Carbon dots are quantum-mechanically confined systems, which have been decorated into the microcline and further into the polymer matrix to restrict the agglomeration of the quantum dots. Agglomerated carbon dots can reduce the fluorescence quality of the sample [16] and this is why a specific amount of carbon dot is required to fabricate the sensor material. Hence concentration beyond 5 % (w/w) results in agglomeration, hence further fluorescence experiments were conducted using a 5 % MCD loaded sensor membrane.

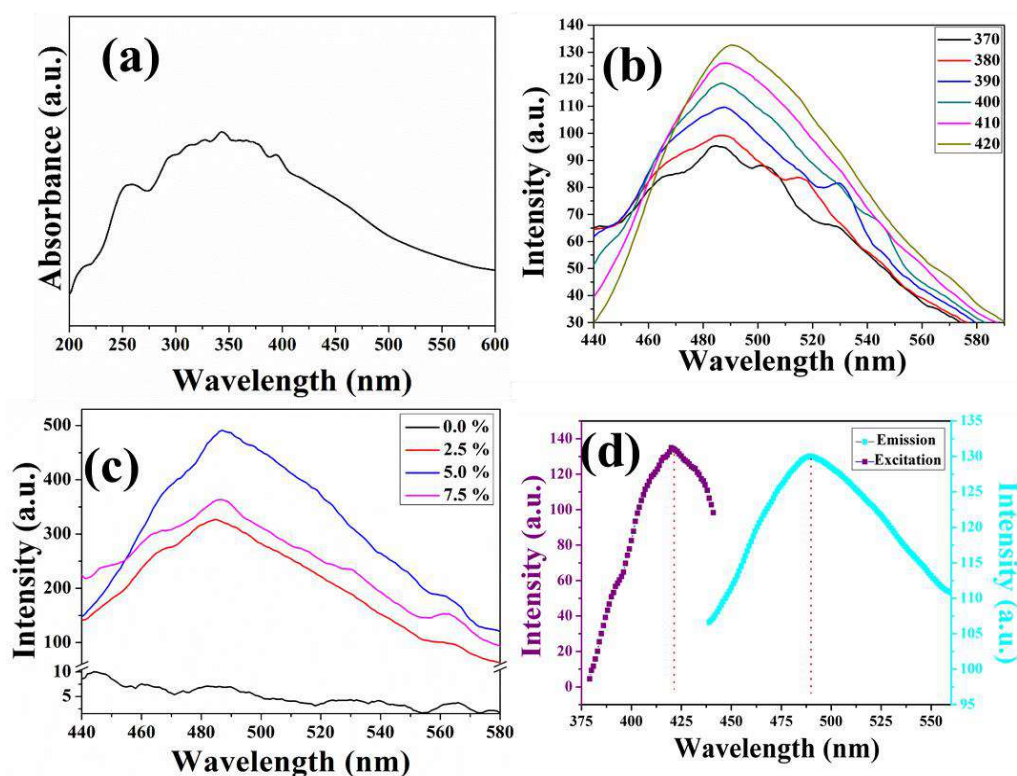


Figure 5.3: (a) Absorbance spectra of MCPV film; (b) Fluorescence spectra of MCPV at different excitation wavelengths ranging from 370 nm-420 nm; (c) Fluorescence intensity variation of the film for different carbon dots concentration (0 %, 2.5 %, 5 % and 7.5 %) in MCPV; (d) Excitation and emission spectra of the sensor film

5.3.4 Estimation of fluorescence stability the sensor membrane

Maintaining the fluorescence quality for a longer duration and with continuously changing environmental conditions is a huge challenge faced by researchers. Fluorescence stability under ambient conditions is a major aspect as the fluorescence properties of most of the sensors may degrade with time due to various environmental conditions like moisture, light, temperature change, etc. Hence, the stability of fluorescence was investigated against varied time temperatures. Time-dependent stability was analyzed for 10 consecutive days as the sensor membrane was kept under ambient environmental conditions (without any vacuum desiccation), exposed to humidity, light, atmospheric pressure, and temperature. The fluorescence intensity was measured everyday under the same excitation energy and the data obtained is illustrated in Figure 5.4a. No significant alteration in fluorescence spectrum was observed, which suggests the membrane is quite stable and does not require any kind of preservation techniques like desiccation or protection from light or temperature change.

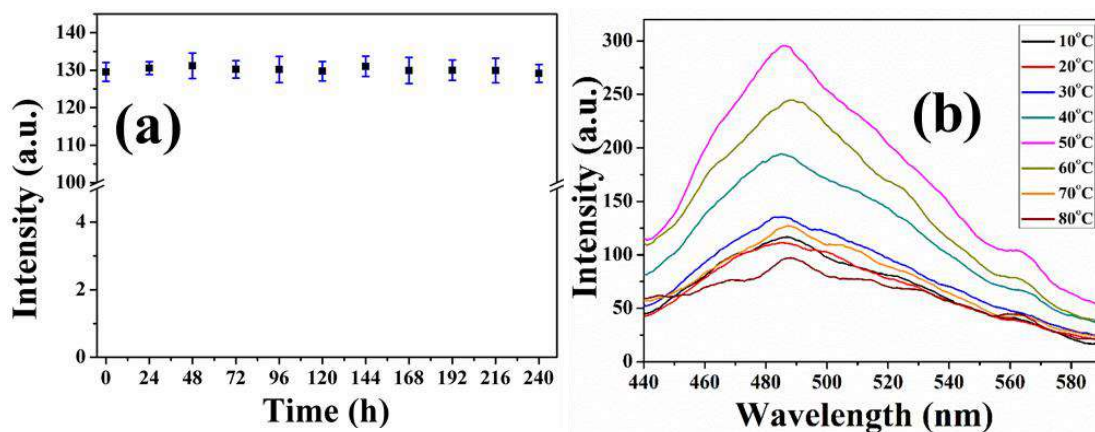


Figure 5.4: (a) Time-dependent fluorescence obtained on 240 h study; (d) Fluorescence stability of MCPV at various temperature

Additionally, to ascertain the fluorescence stability with varying temperatures, fluorescence intensity was examined at different temperatures (10-80 °C). It was observed that there was an increment in the fluorescence intensity with increasing temperature till 50 °C, beyond which a slight reduction in intensity occurred till 80 °C (Figure 5.4b). Since at higher temperature alterations of radiative and non-radiative transitions may occur as there are higher chances of collisional quenching between the fluorophores [13], a slight reduction of intensity takes place. Even at a higher temperature, no significant shift in emission maxima takes place, thus validating the fluorescence stability of the sensor membrane. Thus,

confirms that the polymeric substrate has well-wrapped the fluorophore and restricts any degradation or agglomeration due to extreme ambient conditions.

5.3.5 Fluorometric detection of the heavy metals in aqueous media using MCPV membrane

Selectivity towards a specific target molecule is the primary factor to be examined for a sensing probe. A fluorometric sensor either alters their fluorescence intensities or their color when exposed to the specific target molecule/ ion. The selectivity response of the fluorometric sensor was evaluated against a diverse range of ions (cations like As^{3+} , Ca^{2+} , Cr^{3+} , Cr^{6+} , Cd^{2+} , Fe^{2+} , Fe^{3+} , Hg^{2+} , Na^+ , K^+ , Pb^{4+} and anions like CO_3^{2-} , S^{2-} , SO_4^{2-} , NO_3^- and OH^-) (Figure 5.5a) at specific concentrations ($50 \mu\text{M}$). No significant change was observed except for Fe^{3+} and Cr^{6+} as significant decay in fluorescence intensity was observed on exposure to Fe^{3+} , while on addition of Cr^{6+} solution, the blue fluorescence shifted to green (530 nm). Such alteration is also visible through naked eyes when illuminated with UV light (Figure 5.5b).

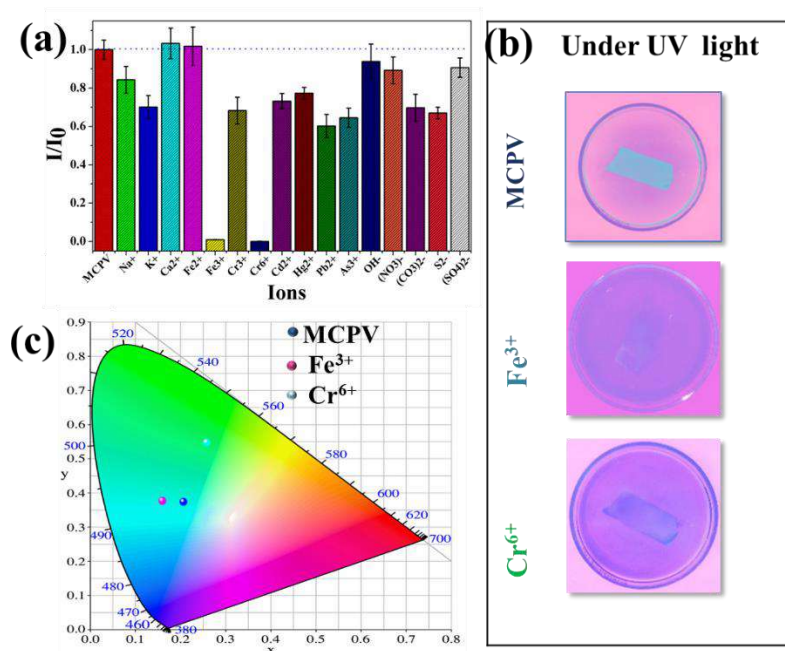


Figure 5.5: (a) Selectivity study of the sensor towards various cations and anions; (b) naked eye visualization of bright blue fluorescence on exposure to UV light and simultaneous real-life quenching on exposure to Cr^{6+} and Fe^{3+} (c) CIE-1931 colour space analysis of the sensor upon heavy metal exposure

The sensitivity of the membrane towards Fe^{3+} and Cr^{6+} was evaluated by immersing the MCPV membrane in varying concentrations (0-120 μM) of Fe^{3+} and Cr^{6+} solutions,

maintaining the same conditions in both cases. A gradual reduction of fluorescence intensity centered at 489 nm was observed on the addition of Fe^{3+} (Figure 5.6b), whereas in the case of Cr^{6+} , a gradual shift of emission maxima from 489 to 530 nm occurred along with a radical drop in fluorescence intensity (Figure 5.6a). To ensure such dual-sensing activity, the color coordinates were computed using CIE-1931 color space [14]. The pure sensor membrane exhibiting bright blue fluorescence shows color space with coordinate of $x = 0.20659$, $y = 0.37790$ (blue region) (Figure 5.5c), while coordinate slightly changes to $x = 0.16062$, $y = 0.38223$ on adding Fe^{3+} . A drastic shift to $x = 0.25897$, $y = 0.55185$ (green region) occurs on Cr^{6+} addition, which corroborates with naked-eye observations. Quantitative determination of sensitivity for both the ions (Fe^{3+} and Cr^{6+}) was carried out using the Stern-Volmer (S-V) equation and has been analyzed from the limit of detection (LOD) and limit of quantitation (LOQ) calculations. The relative fluorescence intensity (I_0/I) was fitted against the concentration of quencher ions (Fe^{3+} and Cr^{6+}) using the Stern-Volmer's equation [18]:

$$\frac{I_0}{I} = 1 + K_{SV} [M] \quad (5.1)$$

Here, I_0 , I , and K_{SV} are fluorescence intensities of pure MCPV, MCPV with quencher ions at various concentrations, and the Stern-Volmer coefficient respectively. With the increase in the concentration of quencher ion in both cases, an exponential increment of relative fluorescence intensity (I_0/I) was observed, suggesting dynamic/collisional quenching of the fluorophores [19].

The Stern-Volmer for Cr^{6+} was taken up to 60.0 μM while for Fe^{3+} , up to 30.0 μM concentration was taken to ensure the linearity in fitting (Figure 5.6c-d). Beyond these concentrations, the upward increments suggest the occurrence of the inner filter effect (Figure 5.6c-d inset). From the S-V plot, the fit coefficient (R^2) of the linear calibration curve for Fe^{3+} and Cr^{6+} was found to be 0.95252 and 0.99129 respectively.

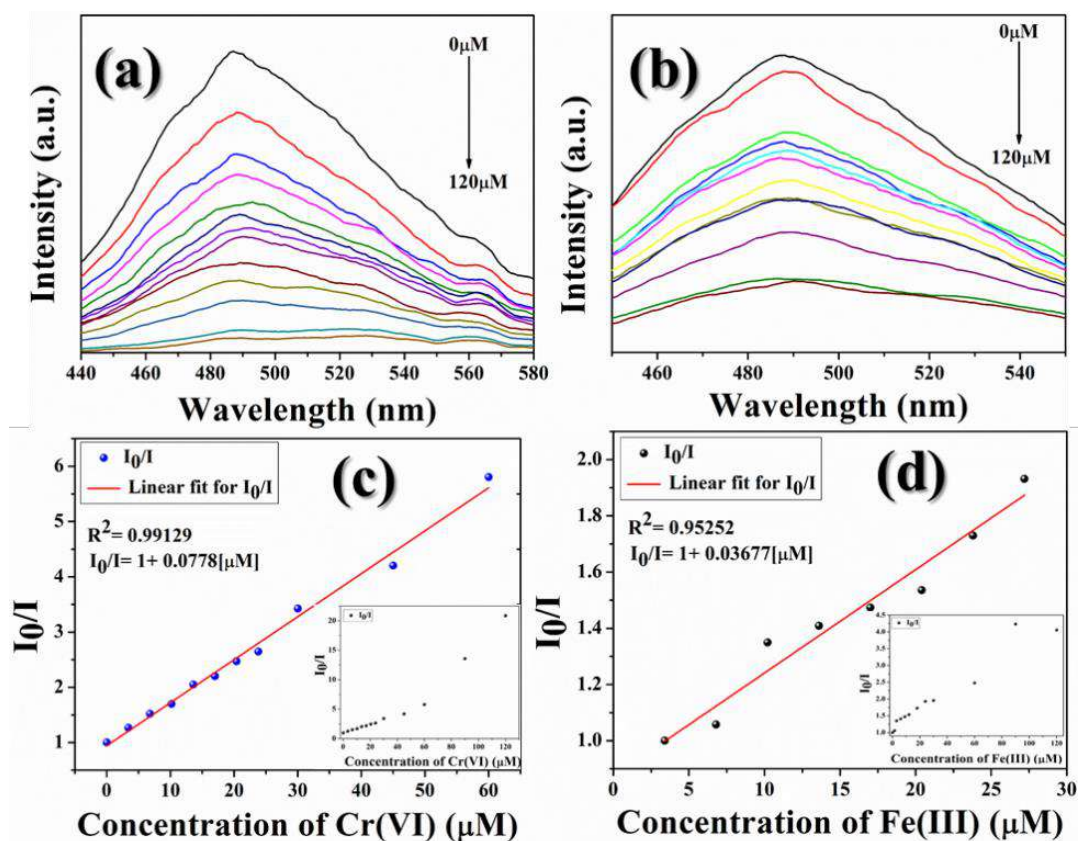


Figure 5.6: Fluorescence titration data for MCPV sensor using (a) Cr^{6+} and (b) Fe^{3+} respectively as the quencher; Stern-Volmer fitting of the corresponding fluorescence quenching data by (c) Cr^{6+} and (d) Fe^{3+} respectively, with the corresponding whole range of Stern-Volmer plot (inset of c and d) showing an upward increment due to dynamic quenching of the fluorophores at higher concentrations

The LOD and LOQ were calculated for both the quenching ions using the following equations [20]:

$$LOD = \frac{3\sigma}{K_{SV}} \quad (5.2)$$

$$LOQ = \frac{10\sigma}{K_{SV}} \quad (5.3)$$

Here, σ represents the standard deviation obtained on taking ten measurements of the fluorescence intensities of pure MCPV. The LOD and LOQ for Cr^{6+} were calculated to be $8.7 \mu\text{M}$ and $29.1 \mu\text{M}$ respectively, while the LOD and LOQ for Fe^{3+} were found to be $18.4 \mu\text{M}$ and $61.6 \mu\text{M}$ respectively. Such low detection limits (in micromolar range) imply that the sensor membrane is highly sensitive to even the presence of a minute quantity of quencher ions in an aqueous solution.

5.3.6 Mechanism of detection

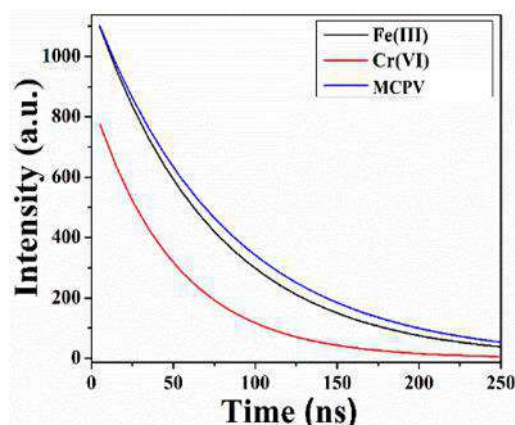


Figure 5.7: Fitted fluorescence decay profiles of the sensor upon the addition of the heavy metals

To justify the fluorometric detection mechanism, initially, time-resolved fluorescence decay of the sensor was measured using a TCSPC technique. The emission and excitation wavelengths for pure MCPV and Fe^{3+} (25 μM) were set at 489 and 414 nm respectively, and excitation wavelength was kept at 530 nm for Cr^{6+} (25 μM). Reduction in decay time was observed on the addition of quencher ions (Figure 5.7) as the average lifetime of pure MCPV was found to be 80 ns, while it reduces to 62 ns when immersed in Fe^{3+} solution, and to 46 ns in Cr^{6+} solution. In both cases, such reduction in fluorophore lifetime in the excited state reveals that the quenching phenomenon occurred due to the collisional quenching mechanism in the excited state. For further insight, quantum chemical calculations were performed using density functional theory (DFT). To minimize the complexity of the computation, carbon dot (fluorophore) and the quenching ions (Cr^{6+} and Fe^{3+}) were considered for calculations. In both cases, quenching ions were placed at a distance of 5 Å from the fluorophore, and the geometries were optimized along with an estimation of frequencies prior to the time-dependent DFT (TDDFT) calculations. At excited state, significant transfer of the molecular orbitals was observed between the quenchers and the fluorophore in the TDDFT studies (Figure 5.8) without any evidence of the formation of any bond between the quenchers and the fluorophore. This confirms that the photoinduced electron transfer (PET) mechanism occurs in both cases which ultimately results in such fluorometric alterations [21-22].

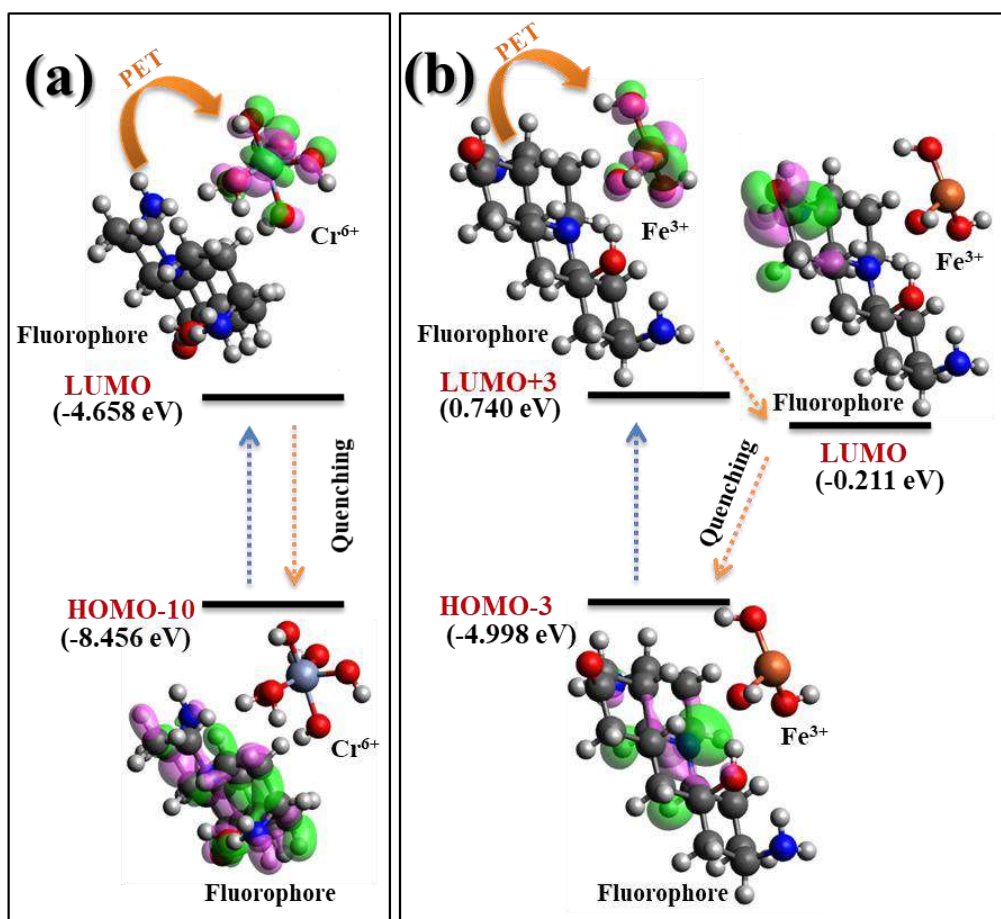


Figure 5.8: Molecular orbitals and electronic transitions involved in fluorescence quenching of the sensor upon (a) Cr^{6+} and (b) Fe^{3+} addition respectively

5.3.7 Performance of the sensor membrane in various conditions

5.3.7.1 Sensing efficacy of the MCPV membrane in different pH conditions

An efficient sensor can maintain its sensing efficacy in varied pH ranges, hence sensing ability and fluorometric performance were examined against various pH (pH 4.0, 7.0, 9.2, and 12.6) (Figure 5.9a). The pH was maintained by HCl and NaOH and 100 μM Cr^{6+} and Fe^{3+} solutions were also added separately. Fluorescence quality and sensing capability do not degrade with change in pH, although a slight decrease in fluorescence intensity occurs at pH 4.0 due to the inner filter effect since a higher concentration of H^+ ions reduces the accessibility of fluorophores [23]. Furthermore, the accuracy of the sensor was validated from recovery rate (RR %) and relative standard deviation (RSD) which were calculated from the calibration graphs (up to 20.0 μM for both Cr^{6+} and Fe^{3+}). A low RSD value (below

1.84) with a great recovery rate (92.6 to 101.1 %) suggests that the sensor maintains its sensing efficiency irrespective of pH alterations.

5.3.7.2 Sensing efficacy of the MCPV membrane in different water sources

Water samples were collected from various sources to determine the sensing ability in various water qualities. The potable water was collected from a water purifier, tap water was collected from the laboratory, and pond water was collected from a nearby pond. All the samples were initially filtered through a membrane (0.45 μm pore size) and fluorescence intensity was measured by immersing the sensor in each sample. Then sensing efficacy was determined by spiking the procured water samples with Fe^{3+} and Cr^{6+} solutions. In all the cases, the sensor efficiently detected the quenching ions (Figure 5.9b). For further validation, interday (consecutive three days) and intraday (3 different times, at 8:00 am, 12:00 pm, and 8:00 pm) studies were performed and recovery and RSD were calculated in each case (Table 6.1). To further analyze the sensing capacity in real-life samples, sensing efficacy was determined using tannery wastewater which was collected from an adjacent canal connected to the tannery industry outlet. Elemental analysis of tannery wastewater was performed by ICP-OES and the data obtained depicts the presence of 20.9 ppm chromium and 4.62 ppm iron along with other impurities (Figure 6c inset). Fluorescence diminishes drastically along with a significant red shift of the emission maximum when the membrane is immersed in the wastewater and exposed to a 414 nm wavelength (Figure 5.9c). Thus this membrane can also be applicable for on-site sensing real-life wastewaters.

Table 5.1: Detection and sensing performance in various water samples

Water Type	Spiking ion	Interday (n=3)				Intraday (n'=3)			
		Added amount (μM)	Recovered amount (μM)	Recovery (%)	RSD (%)	Added amount (μM)	Recovered amount (μM)	Recovery (%)	RSD (%)
Distilled water	Cr^{6+}	6.80	6.89	101.32	0.30	6.80	7.11	104.56	0.12
		13.6	13.90	102.21	0.13	13.6	13.88	102.06	0.07
		20.40	19.60	96.08	0.13	20.40	19.89	97.50	0.20
	Fe^{3+}	10.00	11.01	110.10	0.27	10.00	10.81	108.10	0.14
		15.00	15.42	102.80	0.31	15.00	14.93	99.53	0.17
		20.00	19.22	96.10	0.15	20.00	19.50	97.50	0.29

Drinking water	Cr ⁶⁺	6.80	6.35	93.38	0.10	6.80	6.18	90.88	0.06
		13.60	14.14	103.97	0.35	13.60	14.78	108.68	0.19
		20.40	19.22	94.22	0.41	20.40	20.16	98.82	0.34
	Fe ³⁺	10.00	10.28	102.80	0.29	10.00	9.90	99.00	0.34
		15.00	14.16	94.40	0.13	15.00	14.70	98.00	0.18
		20.00	19.50	97.50	0.26	20.00	20.23	101.15	0.16
Tap water	Cr ⁶⁺	6.80	7.08	104.12	0.28	6.80	7.15	105.15	0.13
		13.60	13.02	95.74	0.20	13.60	12.97	95.37	0.24
		20.40	21.91	107.40	0.72	20.40	22.01	107.89	0.38
	Fe ³⁺	10.00	10.30	103.00	0.34	10.00	10.50	105.00	0.18
		15.00	14.10	94.00	0.31	15.00	13.98	93.20	0.16
		20.00	19.80	99.00	0.20	20.00	19.98	99.90	0.10
Pond water	Cr ⁶⁺	6.80	7.25	106.62	0.24	6.80	7.21	106.03	0.20
		13.60	13.92	102.35	0.31	13.60	14.30	105.15	0.33
		20.40	20.93	102.60	0.51	20.40	20.74	101.67	0.59
	Fe ³⁺	10.00	10.70	107.00	0.35	10.00	10.41	104.10	0.66
		15.00	14.20	94.67	0.30	15.00	14.45	96.33	0.41
		20.00	20.22	101.10	0.17	20.00	19.67	98.35	0.36

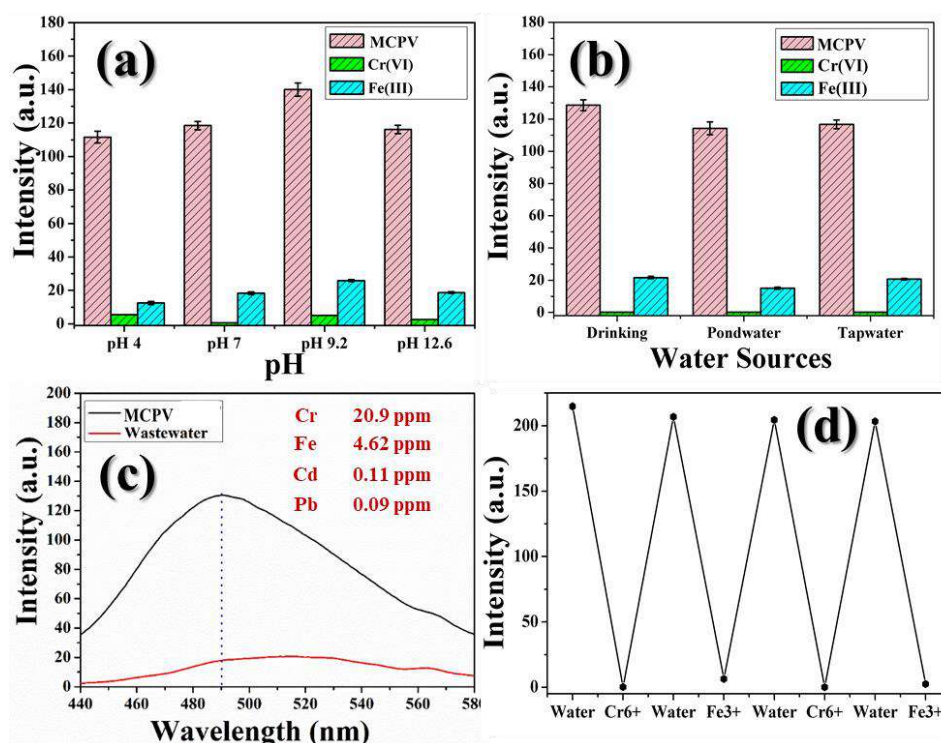


Figure 5.9: Sensing performances of the sensor upon Cr⁶⁺ and Fe³⁺ exposure at (a) different pH and (b) different water sources; (c) Fluorescence quenching observed using industrial wastewater and ICP-OES data of the collected tannery wastewater sample (inset); (d) Repetitive sensing using the same MCPV membrane illustrating its reusability

5.3.7.3 Sensing efficacy when used in a repetitive manner

Reusability without degradation in performance is an important factor for the commercialization of a synthesized sensor. Hence recycling capability was checked by alternatively immersing the sensor membrane into Millipore water, Cr^{6+} and Fe^{3+} solutions and measuring fluorescence at 414 nm excitation. Irrespective of several cycles of immersion, no significant alteration in its performance occurs and even after repetitive usage, the membrane retains its fluorescence property (Figure 5.9d).

5.3.8 Heavy metal induced early-stage carcinogen detection applications

The sensing capability of Cr^{6+} and Fe^{3+} in glutathione (GSH) solution was analyzed as glutathione (a non-thiol protein) is found in almost every living cell. It acts as an antioxidant that protects cells from reactive oxygen species (ROS) induced damage. Heavy metals like Cr^{6+} which is a potent carcinogen can initiate a Fenton-like reaction in presence of enzymes like glutathione and generate ROS like $\cdot\text{OH}$ radicals that can damage the nucleotide, leading to cancer development [24-25]. Even the presence of higher concentrations of Fe^{3+} can also initiate ROS formation in living cells [26]. Hence detection of Cr^{6+} and Fe^{3+} in glutathione can be beneficial for early-stage cancer detection.

Molecular docking was performed to theoretically study the interaction between the sensor and glutathione (PDB ID: 1PKW) [27]. Molecular docking is a technique that is used for the prediction of appropriate configurations to study various biomolecular interactions with a receptor [28]. This is a useful tool for studying the interaction between protein and ligand from the computer-generated 3-D structure of protein-ligand. It can predict the predominant binding modes and binding affinities. Autodock Tools v.1.5.6 is used to prepare the proteins and the ligands. PyMol v.2.0.7 program is used to identify and visualize the different binding pockets.

The lowest pose exhibiting binding affinity between fluorophore and glutathione to be $-6.7 \text{ kcal mol}^{-1}$ was considered among the nine different docked poses predicted by the molecular docking simulation (Figure 5.10a). Studies revealed that the $-\text{OH}$ moiety present in the fluorophore forms a weak polar hydrogen bond with the arginine sequence of glutathione, making a bond length of 2.3 \AA . Thus, the molecular docking results confirm the interaction between glutathione and fluorophores.

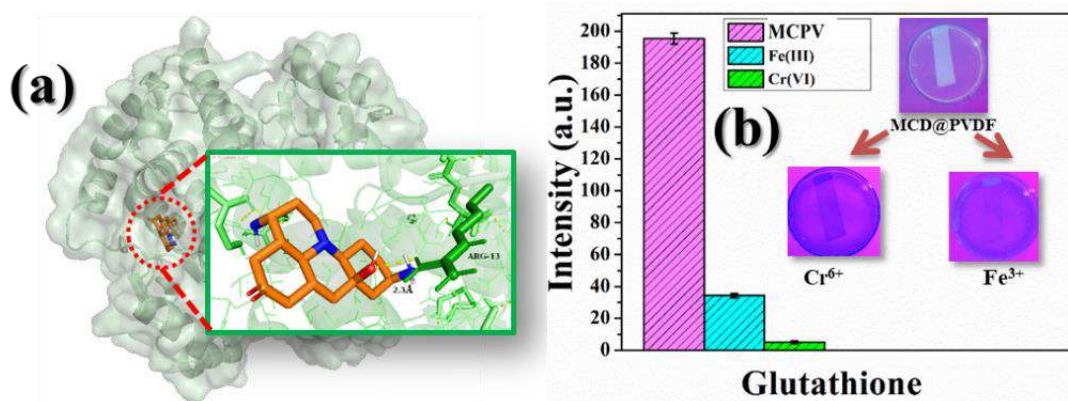


Figure 5.9: (a) Molecular docking simulation depicting interaction between fluorophore and glutathione; (b) Sensing of Cr^{6+} and Fe^{3+} in Glutathione solution and simultaneous naked eye observation under UV illumination

Table 5.2: Molecular docking results showing various poses between MCPV and glutathione

Pose	Binding affinity (kcal/mol)	Distance from best mode	
		rmsd l.b.	rmsd u.b.
1	-6.7	0.000	0.000
2	-6.6	22.598	24.234
3	-6.5	12.235	14.667
4	-6.4	22.994	24.442
5	-6.3	17.040	18.892
6	-6.1	16.616	17.722
7	-6.1	15.831	18.655
8	-6.0	32.202	35.025
9	-5.8	20.583	22.791

Experimental validation of Cr^{6+} and Fe^{3+} detection in glutathione was performed by immersing sensor membrane in glutathione solution which contained $500 \mu\text{M}$ glutathione dispersed in SBF solution. Initially, on irradiation at 414 nm , bright blue fluorescence was observed which drastically quenches when the solution was spiked separately with $50 \mu\text{M}$ Cr^{6+} and Fe^{3+} . Such phenomenon is also visible through naked eyes when exposed to a UV lamp (Figure 5.10b).

5.4 Summary

In this work, a flexible, durable, cost-effective, lightweight, portable fluorescent sensor membrane has been developed using natural microcline-carbon dot loaded PVDF-HFP polymer. The membrane can successfully detect the presence of Cr^{6+} and Fe^{3+} in water irrespective of the presence of other impurities. Moreover, low limits of detection and

excellent figures of merit, even in different water qualities and pH ranges make it a potential candidate for real-life applications. Even after repetitive usage and exposure to the ambient environment for a long duration, the membrane does not show any degradation in performance or mechanical damage. Furthermore, no tedious pre-treatment of water samples is required prior to experimentation and it is suitable for on-site sensing applications, thus cutting down treatment and storage costs. The membrane can also detect the presence of Cr^{6+} and Fe^{3+} in the glutathione environment, as validated theoretically and experimentally. Hence this sensor can also be beneficial in the future for heavy metal-induced early-stage cancer detection.

References

1. Patro, T.U., Mhalgi, M.V., Khakhar, D.V. and Misra, A., 2008. *Polymer* 49(16), 3486-3499.
2. Roy, S., Thakur, P., Hoque, N.A., Bagchi, B. and Das, S., 2016. *RSC Adv.* 6(26), 21881-21894.
3. Cai, X., Lei, T., Sun, D. and Lin, L., 2017. *RSC Adv.* 7(25), 15382-15389.
4. Mondal, P. and Purkait, M.K., 2017. *Polym. Test.* 61, 162-176.
5. Li, C., Liu, W., Sun, X., Pan, W., Yu, G. and Wang, J., 2018. *Sens. Actuators B: Chem.* 263, 1-9.
6. Sun, X. and Lei, Y., 2017. *TrAC, - Trends Analyt Chem.* 89, 163-180.
7. Pérez-Rodríguez, C., Martín, L.L., León-Luis, S.F., Martín, I.R., Kumar, K.K. and Jayasankar, C.K., 2014. *Sens. Actuators B: Chem.* 195, 324-331.
8. Fairman, H.S., Brill, M.H. and Hemmendinger, H., 1997. *Colour Society of Australia, Centre Français de la Couleur*, 22(1), 11-23.
9. Roy, S., Pal, K., Bardhan, S., Maity, S., Chanda, D.K., Ghosh, S., Karmakar, P. and Das, S., 2019. *Inorg. Chem.* 58(13), 8369-8378.
10. Kubista, M., Sjöback, R., Eriksson, S. and Albinsson, B., 1994. *Analyst* 119(3), pp.417-419.
11. Li, C., Liu, W., Sun, X., Pan, W., Yu, G. and Wang, J., 2018. *Sens. Actuators B: Chem.* 263, 1-9.
12. Sun, X. and Lei, Y., 2017. *TrAC, - Trends Analyt Chem.* 89, 163-180.
13. Pérez-Rodríguez, C., Martín, L.L., León-Luis, S.F., Martín, I.R., Kumar, K.K. and Jayasankar, C.K., 2014. *Sens. Actuators B: Chem.* 195, 324-331.
14. Fairman, H.S., Brill, M.H. and Hemmendinger, H., 1997. *Colour Society of Australia, Centre Français de la Couleur*, 22(1), 11-23.
15. Roy, S., Pal, K., Bardhan, S., Maity, S., Chanda, D.K., Ghosh, S., Karmakar, P. and Das, S., 2019. *Inorg. Chem.* 58(13), 8369-8378.
16. Kubista, M., Sjöback, R., Eriksson, S. and Albinsson, B., 1994. *Analyst* 119(3), pp.417-419.
17. Pajewska-Szmyt, M., Buszewski, B. and Gadzała-Kopciuch, R., 2020. *Mater. Chem. Phys.* 242, 122484.
18. Htun, T., 2004. A negative deviation from Stern–Volmer equation in fluorescence quenching. *Journal of fluorescence*, 14(2), pp.217-222.

19. Lakowicz, J.R., 1983. Quenching of fluorescence. Principles of fluorescence spectroscopy, pp.257-301.
20. Uhrovčík, J., 2014. Strategy for determination of LOD and LOQ values–Some basic aspects. Talanta, 119, pp.178-180.
21. Zu, F., Yan, F., Bai, Z., Xu, J., Wang, Y., Huang, Y. and Zhou, X., 2017. Microchim. Acta 184(7), 1899-1914.
22. Nugent, J.W., Lee, H., Reibenspies, J.H., Lee, H.S. and Hancock, R.D., 2017. Polyhedron 130, 47-57.
23. Mittal, M. and Sapra, S., 2017. ChemPhysChem 18(18), 2509-2516.
24. Grahn, E., Novotny, M., Jakobsson, E., Gustafsson, A., Grehn, L., Olin, B., Madsen, D., Wahlberg, M., Mannervik, B. and Kleywegt, G.J., 2006. Acta Crystallogr. Sect. D. Biol. Crystallogr. 62(2), 197-207.
25. Mazzer, P.A., Maurmann, L. and Bose, R.N., 2007. J. Inorg. Biochem. 101(1), 44-55.
26. Nakamura, T., Naguro, I. and Ichijo, H., 2019. Biochim Biophys Acta Gen Subj. 1863 (9), 1398-1409.
27. Ruzza, P. and Calderan, A., 2013. Pharmaceutics 5(2), 220-231.
28. Morris, G.M. and Lim-Wilby, M., 2008. Humana Press. 365-382



Chapter 6

Conclusion and perspective



Chapter 6

In the current scenario, heavy metal contamination and water pollution are one of the major ongoing crisis that requires immediate action. Despite the fact that numerous researches are performed to combat this issue, various drawbacks are faced in real-life applications. It is primarily important to detect heavy metal contaminants in order to deal with such pollution. Hence, several studies on nanomaterials for heavy metal detection dramatically increased in the past decade, yet their potential adverse effect deriving from the release, disposal, and leaching in the environment is a growing concern. Fluorescent sensors have gained enormous scientific interest in the modern era for investigating the dynamic transport and fate of heavy metals in the aquatic environment. Moreover, high specificity towards target organic and inorganic pollutants and the non-invasive nature of these techniques made them widely popular for the analysis of environmental pollutants. Synthesis of efficient and non-toxic sensing devices that have benefits like rapidness, robustness, simplicity, and efficiency of their quantitative assessment along with real-time monitoring adaptability has become a challenge to researchers. This thesis thus deals with size moderation/ carbon-dot loading into two widely available natural minerals due to their excellent biocompatibility, less toxicity, and cost-effectiveness due to high abundance in nature.

Initially, in *Chapter 1*, an overview of the present global and national scenario of heavy metal pollution has been illustrated. As the thesis reports about sensor synthesis from two selected silicate minerals (potassium aluminum silicate or microcline (KAlSi_3O_8) and aluminum silicate or kyanite (Al_2SiO_5)), the tools and techniques for the synthesis and characterization has been elucidated. Size fractionation of microcline and kyanite into two size-fractions, bulk (M1 and KY1) and nano-size (M2 and KY2).

In *Chapter 2*, the variation of structural, microstructural, optical, and electrical properties with the modification of size has been discussed. Since the work is based on natural minerals, proper characterization and determination of purity prior to experimentations is of utmost importance. The step-down synthesis method by mechanical ball-milling not only increases the surface to volume ratio but also enhances the oxygen vacancies and defect states which in turn have a huge influence on various physicochemical properties. Such change influences the fluorescence properties, as required for the development of the optical sensor. The dielectric permittivity values of bulk-sized microcline (M1) and kyanite (KY1)

at room temperature at 40 Hz were found to be 48.25 and 450.88, which remarkably increased to 7.8×10^4 and 8.2×10^3 respectively in finer fractions (M2 and KY2).

The primary focus of **Chapter 3** is the determination of biocompatibility and antibacterial efficacy of the mineral samples. An important aspect to be considered prior to the commercialization of a sensor is its biocompatible nature so that no secondary toxicity is produced. The MTT assay shows the survivability of more than 92 % of cells at a concentration of $800 \mu\text{g mL}^{-1}$ (median MIC value), thus confirming the non-toxic nature of the samples. Additionally, antibacterial efficacy was measured in order to determine whether the samples can also be useful to combat pathogenic pollution issues in the aquatic medium along with sensing applications. In the case of the nano-fractions (M2 and KY2), strong bacterial inhibition activity was observed on *E. coli* and *S. aureus*. Oxidative stress generation and morphological changes accompanied membrane leakage and blebbing was observed in the bacterial cells. Thus, the higher penetration capability of the finer fractions enhances the antibacterial efficacy.

In **Chapter 4**, the development of fluorescent sensors using the two finer fractions has been discussed. Fluorescent and non-toxic carbon dot (c dot) was loaded into the structure of both microcline (M2) and kyanite (KY2). While c dot-loaded kyanite (KYCD) only detects the presence of hexavalent chromium, c dot-loaded microcline (MCD) can simultaneously detect the presence of trivalent iron along with hexavalent chromium in aquatic medium. The detailed mechanism behind such “turn-off” sensing has been elucidated by density functional theory (DFT), which suggests the occurrence of photoinduced electron transfer (PET) based quenching of fluorescence in both the cases of MCD and KYCD. Since most of the reported sensors have limitations in performance under severe environmental conditions and real-life water samples in presence of multiple interfering ions, both MCD and KYCD showed immense stability and versatility irrespective of the water sample used. The unhindered performance and very low detection limits (LOD for Cr^{6+} and Fe^{3+} in case of MCD were estimated to be $4 \mu\text{M}$ and $19 \mu\text{M}$ respectively, while for KYCD, LOD for Cr^{6+} was calculated to be $0.11 \mu\text{M}$). The sensors can also efficiently detect the quenching metal ions in living cells.

Lastly, in **Chapter 5**, the fabrication of fluorometric sensing devices using dual-sensing MCD has been discussed. Since there is a chance of carbon dot leaching, fluorescence degradation with time, and other restricted functionalities, polymeric encapsulation of the nanocomposite (MCD) was done by wrapping MCD into the polymeric matrix of PVDF-HFP. This not only provided a flexible substrate for reusable use without wearing off but

also maintained the fluorescence stability for a longer duration, thus providing a longer lifetime and rigidity. Various analytical and statistical studies on an intraday-interday basis confirmed the accuracy of the sensor. Hence, an efficient and sensitive device for heavy metal sensing on-field is successfully designed using the most abundant mineral nanoparticles.

This thesis addresses new avenues for tackling environmental issues using materials extracted from the environment itself. Low cost, non-toxicity even in nano-regime, and abundance in nature is key point for these samples, which creates industrial feasibility. Processing cost is very low for natural samples lowers the cost of industrial production. Thus, one can argue that naturally formed nanoparticles could be one of the adverse fields in near future. Some of the future prospects are discussed below:-

- ❖ ***Antibacterial/ antimicrobial products:*** Since there is a very high demand for new antimicrobial materials that have low cost, non-toxic, have high antimicrobial activity and environmentally friendly characteristics, the efficient antibacterial nature in nano-regime, as determined in the study can be very useful for developing commercial products like antibacterial tiles and ceramics, antibacterial architectural coatings, different medical and dermatological products.
- ❖ ***Green nano-sensors:*** High stability, specificity, rapid response, and convenience in handling even in real-life samples make these materials a potential candidate for commercial and industrial purposes.
- ❖ ***Fabrication of fluorescent and antibacterial hand-held devices:*** The flexible and reusable can be used to develop hand-held electrical devices as the membrane shows high accuracy and does not require any pretreatment of water samples. This will cut down the treatment and storage costs associated with conventional heavy metal sensing devices.
- ❖ ***Heavy metal-induced early-stage cancer detection:*** The biological and biosensing assays and molecular docking studies substantiate the fact that the sensor can efficiently probe a true heavy metal-induced carcinogen sensor.



Thesis Publications



Nanoparticle Size-Dependent Antibacterial Activities in Natural Minerals

Souravi Bardhan¹, Kunal Pal², Shubham Roy¹, Solanky Das³, Abhijit Chakraborty⁴, Parimal Karmakar², Ruma Basu⁵, and Sukhen Das^{1,*}

¹Department of Physics, Jadavpur University, Kolkata 700032, India

²Department of Life Science and Biotechnology, Jadavpur University, Kolkata 700032, India

³Department of Geology, Jadavpur University, Kolkata 700032, India

⁴Department of Geology, Jogamaya Devi College, Kolkata 700026, India

⁵Department of Physics, Jogamaya Devi College, Kolkata 700026, India

The size-dependent antibacterial activities of three minerals namely; alkali feldspar, calcite and stibnite are reported as examined individually against *Escherichia coli* and *Staphylococcus aureus* by evaluating minimum inhibitory concentration (MIC) with colony counting method, along with cell survivability assay (MTT). Each of these minerals were grinded into fine-size fractions—S1 (bulk), S2 (ball milled) and S3 (nanosized) and spectroscopically characterized using X-ray diffraction (XRD), field emission scanning electron microscopy (FESEM) and ultraviolet-visible (UV-Vis) spectroscopy. Antibacterial activity was found to be highest in the nanosized (S3) minerals. Interaction between bacteria and nanosized mineral samples produce intracellular reactive oxygen species (ROS), which might cause higher bacterial mortality. The penetration due to nano-dimension is another significant observation as evidenced by bacterial FESEM micrographs. The current findings thus provide a pathway for future research on antibacterial products retrievable from widely available geological materials. The size dependant antibacterial activity of naturally formed minerals is a new insight to reduce bacterial contamination in living systems.

Keywords: Nanoparticles, Bacteria-Mineral Interaction, MIC, ROS, FESEM.

1. INTRODUCTION

Minerals are essential natural resources that have huge impact on human health and have been used for medical and other purposes for thousands of year.¹ By linking the naturally available materials with biomedical aspects, the researchers and geoscientists are attempting to discover ways of mitigating environmental health problems.² The recognition of an intimate relationship between the environment, particularly geological materials and human health has led to the emergence of a new field of science called medical geology,³ which deals with the relationship between geological materials such as rocks and minerals, with the health problems in humans, animals and plants.^{3,4} New products are now developed from minerals due to their bacteriological properties, such as in minerals like Talc, Halloysite, Sericite^{5,6} which are used in different medical and dermatological products. Antibacterial tiles

and ceramics, antibacterial architectural coatings, etc. can also be made from commonly occurring minerals.^{7,8} This is leading to the emergence of geomicrobiology which is an emerging frontier of interdisciplinary science.

The science of geomicrobiology focuses mainly on the studies of mineral-microbe interactions and their applications⁹ since minerals and rocks are the most fundamental earth materials with which microbes interact at all scales, from macroscopic to microscopic.¹⁰⁻¹² Many rocks and minerals contain the essential nutrients and energy required for microbial growth, and microbes actively extract nutrients from solid materials to sustain their metabolism and growth.¹³ The modern era is giving emphasis on researches on novel, active and eco friendly antibacterial reagents,¹⁴ as microbes are developing increasing resistance to multiple antibiotics. Thus demand of low cost, non-toxic natural antibacterial products have increased^{15,16} beside various well known metal and metal oxide nanoparticles, such as CuO, ZnO, Ag⁺, etc.¹⁷⁻²²

*Author to whom correspondence should be addressed.

Our study specifically focuses to this diversifying field. The present experiment emphasizes on the effect of three naturally available minerals, namely alkali feldspar (KAlSi_3O_8), calcite (CaCO_3) and stibnite (Sb_2S_3) on growth of both gram negative and gram positive bacteria, namely, *Escherichia coli* (*E. coli*) and *Staphylococcus aureus* (*S. aureus*) respectively, with special emphasize on size. The samples have been characterized employing XRD, FESEM, EDX and UV-Vis spectroscopy. Antibacterial efficacy as a function of three distinct size ranges for the three naturally formed minerals have been determined by using the traditional MIC and MBC technique, while bacterial cell mortality has been investigated using MTT assay. Our investigation shows that the nano-sized mineral samples play more detrimental role against the bacterial species, which was further confirmed by the generation of chemically formed ROS and the physical damage caused by bacteria and sample interaction. The efficacy of nano-sized minerals further proves that the naturally derived products can act as remarkable antibacterial agents, the efficiency of which could be tuned by tuning its size. This “size-tuned” antibacterial property of naturally formed mineral samples is a new age technology to combat pathogenic bacterial contaminations.

2. EXPERIMENTAL DETAILS

2.1. Materials

The minerals (alkali feldspar, calcite and stibnite) were purchased in bulk form without any impurities from Hindustan Minerals, Kolkata. Thiazolyl blue formazan (MTT) and 2',7'-dichlorofluorescein diacetate (DCFDA) were purchased from Sigma-Aldrich. Phosphate buffer saline (PBS), Luria–Bertani (LB) was obtained from HiMedia Pvt. Ltd., India, ethanol and glutaraldehyde from Merck, India. *Escherichia coli* DH5 α (MTCC-1652) and *Staphylococcus aureus* (MTCC 25923) were obtained from Institute of Microbial Technology, Chandigarh, India. All the chemicals used were of analytical grade and used without further purification. Throughout the experiment Millipore water (resistivity $\approx 18 \Omega \cdot \text{cm}$) was used.

2.2. Particle Size Fractionation

The minerals were washed thrice with distilled water and comminuted using mortar and pestle. The grinded samples were sieved below 400 mesh (0.037 mm) and was marked as S1 fraction (coarse). A portion of bulk samples were further crushed using Fritsch Planetary Mono Mill Pulverisette 6. Grinding was carried out at 300 rpm in room temperature for 12 hours with ball to mass ratio of 20:1, using Tungsten Carbide vials and balls and marked as S2 fractions. In order to obtain finer fraction (S3), a portion of ball milled samples were dispersed in acetone and ultra-sonicated for 6 hr with 15 min step duration. After a series of ultra-sonication, the supernatant were dried and

collected. All the mineral fractions were sterilized by autoclaving at 121 °C for 1 h prior to performing the antimicrobial assays.

2.3. Physical Characterization of Minerals

Sample purity and crystallite size was determined by X-ray powder diffractometer (model-D8, Bruker AXS, Winconsin, USA), using Cu-K α target employing wavelength of 1.5418 Å and operating at 35 kV and 35 mA with scan speed of 1 sec/step. Surface morphology and distribution in grain size of the powdered mineral samples were investigated by field emission scanning electron microscope using (FEI, INSPECT F50, Netherlands).

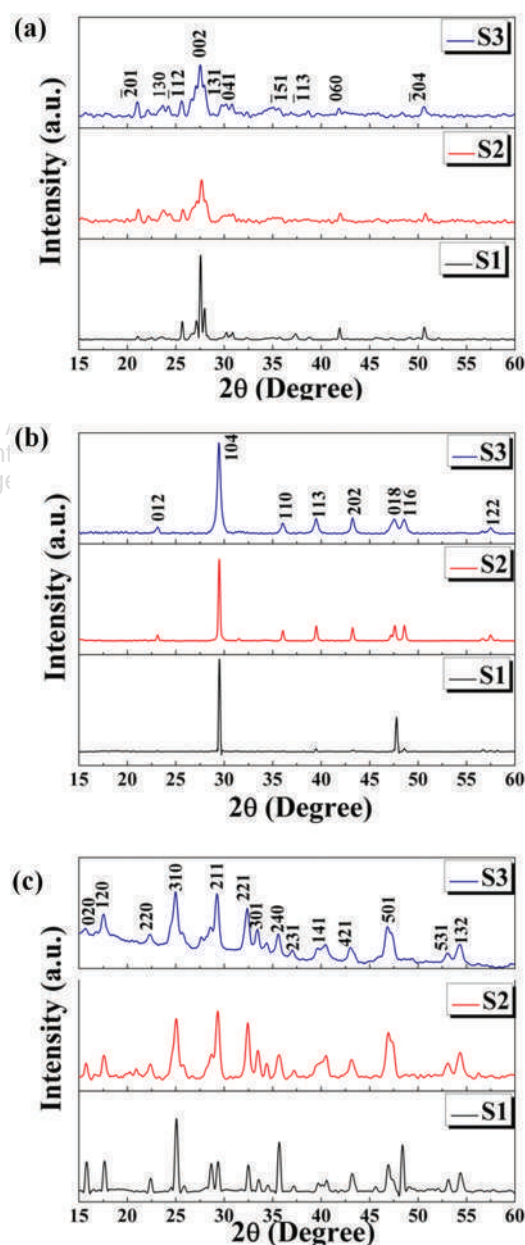


Figure 1. XRD pattern of the minerals—(a) Alkali feldspar; (b) calcite and (c) stibnite in three size fractions S1, S2 and S3.

Table I. Full width at half maximum (FWHM) values of samples calculated from XRD data.

Materials	FWHM ($\times 10^{-3}$ rad)		
	S1	S2	S3
Alkali feldspar	3.30	3.43	5.03
Calcite	3.40	3.79	6.66
Stibnite	4.81	6.85	7.42

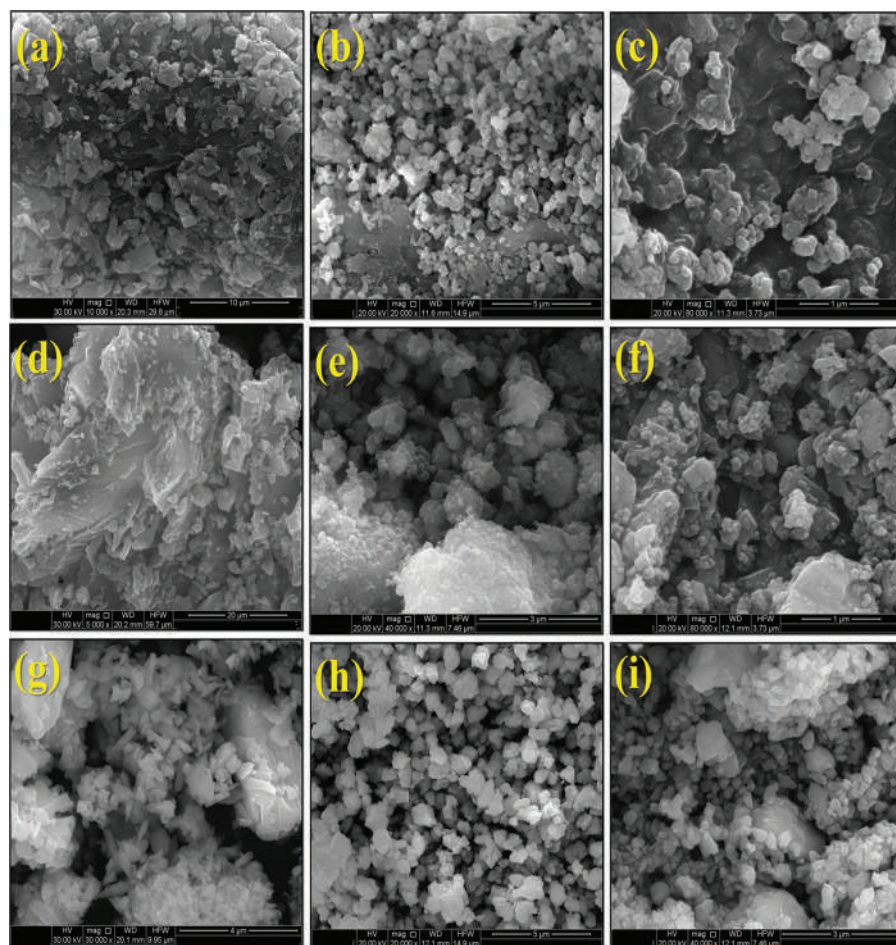
In order to determine the elemental composition and purity of the bulk samples EDX analysis was performed. Minute amount of powdered samples were directly placed on the carbon coated grid, sputter coated with gold and then observed under the microscope. The absorption spectra of the dispersed samples were recorded in Perkin Elmer Lambda-365 UV-Vis Spectrometer using a concentration of 1 mg/ml.

2.3.1. Bacterial Viability Assay and Biological Characterizations

The antibacterial activity of the mineral fractions was evaluated by determining the minimum inhibitory

concentrations (MICs) in Luria Broth (LB) medium using *Escherichia coli* DH5 α and *Staphylococcus aureus*. MIC is defined as the lowest concentration of antibacterial agent that inhibits visible growth of microorganisms.²³ *E. coli* is a common bacterium in the lower intestine of warm-blooded animals.²⁴ Most *E. coli* strains are harmless, but some, such as serotype O157:H7, can cause serious food poisoning in humans.^{25,26} On the other hand *Staphylococcus aureus* is the most common cause of staph infection in human.⁵ It is a spherical bacterium, commonly found on the skin or in the nose, but it may also infect soft tissue, respiratory organs, bones, joints, endovascular system, and wounds.²⁷

Bacterial strains were grown overnight and adjusted to the 0.5 McFarland standards in each case, which approximately is comparable to bacterial suspension of 1.5×10^8 CFU/mL.²⁸ To check the inhibitory values, colony counting method has been adopted after spreading the treated and untreated (control) bacterial samples on agar plates. For colony-counting experiments, 100 μ l from each tube were spread on a plate of LB, nutrient containing 2% agar. The agar plates were then kept for incubation at 37 °C and examined after 24 hr for documenting the

**Figure 2.** FESEM micrographs of alkali feldspar (a–c), calcite (d–f) and stibnite (g–i).

colonies formed. All the experiments were triplicated to obtain the standard error. The antibacterial effect is calculated using the equation:²⁹

$$M (\%) = \frac{(B - C)}{B} \times 100 \quad (1)$$

Where, M is the mortality rate (%), B is the mean number of bacteria in the control samples (CFU/ml), where CFU is the colony forming unit, and C is the mean number of bacteria on the treated samples (CFU/ml).

Bacterial viability assay was performed using MTT [3(4,5-dimethylthiazol-2-yl)-2,5-diphenyl tetrazolium bromide] assay.³⁰ Fresh broth was inoculated from freshly prepared well grown culture at mid log phase (approximately 10^4 CFU/ml) and was treated with $800 \mu\text{g/ml}$ sample and was then allowed to grow at temperature 37°C for 4 hrs. The bacterial cells were then washed and suspended in PBS buffer. MTT stock (5 mg/ml) was added and the cells were incubated for 1 hr.³¹ The intracellular formazan formed during incubation was dissolved in $500 \mu\text{l}$ DMSO and the intensity of the formazan produced was measured spectrophotometrically at 570 nm in Biotek 96 well plate

reader. The percentage bacterial viability was calculated using the following equation:³²

$$\text{Cell survivality (\%)} = \frac{(A_t - A_b)}{(A_c - A_b)} \times 100 \quad (2)$$

Where, A_t is the absorbance value of sample, A_c is the absorbance value of control, and A_b is the absorbance value of blank (0.042).

In order to compare the ability of induction of intracellular oxidation and superoxide formation of different minerals in different size ranges, the oxidative stress in the bacterial cells were detected using reactive oxidative species (ROS) assay. Certain agents or compounds can cause oxidative stress³³ which arises when the concentration of active oxygen increases to a level above the cell's defence capacity.³⁴ ROS generation was measured according to Su et al.³⁵ A fluorescent dye 2',7'-dichlorofluorescein diacetate (DCFHDA) was used as an indicator of ROS generation. Fresh broth of 5 ml was inoculated with approximately 10^4 CFU/ml, and treated with $800 \mu\text{g/ml}$ sample, while the untreated sample was kept as control. The cultures were then allowed to grow at 37°C for 1 hr. $10 \mu\text{M}$ DCFHDA was then added

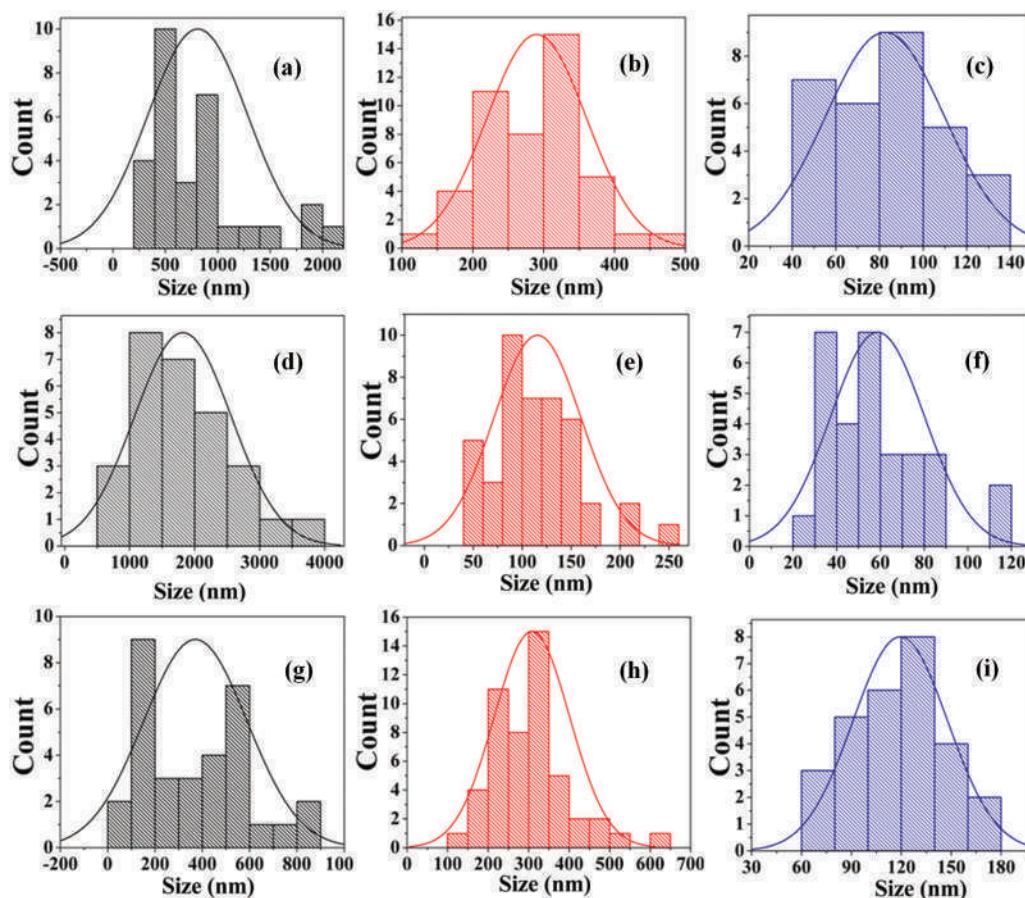


Figure 3. Size distribution curves showing modal particle size of alkali feldspar (a–c), calcite (d–f) and stibnite (g–i) (size data obtained from FESEM).

to bacterial cell suspension and incubated for 30 min in dark condition. The fluorescence spectrophotometer (BIOTEK) with an excitation at 504 nm and the emission at 529 nm was used to evaluate the level of intracellular ROS, which is proportional to the intensity of fluorescence activity.

FESEM analysis of the bacterial samples was executed to understand the physical interaction and the extent of damage caused on bacterial cell morphology by the minerals at different sizes (S1, S2 and S3). The sample preparation was performed according to Ansari et al.³⁶ 1 ml of treated cells, along with control was taken after 6 hrs of incubation and was centrifuged (4000 RPM, 4 min) to collect the pellet. The pellets were washed thrice with sterile filtered PBS containing 2% glutaraldehyde and were dehydrated using serial dilution of ethanol. The cells were then drop casted on cover slips and dried under laminar air flow and were placed on carbon tape and sputter coated with gold for FESEM analysis (FEI, INSPECT F50, Netherlands).

3. RESULTS AND DISCUSSION

3.1. Structural Studies of the Samples

XRD is an efficient characterization technique that can quantify and detect crystallite phases and impurities present in the crystal. The XRD pattern of all the mineral samples in three size fractions (S1, S2, S3) were recorded using powder X-ray diffractometer from 15°–60° (Figs. 1(a–c)). The diffraction patterns of alkali feldspar samples were matched with Joint Committee on Powder Diffraction Standards (JCPDS) card no. 19-0931, diffraction pattern of calcite samples were well matched with JCPDS card no. 24-0027 and stibnite samples show a good agreement with JCPDS card no. 06-0474, which is an indicator of purity of our mineral samples. Full Width at Half Maxima (FWHM) of the most intense peak of all the samples were calculated and depicted in Table I. The XRD patterns indicate high purity of samples evident from the absence of unwanted peaks. The S1 samples of each mineral shows sharp diffraction patterns that indicates higher crystallinity in these samples.³⁷ The higher values of FWHM and simultaneous broadening of peak in case of S2 and S3 samples respectively suggests the reduction in nanocrystallite sizes.^{38, 39}

3.2. Morphological and Elemental Analyses

FESEM analysis was employed to determine the size and particle morphology of the samples. The particle size of bulk samples was found to be coarsest, whereas, ball milled and fine samples are relatively finer. In fact, all the fine samples are in nano-regime which has been confirmed and verified with the help of XRD and FESEM analysis. FESEM micrographs (Figs. 2(a–i)) show that, in all the three minerals, the particle size of S1 fraction is distinctly large, while the S2 and S3 fractions are

successively finer. Stibnite has a spindle shaped structure in bulk form, while alkali feldspar and calcite particles are more equant. It is evident from FESEM micrographs that, the particles are the aggregates of constituent smaller particles and the minimum size is achieved in S3 fraction for all the samples. The modal grain sizes of all the samples were calculated taking around 50 grains counted per samples that are depicted in Figures 3(a)–(i). Due to ball milling, individual particles of the bulk samples (S1) acquire a more rounded shape in S2 fraction. S3 samples are largely agglomerated due to greater surface to volume ratio. High surface to volume ratio of smaller particles provides a very high surface energy. To minimize its surface energy the particles create agglomeration,^{40, 41} which is significant in S3 samples. These agglomerates were made to disperse in water using bath sonication prior to their application in bacterial assay. Other than size, grain morphology of the mineral samples can also induce bacterial cell rupture. For example, our stibnite sample attains

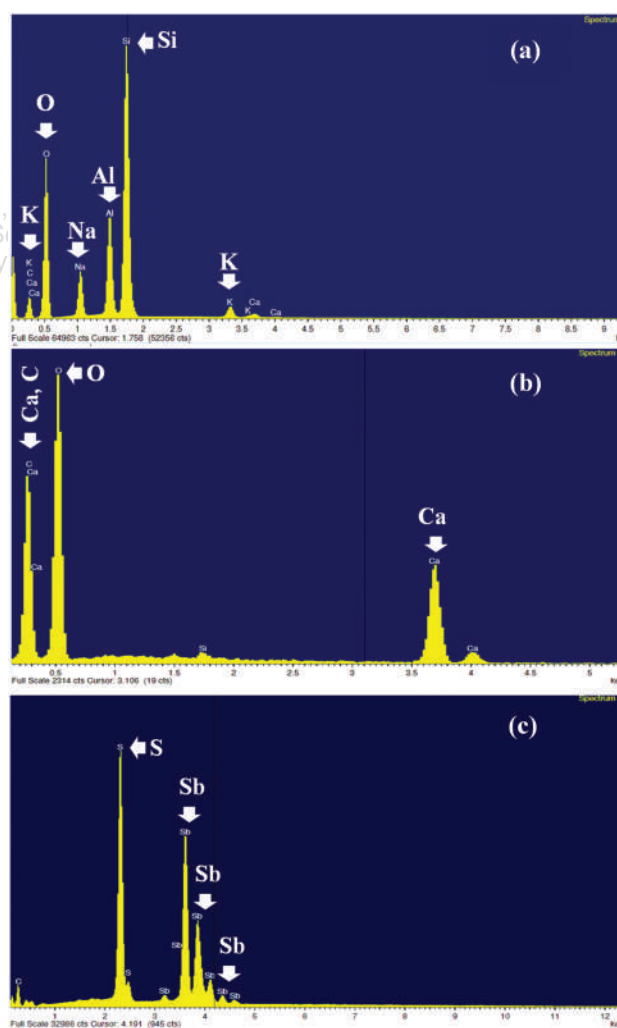


Figure 4. EDX images of (a) alkali feldspar; (b) calcite and (c) stibnite, showing their purity.

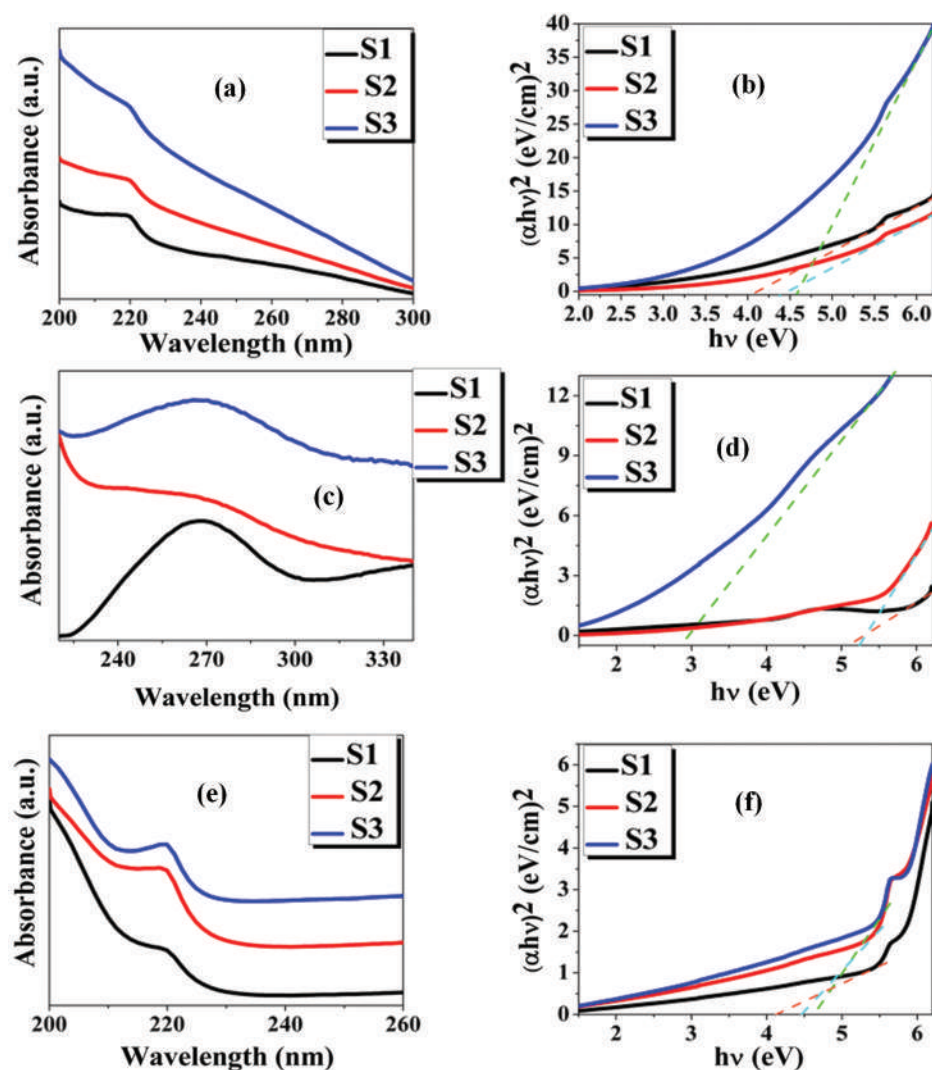


Figure 5. Absorbance spectra of alkali feldspar (a), calcite (c) and stibnite (e) as detected from UV-Vis spectroscopy. The optical band gaps of alkali feldspar (b), calcite (d) and stibnite (f) in S1, S2 and S3 size fractions obtained from Tauc plots.

a sharp edged spindle shape in bulk fraction (S1), which perhaps led to the enhanced membrane puncture resulting in high mortality rate in the treated bacteria, even in the S1 fraction.

In order to identify the constituents of our samples, we have employed EDX analysis. EDX spectra (Fig. 4) confirmed the presence of potassium, aluminum, oxygen, sodium, calcium and silicon in our alkali feldspar sample, whereas, our calcite sample has calcium, carbon and oxygen with a minute amount of silicon as impurity. Our stibnite sample is composed of sulfur and antimony, which confirms its purity. Thus, it can be argued that, all the samples are of pure grade with no such impure phases of any other foreign element.

3.3. Spectroscopic Studies

The optical absorption spectra of the minerals show peak broadening and a slight blue shift for S2 and S3 samples

(Figs. 5(a, c, e)). Band gap energies of the samples were calculated using the following formula:³⁷

$$\alpha E = A(E - E_g)^n \quad (3)$$

Table II. MIC values of mineral samples for *E. coli* and *S. aureus*.

Materials	<i>E. coli</i>	<i>S. aureus</i>
	MIC (mg/ml)	MIC(mg/ml)
Alkali feldspar		
S1	2.0	1.2
S2	1.2	0.8
S3	0.8	0.8
Calcite		
S1	2.0	1.0
S2	1.2	0.8
S3	0.6	0.6
Stibnite		
S1	1.0	0.8
S2	0.8	0.6
S3	0.6	0.4

Where E and E_g are the photon energy and the optical band gap energy, in electron volt (eV) respectively. Other two terms α and A are the absorption coefficient and a constant term, respectively. In Tauc plot, $(\alpha h\nu)^2$ is plotted against photon energy ($h\nu$) and the band gap energy was calculated by extrapolating the linear region and intersecting the linear portion of the curve to the energy axis have been shown in Figures 5(b), (d), (f). For alkali feldspar, the optical band gap varies from 4.05 eV (S1) to 4.61 eV (S3). The stibnite samples show the same trend. For stibnite S1 sample, the band gap is 1.63 eV and that is 1.97 eV for S3 sample. Thus, finer particles show higher band gap values from Tauc plot. The same observation has been reported

by Versavel and Haber.⁴² Calcite samples show a different trend in Tauc plot. The optical band gap increases with increasing particle size. For S1 sample it is 5.36 eV and 2.31 eV for S3.⁴³ The band gap values found to decrease with increasing particle size. Smaller particle contributes to a very small number of atoms, which reduces the number of overlapping orbitals. Thus, the width of the energy level gets narrower, creating wider band gap.

3.4. Antibacterial Assay

The effect of different minerals at varied concentrations and different sizes are determined using MIC (Table II) by employing colony counting method. The mortality rate

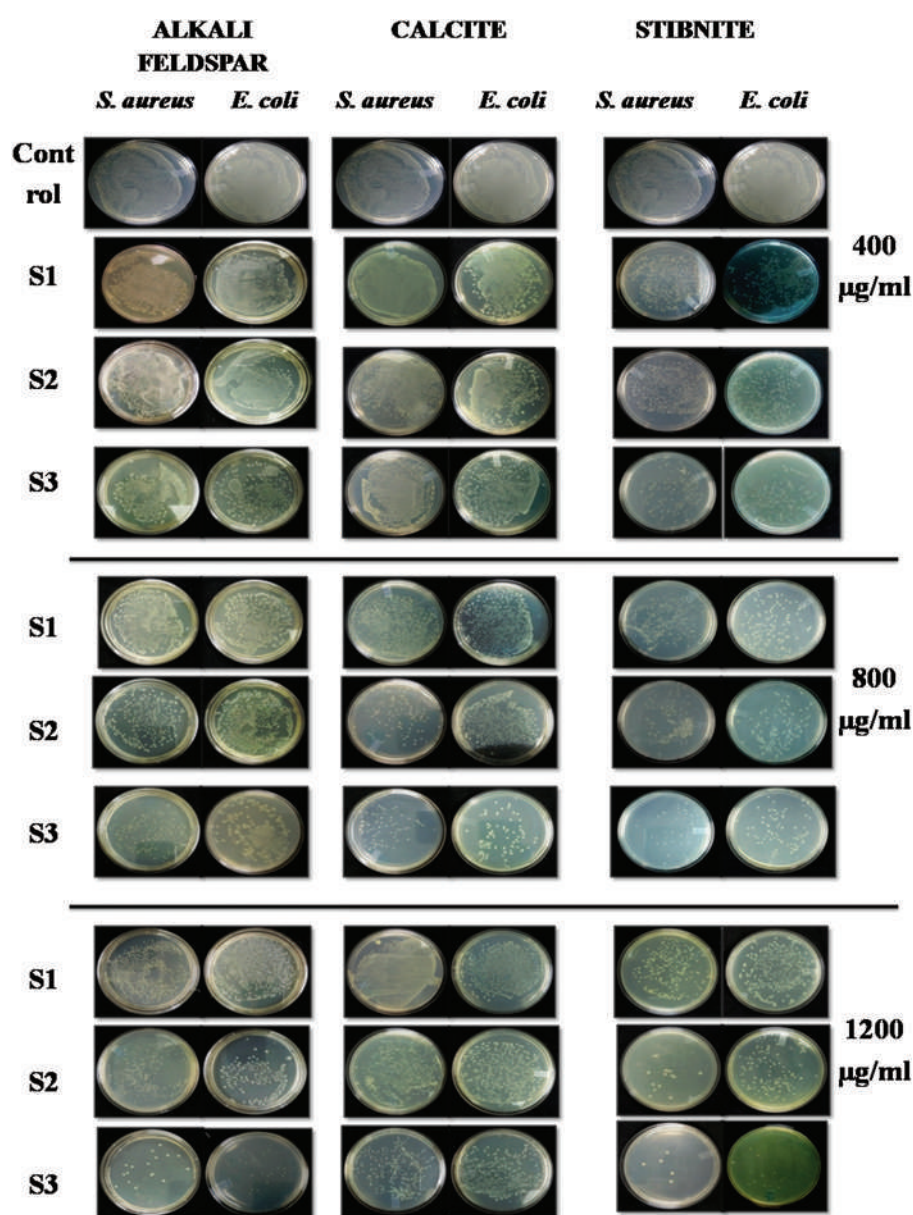


Figure 6. Plate count images showing visual display of the surviving colonies on agar plates of alkali feldspar, calcite and stibnite after 24 h of incubation at different concentrations (400, 800 and 1200 µg/ml respectively) with respect to control plates.

of the gram negative bacteria *Escherichia coli* DH5 α are slightly lower than those of the gram positive bacteria *Staphylococcus aureus* (Fig. 7). The result shows that the antibacterial effect of stibnite is more pronounced compared to the other two minerals for both the bacterial strains. Moreover, stibnite was found to be lethal even at lower concentration, especially in case of *Staphylococcus aureus*. Alkali feldspar and calcite were both found to have antibacterial effect on *Staphylococcus aureus* and *Escherichia coli* DH5 α in the S2 and S3 fraction. The S1 samples showed feeble or no antibacterial effect as detected from little deviation in MIC of the control. On the contrary, a sharp decrease in bacterial growth is observed in the finer fraction. The antibacterial effects of all the samples were detectable from the colony count from agar

plates. The comparative analysis of residual colony count (CFU/ml) is illustrated in Figure 6. The agar plates for the concentration 400, 800 and 1200 $\mu\text{g/ml}$, along with control samples has been depicted in Figure 6. The MIC data obtained from colony study shows that there is a considerable increase in cell death and growth inhibition with increase in concentration, especially in case of stibnite samples. The bacterial growth inhibition is evident for both the bacterial strains which testify the significant bacteriostatic effect of the finer samples. Even in the case of alkali feldspar and calcite, a detectable antibacterial effect is perceived in the finer fraction with increase in concentration, while their bulk fraction does not show much deviation from control plates. Hence size reduction below a critical value does play a significant role

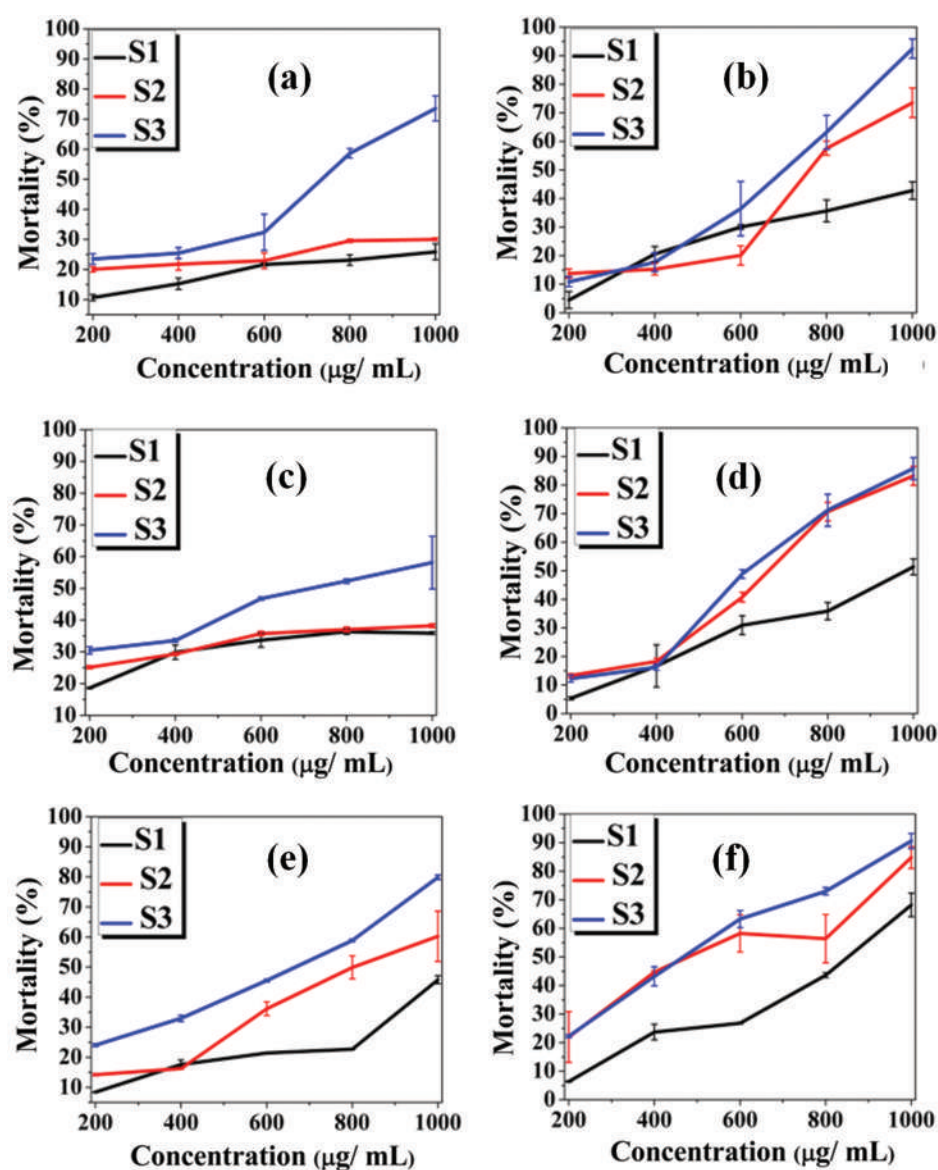


Figure 7. Mortality % calculated from plate counting (MIC) of alkali feldspar (a, b), calcite (c, d) and stibnite (e, f) for *E. coli* and *S. aureus* respectively. Error bars represent standard deviation of mean from three replicates.

in antibacterial efficacy in spite of being non toxic in lump.

3.5. Bacterial Viability Studies

The viability assay (MTT) of bacterial cells was performed at 800 $\mu\text{g/ml}$, and the decrease in absorbance with decrease in size clearly shows that for both the bacterial strains S1 samples show more formazan formation indicating high viability,³⁰ compared to other two fractions. Bacterial viability is represented in the Figures 8(a), (b). Stibnite is found to be antibacterial even in the S1 fraction. The OD value of blank was found to be 0.042. The content of ROS has significantly increased in case of the finer fraction, especially in the case of stibnite sample, which is simultaneously accompanied by decrease in cell viability, as seen in MTT assay. The MTT (3-(4,5-dimethylthiazol-2-yl)-2,5-diphenyl tetrazolium bromide) assay is a colorimetric assay for determining the cell metabolic activity which in turn is an indication of cell viability. MTT is a yellow colored tetrazolium salt that is converted into a blue formazan by NAD(P)H dependent cellular oxidoreductase enzymes largely in the cytosolic compartment of a viable cell. The assay is dependent on the principle that the amount of formazan produced is directly proportional to the number of live cells.

3.6. Mechanisms of Bacterial Growth Inhibition

3.6.1. Oxidative Stress Generation

The oxidative stress of the minerals along with control is represented in Figures 8(c), (d). The intracellular ROS

production has a sharp increase in finer samples, especially in finer fraction of stibnite, whereas it is much less in the coarse fraction (S1). A gradual increase in ROS production in case of S2 and S3 samples for all the minerals have been observed which indicates the higher degree of oxidative stress as well as superoxide production in bacterial cells that might be the plausible augmentation for cell mortality. The finer fraction can easily reach the nuclear content of bacteria by physically disrupting and penetrating through the cell envelope, or may interrupt trans-membrane electron transfer.⁴⁴⁻⁴⁶ They may also oxidize cell components, or produce secondary products like ROS that may cause damage to the cells.³¹ ROS generation is an important factor which may enhance the antimicrobial capacity since the free radicals, such as superoxide anion radical (O_2^-), hydrogen peroxide (H_2O_2), and reactive hydroxyl radicals ($\cdot\text{OH}$) have an inherent property for attacking polyunsaturated fatty acids in membranes, thus initiating lipid peroxidation. Lipid peroxidation mainly results in decreasing membrane fluidity, thus resulting in alteration of membrane properties that disrupt membrane-bound proteins. The ROS then targets DNA, RNA, proteins and lipids, thus initiating lipid peroxidation and further leading to membrane disruption.³⁴ The nano grade mineral samples may interfere with the normal functioning of bacterial intracellular proteins and enzymes by binding with proteins, DNA molecules and with enzymes such as nicotinamide adenine dinucleotide dehydrogenase (NADH), thus inducing oxidative stress.⁴⁷

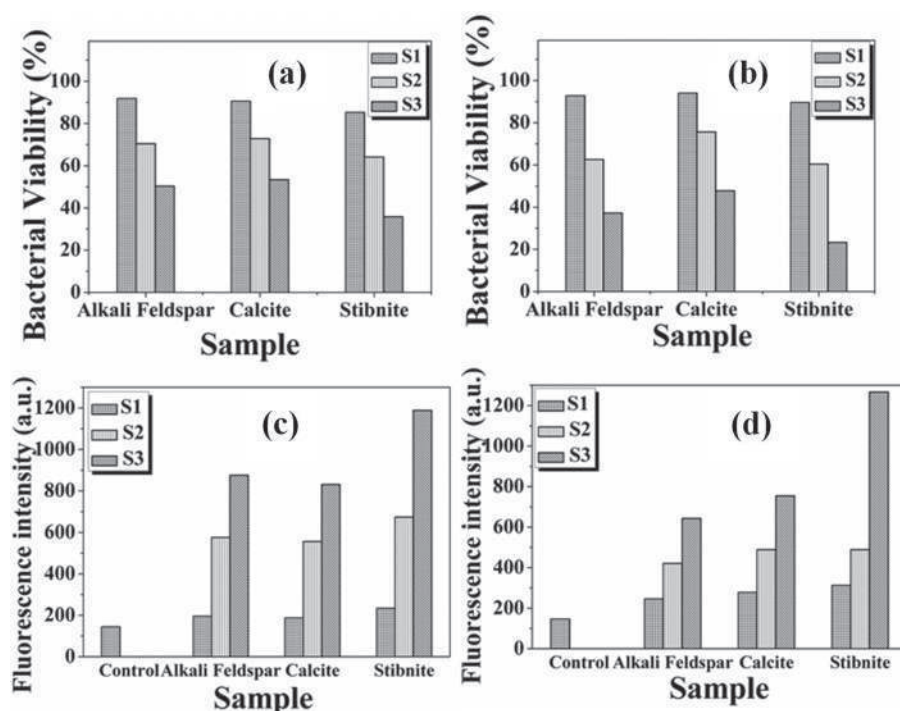


Figure 8. MTT assay depicting decreasing bacterial cell viability for (a) *E. coli* and (b) *S. aureus* in finer size fractions; Size dependant enhancement of intracellular ROS generation in successive finer size fractions as measured from fluorescence intensity of DCFHDA for (c) *E. coli* and (d) *S. aureus*.

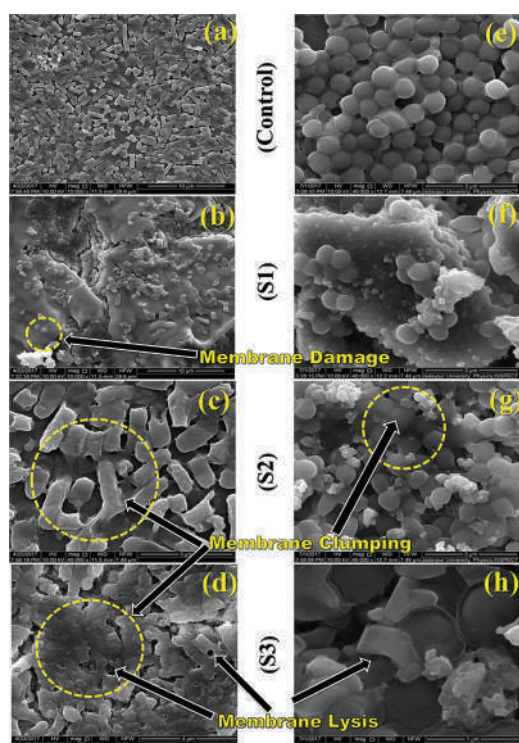


Figure 9. FESEM micrographs of *E. coli* (a–d) and *S. aureus* (e–h) depicting increased membrane disruption in successive finer size fractions in comparison to control.

3.6.2. Results of Physical Interaction of Samples and Bacteria

The bacterial FESEM analysis further revealed that the treated cells showed membrane disruption and perforations, causing rupture of cytoplasmic material with particle penetration whereas the control shows healthy live cells having distinct rod shaped morphology of *E. coli* (Figs. 9(a–d)) and intact spherical morphology of *S. aureus* (Figs. 9(e–h)). The FESEM micrographs (Fig. 9) confirmed that there is an enhanced permeability of cell membrane with the subsequent elevation of ROS generation with the reduction of particle size. Both membrane damage and ROS mediated DNA damage might have synergistically aggravated the antibacterial activity, especially in nano grade.

4. CONCLUSION

A size dependent antibacterial property is envisaged for some natural minerals namely stibnite, alkali feldspar and calcite. The decrease in particle size, particularly in the threshold of nanoscale enables their greater prohibitory interaction with bacteria. Mineral specific variations in antibacterial activities are discernible for the studied minerals, as well as, with the varying concentrations of minerals in which they are introduced. However, the particle size remains the predominant and constant factor. Our present study indicates that the physical rupture of bacterial cell

membranes and coincidental increase in ROS production in the threshold of nanoparticle fractions for all the studied minerals have mediated the bacterial cell death.

Conflicts of Interest

Authors have no conflict to declare.

Acknowledgments: We are grateful to the Department of Physics, and the Department of Life Science and Biotechnology, Jadavpur and Jogomaya Devi College for extending experimental facilities.

References and Notes

- G. M. Gadd, *Microbiology (Microbiology Society)* 156, 609 (2010).
- O. Selinus, *Medical geology: Method, theory and practice, Geo-environmental Mapping: Methods, Theory and Practice*, edited by P. T. Bobrowsky and A. A. Balkema (2002), pp. 473–496.
- C. A. Bowman, P. T. Bobrowsky, and O. Selinus, *Episodes* 26, 270 (2003).
- R. B. Finkelman, H. C. W. Skinner, G. S. Plumlee, and J. E. Bunnell, *Geotimes* 20, 3 (2001).
- S. K. Park, C. W. Lee, and M. Y. Lee, *J. Environ. Biol.* 30, 151 (2009).
- E. Joussein, S. Petit, J. Churchman, B. Theng, D. Righi, and B. Delvaux, *Clay Miner.* 40, 383 (2005).
- M. I. Carretero, *Appl. Clay Sci.* 21, 155 (2002).
- P. Sultana, S. Das, B. Bagchi, A. Bhattacharya, R. Basu, and P. Nandy, *Bull. Mater. Sci.* 34, 1663 (2012).
- H. Dong and A. Lu, *Elements* 8, 95 (2012).
- H. Dong, *Front. Earth Sci.* 4, 127 (2010).
- J. F. Banfield and K. H. Nealson, *Geomicrobiology: Interactions between microbes and minerals*, Rev. Mineral Geochem., Mineralogical Society of America, Washington, DC (1997), Vol. 35.
- K. O. Konhauser, *Introduction to Geomicrobiology*, Blackwell Publishing, Oxford (2007), p. 425.
- S. Uroz, C. Calvaruso, M. P. Turpault, and P. Frey-Klett, *Trends Microbiol.* 17, 378 (2009).
- J. A. Centeno, R. B. Finkelman, and O. Selinus, *Geosciences* 6, 8 (2016).
- C. de S. F. Gomes and J. B. P. Silva, *Appl. Clay Sci.* 36, 4 (2007).
- J. R. Lloyd, C. I. Pearce, V. S. Coker, R. A. D. P. Patrick, G. van der Laan, R. Cutting, D. J. Vaughan, M. Paterson-Beedle, I. P. Mikheenko, P. Yong, and L. E. Macaskie, *Geobiology* 6, 285 (2008).
- K. P. Miller, L. Wang, B. C. Benicewicz, and A. W. Decho, *Chem. Soc. Rev.* 44, 7787 (2015).
- G. Ren, D. Hu, W. Eileen, C. Cheng, A. Migue, V. Reus, P. Reip, and R. P. Allaker, *Int. J. Antimicrob. Agents* 33, 587 (2009).
- A. Sirelkhatim, S. Mahmud, A. Seeni, N. H. M. Kaus, L. C. Ann, S. K. M. Bakhori, H. Hasan, and D. Mohamad, *Nano-Micro Lett.* 7, 219 (2015).
- P. K. Stoimenov, R. L. Klinger, G. L. Marchin, and K. J. Klabunde, *Langmuir* 18, 6679 (2002).
- W. Ting, A. G. Xie, S. Z. Tan, and X. Cai, *Colloids Surf. B* 86, 232 (2011).
- H. S. Nalwa (ed.), *Encyclopedia of Nanoscience and Nanotechnology*, American Scientific Publishers, Los Angeles (2004), Vols. 1–10.
- M. T. Yilmaz, *Turk. J. Med. Sci.* 42, 1423 (2012).
- P. I. Tarr, *Clin. Infect Dis.* 20, 1 (1995).
- R. L. Vogt and L. Dippold, *Public Health Rep.* 120, 174 (2005).
- T. J. Beveridge and J. A. Davies, *J. Bacteriol.* 156, 846 (1983).
- R. D. L. Fuente, G. Suarez, and K. H. Schleifer, *Int. J. Syst. Bacteriol.* 35, 99 (1985).
- M. Ieven, H. Jansens, D. Ursi, J. Verhoeven, and H. Goossens, *J. Clin. Microbiol.* 33, 2183 (1995).

29. B. Bagchi, S. Banerjee, A. Kool, P. Thakur, S. Bhandary, N. A. Hoque, and S. Das, *Phys. Chem. Chem. Phys.* 18, 16775 (2016).
30. K. Bajpai, B. Balani, and B. Basu, *J. Am. Ceram. Soc.* 96, 2100 (2013).
31. S. Kar, B. Bagchi, B. Kundu, S. Bhandary, R. Basu, P. Nandy, and S. Das, *Biochim. Biophys. Acta* 1840, 3264 (2014).
32. D. Sarkar, A. Pramanik, S. Jana, P. Karmakar, and T. K. Mondal, *Sensors Actuators B* 209, 138 (2015).
33. B. Kalyanaraman, V. D. Usmar, K. J. A. Davies, P. A. Denney, H. J. Forman, M. B. Grisham, G. E. Mann, K. Moore, L. J. Roberts II, and H. Ischiropoulos, *Free Radic. Biol. Med.* 52, 1 (2012).
34. E. Cabisco, J. Tamarit, and J. Ros, *Int. Microb.* 3, 3 (2000).
35. H. L. Su, C. C. Chou, D. J. Hung, S. H. Lin, I. C. Pao, J. H. Lin, F. L. Huang, R. X. Dong, and J. J. Lin, *Biomaterials* 30, 5979 (2009).
36. M. A. Ansari, H. M. Khan, A. A. Khan, S. S. Cameotra, Q. Saquib, and J. Musarrat, *J. Appl. Microbiol.* 116, 772 (2013).
37. S. Roy, S. Bardhan, K. Pal, S. Ghosh, P. Mandal, S. Das, and S. Das, *J. Alloys Compd.* 763, 749 (2018).
38. S. Roy, A. Maity, P. Mandal, D. K. Chanda, K. Pal, S. Bardhan, and S. Das, *CrystEngCom.* 20, 6338 (2018).
39. T. Debnath, S. Das, D. Das, and S. Sutradhar, *J. Alloys Compd.* 696, 670 (2017).
40. D. Guo, G. Xie, and J. Luo, *J. Phys. D Appl. Phys.* 47, 25 (2014).
41. G. Oskam, *J. Sol-Gel Sci. Technol.* 37, 161 (2006).
42. M. Y. Versavel and J. A. Haber, *Thin Solid Films* 515, 7171 (2007).
43. G. J. G. Aboutaleb and I. Mohammad, *Iran J. Chem. Chem. Eng.* 32, 27 (2013).
44. T. J. Beveridge and R. G. E. Murray, *J. Bacteriol.* 127, 1502 (1976).
45. G. G. Geesey, T. Borch, and C. L. Reardon, *Geobiology* 6, 263 (2008).
46. T. J. Beveridge and S. F. Koval, *Appl. Environ. Microbiol.* 42, 325 (1981).
47. S. Shamailla, N. Zafar, S. Riaz, R. Sharif, J. Nazir, and S. Naseem, *Nanomaterials* 6, 71 (2016).

Received: 27 September 2018. Accepted: 22 October 2018.

IP: 5.101.220.114 On: Sun, 04 Aug 2019 09:19:40
Copyright: American Scientific Publishers
Delivered by Ingenta

Microstructure and Dielectric Properties of Naturally Formed Microcline and Kyanite: A Size-Dependent Study

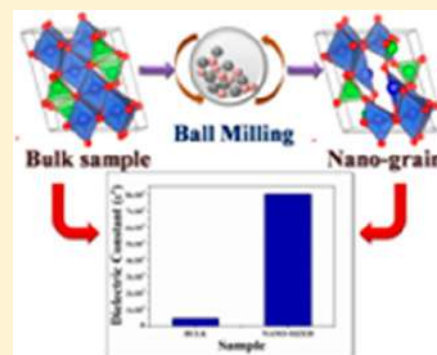
Souravi Bardhan,[†] Shubham Roy,[†] Dipak Kr. Chanda,[‡] Solanky Das,[§] Kunal Pal,^{||} Abhijit Chakraborty,[⊥] Ruma Basu,[#] and Sukhen Das^{*,†}

[†]Department of Physics, [‡]School of Materials Science and Nano-Technology, [§]Department of Geology, and ^{||}Department of Life Science and Biotechnology, Jadavpur University, Kolkata 700032, India

[⊥]Department of Geology and [#]Department of Physics, Jogamaya Devi College, Kolkata 700026, India

Supporting Information

ABSTRACT: The present article reports the crystal defect-mediated changes in electrical characteristics, especially, dielectric properties, of naturally formed microcline and kyanite in two different size fractions. A facile top-down synthesis approach has been adopted to achieve the nanosized samples. Structural and morphological studies have been carried out using X-ray diffraction, field emission scanning electron microscopy, and Fourier transform infrared spectroscopy. Phase purity and microstructural characteristics of the samples were investigated by performing the Rietveld refinement method. Microstructural analysis reveals that the sample size has been greatly reduced to the nano regime after the mechanical ball-milling process, and the milling process eventually introduced some defects in the nanosized samples. UV–vis spectroscopy reveals the optical absorption characteristics and the band gap values of the samples. A major outcome of the present study is the enhancement of the defect states naturally formed samples using the mechanical milling method and the defect-mediated electrical response with varying temperature and frequency. Remarkably high dielectric permittivity values (77.3×10^3 for AF2 and 8.036×10^3 for KY2) in the nanosamples along with low tangent losses and good industrial feasibility of synthesis make the nanosized samples a potential material for fabricating low-cost energy storage devices.



1. INTRODUCTION

Naturally formed minerals are continually disintegrating in nature due to their exposure to various environmental stresses, such as rainwater, ice, temperature changes, and oxidative conditions along with dissolution and crystallization of minerals.¹ They are found in various size ranges in nature, which may be coarse (1–2 μm) or colloidal or of finer sizes (<0.2 μm), depending on the duration of exposure to the mechanical disintegration of the parent rock.^{2,3}

Materials show radically different physicochemical properties such as optical, electrical, magnetic, catalytic behavior, etc. as compared to the corresponding bulk counterparts in the nanoregime due to enhanced surface to volume ratios.^{4–8} New methods are employed that utilize those properties of solids and colloids to fabricate cost-effective devices such as solar cells, supercapacitors, sensors to increase their functionalities.^{9,10} Moreover, in recent times, scientists are giving more emphasis to ecofriendly, biocompatible, economical, and easily accessible natural materials for fabrication of new technologies such as supercapacitors, solar cells, etc.

Silicates are the most abundant mineral found on the earth's surface, especially feldspar minerals.¹¹ Generally silicates, aluminosilicates, and feldspar materials are reported to have a low dielectric constant value of approximately in the range of 3–8, and hence they are extensively used in semiconductor

devices, microelectronics, and integrated circuits.^{12–16} Various studies revealed that the dielectric constant considerably decreases with the increase in the silicate content within the structure.^{17,18} Moreover, the presence of modifying cations such as K^+ , Na^+ , Mg^{2+} , Ca^{2+} , etc. and their consecutive migration within the structure determine the electrical properties of the aluminosilicates.¹⁸ Feldspars are aluminosilicates comprising AlO_4 and SiO_4 linked structures and also may contain cations having ionic radii larger than 1.0 Å such as Na^+ , K^+ , and Ca^{2+} that stoichiometrically balance the aluminum in the structure.^{19,20}

Although they are abundant in nature, an insufficient amount of interest has been paid to study the electrical properties of naturally obtained silicates as a function of both size and crystallinity. Besides, it is a challenge to bring naturally formed minerals to usable form, mainly due to the presence of impurities. Being a natural compound, it has various useful properties as well as major applications in industries, but no such studies have been carried out to understand the size- and crystallinity-mediated electrical properties of these naturally formed materials. Besides the size factor, the presence of alkali

Received: April 10, 2019

Revised: June 15, 2019

Published: June 26, 2019

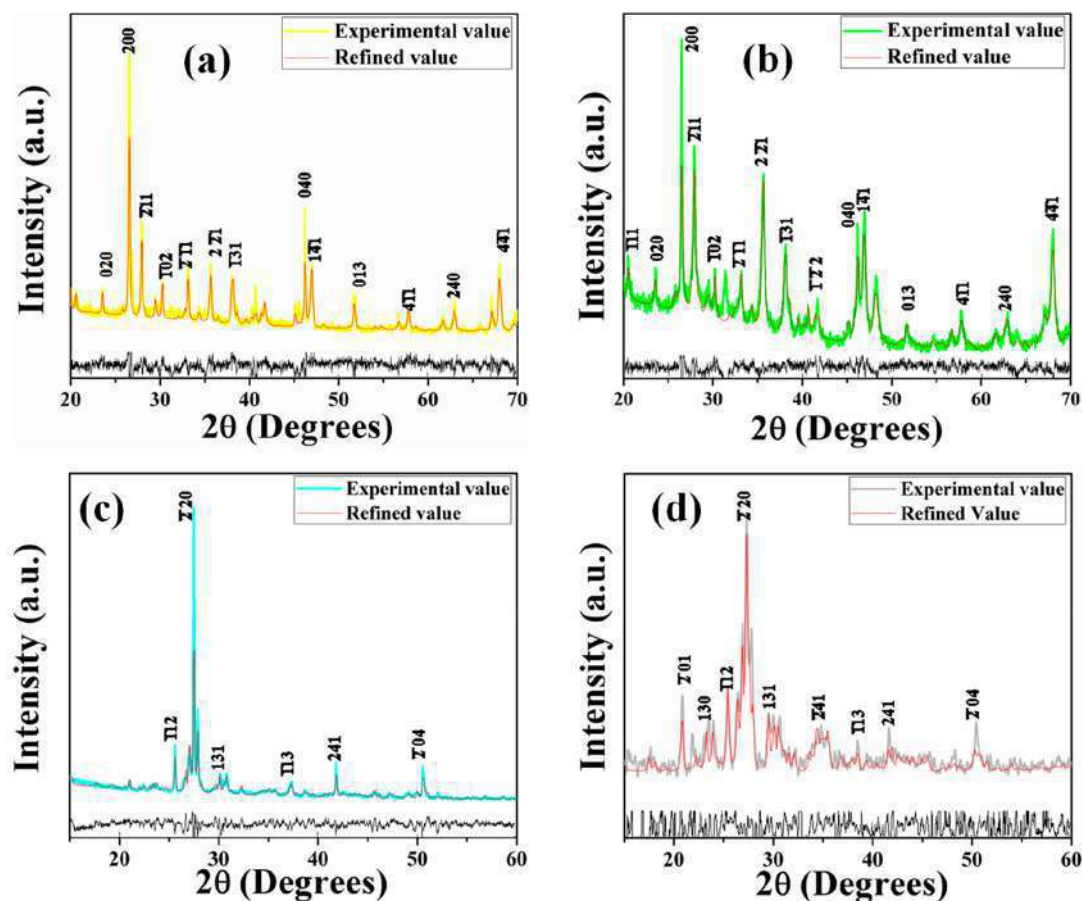


Figure 1. Indexed XRD pattern of the sample (a) yellow for AF1, (b) green for AF2, (c) blue for KY1 and (d) gray for KY2, and the simulated Rietveld refinement plot (continuous red line) obtained by fitting the experimental PXRD pattern using the MAUD program. The respective residue is plotted at the bottom (black line).

metal such as potassium in the crystal structure can also play a pivotal role in influencing electrical conductivity and dielectric properties of these minerals. Hence, two silicates were accordingly selected for our study: alkali feldspar (microcline) (KAlSi_3O_8) containing potassium within its structure, and another is kyanite (Al_2SiO_5), which is devoid of potassium in its structure.

Our study looks at the structural and electrical properties of the coarser and finer fraction of naturally formed aluminum silicate or kyanite and its potassium aluminum silicate or microcline using a common top-down approach to physically disintegrate the bulk minerals into the finer grains. The minerals were further characterized using X-ray diffraction (XRD), field emission scanning electron microscopy (FESEM), UV-vis, and Fourier transform infrared (FTIR) spectroscopy. A detailed top-down synthesis mechanism is illustrated herein. Microstructural details of the synthesized samples have been evaluated performing the standard Rietveld refinement method. In order to understand the effect of temperature and frequency on the electrical properties of our samples, the study of frequency dependent dielectric and other electrical properties at different temperatures has been carried out. This study is the first one to report the defect-mediated temperature-dependent frequency response of the real part of dielectric permittivity and the conduction mechanism in two different size fractions of natural kyanite and microcline, which shows a good dielectric response and low tangent loss

maintaining subsequent ac conductivity values. Such ultrahigh dielectric constant values make our sample desirable for various industrial applications such as storage devices.

2. EXPERIMENTAL SECTION

2.1. Materials. In our experiment, naturally occurring microcline and kyanite were purchased from Hindustan Minerals, Kolkata, India. The KBr and acetone used were obtained from Merck, India. Purchased reagents are of analytical grade and were used without further purification. Millipore water used was obtained at a resistivity of $\sim 18 \text{ M}\Omega\text{-cm}$.

2.2. Sample Preparation. Initially, both the purchased samples were ground in a diamond mortar manually to bring down the size, and then further ground in an agate mortar for 15 min and sieved by using a 400 mesh ($37 \mu\text{m}$) sieve. The sample thus obtained was marked as AF1 and KY1 for microcline and kyanite, respectively. Five grams of agated samples were further subjected to mechanical ball milling in a ball-mill grinder (Fritsch Planetary Mono Mill Pulverisette 6) using tungsten carbide vials and balls for 12 h with ball to sample mass ratio of 20:1 at 300 rpm and then dispersed and sonicated in acetone for 6 h with 15 min step duration. The supernatant was collected after bath-sonication containing finer samples and marked as AF2 and KY2 accordingly.

2.3. Characterization. The purity of the samples were confirmed by using X-ray powder diffractometer (XRD) (D8, Bruker AXS, Winconsin, USA) recorded in the range of 2θ from 15 to 60° using Cu-K α target employing wavelength of 1.5418 \AA and operated at 35 kV, 35 mA with scan speed of 2 s/step . Structural refinement of the obtained samples was done using Rietveld based MAUD program

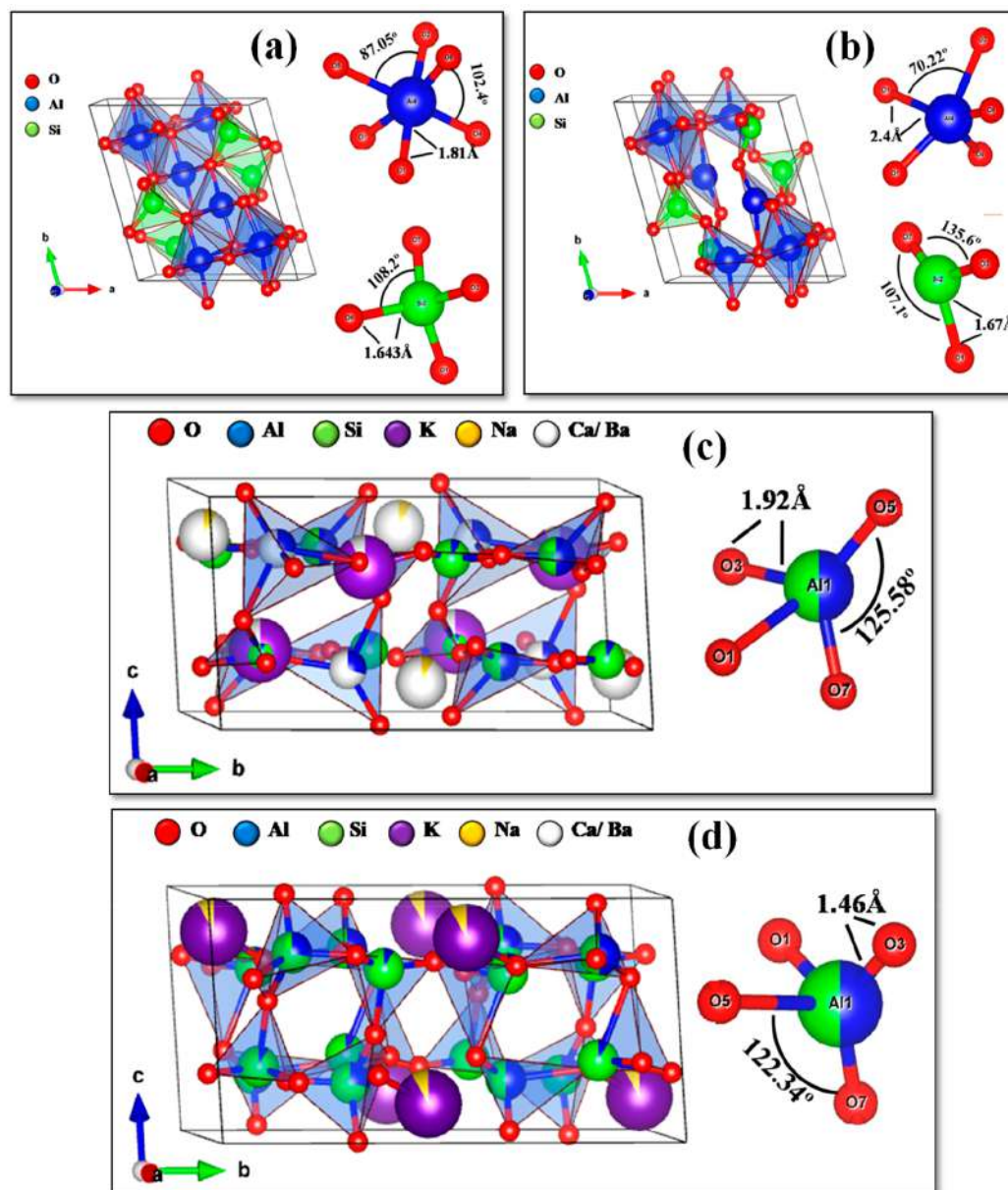


Figure 2. Unit cells of the sample (a) KY1, (b) KY2, (c) AF1 and (d) AF2, along with their bond angles and bond lengths.

(version: 2.8). The refined structures were theoretically constructed using the VESTA program (version: 3.4.3) to perform the microstructural analysis. The software used in our study was downloaded as a freeware from the respective Web sites.

Field emission scanning electron microscopy (FESEM) of our samples was done by employing an INSPECT F50 (FEI, Netherlands) electron microscope. EDX was performed by Supra 55 (ZEISS) in order to determine the chemical composition. The powder samples were directly mounted on carbon-coated meshes followed by a sputter coating of gold. The samples were further characterized using a JEOL JEM-2000 transmission electron microscope (TEM) which was operated at 200 kV. Minute amounts of samples were dispersed in HPLC-grade acetone, ultrasonicated to prepare homogeneous solution, and then drop casted on the carbon-coated copper grid of 300 mesh for subsequent observation.

In order to determine the oxygen vacancy formation from mechanical milling action, X-ray photoelectron spectroscopy (XPS) of AF1 and AF2 was conducted by using PHI 5000, Versaprobe II, USA, having an Al K α radiation source and the 284.5 eV C 1s signal as internal calibrator, with a survey scan from 0 to 1200 eV.

An FTIR study was performed by using a PerkinElmer RXI spectrophotometer in the wavenumber range from 500 to 4000 cm^{-1} . The samples were mixed with KBr in a ratio of 1:50 (1 mg of the sample was homogenized with 50 mg KBr) to perform the FTIR analysis. The mixtures were pressed for 5 min at 5 ton using a hydraulic hand press to form a 13 mm thin pellet and were dried at 80 $^{\circ}\text{C}$ for 4 h in order to remove excess moisture.

The optical absorption spectrum of the samples was recorded in PerkinElmer Lambda-365 UV-vis spectrometer by suspending them in Millipore water at a concentration of 1 mg/mL.

The dielectric constant and electrical conduction mechanism of our samples were investigated by using an Agilent 4294A Precision Impedance analyzer employing 0.5 V bias voltages in a frequency range that was set from 40 Hz to 100 MHz. Pellets were prepared from prepowdered mineral samples by compacting dried powder samples in a hydraulic press system at 5 ton for 10 min, using a small metallic sample holder. The radius and thickness of the samples were measured to evaluate the electrical properties. Dc measurements were carried out using the pellets by a B2985A electrometer.

Table 1. Structural and Microstructural Parameters of the Samples Obtained from Rietveld Analysis of the XRD Pattern

	KY1	KY2	AF1	AF2
<i>a</i> (Å)	7.11000	7.12653	8.58040	8.63185
<i>b</i> (Å)	7.83000	7.85469	12.94830	12.91452
<i>c</i> (Å)	5.58000	5.57644	7.21186	7.25889
alpha (°)	89.8800	90.0160	89.9249	90.7119
beta (°)	101.2300	101.1910	116.0136	116.1617
gamma (°)	106.1000	106.0750	89.1164	88.0176
<i>V</i> (Å ³)	292.302999	293.758594	719.959933	725.856250
size (Å)	2238.6355 ± 214.85672	427.10767 ± 6.618003	2050.8264 ± 235.61292	669.3113 ± 25.507347
strain	1.780148 × 10 ⁻⁴ ± 5.3981512 × 10 ⁻⁵	7.3127674 × 10 ⁻⁵ ± 0.0010631591	0.0011121961 ± 1.3576094 × 10 ⁻⁴	1.8131336 × 10 ⁻⁴ ± 2.0846297 × 10 ⁻⁵
χ ²	1.786	1.8373	1.6598	1.7743
R _p (%)	0.164148	0.07373031	0.12147936	0.4250597
R _{wp} (%)	0.21936631	0.09993974	0.15650387	0.5661985

3. RESULTS AND DISCUSSION

3.1. Microstructure and Elemental Analysis. Any natural mineral contains various impurities. Not only it is hard to eliminate such impure phases from its structure, but also it is difficult to detect such impurities. XRD is an efficient characterization tool which can detect and quantify such kinds of impurities occurring at the crystal level. Investigation of crystalline properties as well as purity of our samples was done using X-ray diffraction measurements (Figure 1). Diffraction maxima of both microcline and kyanite are in good agreement with the Joint Committee on Powder Diffraction Standards (JCPDS) card no. 84-0708 and 11-0046 respectively.

In order to determine the phase purity of the samples along with structural and microstructural characteristics, Rietveld refinement was performed using the Rietveld based software package MAUD v2.8 (Material Analysis Using Diffraction) following the standard methodology.²¹ The XRD pattern of the samples was superimposed with corresponding Miller indices, which showed well-matched peak positions indicating high purity and microstructural properties simultaneously. Figure 2 shows the well-matched experimental and computed patterns of the samples that further confirm the crystalline nature of AF1 and KY1, while peak broadening can be observed in our AF2 and KY2 samples. This kind of peak broadening indicates the reduction in particle sizes.¹⁰ In our case, we have observed that our finer samples (AF2 and KY2) possess smaller sizes which we have reported in Table 1. This further supports that particle sizes have been greatly reduced due to ball milling and further processing of the agated samples. Results of our refinement reveal that kyanite samples have triclinic structure belonging to the $P\bar{1}$ space group,²² whereas triclinic microcline samples have a *C*-1 space group.²³ The results obtained after the final cycle regarding structural, microstructural, and reliability parameters of the samples are provided in Table 1.

Detailed investigation of structural properties and bonding networks of the samples were analyzed using Vesta v3.4.3 (Visualization for Electronic and STructural Analysis) and are depicted in Figure 2. Agated kyanite sample contains octahedral AlO₆ stacked together with two corner-shelved SiO₄ tetrahedra sharing an oxygen molecule in a zigzag manner. This type of symmetry is missing in our nanosized kyanite sample. In KY2 sample, oxygen molecules are missing in some AlO₆ and SiO₄ sites creating defects in the crystal symmetry. Variation of bond angles and bond lengths (Tables

S1–S4) of such polyhedral species has also been seen, which confirms the interstitial defects in the nanosized KY2 sample.

A similar phenomenon has also been observed in the case of our microcline sample (AF1 and AF2). In order to ascertain the crystal structure, we have observed that potassium polyhedron is being shared with silicon polyhedron and aluminum polyhedron on either side, though this type of symmetry is missing in the AF2 sample. The number of defect states is quite high in AF2 than the bulk AF1. These defects could be very beneficial for the enhancement of electrical properties. A commendable change in bond angles and bond lengths has also been observed in AF2 (Figure 2). Although the microcline crystal consists of some impurities such as Na, Ca, and Ba, which has been detected through our refinement, the occupancy of these impure atoms are much less (Tables S1–S4). Thus, no such prominent effect has been observed in our dielectric permittivity part due to such impurities.

After proper assessment of the purity and crystallinity, the morphology and particle size of the samples must be investigated in order to obtain a stable dielectric value as it can be tuned by varying particle size and morphology.²⁴ In our case, particle morphology of the entire sample set was observed by using field emission scanning electron microscopy and transmission electron microscopy, and the micrographs are displayed in Figure 3a–d and Figure 4a–d respectively. FESEM micrographs of our bulk samples (AF1 and KY1) are distinctly larger than that of the finer samples (AF2 and KY2). Mechanical milling smoothens the sharp edges of the bulk fraction, which results in the change of morphologies in finer fractions. The full width at half maxima (fwhm) of the grain size distribution graph (Figure 3, Figure 4) has also been reduced, which allows us to determine that the finer samples show greater uniformity.

Around 50 particles were taken randomly from the micrographs with a grain size distribution in the range 150–650 nm and from 50 to 450 nm for AF1 and KY1 respectively, while 60–180 nm and from 20 to 100 nm for AF2 and KY2 respectively, as shown in Figure 3e–h. The average grain size based on the histogram was found to be around 355 and 109 nm for AF1 and AF2 respectively. The mean particle size was found to be 202 and 53 nm for KY1 and KY2 respectively, which is nearly equal to the crystallite sizes estimated from our refined XRD data. The EDX spectra of microcline sample (Figure 5a) confirm the presence of potassium, silicon, oxygen, and aluminum, along with a minute quantity of sodium and calcium, which is concordant with Figure 2c. The EDX spectra

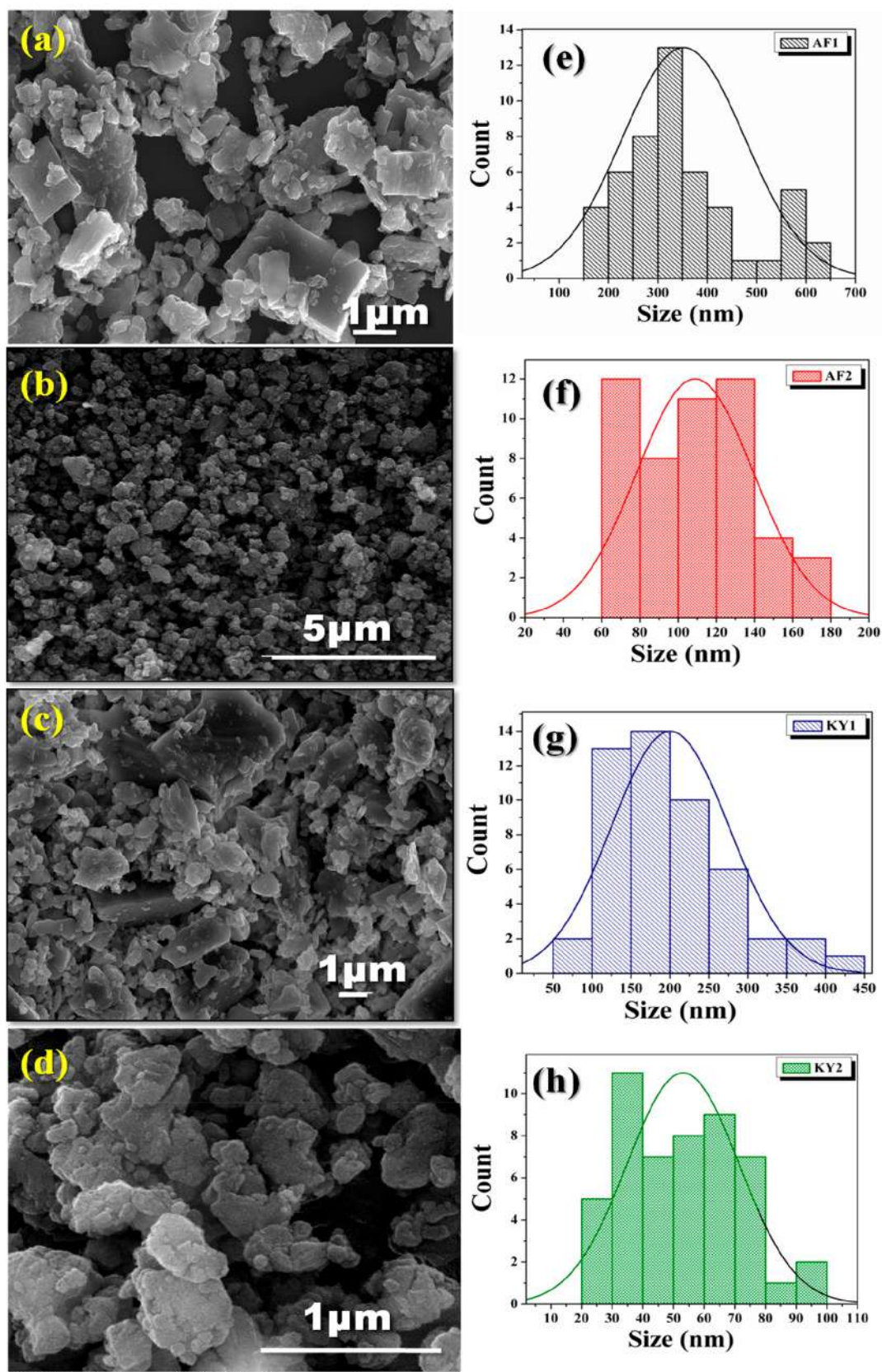


Figure 3. FESEM micrographs of the samples (a–d), corresponding size distribution plots from the FESEM images (e–h).

also confirmed the purity of kyanite (Figure 5b) which contains silicon, oxygen, and aluminum.

To ascertain the oxygen vacancy more prominently, we have employed XPS measurements for our microcline samples (AF1

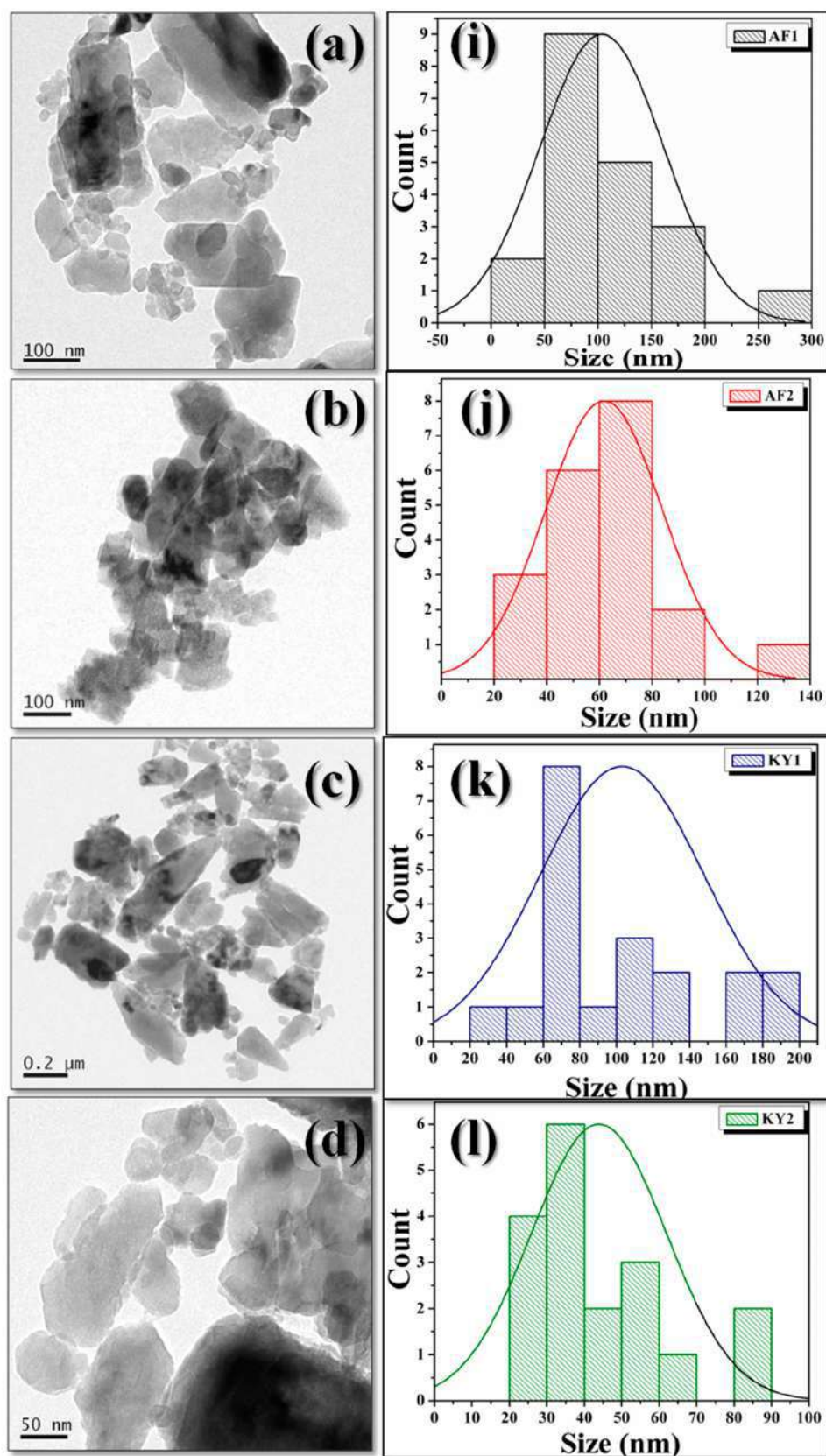


Figure 4. TEM micrographs of the samples (a–d), corresponding size distribution plots from the TEM images (i–l).

and AF2) (Figure S1). Our XPS data agree well with previous literature,²⁰ confirming the presence of O 1s (530.4 eV), Si 2p

(101.6 eV), Al 2p (72.8 eV), K 2p (292.0 eV), and Na 1s (1071.2 eV) states, which justifies the purity of these samples.

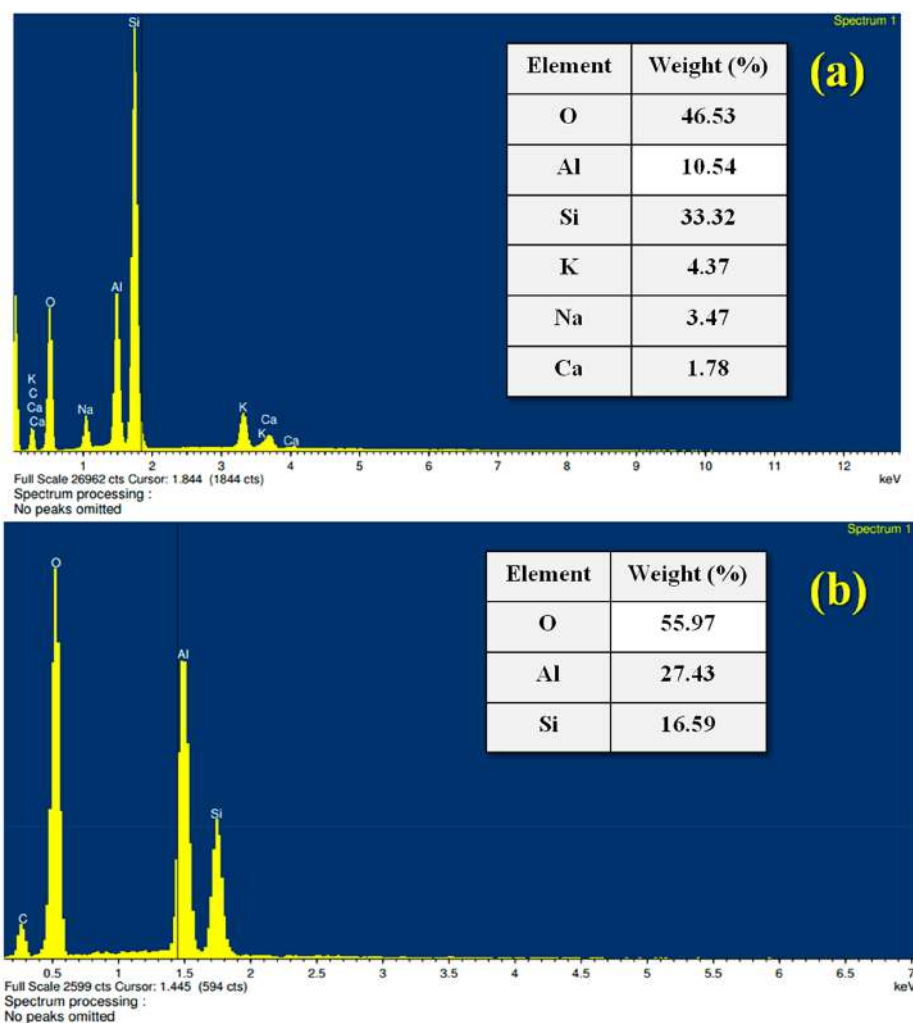


Figure 5. EDX images of (a) microcline and (b) kyanite, showing their purity.

The XPS spectra have been investigated, and the compositions of our samples are analyzed by using the CASA XPS software platform. Proper elemental analysis illustrates that the atomic percentage of oxygen in our AF1 sample is 50.13%, while the nanosized microcline (AF2) sample has 46.68% of oxygen. This corroborates the fact that the atomic oxygen content has been reduced significantly during the synthesis, creating more oxygen vacancies in nanosized AF2, which was reflected in our microstructural analysis.

In order to understand the size and morphology more precisely, a TEM study was performed, and the micrographs along with the corresponding size distributions are provided in Figure 4i–l. In the case of agated samples (AF1, KY1), they appeared to be a mixture of various forms of bulk agglomerates, while the finer samples eventually are smaller in size having blunt edges. Size distribution was determined by considering 20 particles randomly in each case, the average size of AF1 and AF2 were found to be 104 and 62 nm respectively, while in the case of KY1 and KY2, the average size was found to be 103 and 44 nm, respectively. Thus, TEM micrographs confirmed that there was a distinct reduction in particle sizes in finer fractions.

3.2. Spectroscopic Study. In order to ascertain the purity of our samples at molecular component level, we have employed FTIR spectrometry. In our case, both microcline and kyanite were collected and further ground to obtain

nanosized mineral samples. Thus, FTIR spectra should thoroughly be studied for fingerprinting the samples.

FTIR spectra of the samples are represented in Figure 6. In the case of microcline, absorption bands are observed at 1090, 1054, 998, 772, 728, 648, 579, and 536 cm^{-1} and are in good agreement with the values reported in the literature.²³ The spectral band located at 536 cm^{-1} is due to the coupling between the O–Si–O bending vibration and the K–O stretching vibration. The bands at 579 and 648 cm^{-1} are attributed to O–Si(Al)–O bending vibrations. The vibrational bands located at 728 and 772 cm^{-1} are attributed to the Si–Al(Si) and the Si–Si stretching vibrations. The broader peaks at 998 and 1054 cm^{-1} are due to Si(Al)–O stretching vibrations. The peak at 1090 cm^{-1} is due to Si–O stretching vibrations.

In the case of kyanite, absorption peaks were observed at 934, 892, 730, 672, 637, 602, 567, and 542 cm^{-1} . Two strong bands located between 500 and 700 cm^{-1} is attributed to the deformation vibration of the Si–O tetrahedron and vibration of the Al–O octahedron. The bands at 892 and 934 cm^{-1} are from vibrations of the Si–O tetrahedron.^{22,25} Thus, FTIR results are quite consistent and corroborate the XRD data.

Optical activity of a material can be justified by using absorption spectra of the sample. It also provides us the value of the optical band gap which in turn gives us the idea of the

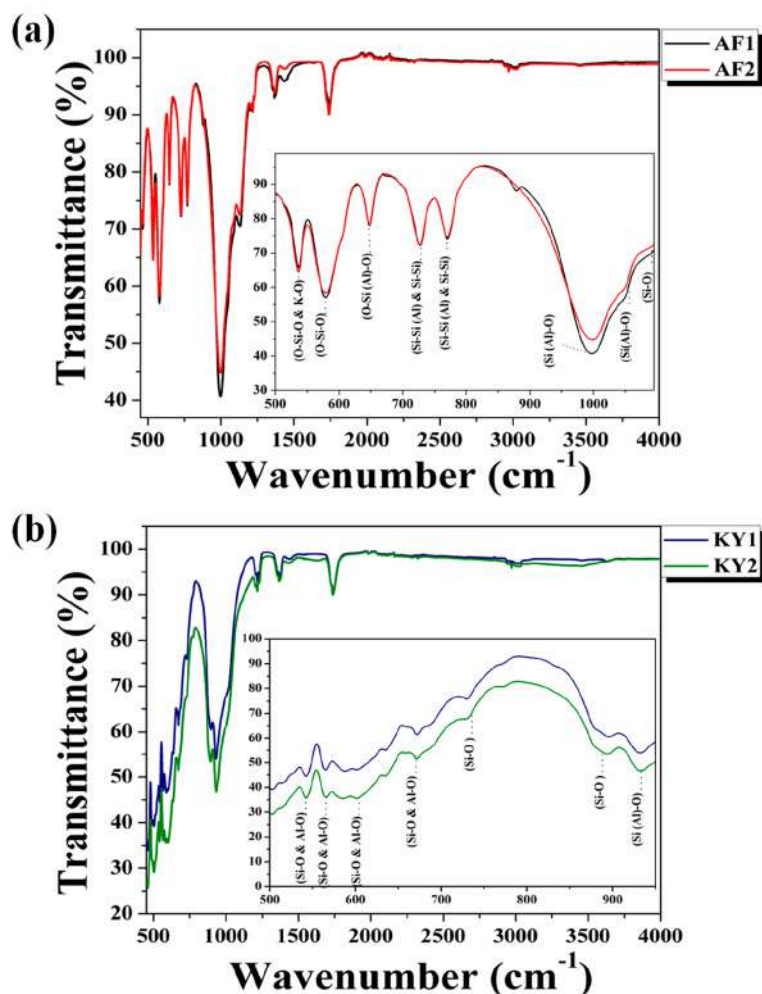


Figure 6. Normalized FTIR spectra of the samples (a) microcline (AF1 and AF2) and (b) kyanite (KY1 and KY2).

conductivity of the sample. In our case, absorption spectra of the samples were performed to characterize the samples (Figure 7a,c). The absorption maxima of AF1 and AF2 were observed at 219.8 and 219.4 nm, while that of KY1 and KY2 were found to be 220 and 219.5 nm, respectively. The optical absorption spectra show peak broadening and a slight blue shift for AF1 and AF2 samples. Band gap energies of the samples were calculated using the following formula:^{10,26}

$$\alpha E = A(E - E_g)^n \quad (1)$$

where E and E_g are the photon energy ($h\nu$) and the optical band gap energy, in electronvolt (eV), respectively. α is the absorption coefficient ($\alpha = 2.303A/t$, here A is the absorbance and t is the thickness of the cuvette) respectively.²⁷ The value of “ n ” depends on the nature of the electronic transition responsible for absorption. Tauc plot $(\alpha h\nu)^2$ is plotted against photon energy $h\nu$, and the band gap energy of three fractions was calculated by extrapolating the linear region and intersecting the linear portion of the curve to the energy axis shown in Figure 7b,d. A variation was observed between the agated and the finer fraction. The band gap of AF1 and AF2 was found to be 2.99 and 3.38 eV, respectively, while that of KY1 and KY2 was found to be 5.34 and 5.06 eV respectively. Kyanite was reported to have band wider band gap,²⁸ and

hence it has insulating properties that makes this sample a better dielectric material even in its bulk form.

Because of the small particle dimensions of our finer sample of microcline which also shows semiconducting band gap,¹⁰ it consists of a very small number of molecules/atoms, so the number of overlapping orbitals and width of the energy level decreases which creates a large band gap. However, insulating kyanite provides the opposite behavior which can be explained on the basis of crystallinity. Previous reports show that in some cases it has been observed that the band gap decreases with the increase in lattice parameters.²⁹ Therefore, the increase of the band gap in the present study with the particle size of kyanite can also be explained on the basis of the decrease in the lattice parameters.

3.3. Dielectric Permittivity Analysis. The dielectric constant and dielectric loss are very important physical parameters for storage materials. They influence the electrical, optical, and several other properties of the materials. Therefore, it is necessary to investigate the dielectric properties of the naturally occurring rock forming kyanite and microcline. The dielectric response of a material can be described using the relation,³⁰

$$\epsilon = \epsilon' + j\epsilon'' \quad (2)$$

where ϵ' and ϵ'' are the real and imaginary part of the relative dielectric constant, respectively. The real part of the dielectric

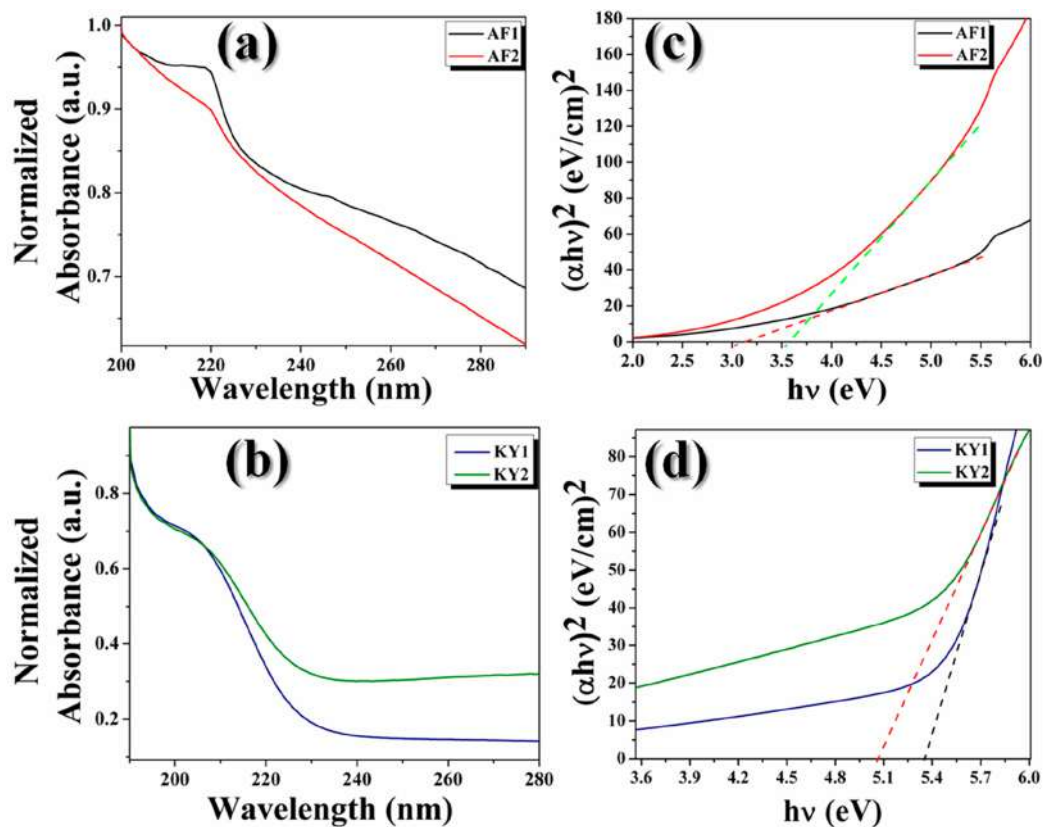


Figure 7. (a) UV–vis spectra of microcline, (b) Tauc plot (band gap) of microcline; (c) UV–vis spectra of kyanite, (d) Tauc plot (band gap) of kyanite.

constant (ϵ') contributes to the amount of energy stored in the material due to polarization effect, whereas the imaginary part (ϵ'') is associated with the energy dissipated by the material. The real part of the dielectric constant can be calculated using the relation:³¹

$$\epsilon' = (C \cdot d) / (\epsilon_0 A) \quad (3)$$

where C is the capacitance of the sample, d and A are thickness and surface area of the sample respectively, and ϵ_0 is the permittivity of free space (8.85×10^{-12} F/m). The variations of the real part of the dielectric constant (ϵ') with applied field frequency (ranging from 40 Hz to 10 MHz) for the entire sample set at different temperatures ranging from 30 to 200 °C have been shown in Figure 8a–d.

At lower frequencies, the high values of dielectric permittivity were due to the Maxwell–Wagner interfacial polarization effect,^{32,33} which is in good accordance with the Koop's theory,³⁴ but after a certain frequency, the real part of the dielectric constant falls off gradually. This phenomenon can be interpreted by virtue of the grain boundary effect. Normally, the dielectric medium contains nonconducting grain boundaries. The formation of these grain boundaries is due to the imperfection in crystal alignment.¹⁰ The free charge carriers are trapped inside the grain boundaries and the resulting nanodipoles which produce the polarization effect.^{35–37} However, there is a gradual declination of dielectric values at a higher frequency domain because the dipoles cannot withstand the rapid change of the applied frequency. The tangent loss associated with our samples is in good agreement with our dielectric data (Figure 8i–l).

A major outcome from the dielectric data in our case is related to the particle sizes. Nanosized mineral sample shows higher dielectric permittivity values in the case of our samples. Our microstructural analysis from XRD and FESEM data show that samples that are in the nanoregime provides more crystal defect states than the agated samples. These defects mainly arise due to oxygen vacancies in the crystal which are shown in Figure 2. An oxygen vacancy traps the free charges and creates nanodipoles which lead to the higher degree of dielectric value in our nanostructured minerals. Agated samples are much more aligned and symmetric from the crystallographic point of view. Thus, no/lower number of crystal defects causes low dielectric values for these samples.

Other than the size-dependent dielectric study, the variation of dielectric behavior with temperature has also been studied and plotted as a temperature response graph (Figure 8e–h). A rapid decrement of dielectric constant from room temperature (30 °C) is visible for all our samples. The high dielectric constant value at the initial temperature is due to the insufficiency of nanodipole energy in overcoming the interdipolar frictional force.³⁸ As part of the U.S. Geological Survey Report (1979),³⁹ microcline was reported to have a dielectric constant of 5.48 at 1 MHz. In our experiment, the dielectric constant of AF1 and AF2 was found to be 8.8 and 17.2 respectively at 1 MHz, whereas in the case of KY1 and KY2, it was found to be 10.03 and 12.79 respectively, whereas it was reported to be 7.8.³⁹ Thus, the obtained values in our case are much higher than that of the previously reported articles (Table S2).

Another important observation can be made on the basis of chemical composition of the samples. The dielectric

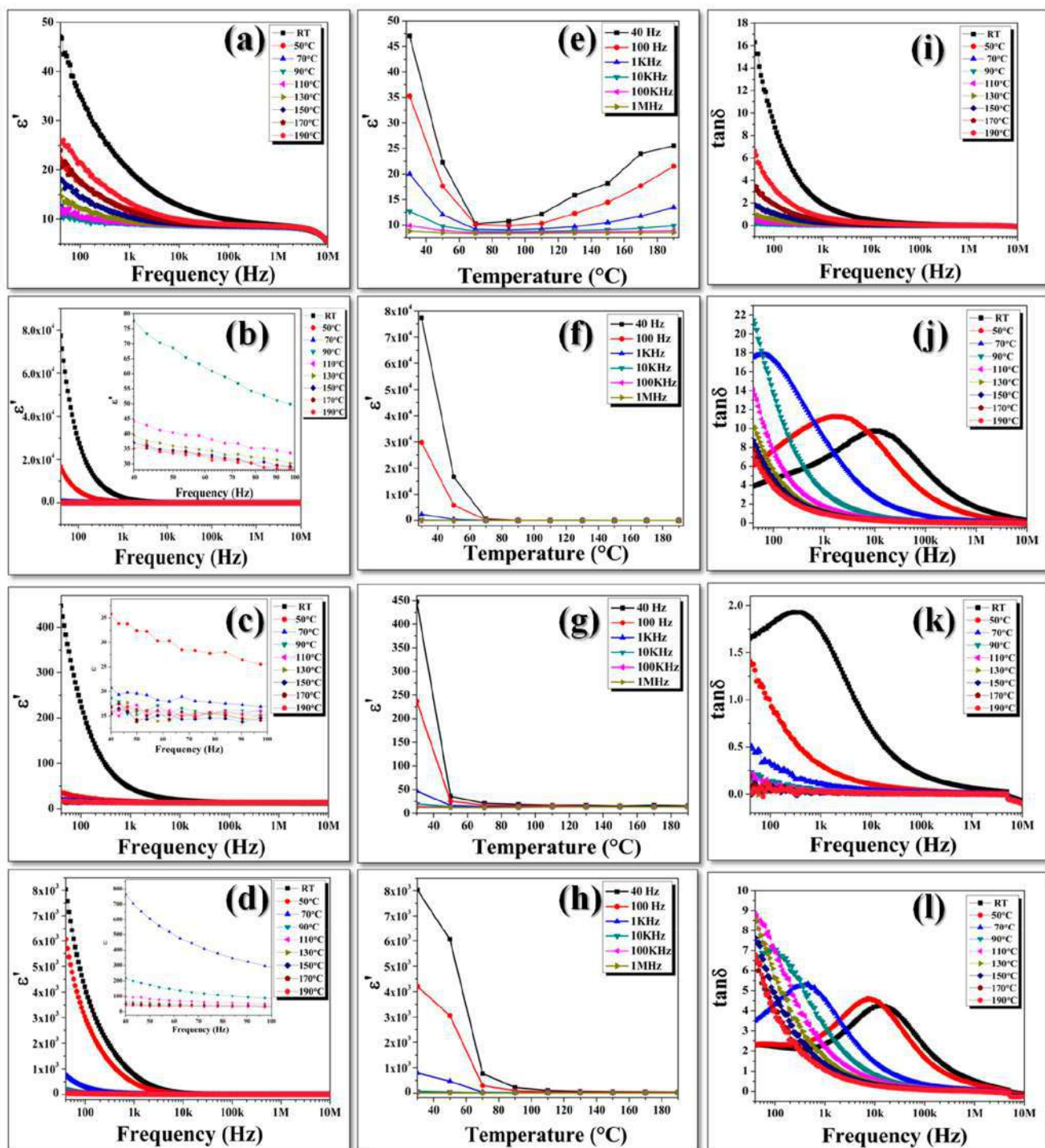


Figure 8. Variation of dielectric constant with frequency for the samples (a–d); variation of dielectric constant with temperature for the samples (e–h); tangent loss ($\tan \delta$) of the samples (i–l).

permittivity value for kyanite is found to be higher than that of the microcline even in the bulk size range at room temperature. This happens because microcline in its bulk form (AF1) consists of larger atoms such as potassium (Figure 2). These potassium atoms restrict the trapping mechanism due to its bulk size and shape which is absent in the case of bulk kyanite (KY1). Thus, the probability of trapping free charges in vacant zones increases the probability of formation of the number of

nanodipoles in our bulk kyanite sample, which results in its higher value of dielectric constant.

3.4. Conduction Mechanism Analysis. A size- and temperature-dependent variation of electrical conductivity with frequency of our samples was also been investigated and is displayed in Figure 9a–d. Ac conductivity is found to be the highest at the room temperature, but decreases with increasing temperature. The values of ac conductivity are low at a lower

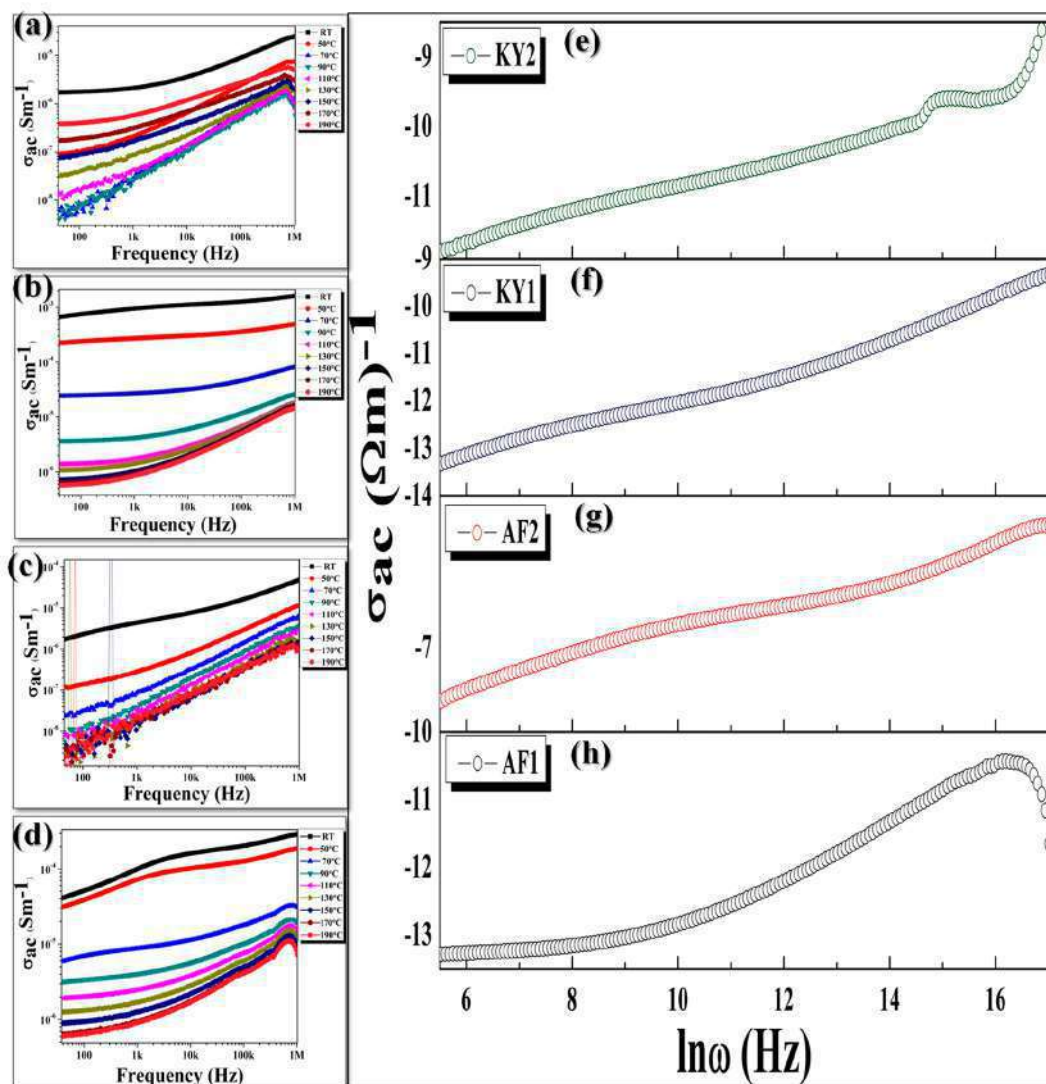


Figure 9. Variation of ac electrical conductivity with frequency for the samples (a–d); Jonscher's plot for the samples (e–h).

frequency but increases with the increasing frequency due to higher electron mobility at higher frequencies.⁴⁰

Frequency response of ac conductivity is also studied through Jonscher's power law relation:⁴¹

$$\sigma_{ac} = B\omega^n \quad (4)$$

where “ B ” and “ n ” are constants. B has the unit of conductivity and n is a dimensionless constant. The value of “ n ” has been estimated for each sample by plotting $\ln \sigma$ vs $\ln \omega$ using the above eq 5 and shown in Figure 9e–h. The estimated values of the “ n ” in our case are found to be around 0.28193 ± 0.0069 and 0.0775 ± 0.00079 for AF1 and AF2 respectively, and 0.31186 ± 0.00325 and 0.20617 ± 0.00181 for KY1 and KY2 respectively, which corroborates that our samples are not perfectly Debye type (where $n = 0$)^{42,43} and diffusion limited hopping is involved in ac conductivity.⁴⁴

The dc conductivities of our samples have also been studied in a same manner and has been illustrated in Figure 10.

The charge carriers need activation energy to overcome the potential barrier to initiate charge hopping mechanism, resulting in higher conduction. It can be calculated from the Arrhenius equation⁴³

$$\sigma = \sigma_0 \exp(-E_a/K_B T) \quad (5)$$

where σ_0 is the pre-exponential factor; E_a is the activation energy, K_B is Boltzmann constant, and T be the absolute temperature. Arrhenius plots were obtained from the conductivity data calculated at frequencies 10 Hz, 100 kHz, and 1 MHz along with the dc activation energy of the applied external field and have been shown in Figure 10. A detailed description of activation energies is given in Table 2.

4. CONCLUSION

This article for the very first time reports detailed microstructural studies of naturally formed microcline and kyanite both in their bulk and nano form and made an excellent effort to enhance the dielectric constant introducing defect states in their crystal structure by mechanical milling. The primary crystallographic data have been obtained by using the XRD method. Rietveld refinement enhances the acceptability of the phase purity as well as lattice constants. Detailed crystallographic mapping has been done using various software platforms to establish our theory behind the dielectric enhancement in the nano regime. FTIR and UV–vis spectra have also been used as characterizing tools for our samples.

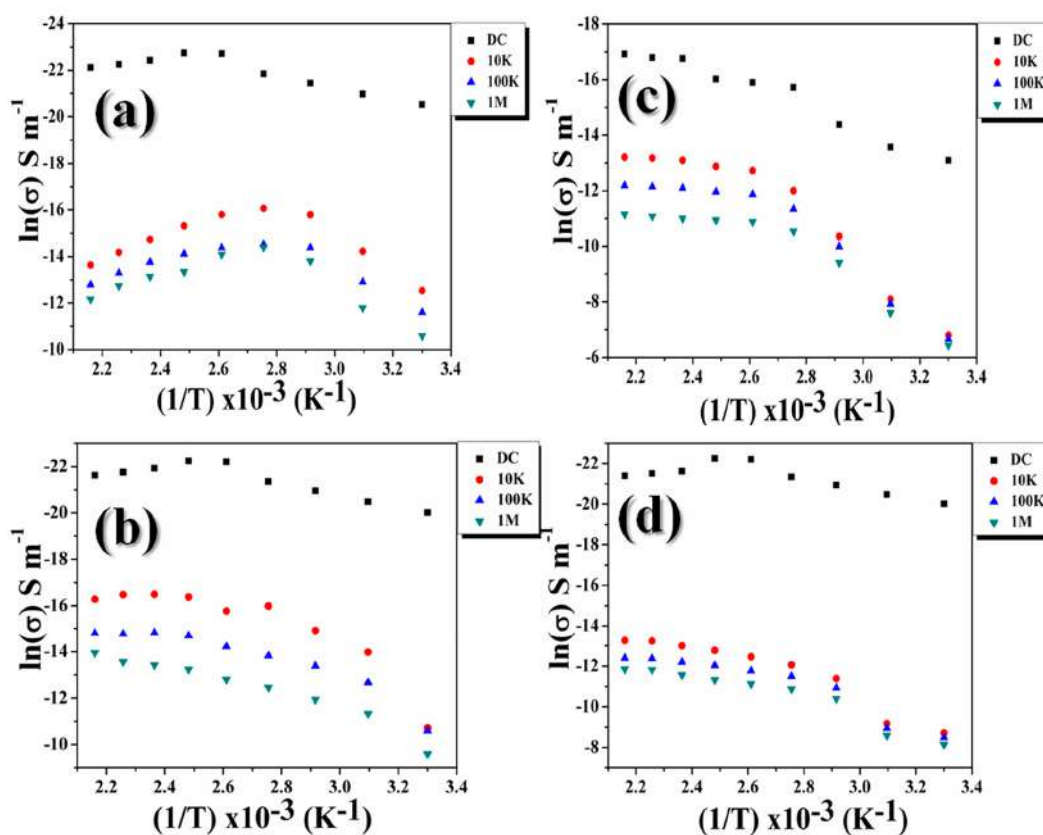


Figure 10. Arrhenius plots for the samples (a) AF1, (b) KY1, (c) AF2, and (d) KY2.

Table 2. Calculated Activation Energies of the Samples from Arrhenius Plots at Different Frequencies

sample	frequency	activation energy (eV)
AF1	DC	0.2979759
	10 kHz	0.7174514
	100 kHz	0.6344525
	1 MHz	0.5483224
AF2	DC	0.3401992
	10 kHz	0.7450689
	100 kHz	0.72029503
	1 MHz	0.5988815
KY1	DC	0.2403712
	10 kHz	0.4157418
	100 kHz	0.3133141
	1 MHz	0.277446719
KY2	DC	0.2853089
	10 kHz	0.382164
	100 kHz	0.3342534
	1 MHz	0.23765686

Morphology and size distribution of the naturally formed samples were investigated using FESEM, where a size reduction is visible between bulk and finer fractions. This size reduction happened due to the mechanical milling which incorporates defect states into the nanosized crystals. Thus, a prominent enhancement has been observed in the dielectric permittivity and ac conductivity in these samples. These remarkable high dielectric values (77.3×10^3 for AF2 and 8.036×10^3 for KY2) of ball-milled samples make these naturally formed samples desirable candidates for various cost-effective energy harvesting devices.

■ ASSOCIATED CONTENT

📄 Supporting Information

The Supporting Information is available free of charge on the ACS Publications website at DOI: 10.1021/acs.cgd.9b00480.

Microstructural analysis of the samples, comparative study of our work with available literature, XPS data (PDF)

■ AUTHOR INFORMATION

Corresponding Author

*E-mail: sdasphysics@gmail.com. Phone: +91 9433091337.

ORCID

Shubham Roy: 0000-0001-5245-3229

Dipak Kr. Chanda: 0000-0003-0147-4972

Sukhen Das: 0000-0001-8372-3076

Notes

The authors declare no competing financial interest.

■ ACKNOWLEDGMENTS

Authors are grateful to the Department of Physics, Jadavpur University, for extending experimental facilities. S.B. and S.D. would like to acknowledge DST-SERB (Grant No. EEQ/2018/000747) for funding.

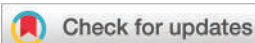
■ REFERENCES

- (1) Winkler, E. M. Decay of Stone. *Stud. Conserv.* **1971**, *16*, 1–14.
- (2) Williams, L. B.; Haydel, S. E. Evaluation of the medicinal use of clay minerals as antibacterial agents. *Int. Geol. Rev.* **2010**, *52*, 745–770.

- (3) Zhou, C. H.; Keeling, J. Fundamental and applied research on clay minerals: From climate and environment to nanotechnology. *Appl. Clay Sci.* **2013**, *74*, 3–9.
- (4) Carretero, M. I.; Pozo, M. Clay and non-clay minerals in the pharmaceutical industry Part I. Excipients and medical applications. *Appl. Clay Sci.* **2009**, *46*, 73–80.
- (5) Shipway, A. N.; Katz, E.; Willner, I. Nanoparticle Arrays on Surface for Electronic, Optical, and Sensor Applications. *ChemPhysChem* **2000**, *1*, 18–52.
- (6) Chattopadhyay, K. K.; Sarkar, S. Size-dependent optical and dielectric properties of BiVO₄ nanocrystals. *Phys. E* **2012**, *44*, 1742–1746.
- (7) Pfeiffer, C.; Rehbock, C.; Huhn, D.; Carrillo-Carrion, C.; de Aberasturi, D. J.; Merk, V.; Barcikowski, S.; Parak, W. J. Interaction of colloidal nanoparticles with their local environment: the (ionic) nanoenvironment around nanoparticles is different from bulk and determines the physico-chemical properties of the nanoparticles. *J. R. Soc., Interface* **2014**, *11*, 20130931.
- (8) Lead, J. R.; Batley, G. E.; Alvarez, P. J. J.; Croteau, M. N.; Handy, R. D.; McLaughlin, M. J.; Judy, J. D.; Schirmer, K. Nanomaterials in the Environment: Behavior, Fate, Bioavailability, and Effects—An Updated Review. *Environ. Toxicol. Chem.* **2018**, *37*, 2029–2063.
- (9) Kenry; Lim, C. T. Nanofiber technology: current status and emerging developments. *Prog. Polym. Sci.* **2017**, *70*, 1–17.
- (10) Roy, S.; Bardhan, S.; Pal, K.; Ghosh, S.; Mandal, P.; Das, S.; Das, S. Crystallinity mediated variation in optical and electrical properties of hydrothermally synthesized boehmite (γ -AlOOH) nanoparticles. *J. Alloys Compd.* **2018**, *763*, 749–758.
- (11) Crundwell, F. K. The mechanism of dissolution of minerals in acidic and alkaline solutions: Part II Application of a new theory to silicates, aluminosilicates and quartz. *Hydrometallurgy* **2014**, *149*, 265–275.
- (12) Mccauley, R. A. Polymorphism and dielectric electric properties of Ba- and Sr-containing feldspars. *J. Mater. Sci.* **2000**, *35*, 3939–3942.
- (13) Maex, K.; Baklanov, M. R.; Shamiryan, D.; Lacopi, F.; Brongersma, S. H.; Yanovitskaya, Z. S. Low dielectric constant materials for microelectronics. *J. Appl. Phys.* **2003**, *93*, 8793.
- (14) Jones, A.; Islam, M. S.; Mortimer, M.; Palmer, D. Alkali ion migration in albite and K-feldspar. *Phys. Chem. Miner.* **2004**, *31*, 313–320.
- (15) Shannon, R. D.; Oswald, R. A.; Rossman, G. R. Dielectric Constants of Topaz, Orthoclase and Scapolite and the Oxide Additivity Rule. *Phys. Chem. Miner.* **1992**, *19*, 166–170.
- (16) Volksen, W.; Miller, R. D.; Dubois, G. Low Dielectric Constant Materials. *Chem. Rev.* **2010**, *110*, 56–110.
- (17) Darwish, H.; Goma, M. M. Effect of compositional changes on the structure and properties of alkali-alumino borosilicate glasses. *J. Mater. Sci.: Mater. Electron.* **2006**, *17*, 35–42.
- (18) Yue, Y.; Zhang, X.; Xu, Y.; Huang, S.; Chen, P. Structural, dielectric and melting properties of aluminosilicate glasses based on blast furnace slag for printed circuit board applications. *Mater. Lett.* **2014**, *136*, 356–358.
- (19) Scaillet, B.; Holtz, F.; Pichavant, M. Experimental Constraints on the Formation of Silicic Magmas. *Elements* **2016**, *12* (2), 109–114.
- (20) Klopogge, J. T.; Wood, B. J. Chemical bonding and electronic structures of microcline, orthoclase and the plagioclase series by X-ray photoelectron spectroscopy. *Spectrochim. Acta, Part A* **2015**, *137*, 711–716.
- (21) Bøjesen, D.; Jensen, K. M. Ø.; Tyrsted, C.; Lock, N.; Christensen, M.; Iversen, B. B. In Situ Powder Diffraction Study of the Hydrothermal Synthesis of ZnO Nanoparticles. *Cryst. Growth Des.* **2014**, *14*, 2803–2810.
- (22) Burt, J. B.; Ross, N. L.; Gibbs, G. V.; Rossman, G. R.; Rosso, K. M. Potential protonation sites in the Al₂SiO₅ polymorphs based on polarized FTIR spectroscopy and properties of the electron density distribution. *Phys. Chem. Miner.* **2007**, *34*, 295–306.
- (23) Theodosoglou, E.; Koroneos, A.; Soldatos, T.; Zorba, T.; Paraskevopoulos, K. M. Comparative Fourier Transform Infrared And X-Ray Powder Diffraction Analysis of Naturally Occurred K-Feldspars. *Bull. Geol. Soc. Greece* **2010**, *43* (5), 2753.
- (24) Yoshimatsu, K.; Reimhult, K.; Krozer, A.; Mosbach, K.; Sode, K.; Ye, L. Uniform molecularly imprinted microspheres and nanoparticles prepared by precipitation polymerization: The control of particle size suitable for different analytical applications. *Anal. Chim. Acta* **2007**, *584*, 112–121.
- (25) Jin, J.; Gao, H.; Ren, Z.; Chen, Z. The Flotation of Kyanite and Sillimanite with Sodium Oleate as the Collector. *Minerals* **2016**, *6*, 90.
- (26) Das, D.; Das, S.; Sutradhar, S. Enhanced dielectric behavior and ac electrical response in Gd-Mn-ZnO nanoparticles. *J. Alloys Compd.* **2017**, *726*, 11–21.
- (27) Debnath, T.; Saha, P.; Patra, N.; Das, S.; Sutradhar, S. Hydrothermal process assisted undoped and Cr-doped semiconducting ZnO nanorods: Frontier of dielectric property. *J. Appl. Phys.* **2018**, *123*, 194101.
- (28) Aryal, S.; Rulis, P.; Ching, W. Y. Density functional calculations of the electronic structure and optical properties of aluminosilicate polymorphs (Al₂SiO₅). *Am. Mineral.* **2008**, *93*, 114–123.
- (29) Azam, A.; Jawad, A.; Ahmed, A. S.; Chaman, M.; Naqvi, A. H. Structural, optical and transport properties of Al³⁺-doped BiFeO₃ nanopowder synthesized by solution combustion method. *J. Alloys Compd.* **2011**, *509*, 2909–2913.
- (30) Usha, V.; Kalyanaraman, S.; Vettumperumal, R.; Thangavel, R. A study of frequency dependent electrical and dielectric properties of NiO nanoparticles. *Phys. B* **2017**, *504*, 63–68.
- (31) Lanje, A. S.; Sharma, S. J.; Ningthoujam, R. S.; Ahn, J. S.; Podes, R. B. Low temperature dielectric studies of zinc oxide (ZnO) nanoparticles prepared by precipitation method. *Adv. Powder Technol.* **2013**, *24*, 331–335.
- (32) Chuprinko, D.; Titov, K. Influence of mineral composition on spectral induced polarization in sediments. *Geophys. J. Int.* **2017**, *209*, 186–191.
- (33) Das, S.; Das, S.; Roychowdhury, A.; Das, D.; Sutradhar, S. Effect of Gd doping concentration and sintering temperature on structural, optical, dielectric and magnetic properties of hydrothermally synthesized ZnO nanostructure. *J. Alloys Compd.* **2017**, *708*, 231–246.
- (34) Koops, C. G. On the Dispersion of Resistivity and Dielectric Constant of Some Semiconductors at Audiofrequencies. *Phys. Rev.* **1951**, *83* (1), 121–124.
- (35) Liu, J.; Duan, C. G.; Yin, W. G.; Mei, W. N.; Smith, R. W.; Hardy, J. R. Large dielectric constant and Maxwell-Wagner relaxation in Bi_{2/3}Cu₃Ti₄O₁₂. *Phys. Rev. B* **1951**, *70*, 144106.
- (36) Singh, L.; Kim, W.; Sin, B. C.; Mandal, K. D.; Rai, U. S.; Ullah, A.; Chung, H.; Lee, Y. Dielectric studies of a nano-crystalline CaCu_{2.90}Zn_{0.10}Ti₄O₁₂ electro-ceramic by one pot glycine assisted synthesis from inexpensive TiO₂ for energy storage capacitors. *RSC Adv.* **2014**, *4*, 52770.
- (37) Duarte, D.; Dodabalapur, A. Investigation of the physics of sensing in organic field effect transistor based sensors. *J. Appl. Phys.* **2012**, *111*, 044509.
- (38) Das, S.; Das, S.; Sutradhar, S. Effect of Gd³⁺ and Al³⁺ on optical and dielectric properties of ZnO nanoparticle prepared by two step hydrothermal method. *Ceram. Int.* **2017**, *43*, 6932–6941.
- (39) Olhoeft, G. R. *Open File Report*; United States Department of the Interior Geological Survey, 1979; pp 79993.
- (40) Kabashima, S.; Kawakubo, T. High frequency conductivity of NiO. *J. Phys. Soc. Jpn.* **1968**, *24*, 493–497.
- (41) Jonscher, A. K. A new understanding of the dielectric relaxation of solids. *J. Mater. Sci.* **1981**, *16*, 2037–2060.
- (42) Majid, S. R.; Arof, A. K. Electrical behavior of proton-conducting chitosan phosphoric acid- based electrolytes. *Phys. B* **2007**, *390*, 209–215.
- (43) K, S. L.; Roy, S.; Rao, K. U. Evaluation of activation energy (E_a) profiles of nanostructured alumina polycarbonate composite insulation materials. *Int. J. Mater., Mech. Manuf.* **2014**, *2*, 96–100.
- (44) Saha, S. K.; Rahman, M. A.; Sarkar, M. R. H.; Shahjahan, M.; Khan, M. K. R. Effect of Co-doping on structural, optical, electrical

and thermal properties of nanostructured ZnO thin films. *J. Semicond.* 2015, 36, 033004.

PAPER



Cite this: *Dalton Trans.*, 2020, **49**, 10554

Nitrogenous carbon dot decorated natural microcline: an ameliorative dual fluorometric probe for Fe³⁺ and Cr⁶⁺ detection†

Souravi Bardhan,^a Shubham Roy,^a Dipak Kr. Chanda,^b Saheli Ghosh,^a Dhananjay Mondal,^a Solanky Das^c and Sukhen Das^{a*}

In the modern era, the escalation of heavy metal discharges, especially from the industrial sector, is causing an enormous threat to nature. This article explores the dual sensing of heavy metals (Cr⁶⁺ and Fe³⁺) using a naturally formed microcline based sensor. A nano-sized microcline (M) was obtained via a facile top-down synthesis. In order to enhance the fluorescence property of the material, nitrogenous carbon-dots were loaded into the porous structure of the microcline (MCD) causing a bright blue fluorescence with remarkable stability. Detailed analysis of the composition and structure of the natural nano-sensor was carried out using X-ray diffraction, X-ray photoelectron spectroscopy, transmission electron microscopy, Fourier transform infrared spectroscopy, and BET analysis. This sensor material is highly selective towards Cr⁶⁺ and Fe³⁺, demonstrating a "turn-off" response in aqueous Fe³⁺ and a radical red shift of the fluorescence maxima for aqueous Cr⁶⁺. Density functional studies suggest that photoinduced electron transfer (PET) based quenching of fluorescence is responsible for these types of fluorescence alteration mechanisms. Efficient sensing of both Cr⁶⁺ and Fe³⁺ in various real-life water samples along with a real wastewater sample is also reported herein. A few studies have previously reported on efficient, natural material-based sensors, but they lack real-life applications due to their complicated synthesis and restricted functionalities. This work manages to overcome those drawbacks in its own fashion, providing a tremendously selective and sensitive (4 μM for Cr⁶⁺ and 19 μM for Fe³⁺) dual fluorescent probe.

Received 18th June 2020,
Accepted 5th July 2020

DOI: 10.1039/d0dt02166k

rsc.li/dalton

1. Introduction

Widespread industrialization and factory effluents are causing massive heavy-metal pollution and creating subsequent damage to aquatic biota and the environment. Among the various heavy metals, hexavalent chromium (Cr⁶⁺) and trivalent iron (Fe³⁺) are quite detrimental in excess levels and are found in abundance, especially around industrial areas.^{1–3}

Hexavalent chromium (Cr⁶⁺) is a well-known toxic carcinogen which is released into the environment mainly via industrial routes like leather tanneries, steel industries, battery manufacturing industries and pigment producing factories, causing malignant tumors, gastrointestinal ulceration, dermal irritation, and liver and lung cancer.^{4–6} On the other hand, tri-

valent iron (Fe³⁺) in excess concentration damages biomolecules, causing cellular toxicity, anemia, renal failure, heart and liver injury and can even result in serious ailments like Alzheimer's disease.^{7,8}

At present, various instrumental and spectroscopic techniques, such as chemiluminescence, X-ray fluorescence spectroscopy, atomic absorption spectrometry (AAS), inductively coupled plasma mass spectroscopy (ICP-MS), and electrochemical and amperometric techniques, have been adopted for heavy metal analysis,^{9–12} but they are mostly time-consuming, complicated, expensive and limited to off-site study. Hence, the development of fluorescent sensors for the detection of industrial contaminants has become a significant focus for numerous studies, as they have immense potential in the field of environmental science, biology, chemistry and also in the industrial field.^{13–15} Fluorescent ion sensors are gaining prominence due to their technical simplicity, high selectivity and superior sensitivity, portability and cost-effective nature.^{16,17} But there is a pressing need for the sensitive and accurate detection of multiple ions simultaneously using the same sensor material.^{18,19} Synthetic or organic fluorescent sensors can produce secondary toxicity,^{20,21} hence greater

^aDepartment of Physics, Jadavpur University, Kolkata-700032, India.

E-mail: sdasphysics@gmail.com; Tel: +919433091337

^bSchool of Materials Science and Nano-Technology, Jadavpur University, Kolkata-700032, India

^cDepartment of Geology, Jadavpur University, Kolkata-700032, India

† Electronic supplementary information (ESI) available. See DOI: 10.1039/d0dt02166k

emphasis is now given to eco-friendly, efficient, economical, easily accessible materials for synthesizing or fabricating fluorescent ion sensors.^{22,23} Although several papers have reported individual detection or sensing of Cr⁶⁺ and Fe³⁺,^{24–27} this work focuses on the development of a fluorescent probe from naturally occurring feldspar (microcline) for the simultaneous detection of Cr⁶⁺ and Fe³⁺.

Feldspar is the most abundant mineral on the earth's crust, yet not much attention has been given to its application as a fluorometric probe. This work introduces microcline feldspar, which is an aluminosilicate with AlO₄ and SiO₄ linked structures and containing mainly potassium.²⁸ The natural microcline has been tailored with nitrogenous carbon dots (C-dots). These carbon dots are highly stable, non-toxic, amorphous carbon based structures with globular shapes below 10 nm in size and with strong emission in the blue region of the spectrum.²⁹ The feasibility of application of these C-dots has been enhanced by decorating the microcline with these carbon based nanostructures, which gives this amorphous material a solid substrate for better applicability. C-dot decorated microclines, apart from their feasible synthesis technique and efficient selectivity and sensitivity, also have the advantages of being highly stable, non-toxic, eco-friendly, and convenient, and they could be useful for widespread application in sensing technologies.^{30,31}

2. Experimental section

2.1 Materials

Naturally occurring microcline was purchased from Hindustan Minerals, Kolkata, India. Anhydrous citric acid (Merck), ethylenediamine (Merck) and potassium bromide (Merck) used in the following experiments were of analytical grade, and were used without further purification. Millipore water (resistivity ~ 18.2 MΩ-cm) was used throughout the experiments.

2.2 Synthesis

2.2.1 Preparation of microcline nanoparticles (M). Microcline nanoparticles were synthesized *via* a top-down method, as reported elsewhere.²⁸ In a typical experiment, the microcline was washed thoroughly to remove debris and impurities and then manually ground in an agate mortar to reduce the size. Then the crushed sample was subjected to mechanical ball milling using a ball mill grinder (Fritsch Planetary Mono Mill Pulverisette 6) for 12 hours with a ball to sample mass ratio of 20 : 1 at 300 rpm using tungsten carbide vials and balls. The sample was collected and marked as M.

2.2.2 Synthesis of carbon dot (CD). Carbon dots (C-dots) were synthesized *via* a facile hydrothermal technique, as reported by Schneider *et al.*, 2017.³¹ Initially, 5.5 mM citric acid solution was prepared by dissolving anhydrous citric acid in water using a magnetic stirrer. The solution was basified by the drop-wise addition of ethylenediamine until the pH of the solution reached 12. After 2 h of continuous stirring, the solution was transferred into a Teflon-lined stainless steel auto-

clave and heated in a dust-free oven at 190 °C for 12 h. After the autoclave had cooled to room temperature, the solution was centrifuged at 5000 rpm for 15 min and the supernatant (C-dots) was collected for further use.

2.2.3 CD loading on the as-synthesized microcline nanostructure (MCD). Primarily, 500 mg of M was stirred with 10 ml of C-dots for 48 h and then centrifuged for 15 min at 5000 rpm. The precipitate was collected and dried under a vacuum for 24 h to develop a dry powder. This brownish nanopowder was further ground into fine grains and named MCD.

2.3 Computational methods

The microstructure, unit cell dimension and other crystallographic phase parameters of the samples were obtained by refining the experimental XRD patterns using the Rietveld based software package MAUD v2.8. A crystallographic information file (.cif) of pure microcline (AMCSD file no. 0020535) was used to refine the experimental diffractograms of the natural microcline. Initially, the refinement of the detector was done by refining the Caglioti PV functions.³² Instrumental broadening was also analyzed in due course. The Popa size-strain model was implemented to compute the crystal sizes and microstrain values.³³ The computed .cif files were further analyzed using the Vesta v3.4.3 (Visualization for Electronic and Structural Analysis) program in order to get a detailed description of the bonding network, such as bond angles and bond lengths.

The quantum chemical analyses with the hybrid Becke, 3-parameter, Lee–Yang–Parr (B3LYP) functional³⁴ coupled with the polarizable continuum aqueous solvent mode (CPCM)³⁵ was implemented to optimize the equilibrium geometries and to calculate the electronic transition properties of the nanostructures. The Gaussian type orbital based 6-31G**³⁶ basis set along with the RIJCOSX auxiliary basis function was used to describe the elements (C, H, O, N) and Cr and Fe ions, respectively. The geometric models were optimized without any symmetry constraint. Frequency analyses of the carbon dot structures were carried out at the same theoretical level, which depicts the absence of any imaginary frequency. Excited state energies and electronic transitions were calculated using the Time Dependent Density Functional Theory (TDDFT) method.³⁷ The TDDFT was used to evaluate the excited state energies for sensor MCD and MCD@Cr⁶⁺ and MCD@Fe³⁺ complexes.³⁸ These theoretical methods have been used to produce reliable results for such types of interactions. All the quantum chemical calculations were performed with the Orca v4.2 package and modeled with the Avogadro v1.2 program.³⁹

3. Results and discussion

3.1 Structural and morphological analyses

Since this work involves natural mineral samples, determination of the purity and quantification of various crystallographic parameters along with information regarding the successful incorporation of C-dots into the natural mineral is an

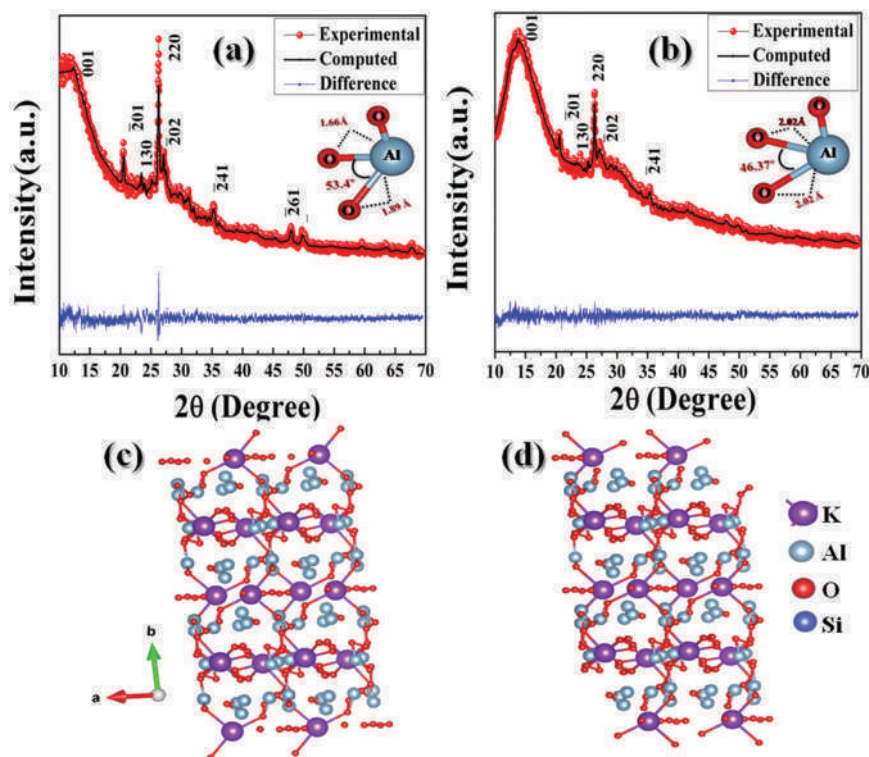


Fig. 1 Experimental (red), refined (black) and difference plot (blue) of XRD patterns of (a) M and (b) MCD, respectively, using the MAUD program; microstructural representation of (c) M and (d) MCD.

essential step. These parameters of the synthesized M and MCD were studied by using an X-ray powder diffractometer (D8, Bruker AXS, Wisconsin, USA) employing a Cu-K α target emitting a wavelength of 1.5418 Å and operated at 35 kV, 35 mA with a scan speed of 2 sec/step. Diffraction maxima of the microcline are in conformity with the Joint Committee on Powder Diffraction Standards (JCPDS) card no. 84-0708. Besides, the absence of undesirable peaks in the pure microcline (M) suggests the nonexistence of any impurities in the synthesized nanostructure.⁴⁰ Since the microcline samples were naturally collected, determination of purity was necessary and the well-matched peak positions indicate the high purity of the samples (Fig. 1a and b). The diffraction maxima of MCD are shifted slightly towards higher diffraction angles compared to the pure microcline. This phenomenon is attributed to the development of microstrain^{41–43} inside the triclinic microcline crystals due to the incorporation of C-dots, as is evident from the microstructural analysis (Table 1). Table 1 shows the results obtained after the final cycle of refinement regarding structural, microstructural, and reliability parameters. An increased value of microstrain in MCD occurs due to the substitution of smaller K⁺ ions (ionic radius 0.138 nm) with foreign C-dots having a larger ionic radius (0.170 nm). The average size for M is found to be 95.5 nm and it is 86.0 nm for MCD. The decrease in size is further evidence of enhanced microstrain in the case of MCD nano-crystals. The detailed bond angles and bond lengths as obtained from VESTA are illustrated in Fig. 1(c and d).

Table 1 Microstructural parameters of M and MCD obtained from Rietveld refinement

Parameters	M	MCD
a (Å)	8.06000	8.08200
b (Å)	13.01100	12.99000
c (Å)	7.03380	7.02600
α (°)	90.0590	90.2400
β (°)	117.0260	116.7400
γ (°)	87.3770	87.6500
V (Å ³)	656.2265	658.1042
Size (Å)	955.3373	860.4234
Microstrain	0.3182×10^{-4}	6.058×10^{-4}
R_p (%)	3.700	2.890
R_{wp} (%)	4.919	3.792

The functional groups and bond structures of the samples were examined by FTIR spectroscopy. FTIR was performed using a PerkinElmer RXI spectrophotometer in the wave number ranges from 500 cm⁻¹ to 4000 cm⁻¹ by making solid pellets of a homogenized mixture of samples with KBr in a ratio of 1 : 50. In both M and MCD (Fig. 2), spectral bands are located at 578 cm⁻¹ due to the coupling between the O–Si–O bending vibration and the K–O stretching vibration.⁴⁴ Absorption bands situated at 728 and 775 cm⁻¹ are attributed to the Si–Al (Si) and the Si–Si stretching vibrations, respectively.²⁸ The relatively broader peak centered at 1034 cm⁻¹ in both cases is due to Si(Al)–O stretching vibrations.⁴⁴ The IR

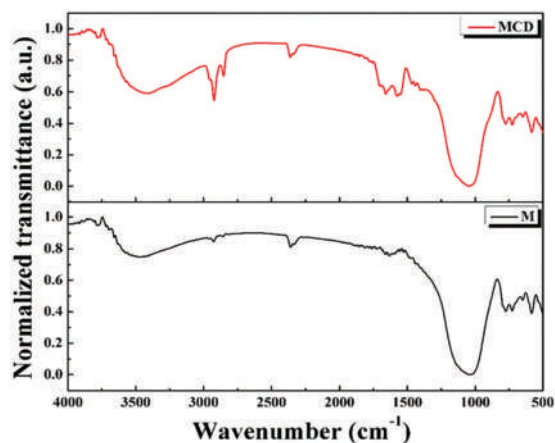


Fig. 2 FTIR spectra of the samples M and MCD.

band visible at 2363 cm^{-1} is ascribed to Al–OH vibration. The absorption bands centered at 1562 cm^{-1} and 1656 cm^{-1} are due to the bending vibrations of N–H, C=N and C=O, respectively.³¹ Similarly, there is an augmentation in IR intensities at 2846 and 2922 cm^{-1} . These bands are ascribed to the stretching vibrations of C–H. This entire set of IR bands was significantly enhanced in the case of MCD, which was caused by the incorporation of nitrogenous C-dots into the microcline.

Morphological characterization of the samples was performed using a JEOL JEM-2000 transmission electron microscope (TEM) operated at 200 kV. Initially, a very small amount of sample was dispersed in acetone and vigorously mixed in an ultrasonic bath for 15 minutes and then caste dropwise onto a carbon coated copper grid (300 meshes) for microscopy. Fig. 3 depicts the TEM micrographs of the samples. Fig. 3a shows tiny spherical/globular structures of nitrogenous carbon dots with an average diameter of 3–4 nm. These C-dots are evenly distributed on the surface and nearly equal in size. The pure microcline particles (Fig. 3b) are quite agglomerated and nearly spherical in shape. These particles have diameters between 40 and 60 nm. The grains of pure microcline are agglomerated in order to minimize their surface energy. It is quite evident from Fig. 3c that the surface of the MCD is rougher than that of the pure microcline. This surface roughness is due to the amalgamation of C-dots. Henceforth, structural and morphological analyses suggest that C-dots are successfully assimilated into the natural microcline matrix.

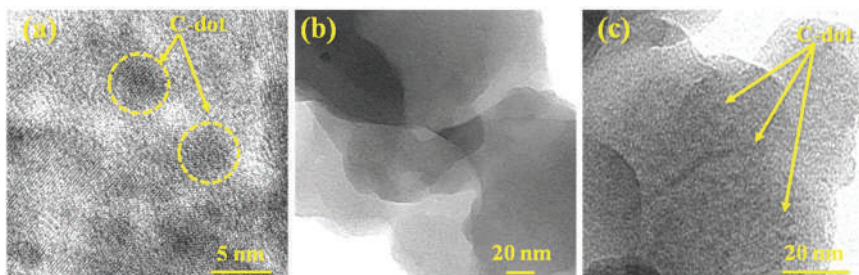


Fig. 3 TEM micrographs of the samples (a) C-dot, (b) M and (c) MCD.

3.2 Elemental analyses of pure and C-dot decorated microcline

In order to study the elemental composition of the synthesized samples, energy dispersive X-ray analysis (EDX) was performed. The EDX data (Fig. S1†) confirms the purity of the nano-sized microcline sample. The presence of a minute amount of sodium (1.98%) in the microcline is quite common and has been reported elsewhere.²⁸ Additionally, the C-dot doped microcline shows the signature peaks of carbon in its spectrum. This study suggests the successful inclusion of C-dots in the natural microcline.

Furthermore, a detailed study was initiated to verify the elemental composition of the nanostructured samples by using an X-ray photoelectron spectroscopy (XPS) method. A PHI 5000, Versa probe II (USA) equipped with an Al-K α radiation source with a survey scan from 0 to 1200 eV was employed for these measurements. The XPS spectra obtained were further analyzed using the CASA XPS software platform and are illustrated in Fig. 4. XPS data confirms the presence of 55.09% O 1s (530.4 eV), 30.74% Si 2p (101.6 eV), 9.75% Al 2p (72.8 eV) and 4.41% K 2p (292.0 eV) in the nano-sized micro-

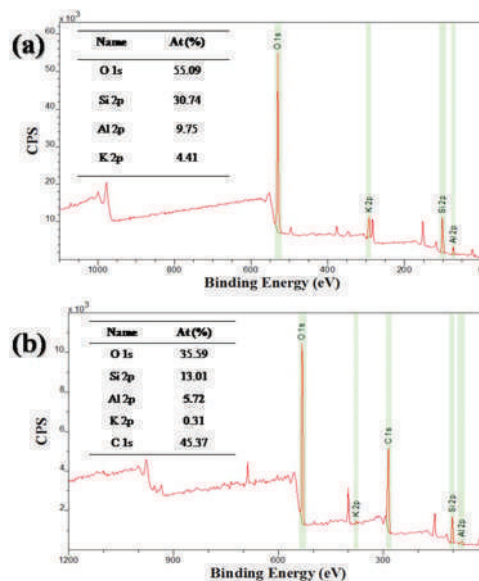


Fig. 4 X-ray photoelectron spectroscopy (XPS) of (a) M and (b) MCD.

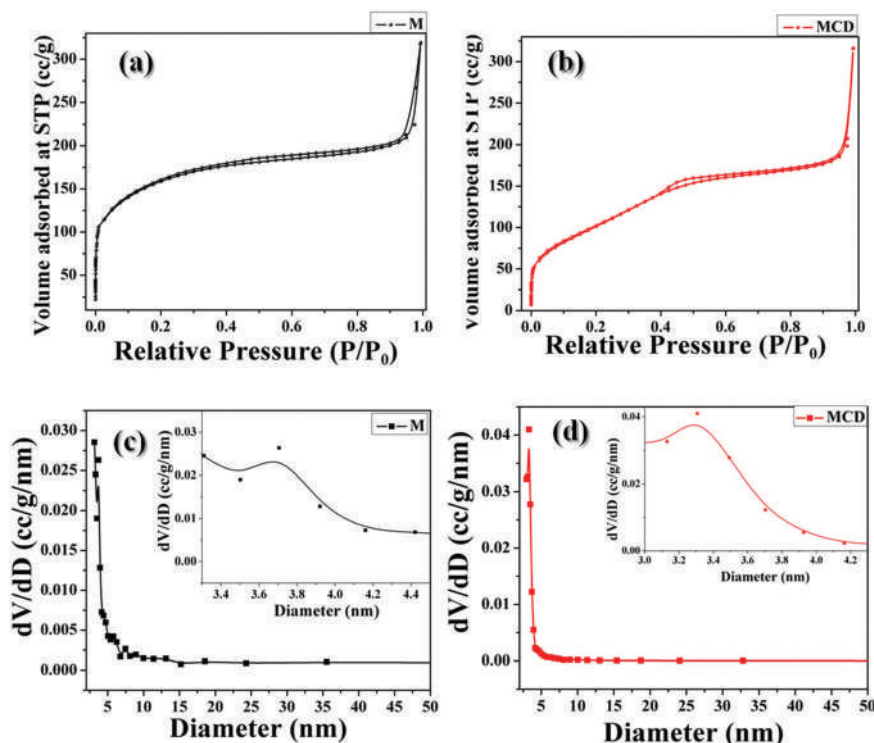


Fig. 5 N_2 adsorption/desorption isotherm of (a) M and (b) MCD; pore size distribution data for (c) M and (d) MCD.

cline sample, which confirms its purity.⁴⁵ The XPS data for the C-dot loaded microcline shows 35.59% O 1s (532.5 eV), 13.01% Si 2p (102.5 eV), 5.72% Al 2p (75.0 eV), 0.31% K 2p (377.5 eV) and 45.37% C 1s (285.0 eV). Since the electro-negativity of carbon is slightly higher than that of the 'parent elements' like Al, Si and K, C-dot loading causes an increase in the binding energy⁴⁶ to some extent for these elements.

Moreover, there is a high reduction in the atomic percentage of potassium in both EDX and XPS data. This corroborates the fact that K^+ ions have been replaced by C-dots, as previously mentioned in the XRD section.

3.3 Estimation of surface behavior of the nanostructures

The average surface area and surface porosity of the nanostructures were estimated using the standard Brunauer-Emmett-Teller (BET) and Barrett-Joyner-Halenda (BJH) method. A Twin Surface Area Analyzer from Quanta-chrome Instruments (USA) was employed in this regard. Nitrogen (N_2) was used to study the adsorption-desorption isotherms and corresponding pore size distributions. The surface areas and pore diameters (Fig. 5) obtained for M and MCD are provided in Table 2. The average pore diameters for both M and MCD imply the mesoporosity of the samples. The mean pore diameter of the pure microcline is around 3.7 nm, whereas it is 3.3 nm for the doped microcline sample. In reality, C-dots are being trapped into the porous surface of the pure microcline during the synthesis of MCD, which in turn causes the reduction in pore diameter for this sample. Thus the microcline acts as a great substrate for C-dot binding. The hysteresis

Table 2 Estimated BET surface area, pore diameter, and pore volume data of M and MCD

Sample name	Surface area ($m^2 g^{-1}$)	Pore size (nm)	Pore volume ($ml g^{-1}$)
M	49.091	3.69	0.242
MCD	137.266	3.28	0.349

loop, which is mainly associated with the capillary condensation in mesoporous material, suggests a type IV isotherm in both cases.⁴⁷ Type IV isotherms are very useful as industrial adsorbents. Moreover, there is an enhancement in surface area in MCD along with pore volume, which might be due to the addition of C-dots in the structure.

3.4 Optical quality of the nanostructures

The optical qualities of the synthesized materials were analyzed with absorption and emission spectroscopy techniques. In a typical absorption experiment, the powdered sample was dispersed in distilled water at a concentration of 500 μM and vigorously mixed in an ultrasonic bath for 20 minutes. The absorbance spectra of the solutions were recorded in a λ -25, PerkinElmer UV-Vis spectrometer and are depicted in Fig. S2a.† It can be observed in Fig. S2a.† that the absorption maxima centered at 250 and 350 nm for MCD are absent in the pure microcline. The DFT formalism is adopted herein to explain the electronic transition pathways of the MCD sample. Initially, a molecular model of the carbon dot was made by

assuming five carbon cycles. It is quite evident from other literature that the optical quality of the MCD is due to the incorporation of C-dots alone.^{48,49} Thus, natural microcline acts as a 'holder' of the optically activated carbon dot, giving it a solid substrate for better applicability. The TDDFT study of the C-dot (Fig. S2b†) shows that π -stacking is mainly responsible for the absorption phenomenon. Similar reports have been published by other groups.^{50,51} In reality, the HOMO-4 (−6.923 eV) to LUMO+1 (−0.393 eV) transition is responsible for the 250 nm band, whereas the HOMO−1 (−6.9141 eV) to LUMO+1 (−0.393 eV) transition is the origin of the 350 nm band of the MCD.

In order to determine the emission and fluorescence characteristics of the samples, photoluminescence spectroscopy was performed using a Cary Eclipse Fluorescence Spectrophotometer (Agilent Technologies) at room temperature. PL spectra were recorded at different excitation wavelengths ranging from 350 nm to 400 nm, but the optimum fluorescence intensity was observed at 370 nm (Fig. S3a†). Hence, the optical studies were carried out at an excitation wavelength (λ_{ex}) of 370 nm. The emission spectra are depicted in Fig. S2c,† which shows a radical enrichment in fluorescence intensity for the MCD sample. The luminescent maxima were found at 428 nm for M and 458 nm for MCD, which also suggests a near-blue emission of our samples. The significant enhancement of fluorescence intensity in the case of MCD is due to surface functionalization of the C-dots.⁵² In fact, nitrogenous carbon dots carry surface functional groups like C=N (in this case), which introduce new energy levels and modulate the band gap, synergistically causing enhanced fluorescence intensity. It has already been established that the presence of N-dopant, which in our case has been introduced by using ethylenediamine, induces charge dislocation, thus efficiently promoting the electron transfer ability of carbon.⁴⁸

The stability of the fluorescence activity of MCD was also investigated with varying time and pH values. Primarily, a 500 μM solution of MCD was used to determine the photostability up to 90 min. Fluorescence was recorded every 5 min under an excitation wavelength of 370 nm, with subsequent exposure to light illumination in each interval (Fig. S3b†). The fluorescence remains stable irrespective of time, confirming the promising photo-stability of the sensor material (MCD).

Furthermore, the effect of pH was examined by adding HCl and NaOH to as-prepared solutions of MCD. The fluorescence spectra decrease slightly under strongly acidic or basic conditions (less than pH 4 or greater than pH 9) but there are no obvious changes in fluorescence intensity at a pH between 4 and 9 (Fig. S3c†). This type of minute fluorescence quenching under strong acidic or basic conditions is attributed to the inner filter effect,⁵³ which happens when some of the fluorophores are less accessible than others. Henceforth, the optimum pH was chosen to be 7.0 for the optical activity assays. Thus, the MCD sample could be used in various fluorometric applications due to its notable stability and emission property in the blue region of the spectrum.

3.5 MCD as a fluorometric probe

3.5.1 Selectivity assay of the probe. Selectivity of the sensing probe to a specific target molecule is an important parameter in sensing technology. The fluorescence responses of the sensor was evaluated against a range of ions (Na^+ , K^+ , Ca^{2+} , As^{3+} , Fe^{2+} , Fe^{3+} , Cr^{3+} , Cr^{6+} , Cd^{2+} , Pb^{4+} , Hg^{2+} , Al^{3+} , Co^{2+} , Mg^{2+} , Mn^{2+} , Ni^{2+} , Ti^{4+} , CO_3^{2-} , S^{2-} , SO_4^{2-} , NO_3^- , OH^- , Cl^- , SO_3^{2-} , PO_4^{3-}) at specific concentrations of 500 μM in each case using a Cary Eclipse fluorescence spectrophotometer from Agilent Technologies with an excitation wavelength (λ_{ex}) of 370 nm. The entire set of ions show nominal change in the luminescent maxima centered at 458 nm, but some significant changes were observed when Fe^{3+} and Cr^{6+} were added to the MCD solution. In the case of Fe^{3+} , the fluorescence intensity centered at 458 nm dropped radically, and along with reasonable quenching it was red shifted to 505 nm when exposed to Cr^{6+} (Fig. 6). Fig. 7(a and b) depicts the results of the selectivity test. This alteration in bright blue fluorescence in both cases could also be visualized with the naked eye on exposing them to a UV lamp with 365 nm excitation (Fig. 8e), which is in accordance with the fluorescence data. Furthermore, the efficiency of selectivity of Fe^{3+} and Cr^{6+} in the presence of common ions (Na^+ , K^+ , Ca^{2+} , Al^{3+} , Mg^{2+} , CO_3^{2-} , SO_4^{2-} , NO_3^- , OH^- , Cl^-) in water was also determined. In each case, 500 μM of each ion was added to MCD and the fluorescence was measured on adding Fe^{3+} and Cr^{6+} at a low concentration (34 μM). Fig. 7(c and d) shows that MCD effectively senses both Fe^{3+} and Cr^{6+} irrespective of the presence of various interfering ions, thus confirming its efficiency.

3.5.2 Sensitivity assay and Stern–Volmer plots. In order to determine the quenching constant (K_{SV}) and sensitivity (LOD) of the sensor material, the fluorescence data obtained from varying the concentrations (0–68 μM) of both ions (Fe^{3+} and Cr^{6+}) were plotted and fitted against the linear Stern–Volmer (S–V) equation⁵⁴ (Fig. 8a–d), expressed as,

$$\frac{I_0}{I} = 1 + K_{\text{SV}}[\text{M}] \quad (1)$$

where, I_0 and I are the fluorescence intensities prior to and after the addition of both quenching ions, respectively, $[\text{M}]$ represents the concentration of the ions and K_{SV} is the Stern–Volmer quenching constant.

In the case of Cr^{6+} , the fluorescence intensity at 458 nm is considered to be I_0 while the fluorescence intensities centered at 505 nm are considered to be I for different concentrations, and the ratio metric change was calculated and plotted (Fig. 8b) against the varying concentration. The plot shows a linear upward increment of I_0/I with increasing quencher concentration, with a fitting coefficient of 0.99464. In a similar manner, linear S–V fitting is obtained for Fe^{3+} and, in this case, the fitting coefficient is found to be 0.99856. As the Fe^{3+} ion does not shift the luminescent maxima during the interaction with MCD, both I_0 and I are fixed at 458 nm in this case (Fig. 8d).

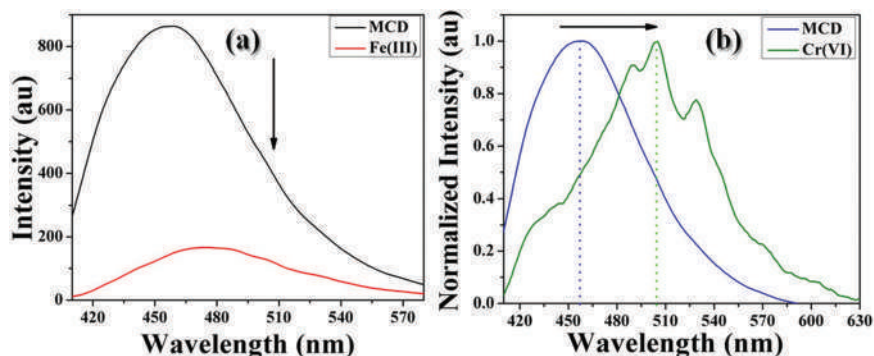


Fig. 6 Alteration in fluorescence intensity of MCD upon addition of (a) Fe^{3+} and (b) Cr^{6+} .

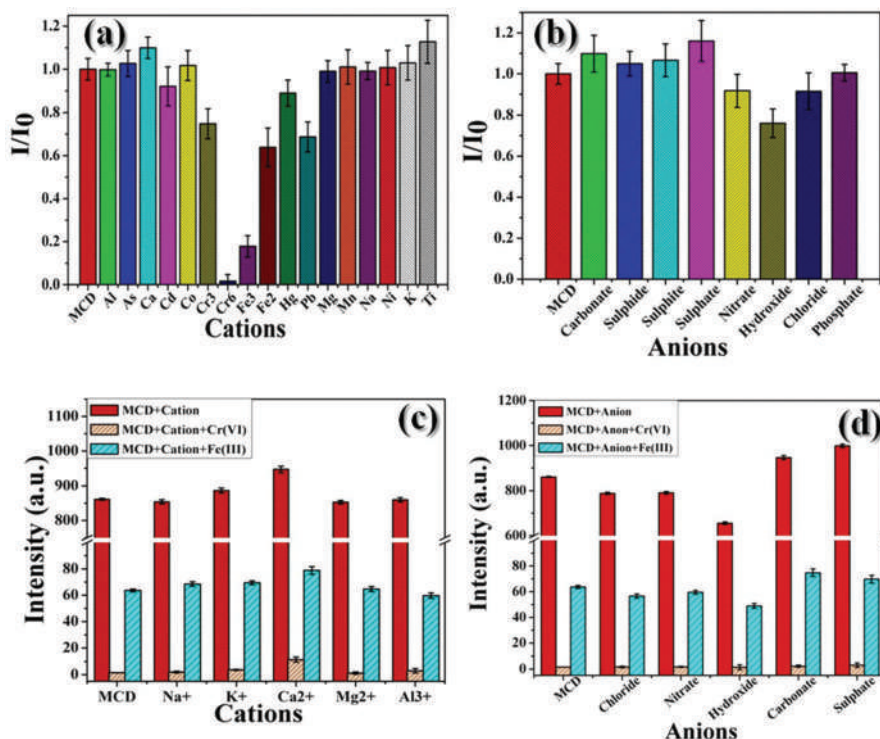


Fig. 7 Selectivity studies of the MCD by using various (a) cations and (b) anions; interference studies of various common (c) cations and (d) anions on Fe^{3+} and Cr^{6+} sensing.

The limit of detection (LOD) is evaluated for both ions from the linear Stern–Volmer plots using the following expression,⁵⁴

$$\text{LOD} = \frac{3\sigma}{K_{\text{SV}}} \quad (2)$$

where, σ is the standard deviation found by taking at least ten measurements of the fluorescence intensities of the pure sensor material without the presence of any quencher and K_{SV} is the quenching constant. The LOD is found to be around $4 \mu\text{M}$ in case of Cr^{6+} and for Fe^{3+} , it is around $19 \mu\text{M}$. These low detection limits make this natural mineral based fluorometric probe a desirable candidate for sensing applications, if properly constructed.

3.6 Mechanism of detection

There are several pathways that can alter the nature of an emission spectrum. Among them, photo-induced electron transfer (PET), energy transfer (ET) and the inner filter effect (IFE) are quite common.⁵⁵ A highly negative surface (Fig. S4[†]), ‘sponge-like’ mesoporous surface morphology (Table 2) and C=N bonds carrying C-dots on the surface of the natural microcline mean superior affinity of this material towards Fe^{3+} and Cr^{6+} .

Time resolved fluorescence spectroscopy (TCSPC) and TDDFT studies were carried out in order to confirm the fluorescence alteration mechanisms. TCSPC depicts the excited state phenomenon or more precisely the fluorescence lifetime value of a sample. In this experiment, an MCD solution of

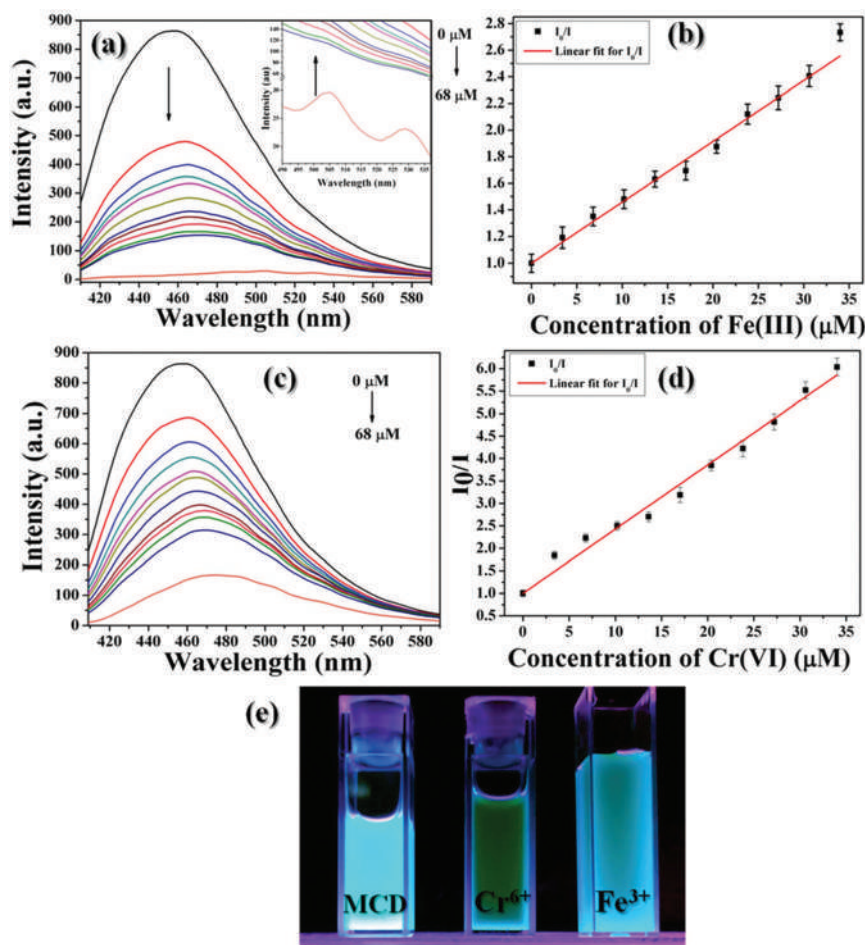


Fig. 8 Fluorescence titration data for MCD sample using (a) Cr⁶⁺ and (c) Fe³⁺ as the quencher; Stern–Volmer fitting of the subsequent fluorescence quenching data by (b) Cr⁶⁺ and (d) Fe³⁺; (e) naked eye observation of the fluorescence quenching of MCD upon addition of Cr⁶⁺ and Fe³⁺ as seen under UV light.

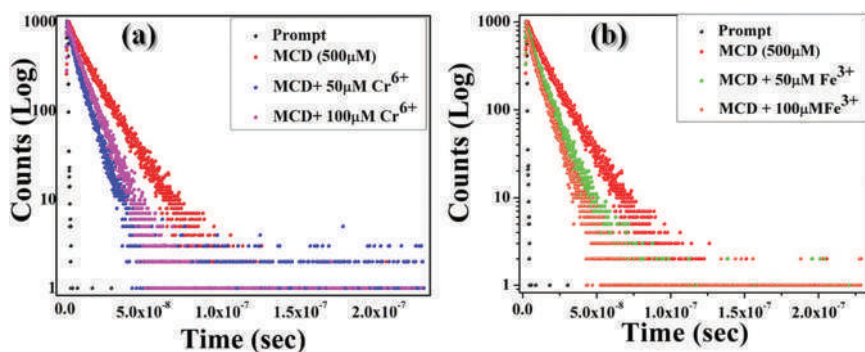


Fig. 9 Time resolved fluorescence spectra (lifetime) of pure MCD, MCD with the addition of 50 μM and 100 μM of (a) Cr⁶⁺ and (b) Fe³⁺, indicating the reduction in fluorescence lifetime with increasing Cr⁶⁺ and Fe³⁺ concentration, which demonstrates electron transfer mechanism between MCD and Cr⁶⁺ and Fe³⁺.

500 μM was prepared and the lifetime was measured in a time-resolved spectrofluorometer from IBH (UK). The fluorescence lifetime of pure MCD is around 13.6 ns, which is greatly reduced to 7.75 and 7.14 ns when exposed to Fe³⁺ and Cr⁶⁺,

respectively (Fig. 9). Table 3 depicts the concentration-dependent quenching in lifetime values upon the addition of these two contaminants. Reduced lifetime values suggest that the fluorescent probe detects the contaminant ions in the excited

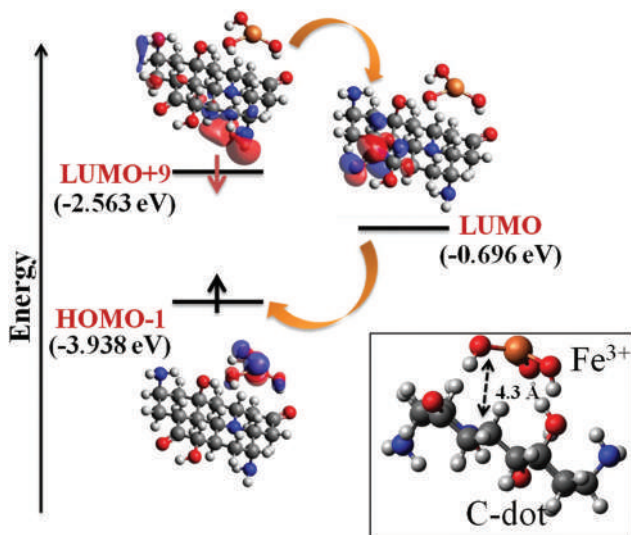
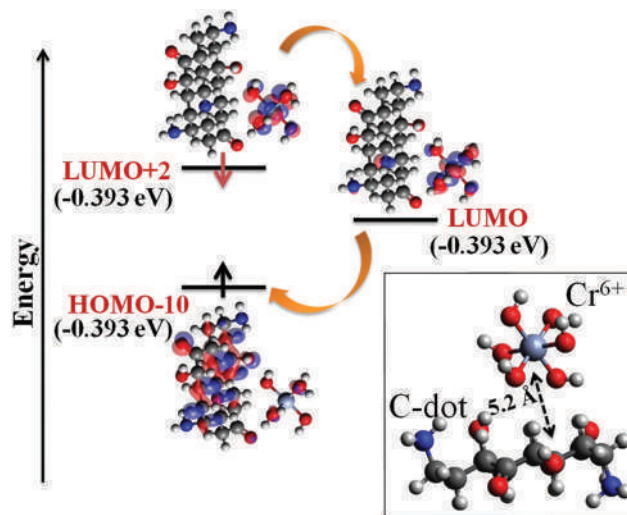
Table 3 Estimated lifetime of MCD on addition of various concentrations of quencher (Cr^{6+} and Fe^{3+})

Concentration of quencher (μM)	Lifetime (ns)	
	Cr^{6+}	Fe^{3+}
0	13.6200	13.6200
50	8.909	9.173
100	7.141	7.7512

state.^{54,55} In addition, TDDFT studies have been carried out in order to ensure the sensing mechanism more accurately. It was mentioned earlier that the microcline 'holds' the optically activated carbon dots as a substrate material; thus carbon dots play the primary role in sensing. Thus, interaction studies using TDDFT were implemented by taking the C-dots alone. Initially, the electrostatic potential of the C-dot surface was mapped and probable binding sites for Fe^{3+} and Cr^{6+} were located (Fig. S5[†]). After locating the binding sites, Fe^{3+} and Cr^{6+} ions are kept in close proximity ($\sim 5 \text{ \AA}$) to those binding sites. It is evident from TDDFT studies that both cations select the nitrogen containing part of the C-dot for interaction.

The TDDFT data for the Fe^{3+} and Cr^{6+} induced C-dot shows no bond formation between the contaminant ions and the C-dot. In reality, they are around 4.3 \AA (for Fe^{3+}) and 5.2 \AA (for Cr^{6+}) apart from the C-dot molecule. It is also observed that for the Fe^{3+} @C-dot complex, the HOMO-1 to LUMO+9 transition (238.7 nm) is mainly responsible for photon absorption as it has the largest oscillator strength (~ 0.933) (Fig. 10). In the case of the Cr^{6+} @C-dot complex, the electron jumps from HOMO-10 to LUMO+2 (624.5 nm) during absorption (oscillator strength ~ 0.790) (Fig. 11).

According to Kasha's rule,⁵⁶ the distribution on the excited state (energetically higher than the LUMO) would decay to the

**Fig. 10** Molecular orbitals and electronic transitions involved in fluorescence quenching of MCD upon addition of Fe^{3+} .**Fig. 11** Molecular orbitals and electronic transitions involved in fluorescence quenching of MCD upon addition of Cr^{6+} .

LUMO state momentarily through the internal conversion (IC) process and finally the LUMO to ground state transition would occur. During emission from the Fe^{3+} @C-dot complex, the LUMO+9 to LUMO transition results in non-radiative decay, which quenches the fluorescence of the C-dot. A similar phenomenon happens when the electron jumps from LUMO+2 to LUMO in the Cr^{6+} @C-dot complex. Finally, the LUMO to ground state transition occurs in both cases. Surprisingly, the Cr^{6+} @C-dot complex shows green emission upon excitation. This could be due to the band gap value of the radiative path (2.49 eV) during emission. This green emission is visible, as the energy value of non-radiative decay is less than the radiative decay during emission from the complex. Henceforth, electron transfer (PET) plays a pivotal role in the sensing of both contaminants.

3.7 Application of the sensor in real-life water and wastewater samples

In order to verify the applicability of the sensor material in real life, the sensing of both ions is conducted against various real-life water samples. Water samples from four different sources were collected; tap water was collected from the laboratory tap, potable water was collected from the water purifier adjacent to our laboratory, groundwater was collected from a borewell within our institute area, and pond water was collected from a nearby pond situated inside our institute campus. Initially, suspended impurities were removed from the water samples by using membrane filters (pore size $\sim 0.45 \mu\text{m}$) and quantitative analysis was performed (Table 4) using a portable pH/TDS/Temperature Meter (Hanna HI991300). Then the water samples were spiked with the targeted ions separately, maintaining $500 \mu\text{M}$ concentrations, and subsequently the fluorescence was measured. Each measurement was repeated three times and Fig. 12a shows the average alteration occurring on addition of the ions in each sample. In all cases, rapid quench-

Table 4 Physical parameters of the collected water samples

Type of water	pH	TDS (ppm)
Drinking water	7.8	184
Tap water	7.4	1009
Pond water	7.78	1201
Borewell	7.2	1490

Table 5 ICP-AES data of the collected tannery wastewater sample

Constituents	Amount (ppm)
Lead (Pb)	0.12
Chromium (Cr)	21.69
Iron (Fe)	5.42

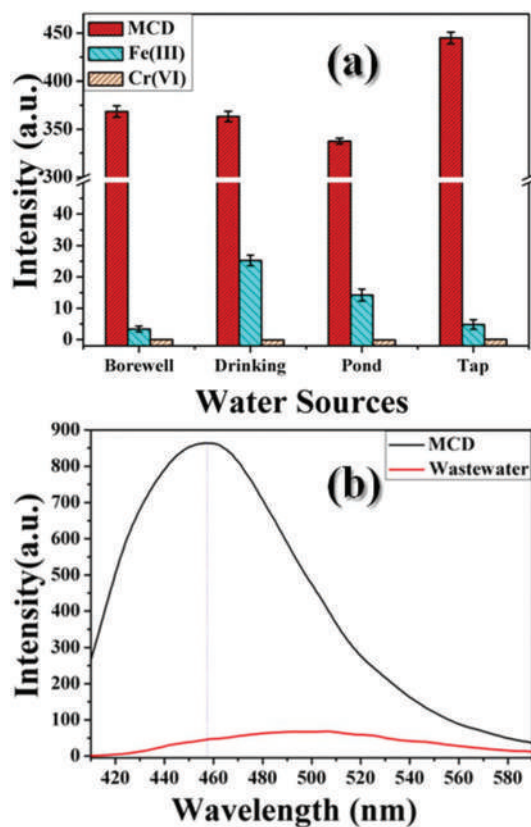


Fig. 12 (a) Sensing of Cr^{6+} and Fe^{3+} in different water samples; (b) fluorescence quenching of a real-life tannery wastewater sample under 370 nm excitation.

ing is visible for Fe^{3+} ions and a red shift in the fluorescent maxima is observed in the case of Cr^{6+} . This phenomenon is analogous to the previous result, confirming that the sensor material can perform efficiently in any type of water sample irrespective of the presence of other disturbing elements.⁵⁷

Application to real-life sensing was also investigated against wastewater collected from the canal connected to a nearby tannery industry. Elemental analysis of the wastewater was performed using an Inductively Coupled Plasma Atomic Emission Spectrometer (ICP-AES; Spectro Analytical; Table 5). The results showed the presence of a high amount of chromium (~ 21.7 ppm), along with traces of iron (~ 5.4 ppm) in the wastewater. The raw wastewater was diluted using Millipore water (1 : 10) and then MCD was added. The fluorescence intensity was measured upon excitation at 370 nm. Significant quenching of fluorescence was also visible in this case (Fig. 12b), con-

firmed the ability of MCD to detect contaminants in real-life water too, irrespective of the presence of various interfering ions.

4. Conclusion

In summary, a fluorescent nano-probe was successfully developed using a naturally collected microcline, whose nanonization was done *via* a 'top-down' synthesis approach. Further modification was done by doping nitrogenous carbon dots into the natural nanostructure (MCD). The carbon dots were successfully synthesized by a one-step hydrothermal method. MCD shows promising fluorescence intensity along with a remarkable pH response and photo stability making it a potential candidate for sensing applications, compared to other sensors (Table S1†). On adding various ions, MCD shows that the fluorescence is selectively altered for Fe^{3+} and Cr^{6+} alone. Additionally, in the case of Cr^{6+} , there is a massive 'red-shift' in the fluorescence maximum towards the green region, which is well visible on exposure to a UV lamp. The 'turn-off' mechanism for both Fe^{3+} and Cr^{6+} is attributed to dynamic quenching due to its affinity towards the electron-rich groups in the C-dot part of the sensor, resulting in photo-induced electron transfer. Such results are also evident in the case of real-life water samples collected from diverse sources including a tannery industry. Henceforth, MCD, being a natural, biocompatible, cost-effective and facile sensor, could be a potential material for widespread use in scientific and industrial applications due to its remarkable selectivity and sensitivity.

Conflicts of interest

The authors declare no conflict of interest.

Acknowledgements

Authors would like to thank the Department of Physics, Jadavpur University, for extending experimental facilities. S.D. would like to acknowledge DST-SERB (Grant No. EEQ/2018/000747) for funding.

References

- 1 P. K. Gautam, R. K. Gautam, S. Banerjee, M. C. Chattopadhyaya and J. D. Pandey, *Heavy metals in the*

- environment: fate, transport, toxicity and remediation technologies, Nova Sci Publishers, 2016, vol. 60, pp. 101–130.
- R. Ying, H. Lu and S. Xu, Ion imprinted dual reference ratiometric fluorescence probe for respective and simultaneous detection of Fe^{3+} and Cu^{2+} , *New J. Chem.*, 2019, **43**, 6404–6410.
 - S. Elabbas, L. Mandi, F. Berrekhis, M. N. Pons, J. P. Leclerc and N. Ouazzani, Removal of Cr(III) from chrome tanning wastewater by adsorption using two natural carbonaceous materials: eggshell and powdered marble, *J. Environ. Manage.*, 2016, **166**, 589–595.
 - M. Fontaine, Y. Clement, N. Blanc and C. Demesmay, Hexavalent chromium release from leather over time natural ageing vs accelerated ageing according to a multivariate approach, *J. Hazard. Mater.*, 2019, **368**, 811–818.
 - F. V. Hackbarth, D. Maass, A. A. U. de Souza, V. J. Vilar and S. M. G. U. de Souza, Removal of hexavalent chromium from electroplating wastewaters using marine macroalga *Pelvetia canaliculata* as natural electron donor, *Chem. Eng.*, 2016, **290**, 477–489.
 - S. Mishra and R. N. Bhargava, Toxic and genotoxic effects of hexavalent chromium in environment and its bioremediation strategies, *J. Environ. Sci. Health, Part C: Environ. Carcinog. Ecotoxicol. Rev.*, 2016, **34**(1), 1–32.
 - S. K. Kailasa, S. Ha, S. H. Baek, S. Kim, K. Kwak and T. J. Park, Tuning of carbon dots emission color for sensing of Fe^{3+} ion and bioimaging applications, *Mater. Sci. Eng., C*, 2019, **98**, 834–842.
 - J. Shanguan, J. Huang, D. He, X. He, K. Wang, R. Ye, X. Yang, T. Qing and J. Tang, Highly Fe^{3+} selective fluorescent nanoprobe based on ultrabright N/P codoped carbon dots and its application in biological samples, *Anal. Chem.*, 2017, **89**, 7477–7484.
 - K. Pomazal, C. Prohaska, I. Steffan, G. Reich and J. F. K. Huber, Determination of Cu, Fe, Mn, and Zn in blood fractions by SEC-HPLC-ICP-AES coupling, *Analyst*, 1999, **124**, 657–663.
 - J. H. Pang, Y. Liu, J. Li and X. J. Yang, Solvothermal synthesis of nano- CeO_2 aggregates and its application as a high-efficient arsenic adsorbent, *Rare Met.*, 2019, **38**(1), 73–80.
 - M. L. Rahman, M. S. Sarjadi, S. E. Arshad, M. M. Yusoff, S. M. Sarkar and B. Musta, Kenaf cellulose-based poly (amidoxime) ligand for adsorption of rare earth ions, *Rare Met.*, 2019, **38**(3), 259–269.
 - M. Sobkowiak, R. Gabrielsson, O. Inganas and G. Milczarek, Amperometric detection of iron(III) on electroconductive hydrogel based on polypyrrole and alkoxy sulfonated poly (3,4-ethylenedioxythiophene) (PEDOT-S), *Synth. Met.*, 2014, **194**, 170–175.
 - S. Hussain, A. H. Malik, M. A. Afroz and P. K. Iyer, Ultrasensitive detection of nitroexplosive-picric acid via a conjugated polyelectrolyte in aqueous media and solid support, *Chem. Commun.*, 2015, **51**(33), 7207–7210.
 - M. Van de Weert and L. Stella, Fluorescence quenching and ligand binding: a critical discussion of a popular methodology, *J. Mol. Struct.*, 2011, **998**(1–3), 144–150.
 - Q. Hu, L. Gao, S. Q. Rao, Z. Q. Yang, T. Li and X. Gong, Nitrogen and chlorine dual-doped carbon nanodots for determination of curcumin in food matrix via inner filter effect, *Food Chem.*, 2019, **280**, 195–202.
 - B. Valeur and I. Leray, Design principles of fluorescent molecular sensors for cation recognition, *Coord. Chem. Rev.*, 2000, **205**, 3–40.
 - A. P. de Silva, H. Q. N. Gunaratne, T. Gunnlaugsson, A. J. M. Huxley, C. P. McCoy, J. T. Rademacher and T. E. Rice, Signaling recognition events with fluorescent sensors and switches, *Chem. Rev.*, 1997, **97**, 1517–1566.
 - S. Sakunkaewkasem, A. Petdum, W. Panchan, J. Sirirak, A. Charoenpanich, T. Sooksimuang and N. Wanichacheva, Dual-analyte fluorescent sensor based on [5] helicene derivative with super large Stokes shift for the selective determinations of Cu^{2+} or Zn^{2+} in buffer solutions and its application in a living cell, *ACS Sens.*, 2018, **3**(5), 1016–1023.
 - Y. Liu, Q. Fei, H. Shan, M. Cui, Q. Liu, G. Feng and Y. Huan, A novel fluorescent ‘off-on-off’ probe for relay recognition of Zn^{2+} and Cu^{2+} derived from N, N bis (2-pyridylmethyl) amine, *Analyst*, 2014, **139**, 1868–1875.
 - A. Kumar, A. R. Chowdhuri, D. Laha, T. K. Mahto, P. Karmakar and S. K. Sahu, Green synthesis of carbon dots from *Ocimum sanctum* for effective fluorescent sensing of Pb^{2+} ions and live cell imaging, *Sens. Actuators, B*, 2017, **242**, 679–686.
 - W. Liu, H. Diao, H. Chang, H. Wang, T. Li and W. Wei, Green synthesis of carbon dots from rose-heart radish and application for Fe^{3+} detection and cell imaging, *Sens. Actuators, B*, 2017, **241**, 190–198.
 - S. Yang, X. Sun, Z. Wang, X. Wang, G. Guo and Q. Pu, One-step facile green synthesis of a highly fluorescent molecule through a way towards carbon dots and detection of dopamine based on *in situ* formation of silver nanoparticles, *Sens. Actuators, B*, 2017, **253**, 752–758.
 - R. Bandi, B. R. Gangapuram, R. Dadigala, R. Eslavath, S. S. Singh and V. Guttena, Facile and green synthesis of fluorescent carbon dots from onion waste and their potential applications as sensor and multicolour imaging agents, *RSC Adv.*, 2016, **6**(34), 28633–28639.
 - A. J. Weerasinghe, F. A. Abebe and E. Sinn, Rhodamine based turn-ON dual sensor for Fe^{3+} and Cu^{2+} , *Tetrahedron Lett.*, 2011, **52**, 5648–5651.
 - L. Long, L. Zhou, L. Wang, S. Meng, A. Gong and C. Zhang, A ratiometric fluorescent probe for iron(III) and its application for detection of iron(III) in human blood serum, *Anal. Chim. Acta*, 2014, **812**, 145–151.
 - C. Y. Li, Z. Chun-Xiang, Y. F. Li, J. L. Tang and C. Weng, A new rhodamine-based fluorescent chemosensor for Fe^{3+} and its application in living cell imaging, *Dyes Pigm.*, 2014, **104**, 110–115.
 - S. Huang, H. Qiu, F. Zhu, S. Lu and Q. Xiao, Graphene quantum dots as on-off-on fluorescent probes for chromium(VI) and ascorbic acid, *Microchim. Acta*, 2015, **182**(9–10), 1723–1731.

- 28 S. Bardhan, S. Roy, D. K. Chanda, S. Das, K. Pal, A. Chakraborty, R. Basu and S. Das, Microstructure and Dielectric Properties of Naturally Formed Microcline and Kyanite: A Size-Dependent Study, *Cryst. Growth Des.*, 2019, **19**(8), 4588–4601.
- 29 S. T. Yang, X. Wang, H. Wang, F. Lu, P. G. Luo, L. Cao, M. J. Meziani, J. H. Liu, Y. Liu, M. Chen, Y. Huang and Y. P. Sun, Carbon dots as nontoxic and high-performance fluorescence imaging agents, *J. Phys. Chem. C*, 2009, **113**, 18110–18114.
- 30 P. Wu, W. Li, Q. Wu, Y. Liu and S. Liu, Hydrothermal synthesis of nitrogen-doped carbon quantum dots from microcrystalline cellulose for the detection of Fe³⁺ ions in an acidic environment, *RSC Adv.*, 2017, **7**(70), 44144–44153.
- 31 J. Schneider, C. J. Reckmeier, Y. Xiong, M. von Seckendorff, A. S. Susha, P. Kasák and A. L. Rogach, Molecular fluorescence in citric acid-based carbon dots, *J. Phys. Chem. C*, 2017, **121**(3), 2014–2022.
- 32 M. T. Cooper and R. Nathans, The resolution function in neutron diffraction. I. The resolution function of a neutron diffractometer and its application to phonon measurements, *Acta Crystallogr.*, 1967, **23**(3), 357–367.
- 33 N. C. Popa, The (*hkl*) dependence of diffraction-line broadening caused by strain and size for all Laue groups in Rietveld refinement, *J. Appl. Crystallogr.*, 1998, **31**(2), 176–180.
- 34 D. Wei, A. Zhang, Y. Ai and X. Wang, Adsorption properties of hydrated Cr³⁺ ions on Schiff-base covalent organic frameworks: A DFT study, *Chem. – Asian J.*, 2020, **15**(7), 1140–1146.
- 35 R. Berraud-Pache, F. Neese, G. Bistoni and R. Izsak, Computational Design of Near-Infrared Fluorescent Organic Dyes Using an Accurate New Wave Function Approach, *J. Phys. Chem. Lett.*, 2019, **10**(17), 4822–4828.
- 36 H. Kruse, L. Goerigk and S. Grimme, Why the standard B3LYP/6-31G* model chemistry should not be used in DFT calculations of molecular thermochemistry: understanding and correcting the problem, *J. Org. Chem.*, 2012, **77**(23), 10824–10834.
- 37 A. A. Safonov, A. A. Bagaturyants and V. A. Sazhnikov, Assessment of TDDFT-and CIS-based methods for calculating fluorescence spectra of (dibenzoylmethanato) boron difluoride exciplexes with aromatic hydrocarbons, *J. Mol. Model*, 2017, **23**(5), 164.
- 38 Y. Ma, L. Feng, J. Liu, Y. Yang and T. Chu, DFT/TDDFT investigation on the D- π -A type molecule probes 4-(5-R-thiophen-2-yl)-2-isobutyl-2H-[1, 2, 3] triazolo [4, 5-e][1, 2, 4] triazolo [1, 5-a] pyrimidines: fluorescence sensing mechanism and roles of weak interactions, *Theor. Chem. Acc.*, 2020, **139**(1), 11.
- 39 F. Neese, The ORCA program system, *Wiley Interdiscip. Rev.: Comput. Mol. Sci.*, 2012, **2**(1), 73–78.
- 40 S. Roy, A. Maity, P. Mandal, D. K. Chanda, K. Pal, S. Bardhan and S. Das, Effects of various morphologies on the optical and electrical properties of boehmite nanostructures, *CrystEngComm*, 2018, **20**(40), 6338–6350.
- 41 O. V. Shiman, L. Balogh and M. R. Daymond, A synchrotron X-ray diffraction study of strain and microstrain distributions in α -Zr caused by hydride precipitation, *Surf. Interfaces*, 2019, **17**, 100388.
- 42 S. Bardhan, K. Pal, S. Roy, S. Das, A. Chakraborty, P. Karmakar, R. Basu and S. Das, Nanoparticle Size-Dependent Antibacterial Activities in Natural Minerals, *J. Nanosci. Nanotechnol.*, 2019, **19**(11), 7112–7122.
- 43 S. Roy, S. Bardhan, K. Pal, S. Ghosh, P. Mandal, S. Das and S. Das, Crystallinity mediated variation in optical and electrical properties of hydrothermally synthesized boehmite (γ -AlOOH) nanoparticles, *J. Alloys Compd.*, 2018, **763**, 749–758.
- 44 E. Theodosoglou, A. Koroneos, T. Soldatos, T. Zorba and K. M. Paraskevopoulos, Comparative Fourier Transform Infrared AndX-Ray Powder Diffraction Analysis of Naturally Occurred K Feldspars, *Bull. Geol. Soc. Greece*, 2010, **43**(5), 2753.
- 45 J. T. Klopogge and B. J. Wood, Chemical bonding and electronic structures of microcline, orthoclase and the plagioclase series by X-rayphotoelectron spectroscopy, *Spectrochim. Acta, Part A*, 2015, **137**, 711–716.
- 46 G. Greczynski and L. Hultman, X-ray photoelectron spectroscopy: towards reliable binding energy referencing, *Prog. Mater. Sci.*, 2020, **107**, 100591.
- 47 D. K. Chanda, D. Mukherjee, P. S. Das, C. K. Ghosh and A. K. Mukhopadhyay, Toxic heavy metal ion adsorption kinetics of Mg (OH)₂ nanostructures with superb efficacies, *Mater. Res. Express*, 2018, **5**(7), 075027.
- 48 X. M. Li, S. L. Zhang, S. A. Kulinich and H. B. Zeng, *Sci. Rep.*, 2014, **4**, 4976–4983.
- 49 W. Li, Z. Zhang, B. Kong, S. Feng, J. Wang, L. Wang, J. Yang, F. Zhang, P. Wu and D. Zhao, Simple and green Synthesis of nitrogen-doped photoluminescent carbonaceous nanospheres for bioimaging, *Angew. Chem., Int. Ed.*, 2013, **52**, 8151–8155.
- 50 C. M. Carbonaro, D. Chiriu, L. Stagi, M. F. Casula, S. V. Thakkar, L. Malfatti, K. Suzuki, P. C. Ricci and R. Corpino, Carbon Dots in Water and Mesoporous Matrix: Chasing the Origin of their Photoluminescence, *J. Phys. Chem. C*, 2018, **122**, 25638–25650.
- 51 Y. Chen, H. Lian, Y. Wei, X. He, Y. Chen, B. Wang, Q. Zeng and J. Lin, Concentration-induced multi-colored emissions in carbon dots: origination from triple fluorescent centers, *Nanoscale*, 2018, **10**(14), 6734–6743.
- 52 M. L. Liu, B. B. Chen, C. M. Li and C. Z. Huang, Carbon dots: synthesis, formation mechanism, fluorescence origin and sensing applications, *Green Chem.*, 2019, **21**(3), 449–471.
- 53 M. Mittal and S. Sapra, Nanocrystal–Dye Interactions: Studying the Feasibility of Co-Sensitization of Dyes with Semiconductor Nanocrystals, *ChemPhysChem*, 2017, **18**(18), 2509–2516.
- 54 S. Roy, K. Pal, S. Bardhan, S. Maity, D. K. Chanda, S. Ghosh, P. Karmakar and S. Das, Gd(III)-Doped Boehmite Nanoparticle: An Emergent Material for the Fluorescent

- Sensing of Cr(vi) in Wastewater and Live Cells, *Inorg. Chem.*, 2019, **58**(13), 8369–8378.
- 55 F. Zu, F. Yan, Z. Bai, J. Xu, Y. Wang, Y. Huang and X. Zhou, The quenching of the fluorescence of carbon dots: a review on mechanisms and applications, *Microchim. Acta*, 2017, **184**(7), 1899–1914.
- 56 R. Anumula, P. Xiao, C. Cui, H. Wu, G. Cui, W. H. Fang, Z. Luo and J. Yao, A small bimetallic Ag₃Cu₂ nanocluster with dual emissions within and against Kasha's rule, *Nanoscale*, 2020, **12**(14), 7864–7869.
- 57 S. Roy, S. Bardhan, D. K. Chanda, S. Ghosh, D. Mondal, J. Roy and S. Das, Development of a Cu(II) doped boehmite based multifunctional sensor for detection and removal of Cr(vi) from wastewater and conversion of Cr(vi) into an energy harvesting source, *Dalton Trans.*, 2020, **49**(20), 6607–6615.



Flexible and reusable carbon dot decorated natural microcline membrane: a futuristic probe for multiple heavy metal induced carcinogen detection

Souravi Bardhan¹ · Shubham Roy¹ · Dipak Kr. Chanda² · Dhananjay Mondal¹ · Solanky Das³ · Sukhen Das¹

Received: 5 November 2020 / Accepted: 15 March 2021

© The Author(s), under exclusive licence to Springer-Verlag GmbH Austria, part of Springer Nature 2021

Abstract

A flexible nano-engineered natural mineral (carbon dot doped natural microcline) based membrane (MCPV) has been developed, which can efficiently detect the presence of hexavalent chromium (Cr^{6+}) and trivalent iron (Fe^{3+}) ions in water by altering its fluorescence emission. Detailed characterization of the membrane was carried out using XRD, FT-IR spectroscopy, FESEM, TEM, and UV-Vis spectroscopy. Mechanical and temperature stabilities were also investigated. This new-generation sensor membrane is designed in such a way that it does not dissolve in water, keeping the water quality unaffected. The fluorescence studies were conducted at 414 nm and “turn-off” response was observed specifically for Fe^{3+} at 489 nm. A prominent red shift (530 nm) of the fluorescence maxima takes place when it comes to Cr^{6+} . Figures of merit, such as LOD (8.7 μM for Cr^{6+} and 18.4 μM for Fe^{3+}) and LOQ (29.1 μM for Cr^{6+} and 61.6 μM for Fe^{3+}), were evaluated from the linear range (0–60 μM for Cr^{6+} and 0–30 μM for Fe^{3+}) of the calibration curve (Stern-Volmer plots) showing high sensitivity of this sensing probe toward Cr^{6+} and Fe^{3+} . Recovery and RSD calculations were done in various real-life water samples on intraday-interday basis to determine the accuracy of the sensor. This work validates the fact that the synthesized sensor membrane is capable of detecting these heavy metals in glutathione environment as well, which could be beneficial for early-stage carcinogen detection in living cells.

Keywords Fluorescent sensor membrane · Natural microcline · Dual sensing · Density functional theory · Molecular docking

Introduction

Heavy metals like hexavalent chromium (Cr^{6+}) and trivalent iron (Fe^{3+}) are known for adverse health hazards and need to be detected and separated properly [1, 2]. Although various techniques are employed for heavy metal sensing, such as ion chromatography (IC), atomic absorption spectroscopy (AAS), or inductively coupled plasma mass spectrometry (ICP-MS) [3, 4], more sensitive and rapid responding materials and devices are needed due to the alarming escalation of heavy metal disposal from various industries. Nowadays, fast and precise

detection of multiple elements in a single material is much needed. Hence, various groups are currently working on fluorometric and colorimetric sensors due to their high precision and tremendous selectivity [5]. Moreover, these optical sensors having very fast response time (in seconds) are mostly in powder or in liquid form. Thus, their fluorescence stability and sensing efficacy vary greatly due to moisture adsorption, temperature, and other ambient factors [6]. Henceforth, a nano-engineered flexible and durable membrane is proposed in this work, which is capable of detecting Cr^{6+} and Fe^{3+} ions simultaneously in aqueous media. The incorporation of microcline-carbon dot nanocomposite in the polymer matrix (poly (vinylidene fluoride-co-hexafluoropropylene)) not only enhances the fluorescence property, but also favors the advancement in the mechanical strength, stability, and reusability of the membrane. The free-standing fluorescent membrane (MCPV) with dual-sensing capability, having immense fluorescence stability, rapid response, high selectivity and sensitivity, and significant mechanical strength maintaining its sensing efficacy irrespective of multiple uses could be a game

✉ Sukhen Das
sdasphysics@gmail.com

¹ Department of Physics, Jadavpur University, Kolkata 700032, India

² School of Materials Science and Nano-Technology, Jadavpur University, Kolkata 700032, India

³ Department of Geology, Jadavpur University, Kolkata 700032, India

changer. This membrane is insoluble in water restricting it for any further reaction in aqueous medium. This property could be beneficial for on-site studies and multiple uses of the membrane. Usage of natural microcline restricts the agglomeration of fluorophores (i.e., carbon dot) and reduces the production cost as it is abundant on earth's crust [7]. Additionally, the synthesized membrane is capable of detecting chromium and iron ions experimentally when these are exposed to glutathione. Previously, it was studied that glutathione minimizes the ROS (reactive oxygen species) production in living cells when exposed to heavy metals and confines their carcinogenic effects [8, 9]. This study depicts that the synthesized membrane can bind with glutathione, and alters its fluorescence level when exposed to the targeted heavy metals (Cr^{6+} and Fe^{3+}). Various theoretical approaches, like molecular docking and density functional methods, have been carried out to validate the experimentations in this work. All such merits make this membrane a strong candidate for portable industrial wastewater monitoring system.

Experimental methods

Materials

The naturally formed microcline was purchased from Hindustan Minerals, Kolkata, India. Anhydrous citric acid ($\text{C}_6\text{H}_8\text{O}_7$, MW 192.13 g mol^{-1} , 99.5% pure), ethylenediamine (EDA) (HPLC grade), N,N-dimethylformamide (DMF) (HPLC grade), potassium dichromate (K_2CrO_7 , MW 294.19 g mol^{-1} , $\geq 99.0\%$ pure), and anhydrous ferric chloride (FeCl_3 , MW 162.20 g mol^{-1} , $\geq 98.0\%$ pure) were purchased from Merck, India. PVDF-HFP and L-glutathione ($\text{C}_{10}\text{H}_{17}\text{N}_3\text{O}_6\text{S}$, MW 307.32 g mol^{-1} , $\geq 98.0\%$ pure) were purchased from Sigma-Aldrich Co. All chemicals used for selectivity analysis (NaCl , NaNO_3 , Na_2CO_3 , Na_2S , Na_2SO_4 , KCl , $\text{CaCl}_2 \cdot 2\text{H}_2\text{O}$, $\text{FeSO}_4 \cdot 7\text{H}_2\text{O}$, $\text{Cr}(\text{CH}_3\text{COO})_3$, CdCl_2 , HgCl_2 , PbCl_2) were purchased from Merck, India, and As_2O_3 was purchased from Sigma-Aldrich. All the reagents used are of analytical grade ($\geq 98.0\%$ pure) and were used without further purification. Stimulated body fluid (SBF) was prepared by dissolving NaCl (7.996 g), NaHCO_3 (0.350 g), KCl (0.224 g), $\text{K}_2\text{HPO}_4 \cdot 3\text{H}_2\text{O}$ (0.228 g), $\text{MgCl}_2 \cdot 6\text{H}_2\text{O}$ (0.305 g), CaCl_2 (0.278 g), Na_2SO_4 (0.071 g), $(\text{CH}_2\text{OH})_3\text{CNH}_2$ (6.057 g), and HCl (1.0 M) in 1 L Millipore water (pH maintained ~ 7.5). Millipore water of resistivity $\sim 18.2 \text{ M}\Omega\text{-cm}$ was used throughout the experiments.

Microcline-carbon dot nanocomposite (MC) synthesis

The purchased microcline was thoroughly washed to remove debris or impurities and broken into smaller size fraction using

agate mortar. Microcline nanoparticle was prepared using a top-down method by mechanical ball milling for 12 h at 300 rpm by using a ball mill machine (Fritsch Planetary Mono Mill Pulverisette 6). Tungsten carbide vials and balls (ball to sample mass ratio of 20:1) were used to crush the sample.

On the other hand, carbon dot synthesis was done via a two-step hydrothermal technique, where 5.5 mM citric acid solution was prepared by dissolving anhydrous citric acid in Millipore water and basified until pH 12.0 using EDA under stirring condition. Continuous stirring at 600 rpm was employed for 2 h and then the solution was poured into a Teflon-lined stainless-steel autoclave and heated in a hot air oven for 12 h at 190 °C. The solution was then collected and centrifuged at 5000 rpm for 15 min, and 10 mL of the fresh supernatant (carbon dots) was added to 500 mg microcline nanoparticle under stirring condition. The stirring was continued for 48 h at 300 rpm, centrifuged, and finally dried to collect microcline-carbon dot (MC) nanocomposite.

Fabrication of fluorescent MCPV sensor membrane

MCPV composite membrane was prepared by dissolving 150 mg PVDF-HFP in 10 mL DMF and subsequently by adding 5% (w/w) of as-prepared MC powder under vigorous stirring conditions (800 rpm). The homogeneous solution was obtained after 8 h of stirring and poured on a clean petri dish. The petri dish was then placed in an oven at 70 °C and allowed to dry. Finally, the dried membrane was peeled off safely for further characterizations. Pure PVDF membrane was also prepared following the same protocol, excluding addition of MC nanocomposite.

Characterization techniques

The synthesized MC nanocomposite and PVDF and MCPV membranes were characterized using X-ray powder diffractometer (D8, Bruker AXS, WI, USA) from 15 to 50° 2 θ values for analyzing their phase purity. The X-ray tube was operated at 35 kV, and 35 mA external field with scan speed of 2 s per step employing a Cu-K α target emitting a wavelength of 1.5418 Å. The Fourier transform infrared spectroscopy (FTIR-8400S, Shimadzu) was used in the wavenumber ranges between 450 and 1200 cm^{-1} to identify the bonding networks of the samples.

The surface morphology of the membrane was determined using field emission scanning electron microscopy (FESEM, INSPECT, F50, Netherlands) operated at 5–20 kV bias voltages. Further morphological characterization of MC was performed by using JEOL JEM-2000 transmission electron microscope (TEM) operated at 200 kV.

The tensile strength was measured using universal testing machine (UTM, Instron-5500R) at ambient lab conditions (~ 31 °C) with crosshead speed fixed at 0.5 mm min^{-1} .

Thermal properties were determined using DTG-60H, Shimadzu. The membranes were heated from ambient lab temperature to 200 °C at a heating rate of 10 °C min^{-1} under N_2 gas atmosphere using platinum crucibles.

Optical quality of the synthesized materials was validated by using its absorption and emission spectra. The absorption spectrum of the sample was measured by UV spectroscopy using a Perkin Elmer λ -25 spectrometer. The fluorescence intensity, fluorometric sensing patterns, and the fluorescence decay profiles were measured using a Cary Eclipse Fluorescence Spectrometer, Agilent Technologies, with excitation and emission slit sizes of 5 nm each.

The elemental analysis of the wastewater was performed by inductively coupled plasma optical emission spectrometry (ICP-OES) (SPECTRO Analytical Instrument, SPECTRO ARCOS II, Germany). The raw wastewater obtained was filtered using a filter membrane of $0.45 \mu\text{m}$ pore size. The filtrate obtained was treated with $\text{HNO}_3\text{-H}_2\text{O}_2$ (6:2 v/v) for 30 min prior to microwave-assisted digestion for 10 min (700 W). After cooling, the resulting solution was diluted (1:10 v/v) with 1.0 M HNO_3 and sent for ICP-OES analysis. The plasma argon flow rate was set to 13.0 L min^{-1} , auxiliary argon flow was set at 0.8 L min^{-1} , nebulizer flow was at 1.0 L min^{-1} , and pump rate at 25 rpm and used cyclonic spray chamber. The analytical lines chosen were 267.72 nm for chromium, 226.50 nm for cadmium, 238.20 nm for iron, and 220.35 nm for lead. Standard graphs were prepared using $0\text{--}50 \text{ ppm}$ concentration in each case to validate the results.

Computational methods

The geometry optimizations of the fluorophore and the foundation of ion sensing were performed by means of DFT calculations using hybrid Becke, 3-parameter, Lee-Yang-Parr (B3LYP) functional coupled with the continuum aqueous solvent mode (CPCM). All the DFT and TDDFT calculations were performed by using Orca v.4.2 package and modeled with Avogadro v.1.2 program. The 6-31G** basis set along with RJCOSX auxiliary basis function was implemented to describe the elements (C, H, O, N) along with Cr^{6+} and Fe^{3+} ions respectively. Frequency optimization of the synthesized carbon dot was done at the same theoretical level, which depicts absence of any imaginary frequency. The TDDFT method was used to analyze the theoretical absorbance spectra and electronic transitions for the sensor and the complexes formed with the quenching ions.

Binding affinity between fluorophore and glutathione was determined using molecular docking. AutoDock Tools v.1.5.6 was employed to prepare the protein by removing the water molecule and adding polar hydrogen and Kollman charges.

AutoDock Vina v.1.1.2 was used to check the binding affinity of the said protein-ligand complex. The exact binding pocket was identified and visualized using PyMol v.2.0.7 program.

Results and discussion

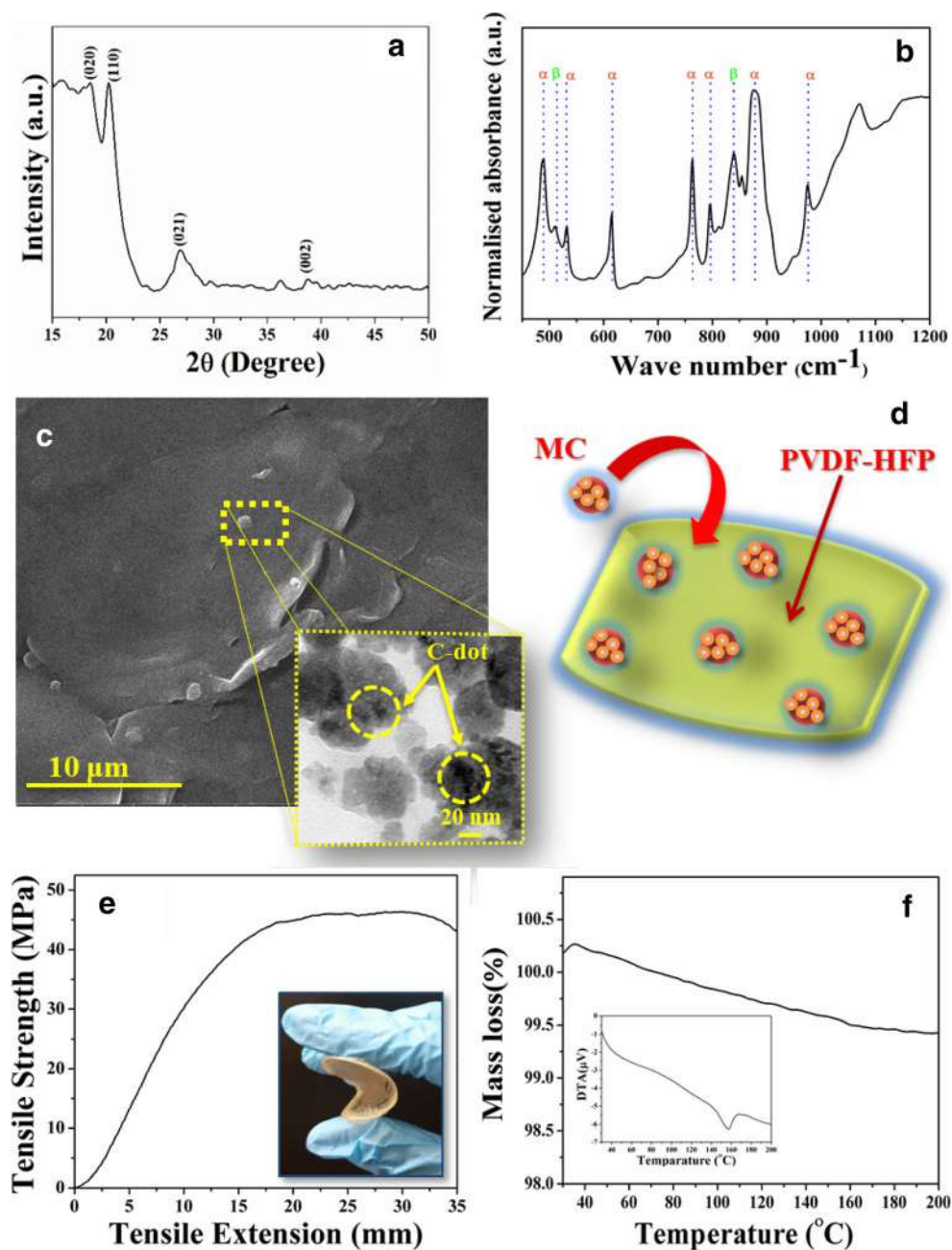
Physical characteristics of the sensor membrane

The phase purity of the synthesized samples has been analyzed using X-ray diffraction (XRD) technique. Microcline was used in order to stabilize the fluorophores (carbon dots) and the carbon dot-doped microcline was further “wrapped” into PVDF-HFP polymer (MCPV) to provide the sensor material a solid and flexible backbone. The XRD pattern of the MCPV sensor membrane is illustrated in Fig. 1a, which depicts the semi-crystalline nature of the membrane. The characteristic peaks observed at 17.6° (020), 26.8° (021), and 38.9° (002) correspond to non-polar α -phase, while the diffraction maximum at 20.7° (110) represents the polar β -phase of the membrane [10]. Moreover, the diffraction lines corresponding to the nonpolar α -phase (17.6° and 38.9°) are slightly reduced, while the diffraction line corresponding to the β -phase (20.7°) increased in MCPV membrane. This suggests the polarization of the CH_2 - moiety [11] to the positively charged surface of the MC nanocomposite (Fig. S1a).

Furthermore, the bonding networks have been analyzed using FT-IR spectroscopy (Fig. 1b). The characteristic IR-absorption bands of PVDF-HFP have been detected at 488 cm^{-1} ($-\text{CF}_2$ wagging), 531 cm^{-1} ($-\text{CF}_2$ bending), 615 cm^{-1} (skeletal bending), 762 cm^{-1} ($-\text{CF}_2$ bending), 795 cm^{-1} ($-\text{CH}_2$ rocking), 877 cm^{-1} ($-\text{CF}_2$ stretching), and 976 cm^{-1} ($-\text{CH}_2$ twisting). These IR bands are associated with the non-polar α -phase [12, 13]. The vibrational maxima located at 510 cm^{-1} ($-\text{CF}_2$ stretching) and 840 cm^{-1} ($-\text{CH}_2$ rocking, $-\text{CF}_2$ asymmetric stretching and skeletal C-C stretching) are related to β -phase of the polymer. The vibrational band observed at 1070 cm^{-1} is attributed to C-O-C stretching, while the band at 1160 cm^{-1} attributes to the stretching vibration of C-F, deformation vibrations, and asymmetric stretching of C-H bond [13, 14]. The slight increment of the absorption peak at 840 cm^{-1} compared to the pure PVDF-HFP spectra (Fig. S1b) illustrates enhancement of the polarity [12] due to MC incorporation. Absence of any unwanted IR-maxima ascertains the fact that the sensor membrane is phase-pure and free from impurity.

The surface morphology of the sensor membrane (MCPV) has been studied by using FESEM (Fig. 1c) showing a rough, slightly wrinkled surface. The pure PVDF-HFP membrane is relatively smooth and uniform as compared to the MC doped PVDF-HFP (Fig. S1c). Further investigation using TEM reveals that the particle size of the dopant (MC) is around $20\text{--}40 \text{ nm}$ having smaller carbon dots (around 5 nm) embedded

Fig. 1 (a) X-Ray diffractogram of MCPV film; (b) FTIR spectra of the film; (c) FESEM micrograph of the film with TEM micrographs of MC (inset); (d) schematic representation of MCPV film; (e) tensile strength of MCPV film showing flexibility of the film (inset); (f) TGA of MCPV film along with DTA (inset)



on its surface (Fig. 1c inset). Figure 1d shows a pictorial representation of the MC embedded PVDF-HFP film.

The incorporation of MC into the polymer matrix not only provides the fluorophores a flexible substrate, but also enhances the mechanical strength of the membrane significantly. Determination of mechanical strength is also essential to validate the real-life application to prevent wear-and-tear from regular and repetitive use of the membrane. The tensile strength-tensile extension data obtained for the membranes of 0.06-mm thickness is being illustrated in Fig. 1e. The tensile strength for the doped sample is found to be 46.1 MPa, whereas the undoped membrane (Fig. S1d) shows a relatively

lower value (34.6 MPa). The mechanical performance considerably improved on addition of MC since the nano-microcline acts as a filler into the pores of the polymer network and provides a better stability. It is observed from XRD and FT-IR that the β -phase of the polymer enhances due to the re-assembly of the bonding networks [14], which might cause strong interaction between the polymer chain and the dopant and results in better durability of the doped membrane.

Temperature stability is another important measure of any functional material. Herein, thermo-gravimetric analysis (TGA) and differential thermal analysis (DTA) have been performed to determine the thermal stability of the sensor

membrane. TGA-DTA data shows a very nominal mass loss (around 0.5%) until 200 °C, with an endothermic peak centered at 157 °C (Fig. 1f) for doped sample, which is otherwise at 154 °C (Fig. S1e) for the undoped membrane. Lower mass loss with enhanced stability up to 157 °C makes the sensor membrane capable to work in any ambient condition.

Optical characteristics of the sensor membrane

The absorption band of carbon dot was reported to be centered at 250 and 350 nm [15], which is quite similar to the absorbance data we have observed in this work. The experimental absorption spectrum of MCPV membrane shows a broad-range absorption (250–450 nm) centered at 350 nm (Fig. 2a), which is otherwise absent in the pure PVDF-HFP (Fig. S1f). These absorption bands are related to π -stacking of the conjugated π -electrons of carbon dots.

Furthermore, the sensor membrane has been further subjected to varying excitation wavelengths from 370 to 420 nm to select the optimum excitation wavelength (Fig. S2a). The sensor membrane shows excellent blue fluorescence at 489 nm when it is exposed to 414-nm wavelength (Fig. 2b). In fact, the said fluorescence is visible through the naked eyes under the optical excitation (Fig. 3b). Various concentrations of MC nanocomposite (0.0%, 2.5%, 5.0%, and 7.5%) have been loaded to examine whether the fluorescence of the system varies with the composition. It is found that the 5% (w/w) doped sample shows the highest fluorescence intensity (Fig.

S2b). In reality, agglomerated carbon dots can reduce the fluorescence quality of the sample and this is why a specific amount of carbon dots is required to fabricate the sensor material [16]. An excess amount of carbon dot (> 5%) creates agglomeration of these quantum mechanical systems and reduces the fluorescence quality. Hence, all the fluorescence experiments were conducted using 5% MC loaded MCPV membrane.

The fluorescence stability is another major aspect, which was found to be high in this case. The fluorescence stability was studied using two different methods. Initially, the doped membrane was preserved for at least 10 days consecutively under ambient pressure, humidity, and temperature (without any vacuum desiccation) and each day the fluorescence intensity was measured under the same excitation energy (Fig. 2c). It is found that there is no alteration in fluorescence spectrum, which suggests the membrane to be stable enough for fluorometric applications. Previously, researchers have struggled enough to maintain the fluorescence intensity for a longer period of time. Primarily, atmospheric moisture and agglomeration of the fluorophores degrade the fluorescence quality of the materials. Herein, a polymeric substrate has been prepared to wrap the fluorophores, which restrict any further damage due to extreme ambient conditions.

Additionally, the fluorescence intensity at different temperatures (10–80 °C) has also been examined to ascertain the fluorescence stability. The fluorescence intensity increased with increasing temperature, and optimum fluorescence

Fig. 2 (a) Absorbance spectra of MCPV film; (b) excitation and emission spectra of the sensor film; (c) time-dependent fluorescence obtained on 240-h study

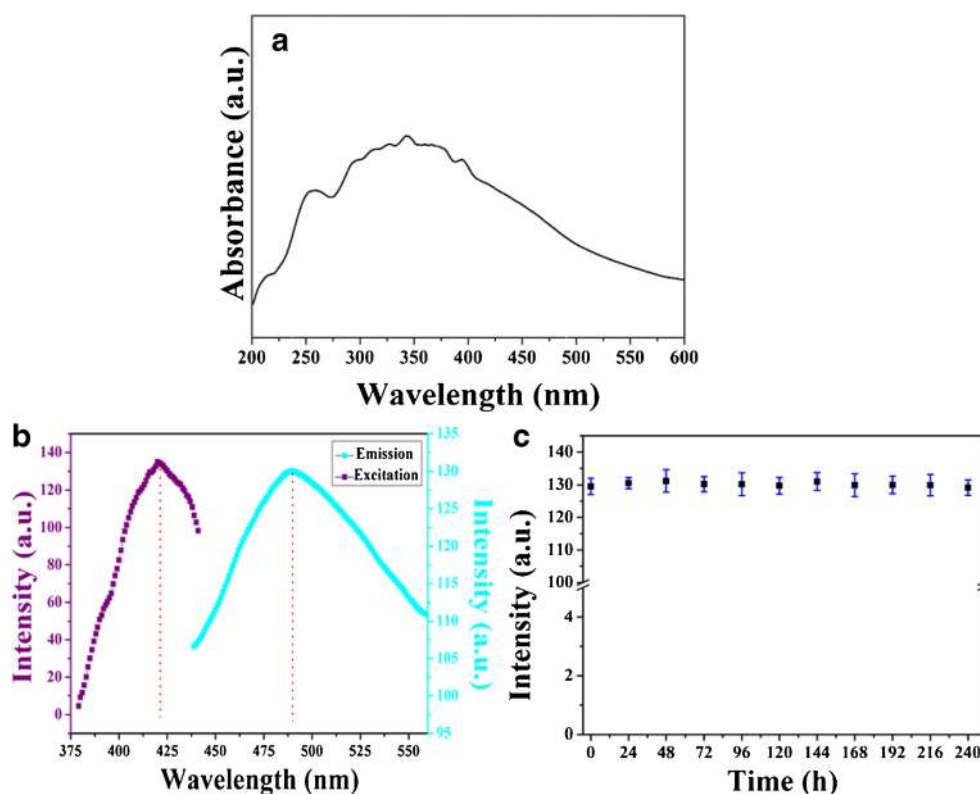
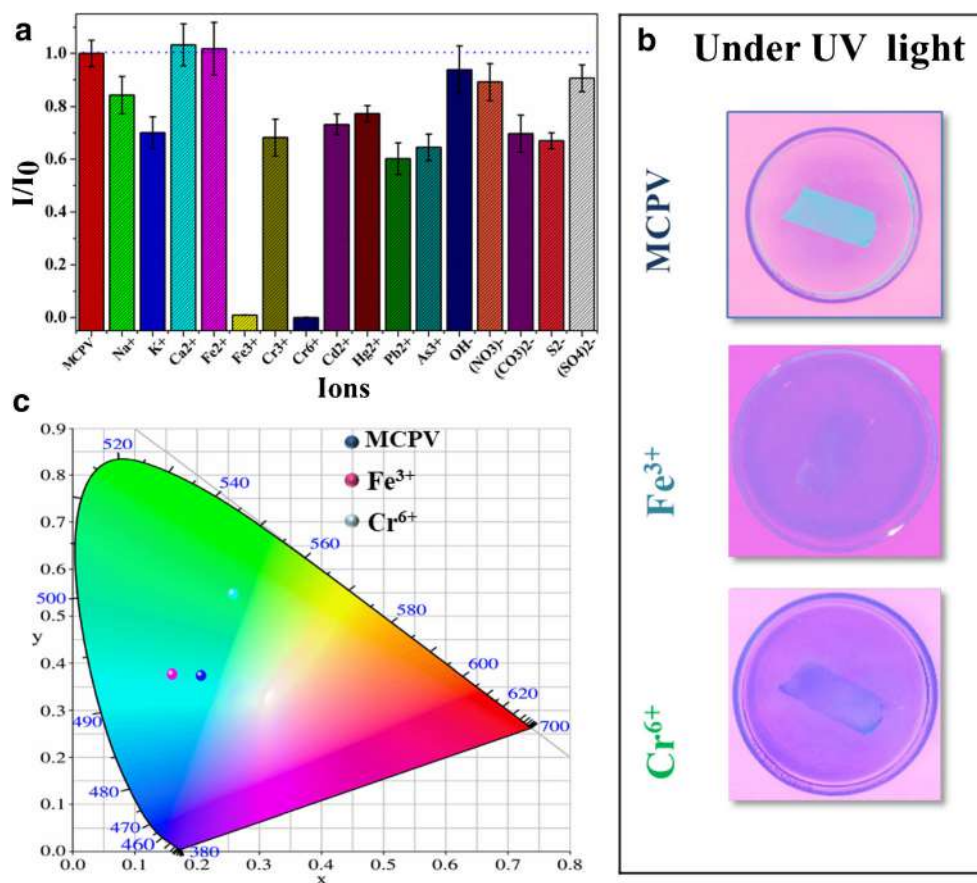


Fig. 3 (a) Selectivity study of the sensor towards various cations and anions; (b) naked eye visualization of bright blue fluorescence on exposure to UV light and simultaneous real-life quenching on exposure to Cr^{6+} and Fe^{3+} ; (c) CIE-1931 color space analysis of the sensor upon heavy metal exposure



intensity has been found at 50 °C, beyond which the intensity slightly reduced until 80 °C (Fig. S2c). Temperature change causes alterations in probabilities of radiative and non-radiative transitions. Thus, at higher temperatures, there is a higher probability of collisional quenching between the fluorophores [17]. Though the fluorescence intensity alters, there is no significant shift in emission maxima, which validates the fluorescence stability of the material.

Fluorometric detection of the heavy metals in aqueous media

Sensing probes are needed to be merely selective and sensitive toward a specific target molecule for better applicability. In order to evaluate the selectivity of a fluorometric sensor, the fluorescence responses of the sensor are evaluated against a diverse range of ions (Na^+ , K^+ , Ca^{2+} , As^{3+} , Fe^{2+} , Fe^{3+} , Cr^{3+} , Cr^{6+} , Cd^{2+} , Pb^{4+} , Hg^{2+} , CO_3^{2-} , S^{2-} , SO_4^{2-} , NO_3^- , and OH^-) at specific concentrations (50 μM). In reality, fluorometric probes alter either their fluorescence intensities or color when exposed to the specified target molecule/ion. In this work, significant decay in fluorescence levels has been observed when exposed to Fe^{3+} and Cr^{6+} solutions (Fig. 3a). Additionally, the blue fluorescence of the membrane shifted

to green when it was put into the Cr^{6+} solution. In fact, this phenomenon is observable through the naked eyes (Fig. 3b).

In order to determine the sensitivity of the probe, the MCPV membrane was immersed in varied concentrations of Fe^{3+} and Cr^{6+} (0–120 μM) separately maintaining other parameters unaltered. In case of Fe^{3+} , the fluorescence intensity centered at 489 nm radically dropped with increasing concentration (Fig. 4a), whereas Cr^{6+} quenched the fluorescence intensity which is accompanied by a gradual shift of emission maxima from 489 to 530 nm (Fig. 4b). The CIE-1931 color space has been used to compute the color coordinates [18] to probe such dual sensing activity. The color coordinate of the pure sensor membrane was found to occupy the blue region of the color space with coordinate $x = 0.20659$, $y = 0.37790$, whereas Fe^{3+} addition slightly changed the coordinate to $x = 0.16062$, $y = 0.38223$. In case of Cr^{6+} , the color space of the membrane drastically shifted to $x = 0.25897$, $y = 0.55185$ lying in the green region (Fig. 3c), corroborating the naked eye observations (Fig. 3b).

The fluorescence alteration was determined quantitatively using the Stern-Volmer (S-V) equation for both the ions (Fe^{3+} and Cr^{6+}), which was calculated by fitting the data with the said equation [19] expressed as:

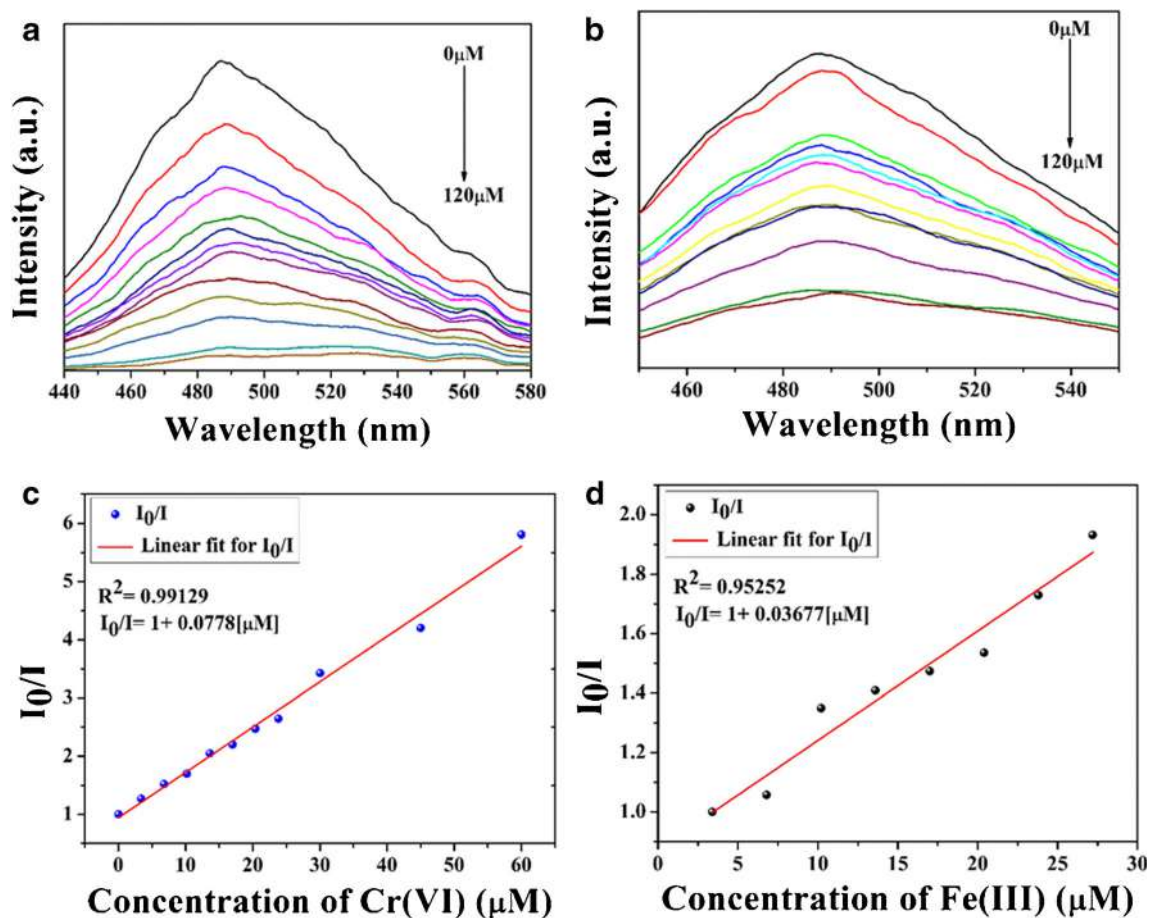


Fig. 4 Fluorescence titration data for MCPV sensor using (a) Fe^{3+} and (b) Cr^{6+} respectively as the quencher; Stern-Volmer fitting of the corresponding fluorescence quenching data by (c) Fe^{3+} and (d) Cr^{6+} respectively

$$\frac{I_0}{I} = 1 + K_{SV}[M] \quad (1)$$

Where, I_0 and I are the fluorescence intensities before and after the addition of both contaminants respectively, $[M]$ represents the concentration of the ions, and K_{SV} is the Stern-Volmer quenching constant. Exponential increment of relative fluorescence intensity (I_0/I) with increasing quencher concentration is observed in both cases, which suggests dynamic/collisional quenching of the fluorophores. The SV plots have been taken up to 60.0 μM concentration in case of Cr^{6+} and up to 30.0 μM for Fe^{3+} to ensure the linearity (Fig. 4). This further validates the SV plots to be the calibration plots of the sensing probe. Beyond these concentrations, upward increments have been observed which might be due to inner filter effect [20] (Fig. S3). In case of Fe^{3+} , the fit coefficient (R^2) of the linear calibration curve is found to be 0.95252, whereas it is 0.99129 for Cr^{6+} . The figures of merit, such as limit of detection (LOD) and limit of quantitation (LOQ), have been calculated for both the ions using the following expressions [21]:

$$LOD = \frac{3\sigma}{K_{SV}} \quad (2)$$

$$LOQ = \frac{10\sigma}{K_{SV}} \quad (3)$$

where σ is the standard deviation obtained on taking at least ten measurements of the fluorescence intensities of the membrane without the presence of any quenching ions and K_{SV} is the quenching constant. The LOD was calculated to be 8.7 μM for Cr^{6+} and 18.4 μM for Fe^{3+} , while LOQ was found to be 29.1 μM and 61.6 μM for Cr^{6+} and Fe^{3+} respectively. Performances of some fluorometric sensors have been compared with this work in terms of their working range, K_{SV} , and multiple ion sensing capability (Table S1).

Detection mechanism of the sensor membrane

Initially, time-resolved fluorescence decay of the sensor is measured with varying concentrations of contaminant ions to justify the fluorometric detection mechanism. The emission and excitation wavelengths were set at 489 and 414 nm,

respectively, and for Cr^{6+} , excitation wavelength was kept at 530 nm. The fitted fluorescence decay profile shows a reduction in decay time when the membrane was exposed to both the contaminants with higher concentrations. The average lifetime of the fluorophores is found to be 80 ns, which drastically reduces to 46 ns on addition of Cr^{6+} , while reducing to 62 ns when the sample was immersed in Fe^{3+} solution (Fig. S4). Time-resolved fluorescence data reveals that the quenching phenomenon might have occurred in the excited state [22]. Hence, in both the cases, the linear Stern-Volmer plot obtained along with the reduced fluorophore lifetime in excited state suggests the occurrence of collisional quenching mechanism [23, 24].

In order to confirm this, quantum chemical calculations using density functional theory (DFT) have been carried out. The complexity of the computation has been minimized by taking the fluorophore (carbon dot) and quenchers (Cr^{6+} and Fe^{3+}) only in these calculations. The quenchers were placed at a distance of 5 Å from the fluorophore in both the cases. The geometries were optimized and frequencies were estimated prior to the time-dependent DFT calculations. Absence of any undesired imaginary vibration validates the theoretical models. It is observed from TDDFT results that there is a significant transfer of the molecular orbitals between the

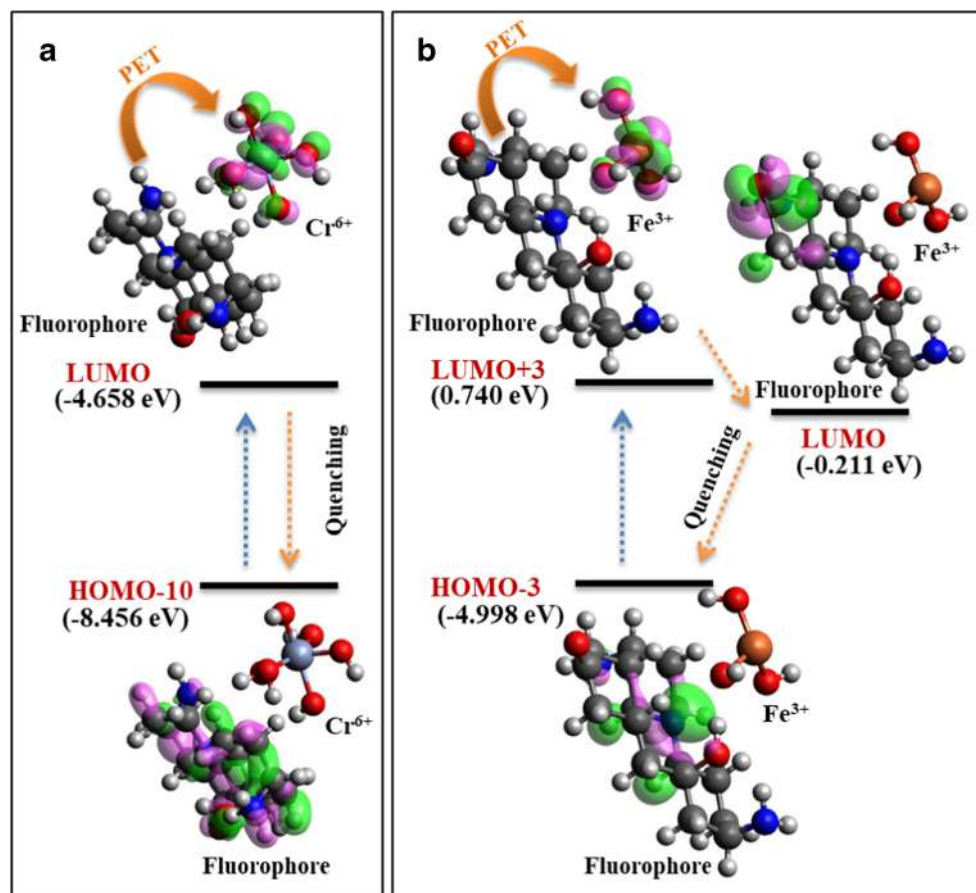
quenchers and the fluorophore at excited states (Fig. 5). In fact, there is no evidence of any bond formation between the quenchers and the fluorophore, which suggests photoinduced electron transfer (PET) mechanism [25, 26] is responsible for such fluorometric alterations.

Sensing efficacy of the sensor membrane in various conditions

Performance of the membrane in different pH conditions

Fluorescence quality and sensing efficacy in varied pH range were examined by immersing the membrane in various pH solutions (pH 4.0, 7.0, 9.2, and 12.6) maintained by HCl and NaOH. Simultaneously, the quencher ions have been added into the pH solutions (100 μM). There is a minor decrease in fluorescence intensity of sensor material at pH 4.0 due to the inner filter effect [27], since fluorophores are less accessible in the presence of more H^+ ions. But there is no change in the overall sensing performance in the varying pH conditions (Fig. 6a). Moreover, in order to validate the accuracy of the sensing, recovery rate (RR%) was calculated from the calibration graphs using 20.0 μM concentration for both Cr^{6+} and Fe^{3+} (Table S2). The recovery rates vary within 92.6 to

Fig. 5 Molecular orbitals and electronic transitions involved in fluorescence quenching of the sensor upon (a) Cr^{6+} and (b) Fe^{3+} addition respectively



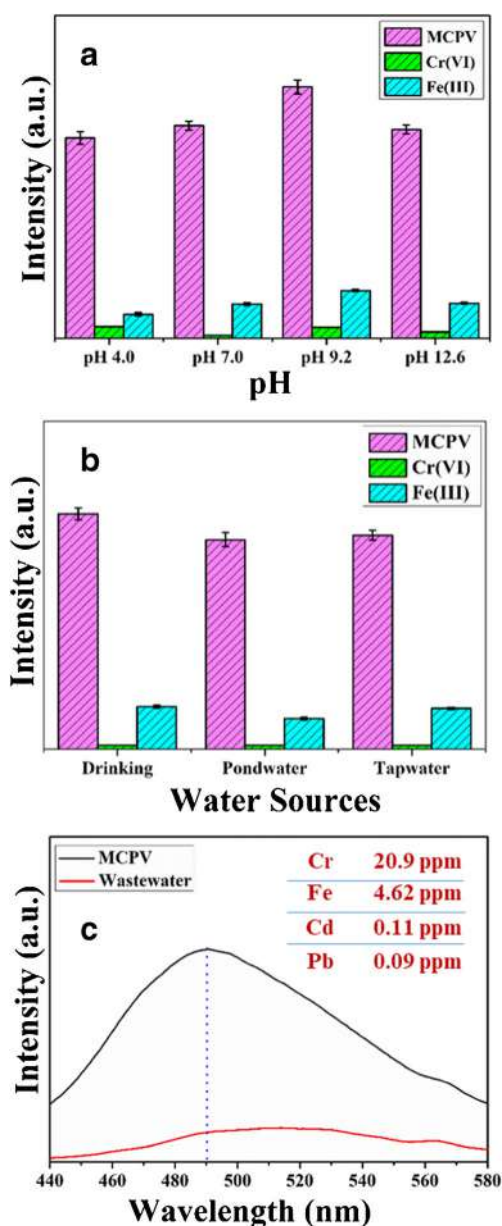


Fig. 6 Sensing performances of the sensor upon Cr^{6+} and Fe^{3+} exposure at (a) different pH and (b) different water sources; (c) fluorescence quenching observed using industrial wastewater and ICP-AES data of the collected tannery wastewater sample (inset)

101.1%, with very low values of relative standard deviation (RSD) (below 1.84). Hence, this sensor material can be used in a wide range of pH without any alteration in sensing efficiency.

Performance of the membrane in different water sources

A wide range of water samples from different sources have been used to check the activity of the sensing probe in varying water qualities. Water samples were collected from various sources; drinking water was collected from a water purifier adjacent to our laboratory, tap water was collected from the

laboratory tap, and pond water was collected from a nearby pond situated inside the institute campus. The collected water samples were filtered through a membrane filter of 0.45 μm pore size and their quantitative physical analyses were performed using a portable pH/TDS/Temperature Meter, Hanna (HI991300) (Table S3). The fluorescence intensity of the sensor was recorded by immersing it into different water samples, showing no significant change in emission patterns. The procured water samples were then spiked with Fe^{3+} and Cr^{6+} in order to determine their sensing performance. Significant fluorescence alteration was observed in both cases (Fig. 6b). The emission maxima shifted to higher wavelength in case of Cr^{6+} . The analytical validation has been done by interday and intraday studies of the collected water samples at different concentrations. Initially, water samples were collected for three consecutive days at 3 different times (8:00 am, 12:00 pm, and 8:00 pm) and similar experimentation was performed as stated above (Fig. S5). The recovery and RSD were calculated in each case and depicted in Table 1. It is found that the RR% is within 90.88 to 110.10% for various interday and intraday studies. Nominal amounts of RSD have also been observed in such cases, confirming the sensing ability of the probe in different water qualities.

Performance of the membrane in real-life tannery wastewater

In order to achieve a better insight into the real-life sensing efficacy of the sensing probe, the sensor membrane has been exposed to various heavy metal-containing tannery wastewater. The wastewater was collected from a local canal connected to a nearby tannery industry. The ICP-OES result of the tannery wastewater shows the traces of chromium and iron with other impurities (Fig. 6c, inset). The sensor membrane was immersed into the wastewater and exposed to 414-nm wavelength, which shows a significant fluorescence quenching with a red shift of the emission maximum. This experiment confirms the presence of chromium and iron in the collected wastewater sample as per the previously obtained results. Although the qualitative assessment has been successfully validated using the sensor membrane, but due to the presence of a high amount of chromium and iron (402.0 μM and 82.8 μM , respectively), the sensing probe was unable to perform any quantitative assessment for these two contaminants. This experiment confirms the on-site applicability of the sensing probe in real-life wastewaters, even in the presence of various interfering elements.

Performance of the membrane when used in a repetitive manner

Recycling capability and reusability are highly essential for the application of synthesized fluorescent probe. The sensor was subjected to alternative exposure to the Millipore water,

Table 1 Detection and sensing performance in various water samples

Water type	Spiking ion	Interday ($n=3$)				Intraday ($n'=3$)			
		Added amount (μM)	Recovered amount (μM)	Recovery (%)	RSD (%)	Added amount (μM)	Recovered amount (μM)	Recovery (%)	RSD (%)
Distilled water	Cr^{6+}	6.80	6.89	101.32	0.30	6.80	7.11	104.56	0.12
		13.6	13.90	102.21	0.13	13.6	13.88	102.06	0.07
		20.40	19.60	96.08	0.13	20.40	19.89	97.50	0.20
	Fe^{3+}	10.00	11.01	110.10	0.27	10.00	10.81	108.10	0.14
		15.00	15.42	102.80	0.31	15.00	14.93	99.53	0.17
		20.00	19.22	96.10	0.15	20.00	19.50	97.50	0.29
Drinking water	Cr^{6+}	6.80	6.35	93.38	0.10	6.80	6.18	90.88	0.06
		13.60	14.14	103.97	0.35	13.60	14.78	108.68	0.19
		20.40	19.22	94.22	0.41	20.40	20.16	98.82	0.34
	Fe^{3+}	10.00	10.28	102.80	0.29	10.00	9.90	99.00	0.34
		15.00	14.16	94.40	0.13	15.00	14.70	98.00	0.18
		20.00	19.50	97.50	0.26	20.00	20.23	101.15	0.16
Tap water	Cr^{6+}	6.80	7.08	104.12	0.28	6.80	7.15	105.15	0.13
		13.60	13.02	95.74	0.20	13.60	12.97	95.37	0.24
		20.40	21.91	107.40	0.72	20.40	22.01	107.89	0.38
	Fe^{3+}	10.00	10.30	103.00	0.34	10.00	10.50	105.00	0.18
		15.00	14.10	94.00	0.31	15.00	13.98	93.20	0.16
		20.00	19.80	99.00	0.20	20.00	19.98	99.90	0.10
Pond water	Cr^{6+}	6.80	7.25	106.62	0.24	6.80	7.21	106.03	0.20
		13.60	13.92	102.35	0.31	13.60	14.30	105.15	0.33
		20.40	20.93	102.60	0.51	20.40	20.74	101.67	0.59
	Fe^{3+}	10.00	10.70	107.00	0.35	10.00	10.41	104.10	0.66
		15.00	14.20	94.67	0.30	15.00	14.45	96.33	0.41
		20.00	20.22	101.10	0.17	20.00	19.67	98.35	0.36

Cr^{6+} and Fe^{3+} solutions, and their subsequent fluorescent intensity was measured at 414 nm excitation. Figure S6 illustrates that irrespective of several cycles of immersion in the quencher ion solutions, there is no significant alteration in its performance and the membrane retains its fluorescence property even after repetitive usage.

Studies of heavy metal-induced early-stage carcinogen detection

Establishment of the framework

Glutathione (GSH) is a non-thiol protein present in almost every living cell and acts as an antioxidant to prevent cellular component damage by reactive oxygen species such as free radicals, peroxides, and heavy metals [28]. Cr^{6+} is a potent carcinogen, which in the presence of enzymes like cytochrome b5 and glutathione reduces to Cr^{3+} via reactive intermediates (such as Cr^{4+} and Cr^{5+}) [29]. This further generates reactive species like $\cdot\text{OH}$ radical through Fenton-like reaction

that induces double bond break or modifies heterocyclic ring of the nucleotide, which might initiate cancer development [30].

Similarly, the presence of iron, although at higher concentrations, can also initiate reactive oxidative species formation in living cells [31, 32]. Henceforth, if one can detect heavy metals like Cr^{6+} and Fe^{3+} in the presence of glutathione, it could be a beneficial step toward early-stage cancer detection.

Interaction study between the sensing probe and glutathione

Initially, the interaction between the sensor membrane and glutathione (PDB ID: 1PKW) [33] was carried out theoretically by using standard molecular docking approach. In order to minimize the computation complexity, the fluorophore part of the sensing probe (carbon dot) was taken to study the interaction. The molecular docking simulation predicted nine different docked poses, among which the lowest pose was considered for further purposes. In this pose, the binding affinity between the fluorophore and glutathione was found to be

$-6.7 \text{ kcal mol}^{-1}$. It is found from the docking results that the -OH moiety of the fluorophore is forming a weak polar hydrogen bond with the arginine amino acid of glutathione making a bond length of 2.3 \AA (Fig. 7). Above all, no alteration in amino acid sequence in glutathione has been found, which corroborates the fact that this sensing probe is capable of producing fluorescence in glutathione environment without altering any of its physicochemical activities.

Experimental verification of Fe^{3+} and Cr^{6+} detection in glutathione solution

Previously, researchers theoretically predicted that carbon dot could detect heavy metals in glutathione environment [34, 35] and proposed theoretical sensing studies using DFT and molecular docking simulations [9]. This time an experimental verification of that study has been conducted using facile fluorometric techniques.

Initially, the sensor membrane was immersed in $500 \text{ }\mu\text{M}$ glutathione solution, which was dispersed in stimulated body fluid (SBF). The system was then irradiated by 414-nm excitation showing bright blue fluorescence (Fig. S7). The similar phenomenon was observed through the naked eyes upon UV

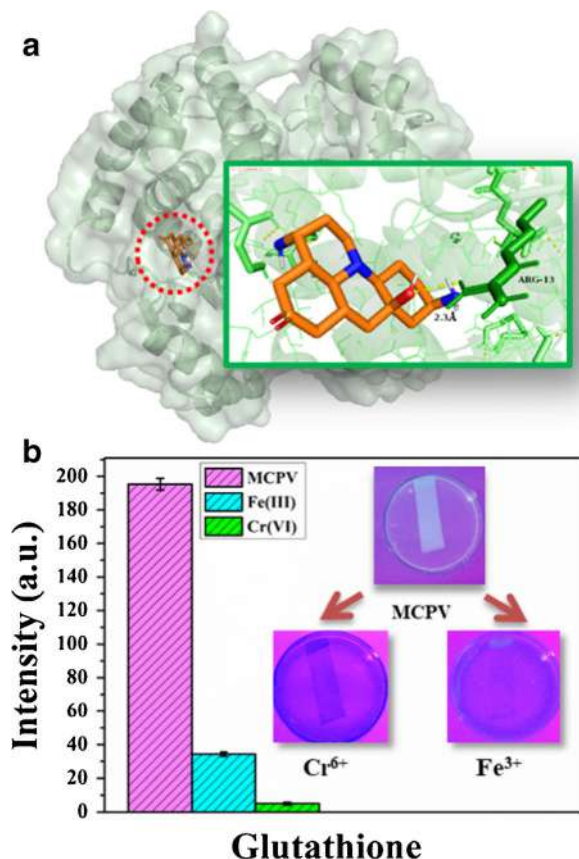


Fig. 7 (a) Molecular docking simulation depicting interaction between fluorophore and glutathione; (b) sensing of Cr^{6+} and Fe^{3+} in glutathione solution and simultaneous naked eye observation under UV illumination

exposure. This ensures the molecular docking results confirming the interaction between fluorophores and glutathione. The solution was then spiked with $50 \text{ }\mu\text{M}$ Cr^{6+} and Fe^{3+} separately and significant fluorometric reductions have been achieved in both the cases (Fig. 7). This validates the previously mentioned theoretical studies and suggests that the material is able to detect both the contaminants in biological species.

Conclusion

Herein, a fluorometric sensor has been developed using carbon dot-decorated natural microcline wrapped into PVDF-HFP polymer. The polymer effectively delivers mechanical and fluorescence stability to the membrane. This flexible and mechanically stable membrane can be used in a repetitive manner and almost free from any mechanical damage due to prolonged usage. This fluorometric sensor detects the presence of Cr^{6+} and Fe^{3+} in water showing excellent figures of merit. Low RSD and significant recovery rates in different water qualities confirm that this membrane will not require any pretreatment of water samples and will cut down such treatment and storage costs. Moreover, it has been validated (both theoretically and experimentally) that the membrane can detect both the contaminating ions in the presence of glutathione. Thus, in near future, in vitro studies could be carried out in order to detect such contaminations in living cells. Such in vitro study would be beneficial for heavy metal-induced early-stage cancer detection.

Supplementary Information The online version contains supplementary material available at <https://doi.org/10.1007/s00604-021-04787-0>.

Acknowledgements The authors would like to thank the Department of Physics, Jadavpur University, Kolkata, for extending experimental facilities.

Funding S.D. would like to acknowledge DST-SERB (Grant No. EEQ/2018/000747) for funding.

Declarations

Conflict of interest The authors declare no competing interests.

References

- Hakak S, Khan WZ, Gilkar GA, Haider N, Imran M, Alkathairi MS (2020) Industrial wastewater management using blockchain technology: architecture, requirements, and future directions. *IEEE Internet Things J* 3(2):38–43
- Lu KH, Lin JH, Lin CY, Chen CF, Yeh YC (2019) A fluorometric paper test for chromium (VI) based on the use of N-doped carbon dots. *Microchim Acta* 186(4):1–7

3. Mihai O, Kawamoto MS, LeBlanc KL, Grinberg P, de Araújo Nogueira AR, Mester Z (2020) Determination of chromium picolinate and trace hexavalent chromium in multivitamins and supplements by HPLC-ICP-QQQ-MS. *J Food Compos Anal* 87: 103421
4. Meucci V, Battaglia F, Marchetti V, Gori E, Intorre L (2020) Rapid and simultaneous electrochemical method to measure copper and lead in canine liver biopsy. *MethodX* 7:101154
5. Duan Q, Wang X, Zhang B, Li Y, Zhang W, Zhang Y, Sang S (2019) A fluorometric method for mercury (II) detection based on the use of pyrophosphate-modified carbon quantum dots. *Microchim Acta* 186(11):736
6. Barone PW, Parker RS, Strano MS (2005) In vivo fluorescence detection of glucose using a single-walled carbon nanotube optical sensor: design, fluorophore properties, advantages, and disadvantages. *Anal Chem* 77(23):7556–7562
7. Welti A, Lohmann U, Kanji ZA (2019) Ice nucleation properties of K-feldspar polymorphs and plagioclase feldspars. *Atmos Chem Phys* 19(16):10901–10918
8. Kart A, Koc E, Dalgınlı KY, Gulmez C, Sertcelik M, Atakisi O (2016) The therapeutic role of glutathione in oxidative stress and oxidative DNA damage caused by hexavalent chromium. *Biol Trace Elem Res* 174(2):387–391
9. Roy S, Bardhan S, Chanda DK, Roy J, Mondal D, Das S (2020) In situ-grown Cd-dot-wrapped Boehmite nanoparticles for Cr (VI) sensing in wastewater and a theoretical probe for chromium-induced carcinogen detection. *ACS Appl Mater Interfaces* 12(39):43833–43843
10. Patro TU, Mhalgi MV, Khakhar DV, Misra A (2008) Studies on poly (vinylidene fluoride)–clay nanocomposites: effect of different clay modifiers. *Polymer* 49(16):3486–3499
11. Roy S, Thakur P, Hoque NA, Bagchi B, Das S (2016) Enhanced electroactive β -phase nucleation and dielectric properties of PVdF-HFP thin films influenced by montmorillonite and Ni(OH)₂ nanoparticle modified montmorillonite. *RSC Adv* 6(26):21881–21894
12. Cai X, Lei T, Sun D, Lin L (2017) A critical analysis of the α , β and γ phases in poly (vinylidene fluoride) using FTIR. *RSC Adv* 7(25): 15382–15389
13. Mondal P, Purkait MK (2017) Effect of polyethylene glycol methyl ether blend humic acid on poly (vinylidene fluoride-co-hexafluoropropylene) PVDF-HFP membranes: pH responsiveness and antifouling behavior with optimization approach. *Polym Test* 61:162–176
14. Wu L, Yuan W, Hu N, Wang Z, Chen C, Qiu J, Ying J, Li Y (2014) Improved piezoelectricity of PVDF-HFP/carbon black composite films. *J Phys D Appl Phys* 47(13):135302
15. Bardhan S, Roy S, Chanda DK, Ghosh S, Mondal D, Das S, Das S (2020) Nitrogenous carbon dot decorated natural microcline: an ameliorative dual fluorometric probe for Fe³⁺ and Cr⁶⁺ detection. *Dalton Trans* 49(30):10554–10566
16. Sun X, Lei Y (2017) Fluorescent carbon dots and their sensing applications. *TrAC Trends Anal Chem* 89:163–180
17. Pérez-Rodríguez C, Martín LL, León-Luis SF, Martín IR, Kumar KK, Jayasankar CK (2014) Relevance of radiative transfer processes on Nd³⁺ doped phosphate glasses for temperature sensing by means of the fluorescence intensity ratio technique. *Sensors Actuators B Chem* 195:324–331
18. Fairman HS, Brill MH, Hemmendinger H (1997) How the CIE 1931 color-matching functions were derived from Wright-Guild data. *Color Research & Application: Endorsed by Inter-Society Color Council, The Colour Group (Great Britain), Canadian Society for Color, Color Science Association of Japan, Dutch Society for the Study of Color, The Swedish Colour Centre Foundation, Colour Society of Australia, Centre Français de la Couleur* 22(1):11–23
19. Roy S, Pal K, Bardhan S, Maity S, Chanda DK, Ghosh S, Karmakar P, Das S (2019) Gd (III)-doped Boehmite nanoparticle: an emergent material for the fluorescent sensing of Cr (VI) in wastewater and live cells. *Inorg Chem* 58(13):8369–8378
20. Kubista M, Sjöback R, Eriksson S, Albinsson B (1994) Experimental correction for the inner-filter effect in fluorescence spectra. *Analyst* 119(3):417–419
21. Pajewska-Szmyt M, Buszewski B, Gadzała-Kopciuch R (2020) Sulphur and nitrogen doped carbon dots synthesis by microwave assisted method as quantitative analytical nano-tool for mercury ion sensing. *Mater Chem Phys* 242:122484
22. Zu F, Yan F, Bai Z, Xu J, Wang Y, Huang Y, Zhou X (2017) The quenching of the fluorescence of carbon dots: a review on mechanisms and applications. *Microchim Acta* 184(7):1899–1914
23. Nugent JW, Lee H, Reibenspies JH, Lee HS, Hancock RD (2017) Effects of anion coordination on the fluorescence of a photo-induced electron transfer (PET) sensor complexed with metal ions. *Polyhedron* 130:47–57
24. Bharadwaj K, Choudhary H, Hazra S, Ghosh S (2019) Role of emissive and non-emissive complex formations in photoinduced electron transfer reaction of CdTe quantum dots. *Chem Asian J* 14(23):4207–4216
25. Nenov A, Borrego-Varillas R, Oriana A, Ganzer L, Segatta F, Conti I, Segarra-Martí J, Omachi J, Dapor M, Taioli S, Manzoni C (2018) UV-Light-induced vibrational coherences: the key to understand Kasha rule violation in trans-azobenzene. *J Phys Chem Lett* 9(7): 1534–1541
26. Mohandoss S, Stalin T (2017) A new fluorescent PET sensor probe for Co²⁺ ion detection: computational, logic device and living cell imaging applications. *RSC Adv* 7(27):16581–16593
27. Mittal M, Sapra S (2017) Nanocrystal–dye interactions: studying the feasibility of co-sensitization of dyes with semiconductor nanocrystals. *ChemPhysChem* 18(18):2509–2516
28. Grahn E, Novotny M, Jakobsson E, Gustafsson A, Grehn L, Olin B, Madsen D, Wahlberg M, Mannervik B, Kleywegt GJ (2006) New crystal structures of human glutathione transferase A1-1 shed light on glutathione binding and the conformation of the C-terminal helix. *Acta Crystallogr Sect D Biol Crystallogr* 62(2):197–207
29. Chiu A, Chiu N, Shi X, Beaubier J, Dalai NS (1998) Activation of a procarcinogen by reduction: Cr⁶⁺ → Cr⁵⁺ → Cr⁴⁺ → Cr³⁺ a case study by electron spin resonance (ESR/PMR). *J Environ Sci Health C Environ Carcinog Ecotoxicol Rev* 16(2):135–148
30. Mazzer PA, Maurmann L, Bose RN (2007) Mechanisms of DNA damage and insight into mutations by chromium (VI) in the presence of glutathione. *J Inorg Biochem* 101(1):44–55
31. Nakamura T, Naguro I, Ichijo H (2019) Iron homeostasis and iron-regulated ROS in cell death, senescence and human diseases. *Biochim Biophys Acta Gen Subj* 1863(9):1398–1409
32. Halliwell B (1991) Reactive oxygen species in living systems: source, biochemistry, and role in human disease. *Am J Med* 91(3):S14–S22
33. Ruzza P, Calderan A (2013) Glutathione transferase (GST)-activated prodrugs. *Pharmaceutics* 5(2):220–231
34. Jalili R, Khataee A, Rashidi MR, Luque R (2019) Dual-colored carbon dot encapsulated metal-organic framework for ratiometric detection of glutathione. *Sensors Actuators B Chem* 297:126775
35. Bhamore JR, Park TJ, Kailasa SK (2020) Glutathione-capped Syzygium cumini carbon dot-amalgamated agarose hydrogel film for naked-eye detection of heavy metal ions. *J Anal Sci Technol* 11: 1–9

Publisher's note Springer Nature remains neutral with regard to jurisdictional claims in published maps and institutional affiliations.



Contents lists available at ScienceDirect

Spectrochimica Acta Part A: Molecular and Biomolecular Spectroscopy

journal homepage: www.elsevier.com/locate/saa

Real-time sensitive detection of Cr (VI) in industrial wastewater and living cells using carbon dot decorated natural kyanite nanoparticles

Souravi Bardhan^a, Shubham Roy^a, Sanghita Das^a, Ishita Saha^b, Dhananjay Mondal^a, Jhilik Roy^a, Dipak Kr. Chanda^c, Solanky Das^d, Parimal Karmakar^b, Sukhen Das^{a,*}

^a Department of Physics, Jadavpur University, Kolkata 700032, India

^b Department of Life Science and Biotechnology, Jadavpur University, Kolkata 700032, India

^c School of Materials Science and Nano-Technology, Jadavpur University, Kolkata 700032, India

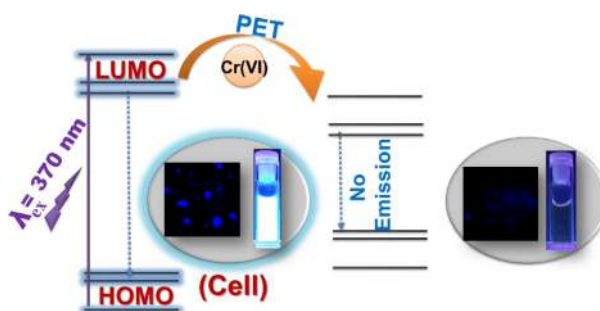
^d Department of Geology, Jadavpur University, Kolkata 700032, India

HIGHLIGHTS

- Synthesis of carbon dot doped natural kyanite nanostructure has been reported.
- Selective detection of Cr (VI) in industrial wastewater and live cells is found.
- Limit of detection is found to be $\sim 0.11 \mu\text{M}$ against hexavalent chromium.
- Theoretical and experimental validation of the detection mechanism is reported.

GRAPHICAL ABSTRACT

Cost-effective and time-efficient synthesis of natural mineral (kyanite) based biocompatible, fluorometric sensor for highly selective and sensitive detection of Cr (VI) in aqueous media, industrial wastewater and living cells.



ARTICLE INFO

Article history:

Received 24 October 2021

Received in revised form 30 January 2022

Accepted 16 February 2022

Available online 19 February 2022

Keywords:

Natural mineral
Rietveld refinement
TDDFT
Molecular docking
Hexavalent chromium

ABSTRACT

This article reports a facile strategy to detect hexavalent chromium (Cr (VI)) using a naturally formed mineral (kyanite) based fluorometric sensor. Nitrogenous carbon dots have been incorporated into natural kyanite (KYCD) nanoparticles causing a stable bright blue fluorescence compared to its pristine counterpart. This sensing probe structurally stabilizes and resists the agglomeration of carbon dots, thus retaining fluorescence quality for a longer period. The promising bright blue fluorescence has been utilized further to detect Cr (VI) in wastewater and living cells. Ease of synthesis, low cost, and stability of the system offers the benefit for large-scale production, which is convenient for industrial production the sensing probe. The sensor shows high selectivity and sensitivity (LOD and LOQ of $0.11 \mu\text{M}$ and $0.36 \mu\text{M}$ respectively in case of linear fitting, whereas $0.26 \mu\text{M}$ and $0.88 \mu\text{M}$ respectively for full range plot) towards hexavalent chromium in presence of other interfering elements. A detailed study of photoinduced electron transfer (PET) mediated rapid 'turn off' sensing mechanism was carried out using Time-Dependent Density functional (TDDFT) calculations. The sensing efficacy of the probe remains unaltered under a wide range of pH and can be effective in various water types. Onsite sampling and probing of Cr (VI) in tannery wastewater has been performed to validate its real-life efficiency that yields excellent results. The sensor can effectively detect chromium at a cellular level (HeLa cells) in a similar way as the bright blue fluorescence diminishes in presence of the quenching ion. Experimental in vitro studies along with theoretical docking analysis has been conducted to substantiate such issues and a higher

* Corresponding authors.

E-mail address: sdasphysics@gmail.com (S. Das).

possibility of fluorophore binding was found for Isoleucine (2.9 Å), Serine (2.96 Å), and Glycine (3.16 Å). This biocompatible sensor rapidly senses hexavalent chromium in living cells, which makes this efficient probe a true heavy metal-induced carcinogen sensor.

© 2022 Published by Elsevier B.V.

1. Introduction

Water is an exceptionally essential resource for life to sustain on the earth but various anthropogenic activities like rapid industrialization and unplanned urbanization are causing uncontrolled contamination and hampering every life-forms. Amongst various sources of pollution, heavy metals are considered as one of the major culprits for widespread water pollution due to their high toxicity and possibility for bioaccumulation [1]. Out of the various constantly releasing heavy metals, hexavalent chromium (Cr (VI)) is comparatively more hazardous due to its carcinogenic nature and high toxicity at the micro-molar concentration (WHO permissible limit in inland surface waters is 0.1 mg l^{-1}) [2]. Hexavalent chromium is assumed to originate from anthropogenic activities [3] like chrome plating, leather industries, textiles, and upon uptake by biota can interact with thiol compounds, inducing mutation and DNA damage. Hence various techniques like chromatography, inductively coupled plasma technique, atomic absorption spectrometry, etc. are employed for the detection of aqueous Cr (VI) [4–5], but most of them are time-consuming require complicated pretreatment and expensive equipment. The quest for rapid detection, easy operation, cost-effective, proper monitoring of selective heavy metal in water and living cells even at low concentration paved the path for widespread recognition of non-invasive fluorometric sensors [6–6d]. Moreover, biocompatibility and eco-friendliness of the sensor material are key factors to reduce the chances of further contamination from the sensing probe. Numerous fluorescent compounds demonstrated their ability to act as Cr (VI) sensors [7–8] to date but reports focus on natural mineral-based biocompatible and efficient sensors that can be practically deployable in industrial or commercial usage. Furthermore, silicates are the most abundant compound found on the earth's crust, thus due to its widespread availability and relatively non-toxic nature, kyanite mineral (AlSiO_5) was selected for the study. The goal of the work was to synthesize a natural-based sensor that can be both industrially and commercially feasible due to biocompatibility, high stability that does not get affected with time and environment, efficiency to detect in real-life samples that contains innumerable impurities, cost-effectiveness due to wide availability of raw materials and ease of synthesis which does not involve tedious steps or toxic chemicals and have a high yield. Even the carbon dots used for fluorescence enhancement are well known for biocompatible, non-toxic, quasi-spherical, amorphous carbon-based structures with diameters less than 10 nm having magnificent tunable fluorescence emission [8a]. Moreover, bioimaging and the ability to detect Cr (VI) at the cellular level opens a new avenue for the sensor in biomedical applications.

The present study aims at the facile top-down synthesis of coarse fractions of natural kyanite into nano-regime and then decorating with nitrogenous carbon dots to develop a stable fluorescent probe for hexavalent chromium. Over the past few years, numerous studies focusing on favorable optical properties of carbon dots have been reported [9–10]. Carbon dots can agglomerate in liquid state which can result in reduced fluorescence intensity. Thus, various strategies have been applied by researchers to stabilize the fluorescence of these tiny quantum dots [11] for a longer period. Interestingly, amorphous carbon dots tailored into the solid substrate of kyanite nanostructure depict better fluorescence sta-

bility herein. The nano-sized kyanite provides better thermal and chemical stability and facilitates a photoinduced electron transfer mechanism to selectively detect Cr (VI). Biocompatibility of the sensor material has been evaluated herein to ensure the safe practice of the material in real life. Apart from detection in real-life industrial wastewater, the biocompatible nature and ability for real-time bioimaging of living cells have also been assessed to determine the potentiality of the probe as an intracellular Cr (VI) sensor.

2. Experimental section

2.1. Materials

The naturally formed kyanite was bought from Hindustan Minerals, Kolkata, India. Ethylenediamine (EDA) (HPLC grade), N, N-dimethylformamide (DMF) (HPLC grade), anhydrous citric acid and potassium dichromate were $\geq 98.0\%$ pure and were purchased from Merck, India. All chemicals used for selectivity analysis (NaCl , KCl , $\text{CaCl}_2 \cdot 2\text{H}_2\text{O}$, $\text{FeSO}_4 \cdot 7\text{H}_2\text{O}$, FeCl_3 , $\text{Cr}(\text{CH}_3\text{COO})_3$, CdCl_2 , HgCl_2 , PbCl_2 , NaOH , NaNO_3 , Na_2CO_3 , Na_2S , Na_2SO_4) were purchased from Merck, India while As_2O_3 was purchased from Sigma-Aldrich. Dulbecco's modified eagle's medium (DMEM) and fetal bovine serum (FBS) were purchased from Thermo Fisher Scientific (Waltham, MA, USA). Phosphate buffer saline (PBS) and MTT (3-(4,5-Dimethylthiazol-2-Yl)-2,5-Diphenyltetrazolium Bromide) were purchased from SRL, India. All chemical reagents and other solvents used throughout the experiments were analytical grade and used without further purification. Millipore water (resistivity $\sim 18.2 \text{ M}\Omega \text{ cm}$) was used for all experimental and rinsing purposes.

2.2. Synthesis of the carbon dot decorated natural nano-sensor

2.2.1. Synthesis of nitrogenous carbon dot (CD)

In a typical synthesis process, citric acid solution (5.5 mM) was prepared by dissolving anhydrous citric acid in 70 mL of Millipore water under stirring conditions at room temperature. EDA was added drop wise for basification till pH became 12.0 and kept under stirring conditions for another 2 h. The solution was then poured into a clean Teflon-lined stainless-steel autoclave and heated in a dust-free hot air oven for 12 h at 190°C . The solution was then normally cooled to room temperature, centrifuged and the supernatant (CD) was collected and stored for further use.

2.2.2. Preparation of nano kyanite (K)

A top-down method using mechanical ball milling was performed to obtain kyanite nanoparticles. The purchased kyanite was initially washed thoroughly to remove debris and other impurities and manually fragmented into smaller fractions. Ball milling of the smaller fractions was carried out using a Fritsch Planetary Mono Mill Pulverisette 6 for 12 h at 300 rpm using tungsten carbide vials and balls, keeping the ball-sample mass ratio of 20:1. After completion of the milling process, powdered mineral sample was collected for further processes.

2.2.3. Preparation of nitrogenous CD doped natural kyanite (KYCD)

A fraction (500 mg) of the powdered mineral sample (K) was collected and added to 10 mL carbon dot solution and stirred over-

night. Solution was then centrifuged for 15 min at 8,000 rpm and the precipitate was collected and dried at 70 °C for 6 h. The dried sample was then crushed in an agate mortar, labeled as KYCD, and sent for characterizations. The detailed synthesis route is illustrated in Scheme 1.

2.3. Characterization techniques

X-ray diffraction (XRD) of CD, K and KYCD was performed using X-ray powder diffractometer (D8, Bruker AXS, Wisconsin, USA) using a Cu-K α target emitting 1.5418 Å wavelength. The instrument was operated at 35 kV, 35 mA external field with 2 θ values ranging between 10 and 70°.

The Fourier transform infrared spectroscopy (FTIR-8400S, Shimadzu) in the range of 400–4000 cm⁻¹ were conducted for determining the surface functional groups and overall bonding networks of the samples using solid pellets of K and KYCD homogenized with KBr in a ratio of 1:50.

Surface morphology along with elemental analyses of kyanite and carbon dot loaded kyanite were determined from field emission scanning electron microscopy (FESEM, INSPECT, F50, Netherlands) equipped with Bruker Quantax EDS analyzer, which operated at room temperature at 5–20 kV bias voltages under the chamber pressure of 3×10⁻⁴ Pa. Further, carbon dot loading was confirmed from Transmission electron microscopy (TEM) image obtained from JEOL JEM-2000 transmission electron microscope (TEM) operated at 200 kV under high vacuum. The sample was cast over a carbon-coated copper grid (300 mesh) for TEM analysis. Both FESEM and TEM experiments were performed using very minute amounts of the sample that was well dispersed in acetone using an ultrasonic bath for at least 30 min and then mounted over the appropriate grids.

The thermal stability of the materials was determined using thermogravimetric (TGA) and differential thermal method (DTA) using DTG-60H, Shimadzu. The instrument was operated from ambient lab temperature (~30 °C) to 400 °C at a constant heating rate of 10 °C min⁻¹ under N₂ atmosphere (50 cc/ min) to estimate the thermal stabilities.

The absorbance spectrum of the samples was measured by using a UV–vis spectrophotometer (UV-1900i, Shimadzu) in a varying wavelength ranging between 200 and 600 nm. Fluorescence spectra were obtained by a Cary Eclipse Fluorescence Spectrometer, Agilent Technologies maintaining excitation and emission slit

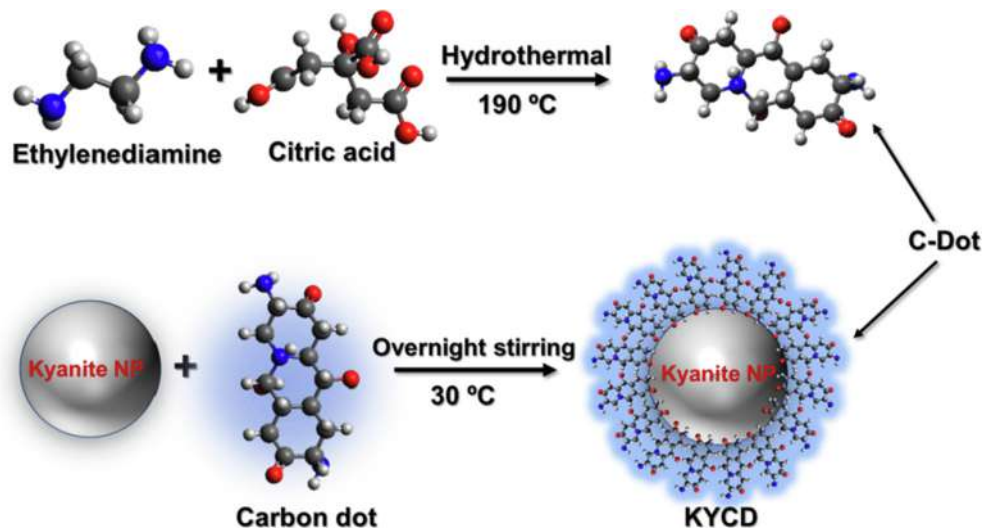
sizes of 5 nm each. In both cases, the powdered samples were dispersed in ultrapure water (1 mg mL⁻¹ solution) followed by ultrasonic treatment for 30 min in each case. Fluorescence lifetimes were measured using a time-resolved spectrofluorometer from IBH, UK. The samples were excited at 370 nm, whereas the emission was set at 470 nm.

Inductively coupled plasma optical emission spectrometry (ICP-OES) using SPECTRO Analytical Instrument, SPECTRO ARCOS II, Germany was done to determine the elemental composition of tannery wastewater. Collected wastewater was filtered (pore size 0.45 μ m) and microwave-assisted digestion was done after treating with HNO₃-H₂O₂ solution. The solution was then diluted to 1:10 (v/v) using 1.0 M HNO₃ and ICP measurement was conducted with a pump rate of 25.0 rpm, nebulizer flow of 1.0 L min⁻¹, plasma argon flow rate of 13.0 L min⁻¹, and auxiliary argon flow of 0.8 L min⁻¹. Standard analytical lines were chosen for chromium, iron, and cadmium, and standard graphs of 0–50 ppm were prepared in each case.

2.4. Computational methods

The detailed information regarding modification of microstructure and crystallographic parameters of the samples was acquired by conducting Rietveld refinement-based curve fitting of the x-ray diffractograms (software package MAUD v2.8). Experimental diffractograms were refined using a crystallographic information file (.cif) of kyanite (Database code AMCS0000733). Initially, Caglioti PV functions along with several Gaussian broadening polynomials were used in the refining process to calibrate the diffraction instrument, thereafter interpolated background parameters (using more than 150 distinct points) were used to refine the background error. Crystal and microstrain parameters were computed using the Popa size-strain model and the arbitrary texture model was utilized to refine the textural parameters of the crystals. Refined structures of both the samples along with the bonding networks were visualized from the computed .cif files using the Visualization for Electronic and Structural Analysis (Vesta v3.4.3) program.

The fluorophore (carbon dot) geometry was optimized by Becke's three-parameter hybrid exchange functional was adopted with Lee–Yang–Parr gradient-corrected correlation (B3LYP) functional coupled with the continuum aqueous solvent mode (CPCM). The Orca v.4.2 package was used for DFT and TDDFT calculations



Scheme 1. Schematic representation of the preparation route for KYCD.

and then the geometries were modeled with Avogadro v.1.2 program. The RIJCOSX auxiliary basis function was implemented to describe the elements (C, H, O, N) and Cr (VI) ion, respectively along with the 6-31G** basis set. Initially, the frequency optimization of the fluorophore (carbon dot) was performed at the same theoretical level depicting the absence of any imaginary frequency. Lastly, the TDDFT method was used to evaluate the electronic transitions of the complex.

The binding affinity between fluorophore (carbon dot) and glutathione was evaluated using the molecular docking technique. Autodock Tools v.1.5.6 was used primarily to prepare the protein, omitting water molecules and adding Kollman charges along with polar hydrogen. The binding affinity of glutathione (PDB ID: 1PKW) with the fluorescent ligand was determined using Autodock vina v.1.1.2. Further identification and visualization of the exact binding pocket, PyMol v.2.0.7 and Ligplot plus v2.2.4 programs were employed [12].

2.5. Preparation of cells

Living HeLa cells (human cervical cancer cell line) and WI38 human lung fibroblast cells were purchased from National Centre for Cell Science (NCCS Pune, India) and maintained in DMEM medium containing 5 % FBS. Cell cultures were performed in the medium and incubated at 37 °C under 5 % CO₂. These cells were washed with PBS (1x) solution and the addition of fresh medium was done on the following day to maintain the culture. The biocompatibility of the fluorescent sensor was determined using the WI38 cell line by MTT assay. Initially, the cells were seeded in well plates at a density of 1 × 10⁴ cells per well and incubated for a day with DMEM medium having 10 % FBS. A homogeneous solution of KYCD was prepared separately by dispersing KYCD powder in filtered PBS solution (0.5 mg mL⁻¹) and the cells were treated with the solution at varying concentrations ranging between 0 and 120 µg mL⁻¹. After 24 h of incubation, the culture medium was replaced by MTT solution (450 µg mL⁻¹) and incubated for another 3 h. The MTT solution was then discarded and cells were dissolved in MTT solubilization buffer and the formation of formazol crystal color was measured by obtaining the absorbance at 570 nm using a micro-plate reader (Biotek, USA).

Bio-imaging was conducted by growing HeLa cells on a sterilized coverslip placed in a 6-well plate. Prior to the treatment, cells were grown in 10 % FBS containing DMEM medium for 24 h at 37 °C under 5 % CO₂ environment followed by the addition of KYCD (50 µg mL⁻¹) solution. The treated sample was incubated for 4 h before fluorescence microscopy. The quenching efficacy on the addition of chromium was also determined by adding a drop of hexavalent chromium solution (20 µg mL⁻¹) on another coverslip containing KYCD treated cells. The cells were then mounted by 50% glycerol and observed under a fluorescence microscope (Leica, Germany) upon UV excitation.

3. Results and discussion

3.1. Structural and morphological analyses

Since this work involves natural mineral samples, determination of purity and quantification of various crystallographic parameters is much needed. It is also very essential to validate the incorporation of carbon dot into the natural mineral. Diffraction maxima obtained in both the cases corroborate well with JCPDS card no. 11-0046 depicting the phases of kyanite mineral [13] (Fig. 1). The absence of any extra diffraction lines suggests the absence of any impurities in the sample. A slight shift of diffraction lines toward higher diffraction angles has been observed on carbon

dot loading. This could be ascribed as the subsequent increase of microstrain [14] due to the incorporation of carbon dot into the triclinic structure as determined from microstructural analysis (Table 1). 500 µL of nitrogenous carbon dot solution was drop-casted on a clean coverslip, dried and used for XRD. The amorphous XRD pattern obtained is illustrated in Fig. S1 which shows broad 2θ patterns at around 23.5° and 42.2° which is assigned to carbon planes at 002 and 100 respectively and is well-matched with reported literature [14a].

Further insight into the detailed bonding networks using Vesta v3.4.3 (Fig. 1) reveals the symmetry of octahedral AlO₆ stacked with SiO₄ tetrahedra sharing an oxygen molecule and showing a zig-zag pattern in the pristine kyanite sample (Fig. 1c). This symmetry is missing in the carbon dot-loaded KYCD sample (Fig. 1d). The refined structure of KYCD shows oxygen molecules are missing in some AlO₆ sites resulting in oxygen vacancies inside the system. Moreover, such vacancies perturbed the stacked architecture of the alumina-silica polyhedral structure and leads to interstitial defects [15].

FTIR spectroscopy was performed to ascertain the presence of functional groups in the samples. In both K and KYCD (Fig. 2a), absorption bands centered at 468 and 537 cm⁻¹ are ascribed to Si—O tetrahedron (O—Si—O) [16]. Absorption bands situated at 668 and 970 cm⁻¹ are attributed to Al—O and asymmetric Si—O stretching vibrations [17]. The wide peaks located in the 2974–3587 cm⁻¹ range signify the stretching vibrations of O—H [18]. In the case of KYCD, the absorption band located at 1559 cm⁻¹ is due to N—H and C=N bending portraying the presence of nitrogen in the carbon dot, while the band at 1662 cm⁻¹ is due to the C=O and CO—NH bond, which belongs to the edge functional groups [19] like carboxylic acid, amino group along with hydroxyl group of carbon dot. Hence carbon dot incorporation in the case of KYCD is quite evident from the FTIR study.

Morphological features have been analyzed using FESEM and TEM. Vigorous ground kyanite using a mechanical ball mill and subsequent purification has resulted in roughly globular morphologies of both pristine and doped kyanite samples (Fig. 2). The TEM micrograph (Fig. 2) of carbon dot doped kyanite shows the presence of carbon dots having an average diameter nearly 3–5 nm evenly distributed on the KYCD surface, thus confirming the successful assimilation of carbon dots into the kyanite matrix. Elemental composition and mapping have been determined using Energy Dispersive X-ray (EDX) analysis. The EDX mapping confirms the presence and weight (%) of oxygen, aluminum, and silicon in the K sample (Fig. S2) while traces of carbon in the case of KYCD (Fig. S3), reveal successful incorporation of the carbon dot on the kyanite surface.

3.2. Optical quality of the nanostructures

The optical properties of the sensor material have been analyzed utilizing absorption and emission spectroscopy techniques. The absorbance spectrum (Fig. 3a) of the modified kyanite (KYCD) shows two distinct absorption maxima centered at 240 and 345 nm [20], which is otherwise absent in the pristine sample. These two peaks confirm the successful incorporation of the carbon dot since the peak at 240 nm corresponds to the π- π* transition of C=C bonds. Similarly, the broader peak situated at 345 nm could be assigned to the n- π* transition of C=O or C=N moiety.

Further, to determine the emission and fluorescence characteristics of the samples, photoluminescence spectroscopy has been performed. The photoluminescence spectra have been recorded initially at varied excitation wavelengths (λ_{ex}) ranging from 310 to 400 nm, among which the optimum emission intensity was observed at 370 nm excitation (Fig. S4). Thus, the fluorescence studies have been conducted at an excitation wavelength of

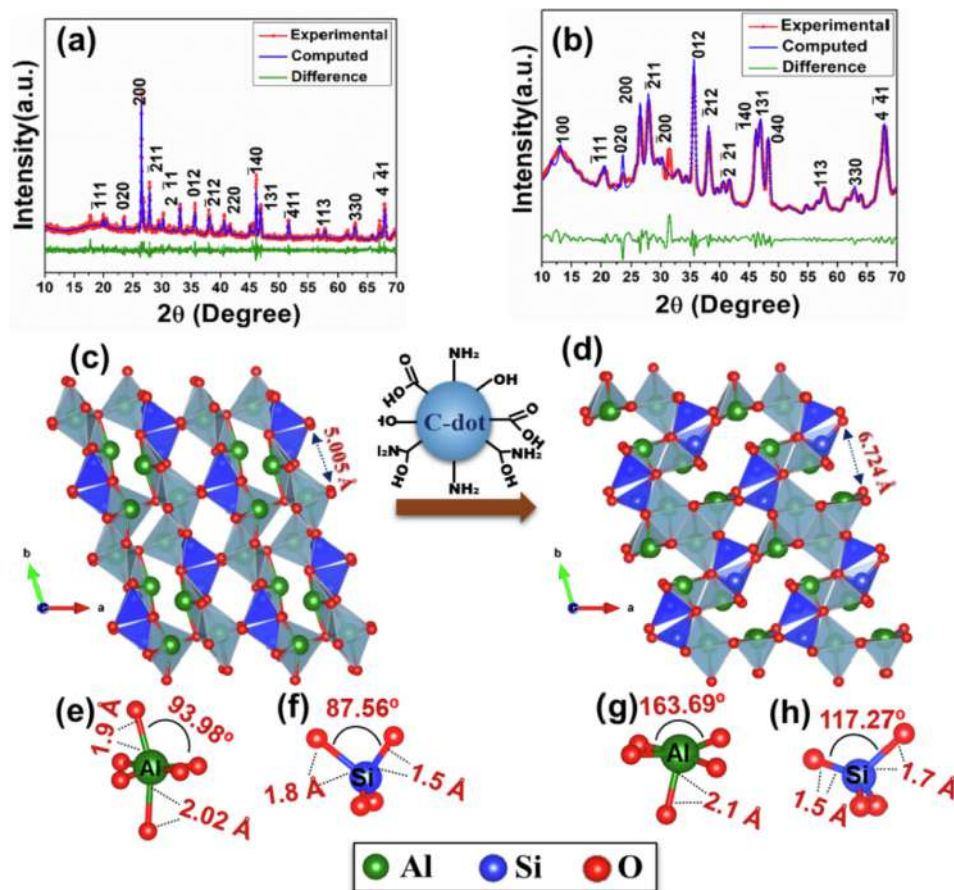


Fig. 1. Experimental (red), refined (blue) and difference (green) plots of XRD patterns of (a) K and (b) KYCD respectively by using the MAUD program; Microstructural representation of (c) K, and (d) KYCD as obtained from Vesta, with subsequent changes observed in bond lengths and bond angles in K (e–f) and KYCD (g–h) due to carbon dot loading.

Table 1
Microstructural parameters of K and KYCD obtained from Rietveld refinement.

Parameters	KY	KYCD
a (Å)	7.129 ± 0.001	7.124 ± 0.001
b (Å)	7.856 ± 0.001	7.856 ± 0.001
c (Å)	5.586 ± 0.001	5.579 ± 0.001
alpha (°)	89.923 ± 0.019	89.764 ± 0.023
beta (°)	101.223 ± 0.011	101.099 ± 0.015
gamma (°)	105.971 ± 0.015	106.008 ± 0.020
Size (Å)	1037.548 ± 35.279	266.509 ± 5.813
Strain	0.001 ± 0.001	0.002 ± 0.001
V (Å ³)	294.167	294.167
χ ²	2.048	1.665
R _p (%)	8.933	8.223
R _{wp} (%)	12.785	10.610

370 nm for further studies. It was observed that the fluorescence intensity has been increased significantly (Fig. 3b) as compared to the undoped sample at the blue region (460 nm) (Fig. 4a) in the modified kyanite sample. This type of enhancement could be ascribed to the carbon dot moiety of the sample [21]. In reality, ethylenediamine was used as a precursor that introduced various nitrogenous functional groups like C=N and N–H on the carbon dot surface, thus inserting new energy levels, which in turn causes enriched fluorescence signal [22]. A similar phenomenon has already been reported elsewhere [23]. Henceforth, carbon dot modified kyanite (KYCD) has been selected for further sensing experiments.

3.3. Determination of photostability of the sensor material

Photostability with varying time and temperature are important parameters for a commercial sensing probe. Photostability of KYCD (1 mg mL⁻¹ solution) with varying time has been investigated by recording the fluorescence intensity of the material at 460 nm upon UV excitation. The fluorescence intensity was recorded at an interval of 15 min up to a total duration of 3 h. No significant change in fluorescence intensity (Fig. 4d) has been observed confirming the stability of the sensor in the aqueous medium.

Initially, the TGA-DTA thermogram shows the inertness of the KYCD till 400 °C. A very nominal amount of mass loss (2.2%) has been observed till 400 °C with a small endothermic peak centered at 50 °C (Fig. S5). Such endothermic transition validates the elimination of the adsorbed moisture from the surface of the sample [24]. Similarly, photostability has been examined at a varying temperature range (10–70 °C) to understand the applicability of the sensing probe in real life. The optimum intensity has been found at 30 °C temperature without any spectral shift of the emission spectrum (Fig. 4c). Beyond this temperature, a slight reduction in fluorescence intensity occurred due to the collisional quenching [25] between the fluorophores at higher temperatures.

To ensure that carbon dots are properly incorporated in the kyanite matrix and do not leach out in the water, 500 μM KYCD solution was subjected to continuous stirring at 500 rpm for 6 h. 2 mL of solution was taken for centrifugation (5,000 rpm for 5 min) at every 20 min and fluorescence intensity was measured.

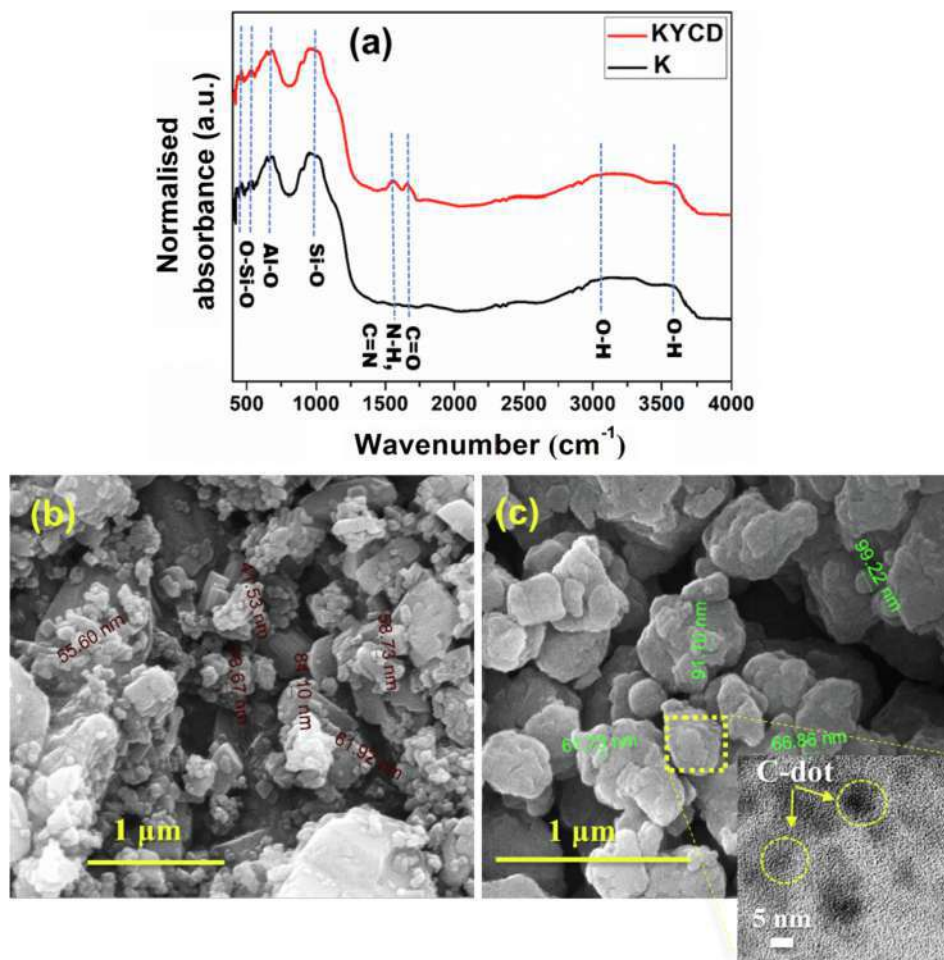


Fig. 2. FTIR spectra of the K and KYCD (a); FESEM micrograph of (b) K and (c) KYCD with TEM micrograph (inset) portraying carbon dots on the surface.

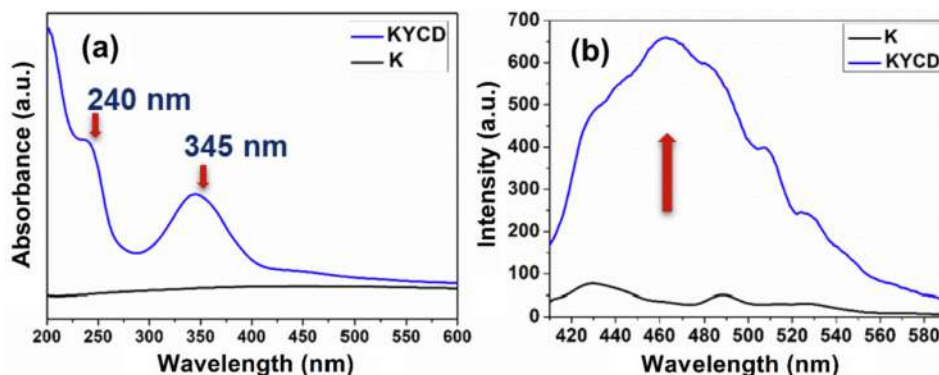


Fig. 3. (a) Alteration in absorbance spectra due to the incorporation of carbon dot in K; (b) Fluorescence enhancement due to carbon dot loading.

Triplicates were done and the fluorescence intensity recorded at 460 nm is illustrated in Fig. S6. The fluorescence intensity does not exhibit any significant alteration which confirms that carbon dot leaching from kyanite does not occur in the course of the experiment.

The alteration of fluorescence properties of pure carbon dots and carbon dot loaded kyanite when exposed to light and environmental conditions was also investigated. Both CD solution and KYCD solution was placed under illumination and fluorescence was measured for 3 h at an interval of 10 min. Fig. S7a shows no significant change with time while the CD solution gradually loses

its fluorescence capacity. Thus the kyanite matrix can successfully stabilize the fluorescence capability, resisting agglomeration when exposed to air, light and moisture.

3.4. KYCD as a fluorometric probe

3.4.1. Spectral response of the probe to Cr (VI)

Selectivity assay of the sensing probe (KYCD) has been performed by recording the fluorescence response at 370 nm excitation wavelength against a range of ions (Na^+ , K^+ , Ca^{2+} , Fe^{2+} , Fe^{3+} , Cr^{3+} , Cr^{6+} , As^{3+} , Cd^{2+} , Pb^{4+} , Hg^{2+} , OH^- , CO_3^{2-} , NO_3^- , S^{2-} , SO_4^{2-}). In each

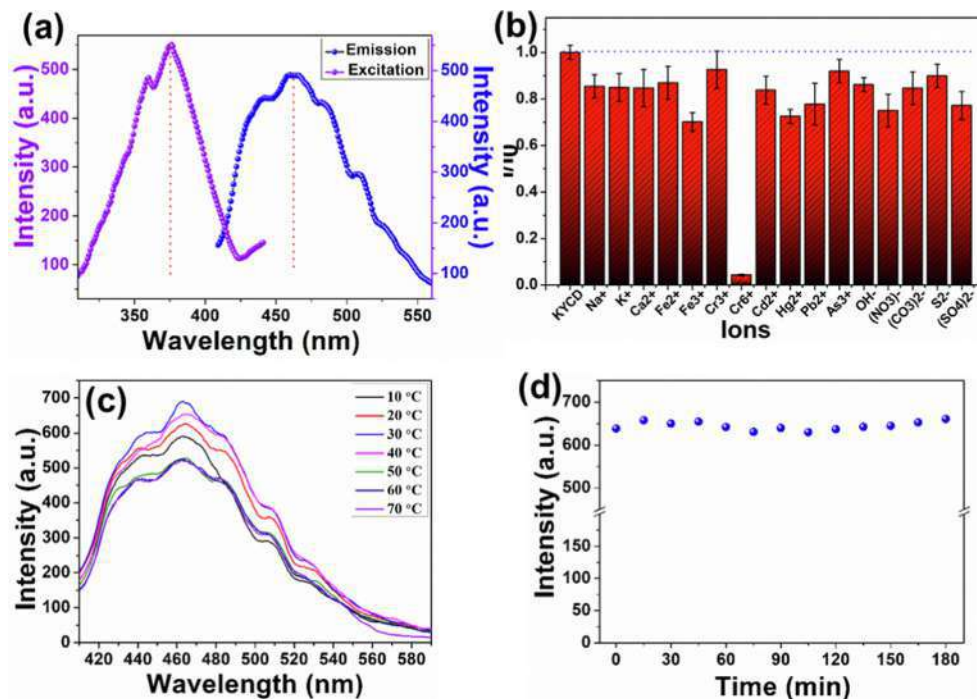


Fig. 4. (a) Excitation and emission spectra of the sensor; (b) Cr (VI) selectivity assay using various common ions; (c) Thermal stability of the fluorescence quality of the sensor; (d) Time-dependent fluorescence obtained on 180 min study.

case, the concentration of the ions was set at 500 μM . An insignificant reduction or shift of emission maxima was observed in each case except for hexavalent chromium. The addition of Cr (VI) ions into the KYCD solution causes radical reduction of fluorescence intensity as depicted in Fig. 4b confirming KYCD as a potential probe for Cr (VI). This fluorescence quenching effect is also visible through naked eyes under UV illumination (Fig. 6 (inset)). The CIE-1931 chromaticity diagram [26] is used herein to validate the visualized emissions in the color space (Fig. 5c). The color coordinate of the pure KYCD ($x = 0.1623$, $y = 0.2304$) slightly shifts ($x = 0.1718$, $y = 0.2787$) to the green region of the color space upon Cr (VI) addition making KYCD a promising sensor material for hexavalent chromium.

The sensitivity of the sensor material has been determined in a varied concentration of Cr (VI) (0–34 μM) and the fluorescence spectra were monitored in each step at 460 nm (Fig. 5a). This titration experiment reveals the drastic fluorometric quenching of the fluorescence intensity of the probe upon Cr (VI) addition. Quantification of such quenching efficiency has been determined by using the Stern-Volmer equations [27–28], expressed as,

$$\frac{I_0}{I} = 1 + K_{SV}[M] \quad (1)$$

$$\frac{I_0}{I} = Ae^{K_{SV}[M]} \quad (2)$$

Herein I_0 and I represent emission intensity of the pristine KYCD prior and post-incorporation of Cr (VI), $[M]$ represents the concentration of Cr (VI) and K_{SV} is the Stern-Volmer quenching constant and A represents an arbitrary constant. The fitting results of the S-V plot at lower concentration (0–10.2 μM) provide a linear fit having a fitting coefficient of $R^2 = 0.95435$, whereas the full range of the S-V plot is showing an upward increment of I_0/I against the Cr (VI) concentrations (fitting coefficient 0.98271) (Fig. 5b). Such fitting results yield significantly high K_{SV} values (181460 and 75400 M^{-1} respectively), which, in turn, indicates better sensitivity of the sensor.

The limits of detection (LOD) and limits of quantitation (LOQ) were calculated for the sensor by using the following expressions [29],

$$LOD = \frac{3\sigma}{K_{SV}} \quad (3)$$

$$LOQ = \frac{10\sigma}{K_{SV}} \quad (4)$$

Herein, σ represents the standard deviation obtained on taking at least ten measurements of the emission intensities of pure KYCD in absence of Cr (VI) ions. From the linear fitting, the LOD and LOQ are found to be 0.11 μM and 0.36 μM respectively, whereas it was found to be 0.26 μM and 0.88 μM respectively for full range S-V plot. These figures of merit are compared with some reported literature depicting the synthesized probe to be a promising Cr (VI) sensor (Table S1).

3.4.2. Fluorescence quenching mechanism

The possible fluorometric sensing mechanism of hexavalent chromium has been analyzed based on time-resolved fluorescence spectroscopy (TCSPC) and Stern-Volmer plots. Additionally, the Time-Dependent Density Functional Theory (TD-DFT) has been used to ascertain the charge transfer process throughout the process.

The Stern-Volmer plots of the sensor show an upward increment of the relative fluorescence intensity (I_0/I), but it follows a straight line at the low concentration domain (0–10.2 μM). Such an exponential growth of I_0/I refers to the simultaneous effect of static and dynamic quenching of the fluorophores. In reality, low quencher concentrations promote purely dynamic quenching, which could be observed in the linear Stern-Volmer plot (Fig. 5). The gradual increment of the quencher ion somehow blocks the emission pathway of the fluorophores and tends to quench the fluorescence intensity rapidly. Simultaneous effects of such static and dynamic quenching [30] at moderate to higher concentrations of

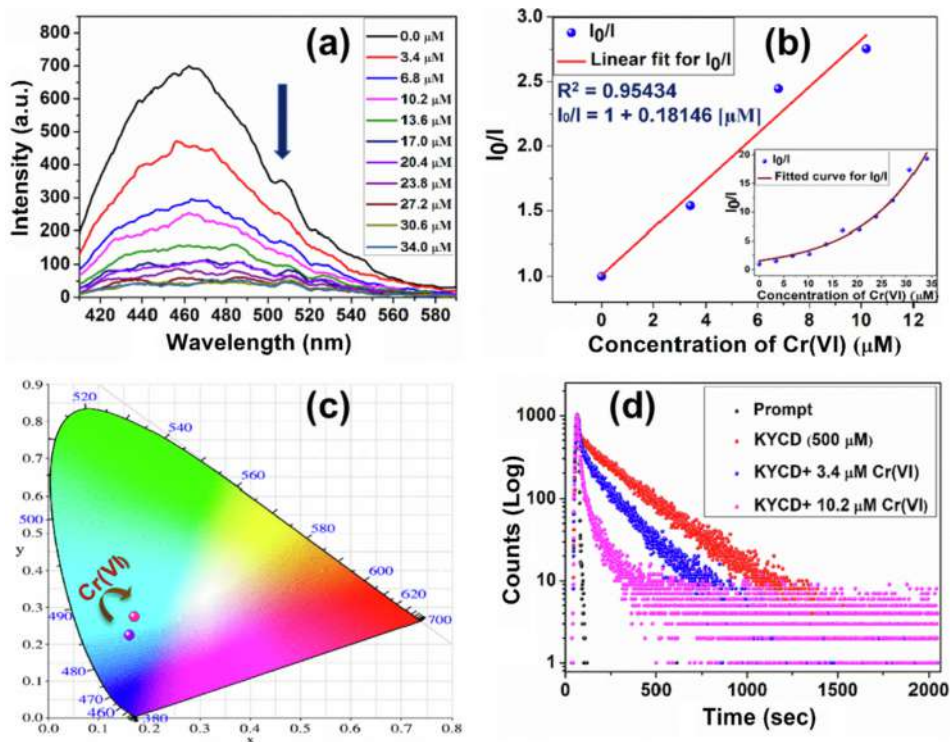


Fig. 5. (a) Fluorescence titration data for KYCD on addition of Cr (VI) as the quencher ion; (b) Stern-Volmer linear fitting of the subsequent fluorescence quenching data and the fitted curve for the data obtained (inset); (c) CIE-1931 colour space analysis of the sensor upon Cr (VI) exposure; (d) TCSPC of the sensor on addition of the quencher.

quencher ion results in fast decay of fluorescence intensity of the sensor and depicts an exponential Stern-Volmer plot. The validation of the dynamic quenching mechanism is carried out using the TCSPC data of the sensor showing a gradual reduction in fluorescent lifetimes (0–10.2 μM) upon Cr (VI) addition. It is found that the lifetime of the pure sensor material is 5.71 ns, whereas it is found to be 2.65 and 0.75 ns for 3.4 and 10.2 μM respectively for Cr (VI) exposed samples.

The reduction in lifetimes on excitation at 370 nm due to the addition of quencher indicated towards photoinduced electron transfer (PET) phenomenon. To identify correctly the PET process, emission properties of the optimized fluorophore (carbon dot) were examined by the Time-Dependent Density functional (TDDFT) method. The quencher (Cr (VI)) and the fluorophore part have been placed at a distance of 5 Å to interact during the TDDFT study. According to Kasha's rule [31], the fluorescence emission from the lowest singlet excited state and on excitation to a higher electronic state will result in fast relaxation. The DFT study suggests that upon excitation, photoinduced charges move directly to the LUMO + 2 state from the HOMO-4 state and then jump back to the LUMO state after a non-radiative internal conversion. A radiative transition then occurs from LUMO to HOMO-4 state showing no photo-emission and thereby resulting in fluorescence quenching (Fig. 6). Such photoinduced charge transfer between the fluorophore and quencher at excited states suggests the occurrence of the photoinduced electron transfer (PET) process [32] during quenching. However, excess amount of Cr (VI) loading (greater than 10.2 μM) blocks the fluorescence path of the fluorophore and contributes to a rapid decay of fluorescence.

3.5. Determination of sensing efficacy of the sensor in different conditions

3.5.1. Sensing behavior at different pH levels

Sensing efficacies at acidic (pH 4.0), basic (pH 9.2), and neutral pH (pH 7.0) were examined to assess the pH stability of the sensor

material. The pH was adjusted by adding HCl and NaOH solutions to the as-prepared KYCD solution. A slight decrease of fluorescence intensity of the probe in higher or lower pH has been observed

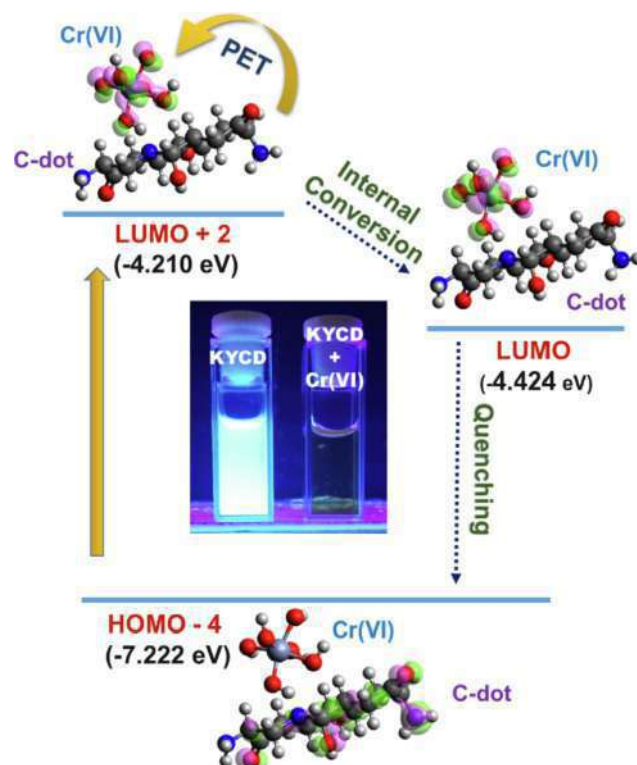


Fig. 6. Photoinduced electron transfer (PET) based 'turn-off' sensing mechanism analysis using TDDFT formalism and naked eye visualization under UV illumination upon Cr (VI) addition.

(Fig. 7a), which is probably due to the inner filter effect [33] caused by lesser accessibility of the fluorophores due to the presence of excess H^+ or OH^- ions in the solution. Yet the sensing efficacy is unaffected at acidic or basic conditions proving its excellent ability to perform in diverse pH conditions.

3.5.2. Sensing performance in real-life water samples

To implement the sensor at the industrial/ commercial level, it is of utmost necessity to validate its efficacy in real-life water samples. Unlike distilled water, water samples from various sources containing numerous interfering ions have been collected to conduct such a study. Potable water was collected from a water purifier situated in our campus, tap water was collected from our laboratory tap and pond water was collected from a nearby pond within the campus. Initially, the water samples were filtered through membrane filters separately (pore size $0.45\ \mu m$) to eliminate macro impurities. Then quantitative physical analyses of the filtered water samples were performed using a Hanna-HI991300 portable pH/TDS/Temperature meter (Table S2). The sensor material was then added to the water samples separately ($500\ \mu M$) and excited at $370\ nm$ to investigate the fluorescence quality. In all the cases no alteration of fluorescence performance was observed (Fig. 7b). Moreover, water samples were then spiked with Cr (VI) ions ($500\ \mu M$) to examine the sensing efficacy. It is found that Cr (VI) ions successfully quench the fluorescence intensity of the sensing probe in all the cases, validating the efficacy of the sensor in real water samples.

3.5.3. Sensing efficacy of the probe in real-life tannery wastewater

One of the major sources of hexavalent chromium in our environment is leather effluents [34]. Hence, tannery wastewater mostly contains Cr (VI) causing immense contamination of the nearby environment. Thus, detecting chromium in such contaminated tannery wastewater is necessary to avert further hazards from such pollution. The tannery wastewater was collected from a local canal connected to the tannery industry. Physical properties and the elemental analysis were conducted using Hanna portable pH/TDS/Temperature meter and ICP-OES respectively (Fig. 7c (inset)). The ICP result finds an alarming amount of chromium ($19.8\ mg\ L^{-1}$) in the wastewater with other interfering elements.

When the sensor material was exposed to the wastewater, a radical drop of fluorescence intensity was observed (Fig. 7c) due to the presence of chromium. Hence, it can be inferred that on-site application of sensor material can be practically possible irrespective of the presence of a variety of other interfering elements.

3.6. Determination of biocompatibility of the probe

A sensor can have excellent performance efficiency, but if it lacks biocompatibility then potential application of that material will be hindered. Hence, the determination of biocompatibility is of utmost necessity for a sensor to prevent the origin of secondary environmental issues. The viability of the cells (MTT assay) under the exposure of the synthesized sensing probe has been verified using the WI38 human lung fibroblast cell line (Fig. S8). The MTT assay indicates the nontoxic nature of the sensor even after 24 h of exposure at a maximum concentration of $120\ \mu g\ mL^{-1}$. It is found that over 99 % of cells survived. This implies that the sensor has great biocompatibility and will not contribute to any secondary toxicity.

3.7. Detection of Cr (VI) in living cells: In vitro carcinogen detection

In reality, Cr (VI), which is a well-known genotoxic element can penetrate the cell membrane via sulfur-ion channel [35] and interacts with proteins like glutathione and cytochrome b5. During such

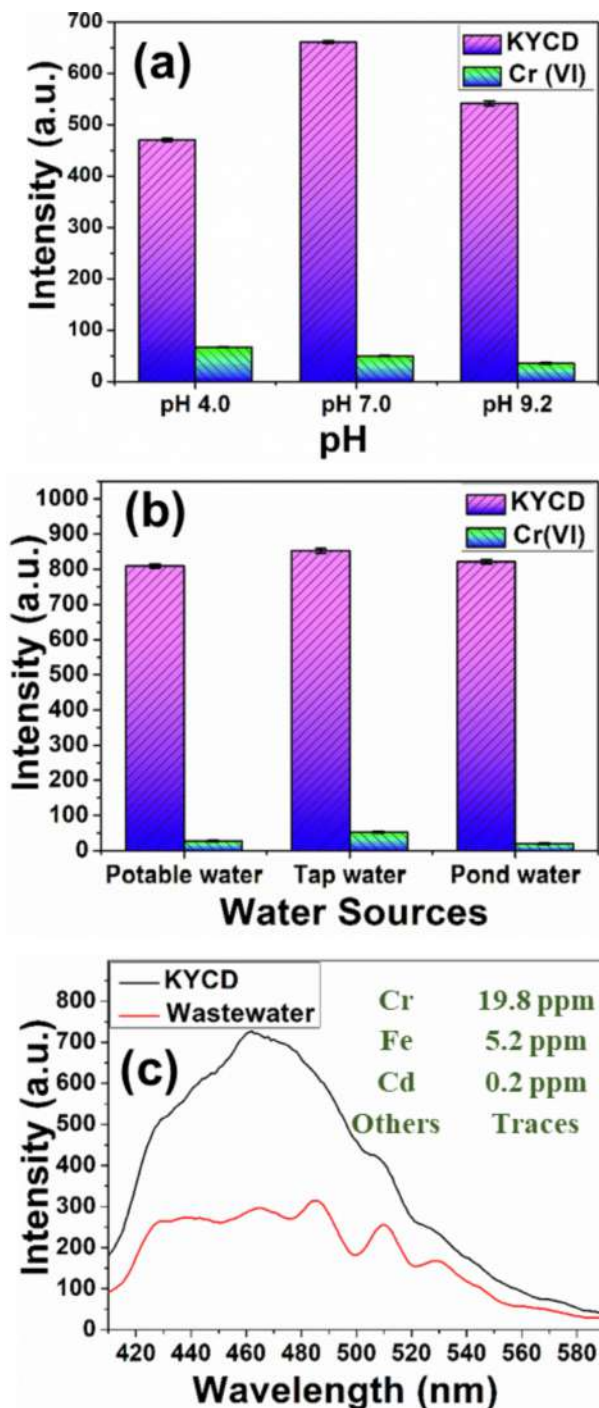


Fig. 7. Sensing efficacy of KYCD at different pH (a) and water sources (b); (c) Fluorescence quenching observed in tannery wastewater and ICP-OES data of the collected wastewater (inset).

interactions, chromium tends to reduce its valent state from six to three producing various super-oxides and reactive oxygen species (ROS) that further promote DNA damage and induce carcinogenicity [36]. Hence, Cr (VI) detection at an early stage is a crucial step to combat the onset of cancer from Cr (VI) contamination.

Efficacy of the synthesized sensor material as an intracellular fluorometric probe for carcinogenic hexavalent chromium was determined by performing cell imaging [37–38]. The HeLa cells were used to determine such biosensing activity of the probe. KYCD-treated cells were initially observed under a fluorescence

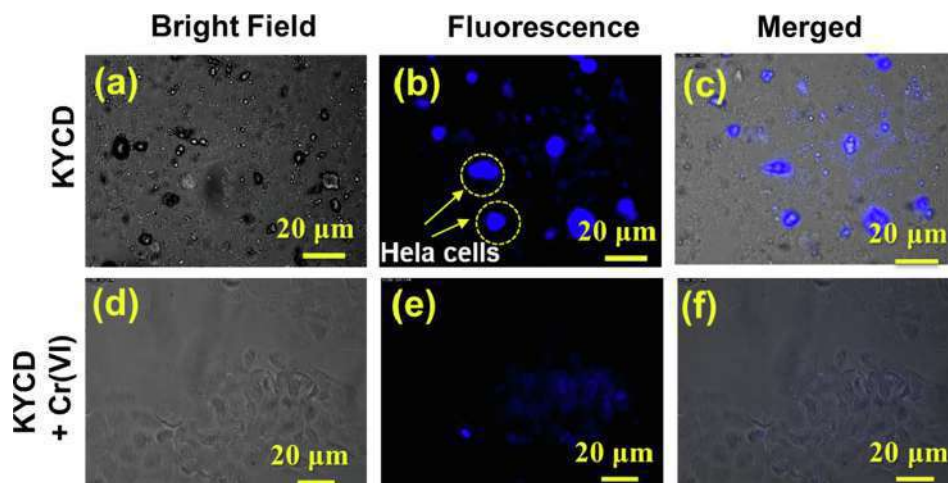


Fig. 8. Biosensing capacity and cellular permeability studies of human cervical cancer cell line using KYCD. (a–c) illustrates bright blue fluorescence on interacting with KYCD, which diminishes (d–f) on adding Cr (VI) in the cells.

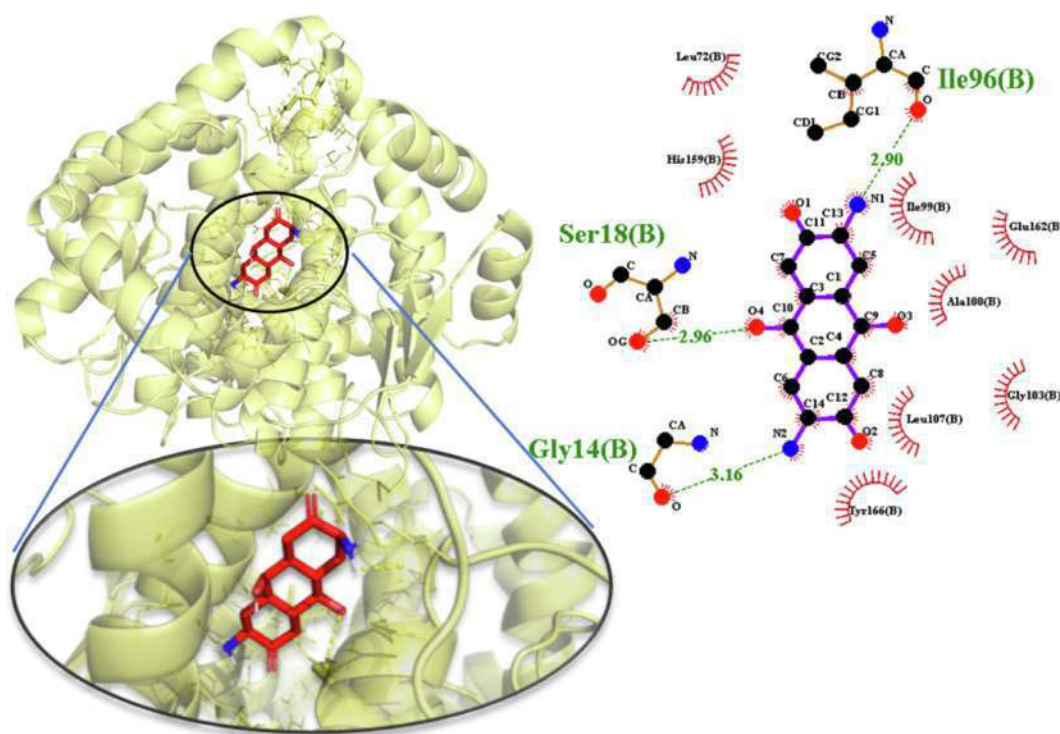


Fig. 9. Molecular docking analysis of the sensing probe showing interactions between fluorophore of the probe and glutathione (1PKW).

microscope and bright blue fluorescence have been observed in the cells upon UV excitation (Fig. 8). This also substantiates successful penetration of the cellular membrane without affecting it (as observed in MTT assay). Moreover, such a commendable cellular fluorescence corroborates the fact that the fluorescence intensity of the sensor is unaffected by the culture medium and other cellular components.

Molecular docking simulation has been adopted herein to investigate the interaction [39] between glutathione protein and the fluorophore moiety of the sensor (carbon dot) to determine the complex binding affinity [40]. Computational complexities have been minimized by taking the best pose among the predicted nine different docked poses as mentioned in Table S3. Amongst these nine poses, the most favorable pose showed $-8.7 \text{ kcal mol}^{-1}$

binding affinity between glutathione and the fluorophore. Detailed study reveals a higher possibility of fluorophore binding with amino acids like Isoleucine (Ile-96), Serine (Ser-18), and Glycine (Gly-14) with the fluorophore maintaining bonding proximities 2.9, 2.96, and 3.16 Å respectively (Fig. 9). Thus, molecular docking reveals the complex binding structure between the sensor material and cells, which leads us to validate the significant cellular fluorescence in KYCD treated cells.

To estimate in vitro chromium sensing, chromium was subsequently added to the KYCD treated cells. Fig. 8 shows quenching of fluorescence on the addition of chromium, thus proving the immense selectivity and sensitivity of the sensor even at the cellular level.

4. Conclusion

This study offers a simple, sensitive, and cost-effective natural mineral-based sensor, namely KYCD for the detection of hexavalent chromium in aqueous medium and living cells. This sensor material uses nitrogenous carbon dots, tailored into kyanite (KYCD) nanoparticles showing promising sensing efficacy in real-life wastewater samples. The sensing probe shows fluorometric 'turn-off' based sensing upon Cr (VI) addition without any pre-treatment or pH adjustment of the water samples. This PET-based sensor material is capable of detecting chromium in the presence of other interfering ions. A remarkably low limit of detection (LOD) and limit of quantitation (LOQ) as low as 0.11 μM s and 0.36 μM respectively makes it a promising Cr (VI) sensor in all water types. KYCD shows high stability in a wide range of temperature, which does not alter with time unlike pristine carbon dot. Furthermore, high sensing efficacy in various pH and real-life water samples proves its potentiality for industrial and commercial applications. The sensing ability is also applicable in living cells as bright blue fluorescence of cell-line (HeLa cells) was seen on interaction with KYCD, which significantly diminishes in presence of Cr(VI). Moreover, the sensor exhibits excellent biocompatibility and such a natural material-based sensor can be useful for combating heavy metal-induced early-stage cancer.

CRedit authorship contribution statement

Souravi Bardhan: Conceptualization, Methodology, Investigation, Data curation, Formal analysis, Validation, Writing – original draft. **Shubham Roy:** Methodology, Investigation, Data curation, Formal analysis, Writing – review & editing. **Sanghita Das:** Methodology. **Ishita Saha:** Methodology. **Dhananjay Mondal:** Data curation, Formal analysis. **Jhilik Roy:** Data curation. **Dipak Kr. Chanda:** Resources, Data curation. **Solanky Das:** Methodology. **Parimal Karmakar:** Supervision, Writing – review & editing. **Sukhen Das:** Conceptualization, Supervision, Writing – review & editing.

Declaration of Competing Interest

The authors declare that they have no known competing financial interests or personal relationships that could have appeared to influence the work reported in this paper.

Acknowledgments

Authors are grateful to the Department of Physics, Jadavpur University, Kolkata for extending experimental facilities. S.D. would like to acknowledge DST-SERB (Grant No. EEQ/2018/000747) for funding. S.R. would like to acknowledge Department of Higher Education, Government of West Bengal for providing him the SVMCM (Non-NET) fellowship.

Appendix A. Supplementary material

Supplementary data to this article can be found online at <https://doi.org/10.1016/j.saa.2022.121061>.

References

- [1] K.H. Vardhan, P.S. Kumar, R.C. Panda, A review on heavy metal pollution, toxicity and remedial measures: Current trends and future perspectives, *J. Mol. Liq.* 290 (2019) 111197, <https://doi.org/10.1016/j.molliq.2019.111197>.
- [2] M. Tripathi, S.K. Upadhyay, M. Kaur, K. Kaur, Toxicity Concerns of Hexavalent Chromium from Tannery Waste, *Biotechnol. Bioeng.* 2 (2) (2018) 40–44.
- [3] R. Saha, R. Nandi, B. Saha, Sources and toxicity of hexavalent chromium, *J. Coord. Chem.* 64 (10) (2011) 1782–1806, <https://doi.org/10.1080/00958972.2011.583646>.
- [4] S. Balasubramanian, V. Pugalenthi, Determination of total chromium in tannery waste water by inductively coupled plasma-atomic emission spectrometry, flame atomic absorption spectrometry and UV-visible spectrophotometric methods, *Talanta* 50 (3) (1999) 457–467, [https://doi.org/10.1016/S0039-9140\(99\)00135-6](https://doi.org/10.1016/S0039-9140(99)00135-6).
- [5] D. Spanu, D. Monticelli, G. Binda, C. Dossi, L. Rampazzi, S. Recchia, One-minute highly selective Cr (VI) determination at ultra-trace levels: An ICP-MS method based on the on-line trapping of Cr (III), *J. Hazard. Mater.* 412 (2021) 125280, <https://doi.org/10.1016/j.jhazmat.2021.125280>.
- [6] M.I. Stich, L.H. Fischer, O.S. Wolfbeis, Multiple fluorescent chemical sensing and imaging, *Chem. Soc. Rev.* 39 (8) (2010) 3102–3114, <https://doi.org/10.1039/B909635N>.
- [6a] L. Hou, J. Feng, Y. Wang, C. Dong, S. Shuang, Y.u. Wang, Single fluorescein-based probe for selective colorimetric and fluorometric dual sensing of Al^{3+} and Cu^{2+} , *Sens. Actuators B* 247 (2017) 451–460, <https://doi.org/10.1016/j.snb.2017.03.027>.
- [6b] C. Zhang, H. Zhang, M. Li, Y. Zhou, G. Zhang, L. Shi, Q. Yao, S. Shuang, C. Dong, A turn-on reactive fluorescent probe for Hg^{2+} in 100% aqueous solution, *Talanta* 197 (2019) 218–224, <https://doi.org/10.1016/j.talanta.2019.01.016>.
- [6c] J. Feng, L.X. Duan, Z.B. Shang, J.B. Chao, Y.u. Wang, W.J. Jin, Colorimetric and fluorometric dual sensing of trace water in methanol based on a Schiff Base- Al^{3+} ensemble probe, *Spectrochim. Acta A* 201 (2018) 185–192, <https://doi.org/10.1016/j.saa.2018.05.016>.
- [6d] C. Zhang, B. Gao, Q. Zhang, G. Zhang, S. Shuang, C. Dong, A simple Schiff base fluorescence probe for highly sensitive and selective detection of Hg^{2+} and Cu^{2+} , *Talanta* 154 (2016) 278–283, <https://doi.org/10.1016/j.talanta.2016.03.067>.
- [7] R. Amini, E. Rahimpour, A. Jouyban, An optical sensing platform based on hexacyanoferrate intercalated layered double hydroxide nanozyme for determination of chromium in water, *Anal. Chim. Acta* 1117 (2020) 9–17, <https://doi.org/10.1016/j.aca.2020.04.001>.
- [8] P. Li, X.-M. Yin, L.-L. Gao, S.-L. Yang, Q.i. Sui, T. Gong, E.-Q. Gao, Modulating excitation energy of luminescent metal-organic frameworks for detection of Cr (VI) in water, *ACS Appl. Nano Mater.* 2 (7) (2019) 4646–4654, <https://doi.org/10.1021/acsanm.9b01088>, <https://doi.org/10.1021/acsanm.9b01088.s001>.
- [8a] S. Roy, S. Bardhan, D. Mondal, I. Saha, J. Roy, S. Das, D.K. Chanda, P. Karmakar, S. Das, Polymeric carbon dot/boehmite nanocomposite made portable sensing device (Kavach) for non-invasive and selective detection of Cr (VI) in wastewater and living cells, *Sens. Actuators B* 348 348 (2021) 130662, <https://doi.org/10.1016/j.snb.2021.130662>.
- [9] D. Das, R.K. Dutta, N-Doped Carbon Dots Synthesized from Ethylene Glycol and β -Alanine for Detection of Cr (VI) and 4-Nitrophenol via Photoluminescence Quenching, *ACS Appl. Nano Mater.* 4 (4) (2021) 3444–3454, <https://doi.org/10.1021/acsanm.0c03329>, <https://doi.org/10.1021/acsanm.0c03329.s001>.
- [10] K. Hola, Y. Zhang, Y. Wang, E.P. Giannelis, R. Zboril, A.L. Rogach, Carbon dots-Emerging light emitters for bioimaging, cancer therapy and optoelectronics, *Nano Today* 9 (5) (2014) 590–603, <https://doi.org/10.1016/j.nantod.2014.09.004>.
- [11] C. Wang, Z. Xu, H. Cheng, H. Lin, M.G. Humphrey, C. Zhang, A hydrothermal route to water-stable luminescent carbon dots as nanosensors for pH and temperature, *Carbon* 82 (2015) 87–95, <https://doi.org/10.1016/j.carbon.2014.10.035>.
- [12] S. Roy, S. Bardhan, D.K. Chanda, J. Roy, D. Mondal, S. Das, In Situ-Grown Cd-dot-Wrapped Boehmite Nanoparticles for Cr (VI) Sensing in Wastewater and a Theoretical Probe for Chromium-Induced Carcinogen Detection, *ACS Appl. Mater. Interfaces* 12 (39) (2020) 43833–43843, <https://doi.org/10.1021/acsami.0c13433>, <https://doi.org/10.1021/acsami.0c13433.s001>.
- [13] S. Bardhan, S. Roy, D.K. Chanda, S. Das, K. Pal, A. Chakraborty, R. Basu, S. Das, Microstructure and dielectric properties of naturally formed microcline and kyanite: a size-dependent study, *Cryst. Growth Des.* 19 (8) (2019) 4588–4601, <https://doi.org/10.1021/acs.cgd.9b00480>, <https://doi.org/10.1021/acs.cgd.9b00480.s001>.
- [14] O.V. Shiman, L. Balogh, M.R. Daymond, A synchrotron X-ray diffraction study of strain and microstrain distributions in α -Zr caused by hydride precipitation, *Surfaces and Interfaces* 17 (2019) 100388, <https://doi.org/10.1016/j.surfin.2019.100388>.
- [14a] T.N.J.I. Edison, R. Atchudan, M.G. Sethuraman, J.-J. Shim, Y.R. Lee, Microwave assisted green synthesis of fluorescent N-doped carbon dots: cytotoxicity and bio-imaging applications, *J. Photochem. Photobiol. B* 161 161 (2016) 154–161, <https://doi.org/10.1016/j.jphotobiol.2016.05.017>.
- [15] J.R. Tolchard, M.S. Islam, P.R. Slater, Defect chemistry and oxygen ion migration in the apatite-type materials $\text{La}_{0.33}\text{Si}_6\text{O}_{26}$ and $\text{La}_2\text{Sr}_2\text{Si}_6\text{O}_{26}$, *J. Mater. Chem.* 13 (8) (2003) 1956, <https://doi.org/10.1039/b302748c>.
- [16] J. Jin, H. Gao, Z. Ren, Z. Chen, The Flotation of Kyanite and Sillimanite with Sodium Oleate as the Collector, *Minerals* 6 (3) (2016) 90, <https://doi.org/10.3390/min6030090>.
- [17] Y.N. Wu, Y.F. Wang, An FTIR study of kyanite in the Maobei kyanite-bearing eclogites from the Sulu Orogenic Belt, Eastern China, *J. Earth Sci.* 29 (1) (2018) 21–29, <https://doi.org/10.1007/s12583-017-0774-0>.
- [18] D.R. Bell, G.R. Rossman, J. Maldener, D. Endisch, F. Rauch, Hydroxide in kyanite: A quantitative determination of the absolute amount and calibration of the IR spectrum, *Am. Min.* 89 (7) (2004) 998–1003, <https://doi.org/10.2138/am-2004-0710>.

- [19] J. Chen, J. Liu, J. Li, L. Xu, Y. Qiao, One-pot synthesis of nitrogen and sulfur co-doped carbon dots and its application for sensor and multicolor cellular imaging, *J Colloid Interf Sci.* 485 (2017) 167–174, <https://doi.org/10.1016/j.jcis.2016.09.040>.
- [20] C.M. Carbonaro, D. Chiriu, L. Stagi, M.F. Casula, S.V. Thakkar, L. Malfatti, K. Suzuki, P.C. Ricci, R. Corpino, Carbon Dots in Water and Mesoporous Matrix: Chasing the Origin of their Photoluminescence, *J. Phys. Chem. C* 122 (44) (2018) 25638–25650, <https://doi.org/10.1021/acs.jpcc.8b08012>.
- [21] M.J. Cho, S.Y. Park, Carbon-dot-based ratiometric fluorescence glucose biosensor, *Sens. Actuators, B* 282 (2019) 719–729, <https://doi.org/10.1016/j.snb.2018.11.055>.
- [22] W. Dong, S. Zhou, Y. Dong, J. Wang, X. Ge, L. Sui, The preparation of ethylenediamine-modified fluorescent carbon dots and their use in imaging of cells, *Luminescence* 30 (6) (2015) 867–871, <https://doi.org/10.1002/bio.2834>.
- [23] S. Bardhan, S. Roy, D.K. Chanda, S. Ghosh, D. Mondal, S. Das, S. Das, Nitrogenous carbon dot decorated natural microcline: an ameliorative dual fluorometric probe for Fe³⁺ and Cr⁶⁺ detection, *Dalton Trans.* 49 (30) (2020) 10554–10566, <https://doi.org/10.1039/D0DT02166K>.
- [24] S. Ghosh, S. Roy, S. Bardhan, N. Khatua, B. Bhowal, D.K. Chanda, S. Das, D. Mondal, R. Basu, S. Das, Effect of Size Fractionation on Purity, Thermal Stability and Electrical Properties of Natural Hematite, *J. Electron. Mater.* 50 (7) (2021) 3836–3845, <https://doi.org/10.1007/s11664-021-08878-9>.
- [25] F. Yan, Z. Sun, H. Zhang, X. Sun, Y. Jiang, Z. Bai, The fluorescence mechanism of carbon dots, and methods for tuning their emission color: A review, *Microchim. Acta* 186 (8) (2019) 1–37, <https://doi.org/10.1007/s00604-019-3688-y>.
- [26] H.S. Fairman, M.H. Brill, H. Hemmendinger, How the CIE 1931 color-matching functions were derived from Wright-Guild data, *Color Res. Appl.* 22 (1) (1997) 11–23.
- [27] S. Roy, K. Pal, S. Bardhan, S. Maity, D.K. Chanda, S. Ghosh, P. Karmakar, S. Das, Gd(III)-Doped Boehmite Nanoparticle: An Emergent Material for the Fluorescent Sensing of Cr (VI) in Wastewater and Live Cells, *Inorg. Chem.* 58 (13) (2019) 8369–8378, <https://doi.org/10.1021/acs.inorgchem.9b00425>.
- [28] J. Carvalho, P. Nottelet, J.L. Mergny, J.A. Queiroz, G.F. Salgado, C. Cruz, Study of the interaction between indole-based compounds and biologically relevant G-quadruplexes, *Biochimie* 135 (2017) 186–195, <https://doi.org/10.1016/j.biochi.2017.02.005>.
- [29] S. Bardhan, S. Roy, D.K. Chanda, D. Mondal, S. Das, S. Das, Flexible and reusable carbon dot decorated natural microcline membrane: a futuristic probe for multiple heavy metal induced carcinogen detection, *Microchim. Acta* 188 (2021), <https://doi.org/10.1007/s00604-021-04787-0>.
- [30] Y. Song, S. Zhu, S. Xiang, X. Zhao, J. Zhang, H. Zhang, Y. Fu, B. Yang, Investigation into the fluorescence quenching behaviors and applications of carbon dots, *Nanoscale* 6 (9) (2014) 4676–4682, <https://doi.org/10.1039/C4NR00029C>.
- [31] M. Kasha, Characterization of electronic transitions in complex molecules, *Discuss. Faraday Soc.* 9 (1950) 14–19.
- [32] S. Roy, S. Bardhan, D.K. Chanda, S. Ghosh, D. Mondal, J. Roy, S. Das, Development of a Cu(II) doped boehmite based multifunctional sensor for detection and removal of Cr (VI) from wastewater and conversion of Cr (VI) into an energy harvesting source, *Dalton Trans.* 49 (20) (2020) 6607–6615, <https://doi.org/10.1039/D0DT00888E>.
- [33] M. Mittal, S. Sapra, Nanocrystal-Dye Interactions: Studying the Feasibility of Co-Sensitization of Dyes with Semiconductor Nanocrystals, *ChemPhysChem.* 18 (18) (2017) 2509–2516, <https://doi.org/10.1002/cphc.201700598>.
- [34] A. Agrawal, V. Kumar, B.D. Pandey, Remediation options for the treatment of electroplating and leather tanning effluent containing chromium—a review, *Miner. Process. Extr. Metall. Rev.* 27 (2) (2006) 99–130, <https://doi.org/10.1080/08827500600563319>.
- [35] S. Mishra, R.N. Bharagava, Toxic and genotoxic effects of hexavalent chromium in environment and its bioremediation strategies, *J. Environ. Sci. Health C* 34 (1) (2016) 1–32, <https://doi.org/10.1080/10590501.2015.1096883>.
- [36] M.D. Cohen, B. Kargacin, C.B. Klein, M. Costa, Mechanisms of chromium carcinogenicity and toxicity, *Crit. Rev. Toxicol.* 23 (3) (1993) 255–281, <https://doi.org/10.3109/10408449309105012>.
- [37] X. Hu, J. Chai, Y. Liu, B. Liu, B. Yang, Probing chromium (III) from chromium (VI) in cells by a fluorescent sensor, *Spectrochim. Acta A* 153 (2016) 505–509, <https://doi.org/10.1016/j.saa.2015.09.008>.
- [38] J.H. Ye, Y. Wang, Y. Bai, W. Zhang, W. He, A highly selective turn-on fluorescent chemodosimeter for Cr (VI) and its application in living cell imaging, *RSC Adv.* 4 (6) (2014) 2989–2992, <https://doi.org/10.1039/C3RA46543H>.
- [39] Q. Xu, Y. Liu, C. Gao, J. Wei, H. Zhou, Y. Chen, C. Dong, T.S. Sreepasad, N. Li, Z. Xia, Synthesis, mechanistic investigation, and application of photoluminescent sulfur and nitrogen co-doped carbon dots, *J. Mater. Chem. C* 3 (38) (2015) 9885–9893, <https://doi.org/10.1039/C5TC01912E>.
- [40] S.C. Yu, I.C. Kim, K.J. Ri, J. Ri, H. Kühn, New insight into the role of glutathione reductase in glutathione peroxidase-like activity determination by coupled reductase assay: Molecular Docking Study, *J. Inorg. Biochem.* 215 (2021), <https://doi.org/10.1016/j.jinorgbio.2020.111276>.

Metal oxide/graphene nanocomposites and their biomedical applications

22

Souravi Bardhan¹, Shubham Roy¹, Mousumi Mitra² and Sukhen Das¹

¹Department of Physics, Jadavpur University, Kolkata, India, ²Department of Physics, University of Virginia, Charlottesville, VA, United States

22.1 Introduction

Graphene, a monolayer two-dimensional (2D) allotrope of carbon has emerged as a rising star since its discovery by Novoselov and his team (Novoselov et al., 2004). Novoselov and Geim received Noble Prize in Physics after discovery since during 2004 graphene was found to be the thinnest known material with tremendous scope for application in various fields. Graphene consists of benzene rings of sp²-hybridized carbon atoms arranged in honeycomb network structure (Li & Kaner, 2008), which exhibit unique physicochemical properties (Brumfiel, 2009). The structural features of graphene impart high specific surface area (Dimiev & Eigler, 2016) and magnificent strength (breaking strength is ~ 42 N/m and the tensile strength or Young modules is 1.0 TPa) (Huang et al., 2011). Since it is stronger than various other metals and has high flexibility, it is used as a substitute for metals in various sectors (Hu, Kulkarni, Choi, & Tsukruk, 2014). The mechanical, chemical, and thermal stability of graphene and its nanocomposites make them suitable for a wide range of applications. Graphene exhibits large theoretical surface area (~2630 m²/g) which is nearly 260 times higher than graphite. Such high surface area provides greater efficiency for various catalytic activities (Chen, Wu, Jiang, Wang, & Chen, 2011). By virtue of the antibacterial nature, amphiphilicity, outstanding electrical conductivity, and easy surface functionalization capability (Balandin et al., 2008; Geim, 2009; Ranjbartoreh, Wang, Shen, & Wang, 2011; Wang, Zhang, Wu, & Wei, 2017), graphene is considered as a potential candidate in biological applications. Moreover biocompatible nature, surface-enhanced Raman scattering (SERS), fluorescence quenching ability, and low-energy requirement for electron movement due to $\pi-\pi^*$ transitions (Abbott's, 2007; Geim & Novoselov, 2010; Novoselov et al., 2005) are quite significant for bioimaging, biosensing, drug/gene delivery, photothermal and photodynamic therapies, and other biomedical studies. Based on the application purpose, several forms of graphene are used in biological applications, such as graphene oxide (GO), graphene quantum dots (GQDs), and reduced graphene oxide (rGO) (Muthurasu, Dhandapani, & Ganesh, 2016). In certain cases, graphene nanosheets (Chong et al., 2015), graphene nanocubes (Govindasamy et al., 2019), graphene nanocrystals (Zhang, Yuan, Zhang, Wang, & Liu, 2011), graphene nanotubes (Wu, Pei, & Zeng, 2009) are also used. Extensive studies regarding surface modification of other

nanoparticles such as metals (Cu, Zn, Au), nonmetals (polymers, epoxy, chitosan or N₂, B, S) and metal oxides (TiO₂, ZnO) are widely performed (Giovannetti et al., 2008; Liu, Liu, & Zhu, 2011; Rajeshkumar & Veena, 2018; Stengl, Popelková, & Vlácil, 2011; Zheng, Jiao, Ge, Jaroniec, & Qiao, 2013). Graphene nanocomposites or graphene-based nanofillers are also popularizing in promoting specific tissue regeneration, providing binding sites for functionalization with biological molecules or in cell behavior regulation (Tadyszak, Wychowaniec, & Litowczenko, 2018). Graphene in combination with ZnO, Ag, chitosan, poly (lactic acid) (PLA) or poly (N-vinylcarbazole) (PVK) can also act as an antibacterial or sterilizing agent by imparting oxidative stress due to its electron transfer capability (Shi et al., 2016). Furthermore, deposition of various metal oxide nanoparticles such as zinc oxide, titanium dioxide, iron oxide, cobalt oxide, copper oxide, nickel oxide, and manganese dioxide on graphene sheets enhances the photophysical and electrochemical properties (Mohd Yazid et al., 2014). Thus graphene and its nanocomposites can be considered as “magic bullet” for the medical science (Fig. 22.1).

22.2 Synthesis of graphene and its derivatives

Graphene was discovered in 2004 during mechanical exfoliation of graphite to obtain single-layer samples (Novoselov et al., 2004). Since the discovery, vast

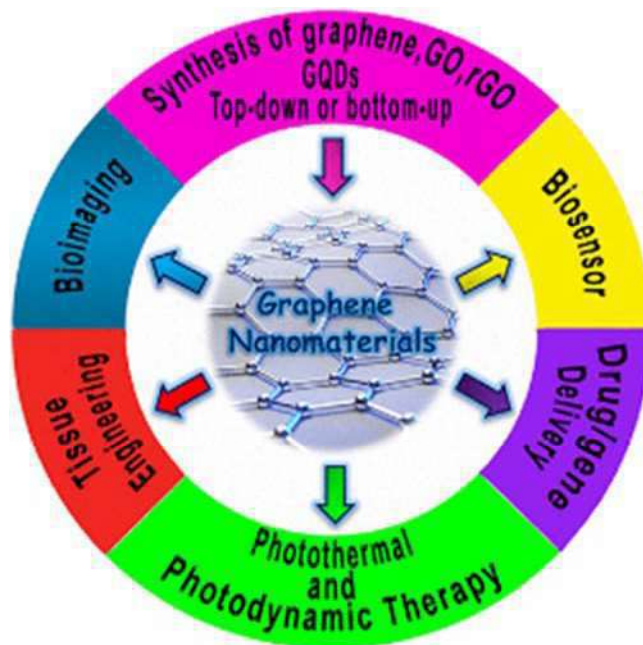


Figure 22.1 Different biomedical applications of graphene-based materials (Ghosal & Sarkar, 2018).

research was conducted because of its unique properties. Initially graphene was synthesized via epitaxial growth, bottom-up organic techniques, or top-down synthesis from graphite by splitting graphite into individual sheets through mechanical cleavage or chemical exfoliation (Li & Kaner, 2008). Graphene synthesis from graphite has gained widespread acceptance due to the cost-effectiveness and ease in synthesis along with large-scale production. Since 2006, graphene synthesis from graphite oxide by ultrasonication method (Stankovich et al., 2006) gained attention due to greater interlayer distance than graphite and hydrophilic nature that makes the exfoliation technique easier. The graphene oxide formed can be deoxygenated by chemical reduction to obtain graphene. A year later McAllister and coworkers (McAllister et al., 2007) introduced a new method to delaminate graphite into graphene sheets via oxidation and rapid thermal expansion. Since graphene sheets have a tendency to agglomerate spontaneously due to presence of strong Van der Waals interactions between the sheets and reform graphite, stabilizing individual sheets during synthesis became an important issue. Thus chemical functionalization and modification of graphene gained attention (Niyogi et al., 2006)(Mitra, Chatterjee, Kargupta, Ganguly, & Banerjee, 2013). This paved the path for graphene nanocomposite synthesis. Initially conversion of GO to graphene resulted in negatively charged surfaces of graphene on dispersion in water. Thus dispersing positively charged polycation into the solution helped in formation of graphene-based composites (Li, Müller, Gilje, Kaner, & Wallace, 2008). Subsequently modification of graphene shape and size also came into play. Graphene nanoribbons (> 10 nm wide) were produced from thermally expanded graphite via controlled ultrasonication (Li, Wang, Zhang, Lee, & Dai, 2008). Various facile techniques such as drop-casting, dip or spin coating, or a simple filtration method was practiced to synthesize graphene film (Gilje, Han, Wang, Wang, & Kaner, 2007; Wu, Pisula, & Müllen, 2007). Graphene nanoplatelets were synthesized by covalently grafting polystyrene–polyacrylamide copolymer onto graphene sheets in order to improve graphene stability in both polar and nonpolar solvents (Shen, Hu, Li, Qin, & Ye, 2009). By 2010 several other techniques were adopted to produce graphene, which involved chemical vapor deposition (CVD) (Juang et al., 2010), arc discharge (Li et al., 2010), electrically assisted synthesis (Liu et al., 2008), solvothermal (Choucair, Thordarson, & Stride, 2009) unzipping CNTs and others methods. Furthermore, large quantity graphene production cost was found to be lower than carbon nanotubes, which fascinated various scientists to explore more dimensions of graphene. Thus various avenues in biomedical fields using graphene and its nanocomposites were thoroughly explored.

Metal or metal oxide-graphene/GO/rGO nanocomposites fabrication has gained special interest in the last decade. Metal or metal oxide nanoparticles provide stability by preventing restacking of individual graphene sheets. Their band gap has direct influence on conductivity and chemical reactivity of the nanocomposite, which can be enhanced according to the requirement (Sharma et al., 2014). Various synthesis routes are adopted for metal oxide-graphene-based nanocomposite formation (Sharma et al., 2014) such as hydrothermal/solvothermal method, sol-gel or precipitation technique, electrostatic or covalent interaction, microwave-assisted synthesis, atomic layer

deposition, or layer-by-layer self-assembly, etc. Wang et al. (2010) had shown a novel strategy to fabricate flexible, free-standing metal oxide-graphene nanocomposite film by surfactant-based ternary self-assembly approach using low conductive metal oxide such as SnO₂. This method demonstrated a facile manner of enhancing electron transport of metal oxides of low conductivity and poor stability (MnO₂, NiO, SiO₂) by adding conductive phases such as graphene (Fig. 22.2).

The cytotoxicity of graphene-based materials was studied. Russier and team (Russier et al., 2013) conducted a detailed study on cellular functionality using graphene flakes. It was concluded that smaller flakes resulted in greater cytotoxicity due to higher cellular internalization. In another study, rGO was used which shows the relation between level of oxidation and cell viability (Shi et al., 2012). Cell viability using MTT ((3-(4,5-dimethylthiazol-2-yl)-2,5-diphenyltetrazolium bromide) assay or WST-based assay (water soluble tetrazolium) were performed using various cell lines such as human osteosarcoma (MG-63), human colon cancer (Caco2), human lung

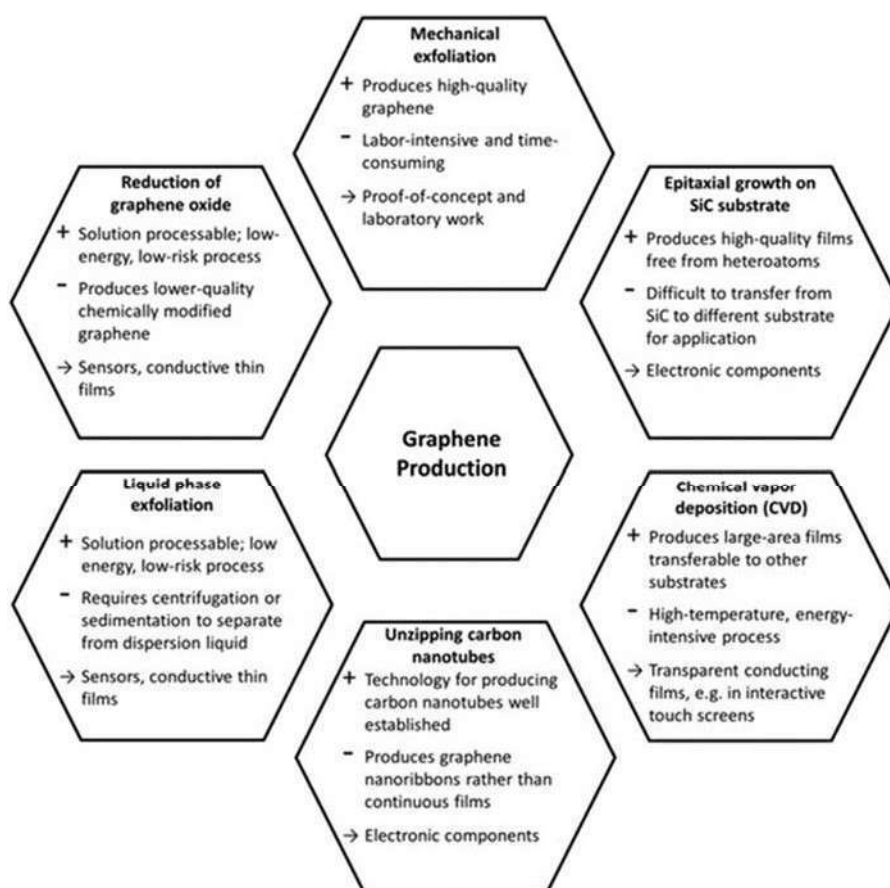


Figure 22.2 Summary of various graphene synthesis techniques (Hernaez et al., 2017).

adenocarcinoma cell line (A549), vero cell lines, etc. in order to quantify the biocompatibility of graphene-based materials (Coleman, Knight, Gies, Jakubek, & Zou, 2017; De Marzi et al., 2014; Ou et al., 2016). No significant reactive oxygen species (ROS) generation was observed in the cell viability assays (Tadyszak et al., 2018). Besides cytotoxicity assays, biodegradation of graphene-based materials studies were also conducted to determine whether the degradation products impart cell or DNA damage. A study by Kurapati et al. (2018) proved the nontoxic nature of biodegradable products of single-layer and few-layer graphene in human lung cells since neutrophils can successfully digest the biodegraded products.

22.3 Graphene-based biosensors

Among the various applications in biomedical field, such as drug delivery, cancer treatment and detection, tissue engineering, nanomedicine, etc., biosensing has emerged as a significant tool for detecting presence of specific biological component or biochemical reaction (Roy et al., 2020)(Bardhan et al., 2021). In general, biosensors are analytical devices that can interact with the target of interest and produce physicochemical signal which is measured by optical, thermal, electron transfer or by electrochemical technique (Chaubey & Malhotra, 2002). Various biosensors are developed throughout the world, but very few are efficient enough to detect biological analytes in picomolar range with high selectivity. Various graphene-based sensors have reported to overcome various drawbacks faced by other biosensors and have reported to be very sensitive due to high charge-carrier mobility and easiness in electron transfer (Ambrosi, Chua, Bonanni, & Pumera, 2014). The edge-plane-like defect sites of graphene provide active sites for electron transfer and also facilitate fluorescence resonance energy transfer (FRET) (Kim, Cote, Kim, & Huang, 2010). Very high surface area enhances electrochemical catalytic activity, thus exhibiting good potentiality in electrochemistry sensing (Shao et al., 2010). Moreover, high conductivity and high transparency of graphene monolayers make them suitable as electrical and optical sensor. The presence of hydrophobic domains or π -systems improves their ability to immobilize biomolecules and helps in target-specific interactions (Szunerits & Boukherroub, 2018). Graphene-based biosensors are often used for detecting DNA, glucose, dopamine, protein, etc. by immunosensing (Fig. 22.3). They are even used for pathogen detection (Jung, Cheon, Liu, Lee, & Seo, 2010). Few of the examples of graphene-based biosensors are elicited in Table 22.1.

Addition of metal oxides into graphene structure enhances sensitivity toward molecular detection with fast response and the biosensors exhibit better electrochemistry without the presence of any other electron mediator (Chen, Zhu, Wu, Han, & Wang, 2010). Graphene/metal oxide nanocomposites-based glucose sensors have gained immense popularity due to high stability, sensitivity, and selectivity with much lower limit of detection (Heller & Feldman, 2008; Toghiani & Compton, 2010). Copper oxide was well known for its application in detection of glucose oxidation and presence of H_2O_2 because of its narrow band gap (1.2 eV), high-electron transfer capacity, great

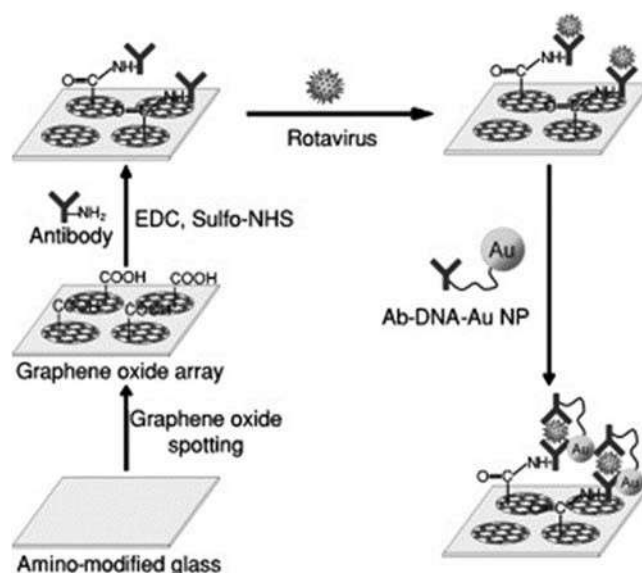


Figure 22.3 Schematic representation of graphene-based immuno-biosensor (Jung et al., 2010).

electrochemical activity, and high surface area (Zhuang et al., 2008). Incorporation of copper oxide into graphene results in a synergistic effects, thus improving sensing capacity (Luo, Zhu, & Wang, 2012). Similarly zinc oxide-graphene nanocomposite has been reported to exhibit high sensitivity with limit of detection for glucose as low as 0.02 mM (Norouzi et al., 2011). Incorporation of low cost metal oxides such as nickel oxide into graphene structure has also gained attention as cost-effective, sensitive electrochemical sensors (Yuan et al., 2013). Ecofriendly, biocompatible graphene/metal oxide biosensors such as titanium dioxide-graphene nanosensor are now gaining lime-light. A report by Luo et al. (2013) shows the excellent performance of rGO-TiO₂ nanocluster in glucose detection with detection limit of 4.8 μM. Other than glucose detection, various other biomolecular sensing has been reported using metal oxide/graphene biosensors. Wu et al. (2014) have synthesized mesoporous Fe₃O₄-NH₂-graphene sheet-based electrochemical biosensor to detect the presence of smaller-sized biomolecules such as ascorbic acid, dopamine, and uric acid. The detection limit for ascorbic acid, dopamine, and uric acid was found to be 0.074 μmol/L, 0.126 μmol/L, and 0.056 μmol/L, respectively. Electrogenerated chemiluminescence-based cholesterol biosensor was prepared by Zhang, Yuan, Chai, Wang, and Wu (2013) by depositing cerium oxide on graphene. The sensor was sensitive enough to detect and quantify cholesterol in the linear range of 12.0 μM to 7.2 mM, with a limit of detection of 4.0 μM. Even graphene-metal oxide nanocomposite such as MnO₂-graphene-based nonenzymatic biosensor could successfully detect the presence of H₂O₂ with quite high sensitivity and stability (Li et al., 2010). The MnO₂ deposition enhanced the surface area, thus promoting better electrocatalytic activity.

Table 22.1 Few examples of graphene-based biosensors for different analytes (Szunerits & Boukherroub, 2018).

Analyte	Sensor design	Detection	Limit of detection (LOD)
Glucose	3D graphene foam—Co ₃ O ₄ nanowires	Electrochemistry	20 nM
Glucose	Graphene + GO _x	Field effect transistor	0.1 mM
Glucose	GQDs—bipyridine boronic acid	Fluorescence	1 mM
Dopamine	rGO—polyvinylpyrrolidone	Electrochemistry	0.2 nM
DNA	DNA GO and GQD—ssDNA	Fluorescence resonance energy transfer	75 pM
DNA	Graphene—Au NPs—ssDNA	Surface plasmon resonance	500 aM
DNA	GO nanowalls	Differential pulse voltammetry	9.6 zM
DNA	Graphene	Field effect transistor	10 fM
Lysozyme	Au/PDDA—GO— <i>Micrococcus lysodeikticus</i>	Surface plasmon resonance	3.4 nM
Folic acid	Au—rGO	Differential pulse voltammetry	1 pM
Folic acid	Graphene	Surface plasmon resonance	5 fM
β-Amyloid	Magnetic/plasmonic GO	Surface-enhanced Raman substrate	100 fg/mL
Prostate-specific antigen	rGO	Field effect transistor	1 fM
<i>Escherichia coli</i>	Graphene—anti- <i>E. coli</i>	Field effect transistor	10 cfu/mL

22.4 Graphene-based nanocomposites for gene and drug delivery

Accurate designing and fabrication of efficient gene and drug delivery systems with ability for controlled release have always been a significant concern in biomedical science (Fig. 22.4). With the discovery of graphene, various studies were conducted regarding successful drug delivery using graphene-based nanocomposites (Su et al., 2015; Wang et al., 2015; Zhang, Wang, & Zhai, 2016). Graphene or graphene-based materials can act as a suitable carrier for drugs (Zhang, Xia, Zhao, Liu, & Zhang, 2010). TiO₂-ZnO nanohybrid was found to be a highly potential anticancer

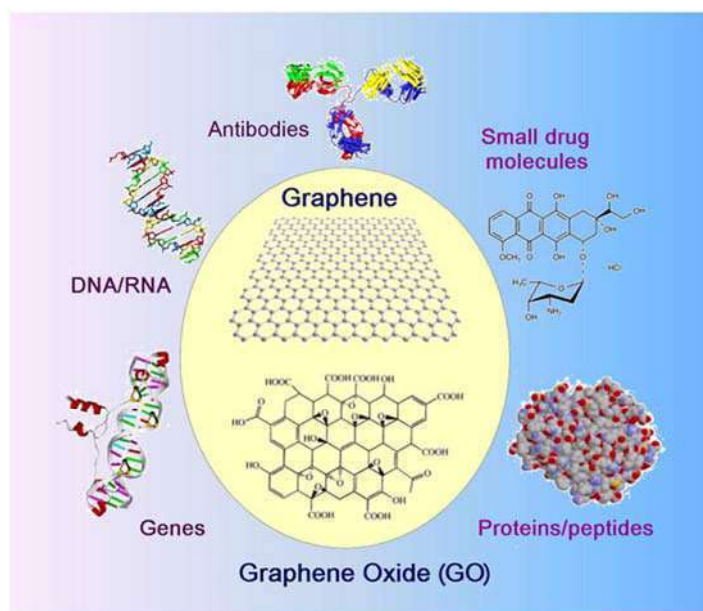


Figure 22.4 Schematic illustration of application of graphene-based materials for drug and various biomolecule delivery (Liu, Cui, & Losic, 2013).

agent (Rasmussen, Martinez, Louka, & Wingett, 2010). Hence Zamani et al. (2018) have designed an effective and efficient drug delivery system by incorporating $\text{TiO}_2\text{-ZnO}$ into GO for slow and sustained colon-specific release. In another report by Fan, Jiao, Gao, Jin, and Li (2013), biocompatible hybrid of Fe_3O_4 -graphene-CNT was prepared for controlled delivery of anticancer drugs with a high loading capacity (0.27 mg/mg).

Since graphene-based materials exhibit unique interactions with DNA and RNA, graphene nanocomposite-based DNA or RNA sensing and delivery have gathered tremendous attention. DNA has a tendency to interact with negative charge of graphene-based materials which enhances DNA adsorption, preferentially single-stranded (ss) DNA adsorption (Ren et al., 2010).

22.5 Metal oxide-modified graphene nanostructures for antibacterial applications

Antibacterial materials are gaining importance in various sectors such as prevention of diseases, prevention of biofilm growth, wastewater management, and especially in biomedical fields. Various antibacterial agents are explored throughout the world, but most of them are either complex or suffers drawback such as secondary toxicity. Hence graphene-based materials have gained

prominence due to its unique morphological properties. The dimensions of graphene are suitable enough to provide extensive coverage to cell surfaces (Upadhyay, Soin, & Roy, 2014), thus exhibiting antibacterial effects. Graphene sheets ($>0.4 \text{ mm}^2$) have the capability of covering the whole bacterial cells blocking all the available active sites, thus inhibiting cell proliferation. Certain metal oxide nanoparticles such as zinc oxide (ZnO), silver oxide (Ag_2O), titanium dioxide (TiO_2), and magnesium oxide (MgO) have been reported earlier to possess antimicrobial activity (Azam et al., 2012; Besinis, De Peralta, & Handy, 2014; Emami-Karvani & Chehrizi, 2011). The surface properties of graphene elevate the antibacterial efficacy of the metal oxides (Kumar, Shaikshavali, Srikanth, & Sankara Rao, 2013) and provide better possibility to penetrate the bacterial membrane to inhibit bacterial growth. Table 22.2 shows some of the examples of antibacterial activity of metal oxide-graphene-based nanocomposites.

22.6 Graphene-based wearable devices for biomedical applications

Wearable devices are a class of device that can be placed over human skin having extraordinary applicability. These new-age devices are flexible and advantageous over conventional rigid devices due to their flexibility and ease of access. Graphene is known to be a smart material for wearable electronics, flexible solar cells, and other energy-harvesting devices (Jang et al., 2016).

Previously, researchers have introduced pure graphene-based wearable biomedical devices such as electrogram monitoring system, heart activity monitoring device, body temperature meter, etc. (Huang et al., 2019; Liu, Pharr, & Salvatore, 2017; Liu et al., 2018). These wearable devices are designed to function alongside the human body or clothes (Mohan, Lau, Hui, & Bhattacharyya, 2018). Recent progress of modified graphene with various metallic and metal oxide nanoparticles is advantageous over pure graphene and enables us with numerous wearable biomedical applications (Kim & Ahn, 2017; Yang, Yang, Tan, & Yuan, 2017). Singh et al. (2020) reported a ZnO-doped graphene-epoxy thin film, which could be used in diverse biomedical applications such as electroactive sensing of glucose, cytochrome c, and cancer cells. Besides, this novel thin film is capable of high-frequency applications, such as ultrasound imaging or MRI. The high-electron transport property of graphene played a pivotal role to reduce the signal-to-noise ratio for better biosensing applications. Similarly, conductive polyoxometalate (POM) equipped with 2D graphene nanosheets was utilized by Xie, Zhang, Wang, Wang, and Wang (2019) to monitor pulse beats by using electrochemical method. This wearable device is super capacitive and insertion of POM into 2D graphene sheets enhanced its storage capacity remarkably, which in turn enriched the sensitivity of the device. Another excellent contribution has been made by Xiao et al. (2012) showing platinum nanoparticle and MnO_2 framework loaded

Table 22.2 Few examples of antibacterial activity of metal oxide/graphene-based nanocomposites.

Material	Hybrid component (metal oxide)	Type of interaction	Bacteria	References
Graphene	ZnO	Van der Waals	<i>Escherichia coli</i>	Kavitha, Gopalan, Lee, and Park (2012)
Graphene	ZnO	Van der Waals	<i>Streptococcus mutans</i>	Kulshrestha, Khan, Meena, Singh, and Khan (2014)
Graphene	ZnO	Van der Waals	<i>E. coli, Salmonella typhi</i>	Bykkam et al. (2015)
Graphene	TiO ₂	Covalent	<i>E. coli</i>	Cao, Cao, Dong, Gao, and Wang (2013)
Graphene	TiO ₂	Covalent	<i>Staphylococcus aureus, E. coli, Candida albicans</i> (fungi)	Karimi, Yazdanshenas, Khajavi, Rashidi, and Mirjalili (2014)
Graphene	TiO ₂	Covalent	<i>S. aureus, E. coli, C. albicans</i> (fungi)	Karimi, Yazdanshenas, Khajavi, Rashidi, and Mirjalili (2015)
Graphene	Au-TiO ₂	Covalent/ Van der Waals	<i>Rhodospseudomonas palustris, E. coli, Candida</i> (fungi)	He, Huang, Yan, and Zhu (2013)
Graphene	Fe ₃ O ₄	Van der Waals	<i>E. coli</i>	Santhosh et al. (2014)
Graphene	SnO ₂	Van der Waals	<i>Pseudomonas aeruginosa,</i>	Mohan and Manoj (2019)
Graphene oxide	SnO ₂		<i>S. aureus</i>	Qiu, Liu, Zhu, and Liu (2018)
Graphene	Fe ₃ O ₄ -TiO ₂		<i>E. coli</i>	Zhou, Zou, and Chen (2020)

free-standing film of rGO for H₂O₂ detection in living cells. This work is beneficial for detecting reactive oxygen species in cells to understand cellular functionalities. The large surface area of MnO₂ framework and high electrical transport property of graphene herein are responsible for excellent sensitivity and selectivity toward H₂O₂. In addition, this work provides an insight into the flexible electrodes for a wide-scale application in biosensing, bioelectronics, and lab-on-a-chip devices.

References

- Abbott's, I. E. (2007). Graphene: Exploring carbon flatland. *Physics Today*, 60(8), 35.
- Ambrosi, A., Chua, C. K., Bonanni, A., & Pumera, M. (2014). Electrochemistry of graphene and related materials. *Chemical Reviews*, 114(14), 7150–7188.
- Azam, A., Ahmed, A. S., Oves, M., Khan, M. S., Habib, S. S., & Memic, A. (2012). Antimicrobial activity of metal oxide nanoparticles against gram-positive and gram-negative bacteria: A comparative study. *International Journal of Nanomedicine*, 7, 6003.
- Balandin, A. A., Ghosh, S., Bao, W., Calizo, I., Teweldebrhan, D., Miao, F., & Lau, C. N. (2008). Superior thermal conductivity of single-layer graphene. *Nano Letters*, 8(3), 902–907.
- Bardhan, S., Roy, S., Chanda, D. K., Mondal, D., Das, S., & Das, S. (2021). Flexible and reusable carbon dot decorated natural microcline membrane: a futuristic probe for multiple heavy metal induced carcinogen detection. *Microchimica Acta*, 188(4). <https://doi.org/10.1007/s00604-021-04787-0>.
- Besinis, A., De Peralta, T., & Handy, R. D. (2014). The antibacterial effects of silver, titanium dioxide and silica dioxide nanoparticles compared to the dental disinfectant chlorhexidine on *Streptococcus mutans* using a suite of bioassays. *Nanotoxicology*, 8(1), 1–6.
- Brumfiel, G. (2009). Graphene gets ready for the big time. *Nature*, 458, 390–391.
- Bykkam, S., Narsingam, S., Ahmadipour, M., Dayakar, T., Rao, K. V., Chakra, C. S., & Kalakotla, S. (2015). Few layered graphene sheet decorated by ZnO nanoparticles for anti-bacterial application. *Superlattices and Microstructures*, 83, 776–784.
- Cao, B., Cao, S., Dong, P., Gao, J., & Wang, J. (2013). High antibacterial activity of ultrafine TiO₂/graphene sheets nanocomposites under visible light irradiation. *Materials Letters*, 93, 349–352.
- Chaubey, A., & Malhotra, B. (2002). Mediated biosensors. *Biosensors and Bioelectronics*, 17(6–7), 441–456.
- Chen, S., Zhu, J., Wu, X., Han, Q., & Wang, X. (2010). Graphene oxide-MnO₂ nanocomposites for supercapacitors. *ACS Nano*, 4(5), 2822–2830.
- Chen, X. M., Wu, G. H., Jiang, Y. Q., Wang, Y. R., & Chen, X. (2011). Graphene and graphene-based nanomaterials: The promising materials for bright future of electroanalytical chemistry. *Analyst*, 136(22), 4631–4640.
- Chong, Y., Ge, C., Yang, Z., Garate, J. A., Gu, Z., Weber, J. K., ... Zhou, R. (2015). Reduced cytotoxicity of graphene nanosheets mediated by blood-protein coating. *ACS Nano*, 9(6), 5713–5724.
- Choucair, M., Thordarson, P., & Stride, J. A. (2009). Gram-scale production of graphene based on solvothermal synthesis and sonication. *Nature Nanotechnology*, 4(1), 30.
- Coleman, B. R., Knight, T., Gies, V., Jakubek, Z. J., & Zou, S. (2017). Manipulation and quantification of graphene oxide flake size: Photoluminescence and cytotoxicity. *ACS Applied Materials & Interfaces*, 9(34), 28911–28921.
- De Marzi, L., Ottaviano, L., Perrozzi, F., Nardone, M., Santucci, S., De Lapuente, J., ... Poma, A. (2014). Flake size-dependent cyto and genotoxic evaluation of graphene oxide on in vitro A549, CaCo₂ and vero cell lines. *Journal of Biological Regulators and Homeostatic Agents*, 28(2), 281–289.
- Dimiev, A. M., & Eigler, S. (2016). *Graphene oxide: Fundamentals and applications*. Hoboken: Wiley.

- Emami-Karvani, Z., & Chehrazi, P. (2011). Antibacterial activity of ZnO nanoparticle on gram-positive and gram-negative bacteria. *African Journal of Microbiology Research*, 5(12), 1368–1373.
- Fan, X., Jiao, G., Gao, L., Jin, P., & Li, X. (2013). The preparation and drug delivery of a graphene–carbon nanotube–Fe₃O₄ nanoparticle hybrid. *Journal of Materials Chemistry B*, 1(20), 2658–2664.
- Geim, A. K. (2009). Graphene: Status and prospects. *Science (New York, N.Y.)*, 324(5934), 1530–1534.
- Geim, A. K., & Novoselov, K. S. (2010). The rise of graphene. In *Nanoscience and technology: A collection of reviews from nature journals* (pp. 11–19). Singapore: World Scientific.
- Ghosal, K., & Sarkar, K. (2018). Biomedical applications of graphene nanomaterials and beyond. *ACS Biomaterials Science & Engineering*, 4(8), 2653–2703.
- Gilje, S., Han, S., Wang, M., Wang, K. L., & Kaner, R. B. (2007). A chemical route to graphene for device applications. *Nano Letters*, 7(11), 3394–3398.
- Giovannetti, G. A., Khomyakov, P. A., Brocks, G., Karpan, V. V., van den Brink, J., & Kelly, P. J. (2008). Doping graphene with metal contacts. *Physical Review Letters*, 101(2), 026803.
- Govindasamy, M., Wang, S. F., Pan, W. C., Subramanian, B., Ramalingam, R. J., & Al-Lohedan, H. (2019). Facile sonochemical synthesis of perovskite-type SrTiO₃ nanocubes with reduced graphene oxide nanocatalyst for an enhanced electrochemical detection of α -amino acid (tryptophan). *Ultrasonics Sonochemistry*, 56, 193–199.
- He, W., Huang, H., Yan, J., & Zhu, J. (2013). Photocatalytic and antibacterial properties of Au-TiO₂ nanocomposite on monolayer graphene: From experiment to theory. *Journal of Applied Physics*, 114(20), 204701.
- Heller, A., & Feldman, B. (2008). Electrochemical glucose sensors and their applications in diabetes management. *Chemical Reviews*, 108, 2482–2505.
- Hernaez, M., Zamarréño, C. R., Melendi-Espina, S., Bird, L. R., Mayes, A. G., & Arregui, F. J. (2017). Optical fibre sensors using graphene-based materials: A review. *Sensors*, 17(1), 155.
- Hu, K., Kulkarni, D. D., Choi, I., & Tsukruk, V. V. (2014). Graphene-polymer nanocomposites for structural and functional applications. *Progress in Polymer Science*, 39(11), 1934–1972.
- Huang, H., Su, S., Wu, N., Wan, H., Wan, S., Bi, H., & Sun, L. (2019). Graphene-based sensors for human health monitoring. *Frontiers in Chemistry*, 7, 399.
- Huang, X., Yin, Z., Wu, S., Qi, X., He, Q., Zhang, Q., . . . Zhang, H. (2011). Graphene-based materials: Synthesis, characterization, properties, and applications. *Small (Weinheim an der Bergstrasse, Germany)*, 7(14), 1876–1902.
- Jang, H., Park, Y. J., Chen, X., Das, T., Kim, M. S., & Ahn, J. H. (2016). Graphene-based flexible and stretchable electronics. *Advanced Materials*, 28(22), 4184–4202.
- Juang, Z. Y., Wu, C. Y., Lu, A. Y., Su, C. Y., Leou, K. C., Chen, F. R., & Tsai, C. H. (2010). Graphene synthesis by chemical vapor deposition and transfer by a roll-to-roll process. *Carbon*, 48(11), 3169–3174.
- Jung, J. H., Cheon, D. S., Liu, F., Lee, K. B., & Seo, T. S. (2010). A graphene oxide based immuno-biosensor for pathogen detection. *Angewandte Chemie*, 122(33), 5844–5847.
- Karimi, L., Yazdanshenas, M. E., Khajavi, R., Rashidi, A., & Mirjalili, M. (2014). Using graphene/TiO₂ nanocomposite as a new route for preparation of electroconductive, self-cleaning, antibacterial and antifungal cotton fabric without toxicity. *Cellulose*, 21(5), 3813–3827.
- Karimi, L., Yazdanshenas, M. E., Khajavi, R., Rashidi, A., & Mirjalili, M. (2015). Optimizing the photocatalytic properties and the synergistic effects of graphene and nano titanium dioxide immobilized on cotton fabric. *Applied Surface Science*, 332, 665–673.

- Kavitha, T., Gopalan, A. I., Lee, K. P., & Park, S. Y. (2012). Glucose sensing, photocatalytic and antibacterial properties of graphene–ZnO nanoparticle hybrids. *Carbon*, *50*(8), 2994–3000.
- Kim, H., & Ahn, J. H. (2017). Graphene for flexible and wearable device applications. *Carbon*, *120*, 244–257.
- Kim, J., Cote, L. J., Kim, F., & Huang, J. (2010). Visualizing graphene based sheets by fluorescence quenching microscopy. *Journal of the American Chemical Society*, *132*(1), 260–267.
- Kulshrestha, S., Khan, S., Meena, R., Singh, B. R., & Khan, A. U. (2014). A graphene/zinc oxide nanocomposite film protects dental implant surfaces against cariogenic *Streptococcus mutans*. *Biofouling*, *30*(10), 1281–1294.
- Kumar, R. N., Shaikshavali, P., Srikanth, V. V., & Sankara Rao, K. B. (2013). Reducing agent free synthesis of graphene from graphene oxide. In *AIP Conference Proceedings* (Vol. 1538, No. 1, pp. 262–265). American Institute of Physics.
- Kurapati, R., Mukherjee, S. P., Martín, C., Bepete, G., Vázquez, E., Pénicaud, A., ... Bianco, A. (2018). Degradation of single-layer and few-layer graphene by neutrophil myeloperoxidase. *Angewandte Chemie*, *57*(36), 11722–11727.
- Li, D., & Kaner, R. B. (2008). Graphene-based materials. *Science (New York, N.Y.)*, *320*(5880), 1170–1171.
- Li, D., Müller, M. B., Gilje, S., Kaner, R. B., & Wallace, G. G. (2008). Processable aqueous dispersions of graphene nanosheets. *Nature Nanotechnology*, *3*(2), 101–105.
- Li, L., Du, Z., Liu, S., Hao, Q., Wang, Y., Li, Q., & Wang, T. (2010). A novel nonenzymatic hydrogen peroxide sensor based on MnO₂/graphene oxide nanocomposite. *Talanta*, *82*(5), 1637–1641.
- Li, N., Wang, Z., Zhao, K., Shi, Z., Gu, Z., & Xu, S. (2010). Large scale synthesis of N-doped multi-layered graphene sheets by simple arc-discharge method. *Carbon*, *48*(1), 255–259.
- Li, X., Wang, X., Zhang, L., Lee, S., & Dai, H. (2008). Chemically derived, ultrasmooth graphene nanoribbon semiconductors. *Science (New York, N.Y.)*, *319*(5867), 1229–1232.
- Liu, H., Liu, Y., & Zhu, D. (2011). Chemical doping of graphene. *Journal of Materials Chemistry*, *21*(10), 3335–3345.
- Liu, J., Cui, L., & Losic, D. (2013). Graphene and graphene oxide as new nanocarriers for drug delivery applications. *Acta Biomaterialia*, *9*(12), 9243–9257.
- Liu, N., Luo, F., Wu, H., Liu, Y., Zhang, C., & Chen, J. (2008). One-step ionic-liquid-assisted electrochemical synthesis of ionic-liquid-functionalized graphene sheets directly from graphite. *Advanced Functional Materials*, *18*(10), 1518–1525.
- Liu, Y., Pharr, M., & Salvatore, G. A. (2017). Lab-on-skin: A review of flexible and stretchable electronics for wearable health monitoring. *ACS Nano*, *11*(10), 9614–9635.
- Liu, Y., Wang, H., Zhao, W., Zhang, M., Qin, H., & Xie, Y. (2018). Flexible, stretchable sensors for wearable health monitoring: Sensing mechanisms, materials, fabrication strategies and features. *Sensors*, *18*(2), 645.
- Luo, L., Zhu, L., & Wang, Z. (2012). Nonenzymatic amperometric determination of glucose by CuO nanocubes–graphene nanocomposite modified electrode. *Bioelectrochemistry (Amsterdam, Netherlands)*, *88*, 156–163.
- Luo, Z., Ma, X., Yang, D., Yuwen, L., Zhu, X., Weng, L., & Wang, L. (2013). Synthesis of highly dispersed titanium dioxide nanoclusters on reduced graphene oxide for increased glucose sensing. *Carbon*, *57*, 470–476.
- McAllister, M. J., Li, J. L., Adamson, D. H., Schniepp, H. C., Abdala, A. A., Liu, J., ... Aksay, I. A. (2007). Single sheet functionalized graphene by oxidation and thermal

- expansion of graphite. *Chemistry of Materials: A Publication of the American Chemical Society*, 19(18), 4396–4404.
- Mitra, M., Chatterjee, K., Kargupta, K., Ganguly, S., & Banerjee, D. (2013). Reduction of graphene oxide through a green and metal-free approach using formic acid. *Diamond and Related Materials*, 37, 74–79. <https://doi.org/10.1016/j.diamond.2013.05.003>.
- Mohan, A. N., & Manoj, B. (2019). Surface modified graphene/SnO₂ nanocomposite from carbon black as an efficient disinfectant against *Pseudomonas aeruginosa*. *Materials Chemistry and Physics*, 232, 137–144.
- Mohan, V. B., Lau, K. T., Hui, D., & Bhattacharyya, D. (2018). Graphene-based materials and their composites: A review on production, applications and product limitations. *Composites Part B: Engineering*, 142, 200–220.
- Mohd Yazid, S. N., Md Isa, I., Abu Bakar, S., Hashim, N., Ab., & Ghani, S. (2014). A review of glucose biosensors based on graphene/metal oxide nanomaterials. *Analytical Letters*, 47(11), 1821–1834.
- Muthurasu, A., Dhandapani, P., & Ganesh, V. (2016). Facile and simultaneous synthesis of graphene quantum dots and reduced graphene oxide for bio-imaging and supercapacitor applications. *New Journal of Chemistry*, 40(11), 9111–9124.
- Niyogi, S., Bekyarova, E., Itkis, M. E., McWilliams, J. L., Hamon, M. A., & Haddon, R. C. (2006). Solution properties of graphite and graphene. *Journal of the American Chemical Society*, 128(24), 7720–7721.
- Norouzi, P., Ganjali, H., Larijani, B., Ganjali, M. R., Faridbod, F., & Zamani, H. A. (2011). A glucose biosensor based on nanographene and ZnO nanoparticles using FFT continuous cyclic voltammetry. *International Journal of Electrochemical Science*, 6(11), 5189–5195.
- Novoselov, K. S., Geim, A. K., Morozov, S. V., Jiang, D., Katsnelson, M. I., Grigorieva, I., ... Firsov, A. A. (2005). Two-dimensional gas of massless Dirac fermions in graphene. *Nature*, 438(7065), 197–200.
- Novoselov, K. S., Geim, A. K., Morozov, S. V., Jiang, D., Zhang, Y., & Dubonos, S. V. (2004). Grigorieva IV, Firsov AA. Electric field effect in atomically thin carbon films. *Science (New York, N.Y.)*, 306(5696), 666–669.
- Ou, L., Song, B., Liang, H., Liu, J., Feng, X., Deng, B., ... Shao, L. (2016). Toxicity of graphene-family nanoparticles: A general review of the origins and mechanisms. *Particle and Fibre Toxicology*, 13(1), 1–24.
- Qiu, J., Liu, L., Zhu, H., & Liu, X. (2018). Combination types between graphene oxide and substrate affect the antibacterial activity. *Bioactive Materials*, 3(3), 341–346.
- Rajeshkumar, S., & Veena, P. (2018). *Biomedical applications and characteristics of graphene nanoparticles and graphene-based nanocomposites. Exploring the realms of nature for nanosynthesis* (pp. 341–354). Cham: Springer.
- Ranjbartoreh, A. R., Wang, B., Shen, X., & Wang, G. (2011). Advanced mechanical properties of graphene paper. *Journal of Applied Physics*, 109(1), 014306.
- Rasmussen, J. W., Martinez, E., Louka, P., & Wingett, D. G. (2010). Zinc oxide nanoparticles for selective destruction of tumor cells and potential for drug delivery applications. *Expert Opinion on Drug Delivery*, 7(9), 1063–1077.
- Ren, H., Wang, C., Zhang, J., Zhou, X., Xu, D., Zheng, J., ... Zhang, J. (2010). DNA cleavage system of nanosized graphene oxide sheets and copper ions. *ACS Nano*, 4(12), 7169–7174.
- Roy, S., Bardhan, S., Chanda, D. K., Roy, J., Mondal, D., & Das, S. (2020). In situ-grown Cd-dot-wrapped Boehmite nanoparticles for Cr (VI) sensing in wastewater and a theoretical probe for chromium-induced carcinogen detection. *ACS Applied Materials & Interfaces*, 12(39), 43833–43843. <https://doi.org/10.1021/acsami.0c13433>.

- Russier, J., Treossi, E., Scarsi, A., Perrozzi, F., Dumortier, H., Ottaviano, L., . . . Bianco, A. (2013). Evidencing the mask effect of graphene oxide: A comparative study on primary human and murine phagocytic cells. *Nanoscale*, 5(22), 11234–11247.
- Santhosh, C., Kollu, P., Doshi, S., Sharma, M., Bahadur, D., Vanchinathan, M. T., . . . Grace, A. N. (2014). Adsorption, photodegradation and antibacterial study of graphene-Fe₃O₄ nanocomposite for multipurpose water purification application. *RSC Advances*, 4(54), 28300–28308.
- Shao, Y., Wang, J., Wu, H., Liu, J., Aksay, I. A., & Lin, Y. (2010). Graphene based electrochemical sensors and biosensors: A review. *Electroanalysis*, 22(10), 1027–1036.
- Sharma, P., Hussain, N., Das, M. R., Deshmukh, A. B., Shelke, M. V., Szunerits, S., & Boukherroub, R. (2014). Metal oxide-graphene nanocomposites: Synthesis to applications. In Handbook of research on nanoscience. *nanotechnology, and advanced materials*, 196–225.
- Shen, J., Hu, Y., Li, C., Qin, C., & Ye, M. (2009). Synthesis of amphiphilic graphene nanoplatelets. *Small (Weinheim an der Bergstrasse, Germany)*, 5(1), 82–85.
- Shi, L., Chen, J., Teng, L., Wang, L., Zhu, G., Liu, S., . . . Ren, L. (2016). The antibacterial applications of graphene and its derivatives. *Small (Weinheim an der Bergstrasse, Germany)*, 12(31), 4165–4184.
- Shi, X., Chang, H., Chen, S., Lai, C., Khademhosseini, A., & Wu, H. (2012). Regulating cellular behavior on few-layer reduced graphene oxide films with well-controlled reduction states. *Advanced Functional Materials*, 22(4), 751–759.
- Singh, M., Kumar, S., Zoghi, S., Cervantes, Y., Sarkar, D., Ahmed, S., . . . Banerjee, S. (2020). Fabrication and characterization of flexible three-phase ZnO-graphene-epoxy electro-active thin-film nanocomposites: Towards applications in wearable biomedical devices. *Journal of Composites Science*, 4(3), 88.
- Stankovich, S., Piner, R. D., Chen, X., Wu, N., Nguyen, S. T., & Ruoff, R. S. (2006). Stable aqueous dispersions of graphitic nanoplatelets via the reduction of exfoliated graphite oxide in the presence of poly (sodium 4-styrenesulfonate). *Journal of Materials Chemistry*, 16(2), 155–158.
- Stengl, V., Popelková, D., & Vlácil, P. (2011). TiO₂-graphene nanocomposite as high performance photocatalysts. *The Journal of Physics Chemistry C*, 115(51), 25209–25218.
- Su, Z., Shen, H., Wang, H., Wang, J., Li, J., Nienhaus, G. U., . . . Wei, G. (2015). Motif-designed peptide nanofibers decorated with graphene quantum dots for simultaneous targeting and imaging of tumor cells. *Advanced Functional Materials*, 25(34), 5472–5478.
- Szunerits, S., & Boukherroub, R. (2018). Graphene-based biosensors. *Interface Focus*, 8(3), 20160132.
- Tadyszak, K., Wychowanec, J. K., & Litowczenko, J. (2018). Biomedical applications of graphene-based structures. *Nanomaterials*, 8(11), 944.
- Toghill, K. E., & Compton, R. G. (2010). Electrochemical non-enzymatic glucose sensors: A perspective and an evaluation. *International Journal of Electrochemical Science*, 5(9), 1246–1301.
- Upadhyay, R. K., Soin, N., & Roy, S. S. (2014). Role of graphene/metal oxide composites as photocatalysts, adsorbents and disinfectants in water treatment: A review. *RSC Advances*, 4(8), 3823–3851.
- Wang, D., Kou, R., Choi, D., Yang, Z., Nie, Z., Li, J., . . . Liu, J. (2010). Ternary self-assembly of ordered metal oxide-graphene nanocomposites for electrochemical energy storage. *ACS Nano*, 4(3), 1587–1595.
- Wang, J., Ouyang, Z., Ren, Z., Li, J., Zhang, P., Wei, G., & Su, Z. (2015). Self-assembled peptide nanofibers on graphene oxide as a novel nanohybrid for biomimetic mineralization of hydroxyapatite. *Carbon*, 89, 20–30.

- Wang, L., Zhang, Y., Wu, A., & Wei, G. (2017). Designed graphene-peptide nanocomposites for biosensor applications: A review. *Analytica Chimica Acta*, 8(985), 24–40.
- Wu, D., Li, Y., Zhang, Y., Wang, P., Wei, Q., & Du, B. (2014). Sensitive electrochemical sensor for simultaneous determination of dopamine, ascorbic acid, and uric acid enhanced by amino-group functionalized mesoporous Fe₃O₄@ graphene sheets. *Electrochimica Acta*, 116, 244–249.
- Wu, J., Pisula, W., & Müllen, K. (2007). Graphenes as potential material for electronics. *Chemical Reviews*, 107(3), 718–747.
- Wu, X., Pei, Y., & Zeng, X. C. (2009). B2C graphene, nanotubes, and nanoribbons. *Nano Letters*, 9(4), 1577–1582.
- Xiao, F., Li, Y., Zan, X., Liao, K., Xu, R., & Duan, H. (2012). Growth of metal-metal oxide nanostructures on freestanding graphene paper for flexible biosensors. *Advanced Functional Materials*, 22(12), 2487–2494.
- Xie, T., Zhang, L., Wang, Y., Wang, Y., & Wang, X. (2019). Graphene-based supercapacitors as flexible wearable sensor for monitoring pulse-beat. *Ceramics International*, 45(2), 2516–2520.
- Yang, Y., Yang, X., Tan, Y., & Yuan, Q. (2017). Recent progress in flexible and wearable bio-electronics based on nanomaterials. *Nano Research*, 10(5), 1560–1583.
- Yuan, B., Xu, C., Deng, D., Xing, Y., Liu, L., Pang, H., & Zhang, D. (2013). Graphene oxide-nickel oxide modified glassy carbon electrode for supercapacitor and nonenzymatic glucose sensor. *Electrochimica Acta*, 88, 708–712.
- Zamani, M., Rostami, M., Aghajanzadeh, M., Manjili, H. K., Rostamizadeh, K., & Danafar, H. (2018). Mesoporous titanium dioxide@ zinc oxide–graphene oxide nanocarriers for colon-specific drug delivery. *Journal of Material Science*, 53(3), 1634–1645.
- Zhang, B., Wang, Y., & Zhai, G. (2016). Biomedical applications of the graphene-based materials. *Materials Science and Engineering C*, 61, 953–964.
- Zhang, C., Yuan, Y., Zhang, S., Wang, Y., & Liu, Z. (2011). Biosensing platform based on fluorescence resonance energy transfer from upconverting nanocrystals to graphene oxide. *Angewandte Chemie*, 50(30), 6851–6854.
- Zhang, L., Xia, J., Zhao, Q., Liu, L., & Zhang, Z. (2010). Functional graphene oxide as a nanocarrier for controlled loading and targeted delivery of mixed anticancer drugs. *Small (Weinheim an der Bergstrasse, Germany)*, 6(4), 537–544.
- Zhang, M., Yuan, R., Chai, Y., Wang, C., & Wu, X. (2013). Cerium oxide-graphene as the matrix for cholesterol sensor. *Analytical Biochemistry*, 436(2), 69–74.
- Zheng, Y., Jiao, Y., Ge, L., Jaroniec, M., & Qiao, S. Z. (2013). Two-step boron and nitrogen doping in graphene for enhanced synergistic catalysis. *Angewandte Chemie*, 125(11), 3192–3198.
- Zhou, X., Zou, T., & Chen, R. (2020). Sunlight-triggered dye degradation and antibacterial activity of graphene-iron oxide-titanium dioxide heterostructure nanocomposites. *Journal of Nanoscience and Nanotechnology*, 20(7), 4158–4162.
- Zhuang, Z., Su, X., Yuan, H., Sun, Q., Xiao, D., & Choi, M. M. (2008). An improved sensitivity non-enzymatic glucose sensor based on a CuO nanowire modified Cu electrode. *Analyst*, 133(1), 126–132.



Certificates of Conferences
&
Seminars





CENTRE OF EXCELLENCE, TEQIP-II
IN

PHASE TRANSFORMATION AND PRODUCT CHARACTERISATION
JADAVPUR UNIVERSITY
Two-Day Workshop
ON

Materials Characterisation Techniques

This is to certify that

Prof./Dr./Mr./Ms.....

Sou Saii Baradhan

of.....

Jadavpur University

has participated in the Workshop during 4-5 October, 2016.

Amrita Kundu

Dr. Amrita Kundu
Organizing Secretary

Pravash

Prof. Pravash Chandra Chakraborti
Coordinator, CoE, TEQIP-II



UGC SPONSORED NATIONAL SEMINAR ON

FRONTIERS IN MODERN PHYSICS

21 & 22 November, 2016

Organised by

DEPARTMENT OF PHYSICS JOGAMAYA DEVI COLLEGE
92, Shyamaprasad Mukherjee Road, Kolkata-700 026

In Collaboration with

Centre for Interdisciplinary Research and Education
404B, Jodhpur Park, Kolkata-700 068



Certified that SMT. SOURAVI BARDHAN of

JADAVPUR UNIVERSITY

has participated / presented a paper the seminar.

Balnarichakravarti 22/11/16

BALLARI CHAKRABARTI / RUMA BASU
Convenors

Abhismita Paul 16.11.16
Principal / Teacher-in-charge

CIRE

CENTRE FOR INTERDISCIPLINARY RESEARCH AND EDUCATION

404B, Jodhpur Park, Kolkata – 700068

25th March, 2017

CERTIFICATE OF PARTICIPATION

This is to certify that

Soukavi Bardhan

has contributed through Lecture / Oral Presentation / Poster Presentation / Participation to the success

of the One Day National Symposium on Nanotechnology:

*From Materials to Medicine and their Social Impact held on 25th March, 2017
at Birla Industrial and Technological Museum, Kolkata.*

Pranab

Prof Sanjib Sarkar
President, CIRE



Jadavpur University



University Grants Commission

INTERNATIONAL WORKSHOP ON

“Advanced Hybrid Separation Techniques in Industrial Wastewater Management”

Sponsored by

UGC, under Indo-Norwegian Collaboration program (INCP - 2014)



NTNU
Norwegian University of
Science and Technology

Certificate of Participation

*This is to certify thatSauravi.....Bardhan..... has participated in the
International Workshop on “Advanced Hybrid Separation Techniques in Industrial
Wastewater Management”, held on December 8 - 9, 2017*

Organized by

**Chemical Engineering Department, Jadavpur University
in association with CHEMBridge**

Prof. Gisle Øye

Professor

Dept. of Chemical Engineering

NTNU, Norway

Prof. Kajari Kar Gupta

Head

Chemical Engineering Department

Jadavpur University, Kolkata, India

Prof. Chiranjib Bhattacharjee

Dean, Faculty of Engineering & Technology

Professor & Former Head

Chemical Engineering Department

Jadavpur University, Kolkata, India

EMERGING TRENDS IN CHEMICAL SCIENCES (ETCS-2018)

International Conference on



DEPARTMENT OF CHEMISTRY, DIBRUGARH UNIVERSITY
Dibrugarh, Assam, India.



This is to certify that Prof./Dr./Mr./Ms. **Souravi Bardhan**

of..... **Jadavpur University** attended/presented research paper

(Invited Lecture/Oral/Poster) in the International Conference "Emerging Trends in

Chemical Sciences" held during 26 -28 February, 2018.

(P. Das)
Convener

(S. Konwer)
Co-Convener

(A. Baruah)
Co-Convener



ONE DAY SEMINAR
ON
Recent Trend in Frontier Research in Physics

Organised By :
Department of Physics, Jadavpur University, Kolkata

CERTIFICATE OF PARTICIPATION

This is to certify that Mr./Mrs./Dr./Prof. *Souravi Bardhan*

has participated/presented (oral/poster) a paper entitled

..... In the one day seminar

on "Recent trend in Frontier research in Physics" on 6th March, 2018 held at Department of Physics, Jadavpur University, Kolkata-700 032.

Dr. Sanat Karnakar
Dr. Soumen Mondal
Dr. Abhijit Samanta
Dr. Subrata Sarkar
(Conveners)

Debasish Lohar
Prof. Debasish Lohar
Head, Department of Physics
Jadavpur University



Association of Indian Universities, New Delhi

Central University of Jharkhand, Ranchi

ANVESHAN - 2018

Student Research Convention (Eastern Zone)



This is to certify that Mr/Ms/Dr Sourav Bordhan

S/o / Daughter of Shri Abhijit Bordhan enrolled in PhD

Department / Faculty of Physics of _____ of

_____ University / Institute participated in

Eastern Zone Student Research Convention held at Central University of Jharkhand, Ranchi during February 18-19, 2019.

His / Her Proposal / project entitled Natural Plant Growth for the Nature.

under the category of Basic Sciences.

[Signature]
Dr. Amarendra Pani

Joint Director & Head Research

Association of Indian Universities, New Delhi

[Signature]
Dr. Ajal Singh

Zonal Co-ordinator

Central University of Jharkhand

[Signature]
Prof. Nand Kr. Yadav 'Indu'

Vice-Chancellor

Central University of Jharkhand



ANVESHAN

National Student Research Convention

March 12-14, 2019

Certificate of Participation

This is to Certify that Mr / Ms. Souravi Bardhan.

affiliated with Jadavpur University, Kolkata

_____ has participated in Anveshan: National

Student Research Convention organized by Association of Indian Universities, New Delhi and hosted by Ganpat University, Gujarat during

March 12-14, 2019. He/She presented a Research Project titled NATURAL PLANT RESIN GUM ACACIA

BASED MULTIFUNCTIONAL NANO-DEVICE FOR HEAVY METAL DETECTION AND REMEDIATION:

"FROM THE NATURE, FOR THE NATURE"

under the category of Basic Science

Dr. Amarendra Pani

Chief Convener

Director/(I/c), Research

Association of Indian Universities, New Delhi

Dr. Satyen Parikh

Anveshan Coordinator

Dean, Faculty of Computer Applications

Ganpat University

Dr. Mahendra Sharma

Director General

Ganpat University



IEM-IC-61

International Conference on

Chemical and Environmental Sciences (ICCAES 2019)

Institute of Engineering & Management, Kolkata

CERTIFICATE OF APPRECIATION

Organized by



ENTER FOR DEVELOPMENT OF
ADVANCED COMPUTING

শীর্ষক
CDAC

This is to certify that Prof./Dr./Mr./Mrs./Ms. Souravari B. Akshari of J. U. presented the paper/poster entitled

" Natural satellite morphology mediated sensing of hexavalent chromium "
in ICCAES 2019 held on 19th -21st September, 2019 at Institute of Engineering & Management, Kolkata.

Prabir K Das
Prabir Kumar Das
Conference Chair,
Institute of Engineering
& Management

Rishi
Rakoli Dutta
Convener,
Institute of Engineering
& Management

She. Tina De
Convener,
Institute of Engineering
& Management



NATIONAL SEMINAR

On

Physics at Surfaces and Interfaces of Soft Materials (PSISM-2019)

Organised by Condensed Matter Physics Research Centre,
Department of Physics, Jadavpur University, Kolkata – 700032.

CERTIFICATE OF PARTICIPATION

This is to certify that Mr./Mrs./Dr./Prof. SOURAJI BARDHAN

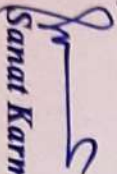
Has participated/presented (oral/poster) a paper entitled Boehmite based 'M.F.N.S.' for

fluorescent sensing & removal: A waste to wealth conversion. In the seminar on

Physics at surfaces and interfaces of soft materials (PSISM-2019) during 26-27th September, 2019 held at

Department of Physics, Jadavpur University, Kolkata – 700032.


Prof. B. D. Chattopadhyay


Dr. Sanat Karmakar
(Conveners)

National Seminar on

New Directions in Physical Sciences 2020 (NDPS 2020)

Organised by

Department of Physics, Jadavpur University
In association with
Indian Photobiology Society



Certificate of Participation

This is to certify that Prof./Dr./Mr./Ms. Soutrav Baradhan of _____

Jadavpur University has participated/presented a poster entitled

Multifunctional Fluorescence Based Nanosensor for Detection and Remedial of Cr(VI) at the

seminar on 'New Directions in Physical Sciences 2020' at Jadavpur University, Kolkata on February 25, 2020.

Dr. Soumen Mondal
Convener, NDPS 2020

Prof. Mitali Mondal
Convener, NDPS 2020

Prof. Sukhen Das
Head, Dept. of Physics

DST-SERB Sponsored

One Day Workshop on Material Synthesis & Characterization Techniques

Organized by: Department of Physics, Jadavpur University, Kolkata-700032



Certificate of Presentation

This Certificate is awarded to

*Mr/ Ms. . Souravi . Baridhar for successfully presenting a paper entitled
Natural . Nanoparticle . Based . Waste . Water . Remediation in the Workshop organized by
Department of Physics, Jadavpur University, Kolkata on 29th February 2020.*

How
29/02/2020

Head, Department of Physics, Jadavpur University



Third International Conference on Material Science (ICMS2020)

04-06 March, 2020

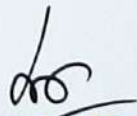
Organized by

Department of Physics
Tripura University (A Central University)
Suryamaninagar-799022, Tripura, India

Certificate of Participation

Certified that Prof./Dr./Mr./Ms. SOURAVI BARDHAN
has participated / presented a paper entitled "Waste capacitor: A fresh
approach... energy harvesting material" in the **Third
International Conference on Material Science (ICMS2020)** organized by
Department of Physics, Tripura University (A Central University)
during 04-06 March, 2020.


(Prof. Debajyoti Bhattacharjee)
Chairman
Local Organizing Committee


(Dr. Syed Arshad Hussain)
Convener
Local Organizing Committee





Certificates of Awards





Association of Indian Universities, New Delhi



Central University of Jharkhand, Ranchi
ANVESHAN - 2018
Student Research Convention (Eastern Zone)



This is to certify that Mr/Ms/Dr Souravi Bardhan

S/o / Daughter of Shri Albhit Bardhan

enrolled in PhD

Department / Faculty of Physics

Jadonpore

University / Institute participated in

Eastern Zone Student Research Convention held at Central University of Jharkhand, Ranchi during February 18-19, 2019.

His / Her Proposal / project entitled Natural Plant Fiber from Waste -- for the Nature

under the category of Basic Sciences and secured First Position.

[Signature]

Dr. Amarendra Pani

Joint Director & Head Research

Association of Indian Universities, New Delhi

[Signature]

Dr. Ajal Singh

Zonal Co-ordinator

Central University of Jharkhand

[Signature]

Prof. Nanda Kr. Yadav 'Indu'

Vice-Chancellor

Central University of Jharkhand



ANVESHAN

National Student Research Convention

March 12-14, 2019

Certificate

This is to Certify that Mr / Ms / Dr. Souravi Barshan,
affiliated with Jadavpur University, Kolkata

participated in **Anveshan: National Student Research**

Convention organized by Association of Indian Universities, New Delhi and hosted by Ganpat University, Gujarat during March 12-14, 2019.

His/Her research project titled Natural plant resin gumm acacia based multifunctional nano- device for heavy metal detection and remediation: "From the nature, for the nature"
under the category of **Basic Sciences** has won **SECOND PRIZE.**

Dr. Amarendra Pani

Chief Convener

Director(I/c), Research

Association of Indian Universities, New Delhi

Dr. Satyen Parikh

Anveshan Coordinator

Dean, Faculty of Computer Applications

Ganpat University

Dr. Mahendra Sharma

Director General

Ganpat University



Connecting Scholars Since 2014

Institute of Scholars

An ISO 9001:2015 certified Institute by International Accurate Certification, Accredited by UASL

Bringing ideas into reality.....



InSc Awards 2020

Certificate

Young Researcher Award 2020

awarded to

Souravi Bardhan

M.Sc

Ph.D Research Scholar
Department of Physics,
Jadavpur University,
Kolkata, West Bengal

For the work with following details:

Publication Type: Journal

Paper Title: Nitrogenous Carbon Dot Decorated Natural Microcline: an Ameliorative Dual Fluorometric Probe For Fe³⁺ And Cr⁶⁺ Detection.

Journal Name: Dalton Transactions

Volume: 49

Issue No.: 30

Month of Publication: July

Year: 2020

Page No.: 10554-10566

ISSN: 1477-9226

A handwritten signature in black ink, appearing to read 'Nanjesh Bennur'.

Nanjesh Bennur
Director, InSc